Universitat de Girona

INTERMITTENCY OF TURBULENCE IN NATURAL WATERS: PATCHINESS IN THE THERMOCLINE OF A LAKE UNDER LOW WINDS AND SMALL-SCALE INTERMITTENCY IN THE BOTTOM BOUNDARY LAYER OF A TIDAL FLOW

Jesús PLANELLA MORATÓ

Dipòsit legal: Gi. 1920-2015
http://hdl.handle.net/10803/320432

Universitat de Girona

DOCTORAL THESIS

INTERMITTENCY OF TURBULENCE IN NATURAL WATERS

Patchiness in the Thermocline of a Lake under Low Winds

and

Small-scale Intermittency in the Bottom Boundary Layer of a Tidal Flow

Jesús Planella-Morató

2015

DOCTORAL THESIS

INTERMITTENCY OF TURBULENCE IN NATURAL WATERS

Patchiness in the Thermocline of a Lake under Low Winds

and

Small-scale Intermittency in the Bottom Boundary Layer of a Tidal Flow

Doctoral Programme in Experimental Sciences and Sustainability

Jesús Planella-Morató

Supervisor:

Elena Roget i Armengol

2015

Thesis submitted for the degree of Doctor of Philosophy by the University of Girona

ELENA ROGET I ARMENGOL, Professora titular de la Universitat de Girona del Departament de Física de la Universitat de Girona,

CERTIFICA:

Que en **Jesús Planella i Morató**, ha dut a terme sota la meva direcció el treball que aquí es presenta, i que du per títol *Intermittency of Turbulence in Natural Waters: Patchiness in the Thermocline of a Lake under Low Winds and Small-Scale Intermittency in the Bottom Boundary Layer of a Tidal Flow*, a fi d'optar al grau de Doctor amb Menció Internacional pel programa de Doctorat de Ciències Experimentals i Sostenibilitat.

I perquè així consti, signo aquest certificat.

Doctora Elena Roget i Armengol

Girona, Setembre 2014

'And during this trip I was fascinated by two amazing eddies:

One was very intermittent, but splendorous while here. Brighter than most, I could not stop watching it, captivated by the light until suddenly, its existence weakened. Weakened so as almost to disappear… but no, it returned and showed its light once again. It was spectacular. Then one day it decided not to come. I do miss it a lot from here.

The other is still near. Strengthened over time. I feel its power; it is beautiful and majestic. I see the light shinning through and I am overjoyed to see its brilliance grow everyday. Maybe something is feeding it….'

To my parents, with love

ABSTRACT

Turbulence intermittency in natural waters is particularly relevant as it influences so many different processes on a wide range of scales, consequently affecting the transport of mass, moment and solutes. Measuring turbulence in natural water systems is still difficult to perform however, and even more so when focusing on intermittency which, depending on the scales, is defined as external (large scales) or internal (small scales). In this work, and based on two different experimental datasets suitable for describing both types of intermittency, we sought to enhance the knowledge regarding each of these two views independently.

The study of external intermittency attempts to broaden the actual state of knowledge by analysing turbulent events in a situation which has yet to be studied in depth. We present the analysis of new measurements taken in Lake Banyoles during the summer and in light wind conditions (<3 $m \cdot s^{-1}$). Powerful wind gusts (wind speeds above 6 $m \cdot s^{-1}$) of an episodic nature which occurred during the study period were also analysed. Turbulent patches were detected by using a new methodology based on small-scale measurements of temperature and shear. Patches were determined based on inspection of pairs of Thorpe displacement and shear profiles, and criteria related to accuracy of the sensors and noise level of the signal. Then, the analysis using Thorpe scales was performed within the patch, which in turn provided new and far more realistic results in comparison to other studies.

We mainly focused on the thermocline of the lake, where shear-induced turbulence is patchy. Data confirmed that the distribution of the patch size h_p is log-normal with the mean and median values being 0.69 m and 0.50 m, respectively. The distribution of the patch Thorpe L_{Tp} scale within the patches also fits to a log-normal model. However, the probability distribution of the normalized Thorpe L_{Tp}/h_p scale is better approximated by the Weibull probability model with a shape parameter $c_w \approx 2$, and also by the beta

probability distribution which coincides with the Weibull model for the upper 95% of the entire data set. For h_p > 25 cm, the ratio L_{Tp}/h_p depends on the patch Richardson and the mixing Reynolds numbers following the parameterization proposed by Lozovatsky and Fernando (2002) for patches detected in ocean and marine coastal waters.

Based on the patch analysis, the averaged vertical diffusivities in the thermocline were found to range from ~$1 \cdot 10^{-4}$ $m^2 s^{-1}$ to ~$5 \cdot 10^{-5}$ $m^2 s^{-1}$, depending on the phase of the dominating internal wave mode on the lake. Episodic wind gusts transfer ~1.6% of the wind energy to the thermocline and ~0.7% to the bottom layer, thus generating large microstructure patches with h_p of several meters.

On the other hand, internal intermittency has been analyzed based on velocity data. Measurements were taken above the bottom in a shallow reversal tidal flow on the continental shelf of the Yellow Sea using an Acoustic Doppler Velocimeter. To the best of our knowledge, this is the first time that this type of analysis using this instrumentation has been performed. The order of magnitude of the mean dissipation rates during measuring ranged between 10^{-7} and 10^{-5} $W \cdot kg^{-1}$.

Structure functions of the vertical component of the velocity and moments of the small-scale dissipation field have been used to characterize internal intermittency. The exponents of the structure functions have been fitted to the log-Lévy and log-normal multifractal models. For energetic episodes (flooding tidal phases) the values of the intermittent parameters are $\tilde{\mu} \approx 0.24$, $\tilde{C}_1 \approx 0.15$ and $\tilde{\alpha} \approx 1.5$, i.e. close to the expected values for fully developed turbulence. However, for relatively low Reynolds numbers the intermittency parameters C_1 and μ deviate from the previous classical values and increase their values up to C_1 ~0.25-0.35 and μ ~0.5-0.6.

These same dependencies in the intermittency parameters of the Reynolds number, i.e. μ, C_1 decreasing with high Reynolds and α decreasing, are also observed from the analysis of the scaling exponents of the moments of the

small-scale dissipation rate ε. A possible explanation for different values obtained from the two methodologies might be related to the estimation of the the small-scale dissipation rate (isotropy).

The large departure of the intermittency parameters from the universal turbulent regime at lower Reynolds number observed in both methods could be attributed to the intermittency of underdeveloped turbulence.

The multifractal analysis using the SF method gives asymptotic values of $\alpha^0 = 1.5$, $C_1^0 = 0.13$ and $\mu^0 = 0.23$ which are close to the results expected for fully developed turbulence, i.e. very high Reynolds numbers. However, the multifractal analysis for the small-scale dissipation field ε, calculated by its isotropic formula, gives asymptotic values that are a little higher; $\alpha_\varepsilon^0 = 1.6$, $C_{1\varepsilon}^0 = 0.20$ and $\mu_\varepsilon^0 = 0.34$. However, it is important to note that the datasets for the estimation of intermittency parameters using the small-scale dissipation field is smaller than that in the SF method and the Reynolds number range is narrow. It could explain the discrepancies observed in both methods.

RESUM

En els sistemes aquàtics naturals el comportament intermitent de la turbulència és d'una gran importància ja que condiciona molts dels processos que s'hi produeixen i a més en un ventall d'escales molt ampli, afectant al transport de massa, de moment i de soluts. Malgrat tot, en aquests sistemes les mesures de turbulència són encara difícils de realitzar i més encara si es té en compte la intermitència, que segons a les escales que afecti pot ser externa (escales grans) o interna (escales petites). En aquest treball s'ha volgut aprofundir en el concepte d'intermitència, en el seu sentit més genèric. Per fer-ho, s'han utilitzat dos conjunts de dades experimentals que han permès tractar de manera independent aquestes dues visions que es té del fenomen de la intermitència.

L'estudi realitzat sobre intermitència externa pretén ampliar el coneixement que se'n té actualment, analitzant episodis turbulents en una situació que fins ara no havia estat estudiada en detall. En el treball es presenta l'anàlisi de noves mesures preses a l'Estany de Banyoles durant l'estiu amb presència de vents febles sota règim de marinada (< 3 $m \cdot s^{-1}$). Durant la campanya es van detectar cops de vent forts esporàdics (amb velocitats superiors a 6 $m \cdot s^{-1}$) detectats durant la campanya i que també han estat analitzats en detall. Els claps turbulents a la columna d'aigua s'han detectat utilitzant un nova metodologia, basada en mesures de microestructura (temperatura i cisallament). Els claps s'han determinat mitjançant l'anàlisi simultània de perfils de desplaçaments de Thorpe i de cisallament, així com criteris relacionats amb la precisió dels sensors i el nivell de soroll al senyal. Un cop detectats, s'ha fet l'anàlisi de les escales de Thorpe en els claps, cosa que ha permès obtenir uns resultats més reals si es comparen amb aquells obtinguts en altres treballs.

L'estudi s'ha centrat en l'estudi dels claps turbulents en el termoclina de l'estany, on aquests es produeixen per cisallament. Les dades han confirmat que

la distribució de la mida dels claps, h_p, és log-normal amb valors de la mitjana i de la mediana per h_p de 0.69 m i 0.5 m respectivament. L'escala de Thorpe, L_{Tp}, avaluada en els claps, també s'ajusta a una distribució log-normal. En canvi, la distribució de l'escala normalitzada de Thorpe, L_{Tp}/h_p, s'aproxima millor a la distribució de Weibull amb paràmetre de forma $c_w \approx 2$ i també a la distribució beta; les dues s'ajusten molt bé a aquestes distribucions per a un 95% del rang de les dades. A més, per claps de mida $h_p > 25$ cm, aquesta escala normalitzada, i.e. L_{Tp}/h_p, segueix bé la parametrització proposada per Lozovatsky i Fernando (2002) determinada partir de claps detectats a l'oceà i a zones marines i costeres.

El valor promig de la difusivitat avaluat en el termoclina i calculat mitjançant l'anàlisi de claps dona valors que oscil·len entre ~ $1 \cdot 10^{-4}$ $m^2 \cdot s^{-1}$ i ~ $5 \cdot 10^{-5}$ $m^2 \cdot s^{-1}$ depenent de la fase del mode dominant de l'ona interna present a l'estany. A més, s'ha determinat que els cops de vent forts i esporàdics observats durant la campanya transfereixen ~ 1.6 % de l'energia del vent a la termoclina i ~0.7 % de la seva energia a la capa de fons, generant claps de microstructura d'uns quants metres dins la columna d'aigua.

D'altra banda també s'ha analitzat la intermitència interna a partir de dades d'un corrent de fons de marea en una zona somera de la placa continental al Mar Grog (nord-est del Mar de la Xina). Les dades han estat obtingudes mitjançant la instrumentació ADV ('Acoustic Doppler Velocimeter'), essent la primera vegada que nosaltres coneguem que es realitza una anàlisi d'aquest tipus en aquests sistemes i amb aquesta instrumentació. L'ordre de magnitud de les dissipacions oscil·lava entre 10^{-7} i 10^{-5} $W \cdot kg^{-1}$.

En l'estudi s'han utilitzat les funcions d'estructura calculades a partir de la component vertical de la velocitat així com els moments de la dissipació d'energia cinètica turbulenta a petita escala per tal de caracteritzar la intermitència interna. Així els exponents de les funcions d'estructura s'han ajustat als models multrifactal basat en la distribució de log-Lévy i al model log-normal. Per aquells casos d'episodis molt energètics, corresponents a les fases de plenamar, els valors dels paràmetres d'intermitència són $\tilde{\mu} \approx 0.24$,

$\tilde{C}_1 \approx 0.15$ and $\tilde{\alpha} \approx 1.5$, molt propers als esperats per turbulència completament desenvolupada. En canvi, per nombre de Reynolds relativament baixos, els paràmetres d'intermitència C_1 i μ es desvien dels valors esperats, augmentant fins a valors de $C_1 \sim 0.25$ - 0.35 i $\mu \sim 0.5$ - 0.6.

Aquestes mateixes dependències per als paràmetres d'intermitència s'han observat a partir de l'anàlisi realitzat amb els exponents d'escalatge obtinguts per als moments de la dissipació d'energia cinètica turbulenta a petita escala (disminució de μ i C_1 i augment de α quan augmenta el nombre de Reynolds). Una possible explicació per a les diferències observades en els valors dels paràmetres d'intermitència obtinguts pels dos mètodes podrien estar relacionats amb l'ús d'aproximacions (isotropia) en el càlcul del camp de dissipació de l'energia cinètica turbulenta a escala petita

Les desviacions dels parametres d'intermitència respecte als valors universals observades que s'han observat per nombre de Reynolds baixos es podrien atribuir al fet que s'estudia intermitència per al cas de turbulència que no està completament desenvolupada.

De l'anàlisi multifractal obtingut mitjançant les funcions d'estructura s'observa que els valors asimptòtics per als paràmetres d'intermitència tendeixen a $\alpha^0 = 1.5$, $C_1^0 = 0.13$ i $\mu^0 = 0.23$, essent valors molt propers als esperats per turbulència completament desenvolupada (és adir, pel cas de nombres de Reynolds molt alts). En canvi, fent-ho a partir dels moments de la dissipació a petita escala, estimada assumint isotropia, s'obtenen uns valors que són una mica superiors: $\alpha_\varepsilon^0 = 1.6$, $C_{1\varepsilon}^0 = 0.20$ i $\mu_\varepsilon^0 = 0.34$. Cal tenir en compte però que el conjunt de segments utilitzats en aquest darrer cas és més reduït i el rang de possibles valors per al nombre de Reynols és més petit, cosa que podria explicar aquestes discrepàncies observades.

RESUMEN

En los sistemas acuáticos naturales el comportamiento intermitente de la turbulencia es de gran importancia ya que condiciona muchos de sus procesos que se producen en él y además en un rango muy amplio de escalas, afectando el transporte de masa, momento y solutos. No obstante, las medidas de turbulencia en estos sistemas son aún difíciles de realizar y todavía más si se considera el efecto de la intermitencia, que según las escalas a las que afecte se identifica como externa (escalas grandes) o interna (escalas pequeñas). Este trabajo pretende profundizar en el concepto de la intermitencia, en su sentido más genérico. Con este fin se han utilizado dos conjuntos de datos experimentales distintos, que han permitido analizar estas dos visiones que se tiene del fenómeno de la intermitencia y de manera independiente.

El estudio realizado sobre intermitencia externa pretende ampliar el conocimiento que se tiene actualmente del fenómeno, analizando los episodios turbulentos en una situación que hasta ahora no se había estudiado con detalle. En el trabajo se presentan y analizan nuevas medidas realizadas en el Lago de Banyoles durante el verano y bajo el régimen de brisas suaves (< 3 m·s^{-1}). Esto incluye también el análisis de ráfagas fuertes de viento y de corta duración (con velocidades superiores a 6 m·s^{-1}) observadas durante la campaña. Los parches de turbulencia se han identificado en la columna de agua mediante una nueva metodología basada en datos de microstructura (temperatura y cizallamiento). Estos parches se determinaron mediante el análisis simultáneo de perfiles de desplazamientos de Thorpe y de cizallamiento, así como usando criterios relacionados con la precisión de los sensores y el nivel de ruido observado en los datos registrados. A partir de éstos se ha analizado la escala de Thorpe en estos parches, que da un enfoque más real a los resultados en comparación con los obtenidos en otros estudios.

El estudio se ha centrado en el estudio de los parches de turbulencia en la termoclina del lago, donde éstos se generan por cizallamiento. Los datos han confirmado que la distribución del tamaño de los parches, h_p, es log-normal (con media y mediana de valor 0.69 m y 0.5 m respectivamente). La escala de Thorpe, L_{Tp}, se ajusta también a una distribución log-normal. No obstante, la distribución de la escala normalizada de Thorpe L_{Tp}/h_p se aproxima mejor a una distribución de Weibull con parámetro de forma $c_w \approx 2$ y también a una distribución beta (las dos ajustan bien para un 95 % del conjunto de los datos). Para parches con tamaño h_p > 25 cm, la escala L_{Tp}/h_p presenta un buen ajuste a la parametrización propuesta por Lozovatsky y Fernando (2002), determinada a partir de parches detectados en el océano y en zonas marinas costeras.

Mediante el análisis de parches de turbulencia se ha calculado el valor promedio de la difusividad en la termoclina y se han obtenido valores que oscilan entre ~$1 \cdot 10^{-4}$ $m^2 \cdot s^{-1}$ y ~$5 \cdot 10^{-5}$ $m^2 \cdot s^{-1}$, dependiendo de la fase del modo dominante de la onda interna presente en el lago. Además, se ha determinado que las ráfagas esporádicas de viento transfieren ~1.6 % de la energía del viento a la termoclina y ~0.7 % de su energía a la capa de fondo, generando episodios turbulentos que abarcan unos cuantos metros en el interior de la columna de agua.

La intermitencia interna ha sido analizada a partir de los datos de una corriente de fondo de marea obtenidos en una zona poco profunda de la placa continental en el Mar Amarillo (noreste del Mar de la China). Los datos se han registrado mediante instrumentación ADV ('Acoustic Doppler Velocimeter') siendo la primera vez, según nuestro conocimiento, que un análisis de este tipo realiza en estos sistemas y con este tipo de instrumentación. El orden de magnitud de las estimaciones de la disipación de la energía cinética turbulenta osciló entre 10^{-7} y 10^{-5} $W \cdot kg^{-1}$.

Para caracterizar la intermitencia interna se han analizado las funciones de estructura calculadas a partir de la componente vertical de la velocidad así como los momentos para la disipación de la energía cinética turbulenta a escalas pequeñas. Los exponentes de las funciones de estructura se han ajustado

a los modelo multifractal basados en las distribución de log-Lévy y al modelo log-normal. Para casos de episodios muy energéticos (fases de pleamar), se han encontrado valores de los parámetros de intermitencia de $\tilde{\mu} \approx 0.24$, $\tilde{C}_1 \approx 0.15$ y $\tilde{\alpha} \approx 1.5$, muy cercanos a los esperados para el caso de turbulencia completamente desarrollada. Por el contrario, cuando el número de Reynolds es relativamente pequeño, los parámetros de intermitencia C_1 y μ se desvían de los valores esperados, y se obtienen valores de C_1 ~0.25-0.35 y μ ~0.5-0.6.

Estas mismas dependencias de los parámetros de intermitencia se han observado a partir del análisis realizado con los exponentes de escalado utilizando los momentos de la disipación a escala pequeña (disminución de μ y C_1 y aumento de α cuando aumenta el número de Reynolds). Una posible explicación a las diferencias observadas para los valores de los parámetros de intermitencia obtenidos mediante los dos métodos podría tener su origen en el uso de aproximaciones (isotropía) en el cálculo de la disipación de la energía cinética turbulenta a escala pequeña.

Las desviaciones de los parámetros de intermitencia respecto a los valores universales para números de Reynolds pequeños podrían atribuirse a que la turbulencia no está completamente desarrollada.

Los valores asintóticos de los parámetros de intermitencia obtenidos mediante el ajuste a una función de los exponentes de las funciones de estructura tienden a $\alpha^0 = 1.5$, $C_1^0 = 0.13$ y $\mu^0 = 0.23$, valores que son muy cercanos a los esperados en el caso de turbulencia completamente desarrollada (correspondientes a números de Reynolds elevados). No obstante, cuando se utilizan los momentos de la disipación a pequeña escala, calculada asumiendo isotropía, se obtienen unos valores que son un poco superiores: $\alpha_\varepsilon^0 = 1.6$, $C_{1\varepsilon}^0 = 0.20$ y $\mu_\varepsilon^0 = 0.34$. No obstante, cabe remarcar que el conjunto de segmentos utilitzados en este último caso es más reducido y el rango de posibles valores para el número de Reynolds es también más pequeño, cosa que podría explicar las discrepancias observadas en los dos métodos.

Acknowledgments

This is the end of a long, long journey. It all started when I received a call asking me if I was interested in teaching physics at the University of Girona. I had been working as a secondary school teacher for ten years and my instincts were telling me to take a step forwards. This work supervised by Dr. Elena Roget is the result of my step forward. Thus, another stage of my life, full of challenges I had never even imagined when I accepted the teaching job at the University, closes.

During that time I have had some very special moments, some difficult times and some incredible experiences. I will always hold these wonderful days and unforgettable stories dear in my memory. During my darkest moments I was fortunate to have the help of so many people who gave me the strength and resolve to move on and never give up. I owe a debt of gratitude to all of you who have made this thesis possible.

First of all, I would like to express my sincere thanks to my supervisor Dr. Elena Roget for her trust and confidence in me. She opened the door and showed me the amazing world of turbulence and I am so indebted to her for sharing her expertise and knowledge. I truly appreciate her support, which helped me to overcome critical situations and finally finish my thesis.

I am also very grateful to Dr Iossif Lozovatsky for his valuable discussions and critical opinions, not only during his stays in Girona, but also during my pre-doctoral stay in the Center of Environmental Fluid Dynamics (CEFD) at Arizona State University (ASU) in Tempe, where I was fortunate to work under his supervision. I would also like to thank Dr Harindra Joseph S. Fernando, the former director of CEFD, for his very warm hospitality. It was indeed a great stay.

I am very thankful to Xavier Sánchez, whom I have had the opportunity to work with in the same research group all through these years, for his good comments and unfailing support. I have learned so many things about

turbulence from him and we have shared some memorable times. Good workmate and dear friend, thanks!

I am very grateful to Lluisa Escoda for her support and good advice. She always has just the right words at just the right time. Thanks also to Marianna Soler, with whom I have shared stories and concerns over our coffee breaks and lunches, and to Laura Carreras: Girl, you know how to give a different approach on things in only just a few minutes! To all of you, you are an incredible team, thanks!

I also wish to thank my office mates and other members of my research group, especially to Jordi Colomer, Josep Massaneda, Marta Peracaula and Teresa Serra for their interest, encouragement and support.

I would like to acknowledge the MEC Spanish Government grant FIS2008-03638, the Catalan Government grant 2009-BE1-00258 and the CLIMSEAS 7FP-IRSES Project (2010-2014) funded by the European Commission for Research, which gave me the opportunity to discuss about data and results during my short stay in Moscow and Kalinningrad. Also thanks to the UdG English Language Service, which partially funded this work and its revision, and especially to Mary Jane Pratt for her comments and invaluable help with the English.

I am deeply grateful to my friends for backing me and helping me to keep moving on. To Núria and Mercè, for being good listeners and also good advisers. I have lost count of how many Saturday afternoon coffees we have shared together at 'L'Enrenou'…a lot! To Albert: you know a lot about this journey, thanks for all your support whenever and wherever and thanks for those lovely dinners with your charming Polish partner Martyna. The great chats with 'Els 6 Magnífics' (Belem and Òscar, Montse and Òscar and…) have been worth it: Yes guys, you are truly incredible! And, not to mention, 'Cafè Dissabte' (Marta and Jordi, Maribel, Montse, Xavier, Sònia and Jordi) and the 'Suai-Suai' teams (Kat, Sònia, Anna, Rita): your dinners (sometimes with presentation included) will never be forgotten. Team 'miniuni' (Anna and Joan, Alba and Òscar, Marta, Jordi, Òscar), I was always able to count on having fun

with you; thanks for everything! And finally, to the two Italian girls, Lívia and Elena, I promise to come back to the beach next year, for sure!

Last but not least, I express my deepest gratitude to my family: my late father Jesus who passed away before the completion of my thesis, my mother Catalina, my four siblings (MaAngels, Helena, Xevi and Cati) and the rest of my family, for their love and full support always. Thank you all for everything.

This is the end of a long, long journey, or maybe not, maybe it is just a stopover along the way. Whatever the road may bring, wherever it may take me, I am looking forward the future.

Agraïments

Aquest és el final d'un llarg, llarg viatge. Vaig tornar-me a trobar amb el món de la Universitat a finals del 2004, quan vaig rebre una trucada per si m'interessava donar classes de Física com a professor associat a la Universitat de Girona. Havia anat a demanar informació sobre cursos de doctorat uns mesos abans, quan el meu cap demanava un pas més després de deu anys en el món de l'Ensenyament. Ara acabo una altra etapa, d'objectius ben diferents als que tenia quan vaig acceptar fer docència a la Universitat, que es tanca amb la finalització de la tesi doctoral que ha estat dirigida per la Dra. Elena Roget.

Durant aquest temps he passat per molts moments, alguns d'ells genials. Tardes increïbles i històries inoblidables en dies de campanya o de feina que me les enduc i les guardo aquí, en el record, per compartir-les quan ens trobem. D'altres moments però han estat difícils i durs, fins i tot diria que crítics, però gràcies a l'ajut de tot un seguit de persones els he pogut superar i seguir endavant amb més força i energia. Són aquestes línies doncs la mostra del meu reconeixement i agraïment per a tots ells.

A l'Elena, la meva directora de tesi, per la confiança dipositada en mi. Per l'orientació, seguiment i supervisió de la tesi, però sobretot per saber motivar-me en la recerca un cop arribat de nou altre cop a la Universitat. Pel

coneixement transmès i pel recolzament i els consells rebuts, alguns d'ells molt importants en moments clau per a mi.

A en Xavier Sánchez, amb qui he tingut l'ocasió també de treballar dins del mateix grup de recerca, pels seus encertats comentaris i savis consells. D'ell he après moltes coses sobre turbulència i amb ell he compartit moltes estones, les últimes al congrés de l'AGU a Viena i les estades a Rússia (al mar Bàltic...memorables!). Bon company i gran amic, seguirem en contacte.

A la Lluïsa Escoda per ser-hi, saber escoltar i tenir la paraula adequada en cada moment. Savis consells també que m'han ajudat a tirar endavant i a veure les coses des d'una altra perspectiva. També a la Marianna Soler, amb qui he compartit històries i maldecaps, gràcies per les estones dedicades entre cafè i cafè, en sopars i sobretot al despatx, i a la Laura Carreras, qui sap bé com fer que 15 minuts la perspectiva de les coses canviï com un mitjó. Sou un bon equip, el millor, gràcies!

A en Jordi Colomer, en Josep Massaneda, la Marta Peracaula i la Teresa Serra, per l'interès mostrat, suport i ànims transmesos en moments que ho necessitava.

Als meus amics, que han estat sempre al meu costat i m'han recolzat en tot moment. D'ells he tret la força i l'energia per tirar endavant i els estic profundament agraït: A la Núria i a la Mercè, quants cafès de dissabte a les 4 h a l'Enrenou! No ho sé...molts! A l'Albert, ei trobador, tu coneixes bé aquest viatge...Gràcies per les estones i els sopars dedicats també amb la Martyna, que és encantadora. Xerrades amenes que han valgut la pena: amb els '6 Magnífics' (Belem i Òscar, Montse i Òscar i...), sí nois sou increïbles!, amb el 'Cafè Dissabte' (Marta and Jordi, Maribel, Montse, Xavier, Sònia and Jordi) i a les 'Suai-Suai' (Kat, Sònia, Anna, Rita i...), sempre recordaré els distrets sopars a vegades amb presentació i fotos incloses, i els 'miniuni' (Marta, Òscar, Alba i Òscar, Anna i Joan, Jordi) per les estones que ens hem divertit plegats per desconnectar una mica del dia a a dia. I finalment a les meves amigues italianes, Lívia i Elena, us prometo tornar a la platja l'any que ve, segur!

Per acabar, el meu agraïment més sincer a la meva família: el meu pare, que ha estat una font d'inspiració i un exemple a seguir per mi, així com la meva mare, pacient i constant, que ha viscut la meva feina de ben a prop en les diferents estades que he fet. També als meus quatre germans (MaAngels, Helena, Xevi and Cati) i la resta de la família per estar sempre al meu costat. Gràcies per tot.

Aquest és el final d'un llarg, llarg viatge. O potser és només una parada a mig camí. Qui sap què ens pot portar el futur...

List of Abbreviations

1D	One Dimensional
2D	Two Dimensional
ADV	Acoustic Doppler Velocimeter
BBL	Bottom Boundary Layer
BL	Bottom Layer
BP	Bottom Patch
CDF	Cumulative Distribution Function
CLT	Central Limit Theorem
CTD	Conductivity Temperature Density
DNS	Direct Numerical Simulation
DTM	Double Trace Method
ECS	East China Sea
erfc	Complimentary error function
ESS	Extended Self-Similarity
FP07	Fastip Probe 07 type
GK tests	Galbraith and Kelley tests
iid	Identical distributed
JG plots	Johnson and Gargett plots
K-S	Komogorov-Smirnov
LHR	Likelihood ratio
LLN	Law of Large Numbers
MAD	Mean Absolute Deviation

max	Maximum
med	Median
min	Minimum
MSS	Microstructure Sea and Sun
PDF	Probability Distribution Function
PK69	Panchev-Kesich 1969
rms	Root mean square
RSH	Refined Self-Similarity
SF	Structure Function
sgn	Sign
SL	Surface Layer
SNR	Signal Noise Ratio
TH	Thermocline
TKE	Turbulent Kinetic Energy
TM	Trace Method
T-S plot	Temperature and Salinity plots
TSF	Transverse Structure Function
UNESCO	United Nations Educational, Scientific and Cultural Organization
V2H1	second Vertical first Horizontal

List of Figures

List of Tables

List of Publications

Lozovatsky, I., E. Roget, J. Planella, H. J. S. Fernando and Z. Liu (2010), Intermittency of near-bottom turbulence in tidal flow on a shallow shelf, *J. Geophys. Res.*, 115, C05006.

Planella Morató, J., E. Roget, and I. Lozovatsky (2011), Statistics of microstructure patchiness in a stratified lake, *J. Geophys. Res.*, 116, C10035.

Sanchez, X., E. Roget, J. Planella, and F. Forcat (2011), Small-scale spectrum of a scalar field in water: The Batchelor and Kraichnan models. *J. Phys. Oceanogr., 41*(11), 2155-2167.

Bastida, I., J. Planella, E. Roget, J. Guillén, P. Puig, and X. Sánchez (2012), Mixing dynamics on the inner shelf of the Ebro Delta, *Sci. Mar.*, 76(S1), 31-43.

Index

1. General Introduction

1.1. The scope of the thesis

Turbulence is ubiquitous in Nature. Being present on such an enormous range of scales, from the smallest to the largest, it influences a vast many aspects of our lives. For example, those motions we observe when mixing milk into our coffee or when our bodies move through the water are turbulent. Turbulence exhibits chaotic, unpredictable and highly non-linear behavior resulting in characteristic structures (eddies) responsible for high levels of mixing, diffusion and dissipation. Generally speaking, turbulence involves a set of eddies that move and interact with each other in a flow.

In a turbulent flow, turbulent motions do not completely fill all of its volume but rather they are clustered in turbulent regions (patches). They appear episodically at different locations of the flow, alternating with laminar or quiescent regions (Mahrt, 1989; Gavrilov et al., 2005; Cava and Katul, 2009). Such behaviour is usually known as external or mesoscale intermittency. In addition, inside these so-called patches, the energy or the scalar dissipation rates demonstrate strong fluctuations concentrated in small subregions (Anselmet et al., 1984; Meneveau and Sreenivasan, 1991; Zhou et al., 2005). They are attributed to the random inhomogeneous spatial distribution of vortex filaments where they stretch and dissipate energy in isolation (Kuo and Corrsin, 1971). This phenomenon is usually referred to as internal or small-scale intermittency. Then in its broadest sense, intermittency involves two aspects: one is related to the clustering of turbulence, while the other is related to amplitude of small-scale fluctuations inside those clusters.

Geophysical environments such as oceans, seas, lakes and reservoirs are usually stratified systems where advection often results in varying degrees of turbulence. In theses systems, intermittency is a characteristic phenomenon. In

recent decades intermittency has received a great deal of attention because of its influence on energy, heat, mass, nutrients and oxygen fluxes through the water column (Seuront et al., 1999; Seuront et al., 2001; Tweddle et al., 2013). For instance, wind energizes basin-scale surface and internal wave fields (Imberger, 1998; Wüest et al., 2000) creating shear instabilities and internal wave breaking which, in turn, favor the formation of patches of turbulence (Nishri et al., 2000; Staquet and Bouruet-Aubertot, 2001; Etemad-Sahidi and Imberger, 2006) Furthermore, inside these patches small-scale turbulent oscillations affect other processes such as chemical reactions (Seuront and Schmitt, 2005) or aggregation, incubation and foraging processes of small-scale planktonic organisms (Druet, 2003).

As described above, winds contribute to the onset and persistence of turbulent patches. However, small and medium-size basins are exposed to low winds most of the time (Kocsis et al., 1998; Wüest et al., 2000; Gale et al., 2006) so, although studies of mixing under low wind regimes are rare, such studies are imperative for those systems. Recently, the importance of ocean dynamics under low winds has been also stated (Hood et al., 2010). Wind gusts can generate intense but short-lived turbulent patches in inner stratified layers which influence the biochemical and physical processes occurring in the water body (Lozovatsky et al., 2005; Evans et al., 2008).

Turbulent events become especially relevant in the thermocline as they drive any exchange between the interior and the upper surface layer (Washburn and Gibson, 1984; Rosenblum and Marmorino, 1990; Saggio and Imberger, 2001; MacIntyre et al., 2009). Their frequency of occurrence, i.e. the degree of intermittency, is important in phytoplankton productivity (Moreno-Ostos et al., 2006; Hendelman, 2009). Therefore in order to better understand the fluxes between the layers it is crucial to question how often turbulence occurs in the thermocline and under what conditions.

Turbulence in the thermocline is patchy, mostly triggered by shear and internal wave breaking and often not very energetic (Imberger and Paterson, 1990; Gibson, 1991b). It has been studied in more controlled stratified systems

such as in laboratory experiments (De Silva et al., 1996; Wells and Helfrich, 2004) and numerical modeling (Smyth et al., 2001; Inoue and Smyth, 2009) but the application to field experiments still remains an open question.

Inside the patches intermittency is relevant in different small-scale processes such as the viscous dissipation of energy, biochemical processes, thermal convection and the redistribution of salinity concentration or multi/double diffusive convective fluxes (Sanchez and Roget, 2007). Other physical processes, such as the propagation of light and sound (Tyson, 1991; Colosi et al., 1999), are also influenced by turbulent small-scale fluctuations.

When applied to aquatic ecosystems, strong small-scale fluctuations affect the encounter rates of small-sized predators and their prey (Delaney, 2003; Rhodes and Reynolds, 2007) as well as ingestion rates (Shimeta et al., 1995; Saiz et al., 2003), particle aggregation and disaggregation (Jago et al., 2006) and small-scale patchiness of nutrients (Seuront et al., 2001; Schernewski et al., 2005). Also small-scale intermittency affects phyto and zooplankton species less than several millimeters in size (Peters and Marrase, 2000), or more specifically, floating microscopic algae that are responsible for photosynthesis in coastal oceans (Margalef, 1987). However, zooplankton larger than ~1 cm does not usually react to small-scale intermittency (Squires and Yamazaki, 1995). In particular, studies on phytoplankton patchiness found that it substantially increased the predator-prey encounter rate (Seuront et al., 2001). In addition, the patchiness of small-scale phytoplankton distribution in a tidal current increased with decreasing turbulence intensity and varied depending on the phase of tidal cycle (Seuront and Schmitt, 2005).

A complete description of intermittency requires a statistical analysis of turbulent variables such as turbulent scales, fluctuations of dissipation or other scalar fields which should be performed in appropriate turbulent segments. Although traditional methods have been working with equal-distance segmentation (Lorke and Wüest, 2002; Lozovatsky et al., 2008c; Paka et al., 2013), more recent research has employed analysis procedures inside well-defined, bounded turbulent regions (Piera et al., 2002; Fer et al., 2004; Preusse et

al., 2010). Different studies found in the literature have demonstrated that the statistics of the vertical and horizontal sizes of the turbulent patches are subjected to specific features (Lozovatsky et al., 1993; Stansfield et al., 2001; Lorke and Wüest, 2002). In particular, the probability distributions of turbulent scales are found to be clearly skewed towards high values and have been well approximated to log-normal distributions (Wijesekera et al., 1993; Lozovatsky and Fernando, 2002; Thompson et al., 2007). This information has revealed a useful tool for modeling, where turbulent scales are introduced as parameters in closures (Piera et al., 2006; Klymak et al., 2010), and in the calculation of biochemical quantities. An example of this latter case is the estimation of photosynthetic rates, which requires the parameterization of the vertical movement of phytoplankton usually performed with the help of turbulent scales and vertical diffusivities (Lande and Lewis, 1989; Yamazaki and Kamykowski, 1991).

Alternatively, Kolmogorov (1941) described the statistics of small-scale turbulence, whereby for homogeneous and isotropic turbulence, the moments of order *p* of the velocity increases between two points separated by a distance *r* (structure functions) scale on *r*, with scaling exponents $\zeta(p) = p/3$. However, to account for the effects of strong fluctuations in the *TKE* dissipation rate, Kolmogorov modified his original idea and postulated the refined similarity hypothesis (RSH). In this theory, the structure functions in the inertial subrange were conditioned on the local averages of the energy dissipation rate, ε_r, over a sphere of radius *r*, with $r << L$, where *L* is the characteristic scale of the energy input. In this model, the variability of ε_r was considered as log-normally distributed and characterized by the parameter μ, which is known as the intermittency exponent and related to the stretching of the distribution of the logarithm of ε_r. Later, the log-normal model was formalized by Monin and Yaglom (1967) in their multiplicative turbulent cascade model of ε_r for fully developed turbulence. However, the log-normal approach has been questioned by many researchers, who, in the inertial subrange, explored the dependence on

r of the statistics of velocity differences and dissipation rates so as to provide a more convincing explanation for intermittency (Frisch et al., 1978; Benzi et al., 1984; Frisch and Parisi, 1985; Yamazaki, 1990). Recent models have been working within a multifractal framework (Schertzer and Lovejoy, 1987; Schmitt et al., 1994; Seuront et al., 2005), where the log-normal distribution is a particular case. However, there is still debate as to whether dissipation and scalar rates are log-normally distributed or fit better in a universal multifractal context.

The abovementioned phenomenological models of turbulence are based on the fact that, at high Reynolds numbers, the small scales in the inertial subrange are statistically independent of the large scales. Under this premise, the intermittency exponent μ is assumed to be a universal constant. In the particular case of the energy dissipation field, extensive research has been done into atmospheric, laboratory and numerical simulations (Sreenivasan and Antonia, 1997, Lauren et al., 2001; Zhou et al., 2006.), which have reported values of $\mu \sim 0.25$ for fully developed turbulence. It is worthy noting that this has not been extensively studied in natural waters, such as within the turbulent patches of the thermocline or in the boundary layers. In particular, Wijesekera et al. (1993) found higher values of μ ($\mu \sim 0.4$) when analyzing internal intermittency within the turbulent patches in the pycnocline of the ocean. Because patch turbulence is usually associated with moderate and low Reynolds numbers, this has raised concerns as to how that exponent behaves in such conditions. Nevertheless, it not only has to be performed in a specific aquatic environment, but also cover a wide range of those numbers, which, to the best of our knowledge, has not yet been explored.

1.2. Goals

Our aim is to provide a statistical description of the intermittency of turbulence that would contribute to a better understanding of both internal and

external intermittency in natural waters. In this work, we present a discussion on the intermittency of turbulence by considering two specific environs: i) the thermocline of a small stratified lake and ii) the bottom boundary layer in a shallow tidal sea.

The first goal of this study was to analyze the external intermittency of turbulence based on patchiness statistics in a stratified water environment. We proposed analyzing the probability distributions of relevant turbulent scales and estimating effective turbulent diffusivities and associated buoyancy fluxes caused by intermittent mixing events. For this study, measurements were taken during the summer at Lake Banyoles, a small sheared strongly stratified lake, in order to obtain a representative sampling of patches.

The second goal was to investigate the internal intermittency of turbulence within the turbulent regions of a specific environment. Unfortunately, the turbulent patches detected in the thermocline of Lake Banyoles were too small (patch size mean ~ 0.5 m and maximum sizes ~ 3 m) and the surface and bottom layers were too thin to perform accurate statistical analysis of internal intermittency.

Internal intermittency was analyzed in the bottom boundary layer of a tidal flow based on the analysis of the velocity field and also the turbulent energy dissipation rates estimated from these velocity data. To the best of our knowledge is the first time that this study had ever been done. We analyzed the possible dependence of the intermittent parameters on the microscale Reynolds number. Measurements for this study were obtained from a field campaign carried out in a tidal flow on a shallow shelf located on the north-east coast of China.

1.3. Outline

This thesis has been divided into eight chapters. The first three chapters focus on researching external intermittency in the thermocline of a small lake under low winds. The following three chapters (Chapters 5, 6 and 7) deal with

internal intermittency in the bottom layer of a non-stratified tidal flow. Both case studies follow the same structure, with the first chapter providing an overview of the phenomenon, the second chapter describing the measurements and data processing and finally, the third chapter showing the results and centering on the discussion. Conclusions and the bibliography make up the final two chapters of the thesis. To provide an overall outline of the thesis, a brief description of each chapter is detailed next.

In Chapter 2 we review the phenomenon of external intermittency by focusing on stratified natural waters. This includes the basic concepts of stratified shear-induced turbulence, a review of the experimental research on turbulent patches and a description of procedures for patch identification.

Chapter 3 focuses on the measurements taken in Lake Banyoles, (a stratified small lake), using a free-falling microstructure profiler. It also includes the CTD data processing required to characterize the water column structure and the microstructure measurements which enable the turbulent parameters for the patches to be evaluated.

In Chapter 4 we show the results for the external intermittency in the lake and under low winds. First we describe and apply the new methodology for patch identification and then we present the basic characteristics of stratification, internal seiches and turbulence in the lake. Next, we present the statistics of the turbulent scales in the thermocline (patch sizes, Thorpe scales and normalized Thorpe scales within the patches) and we test a possible parameterization for the ratio normalized Thorpe scale. Finally, we estimate the effective diffusivities and buoyancy fluxes across the thermocline.

In Chapter 5 we compile the conceptual framework of the internal intermittency of turbulence. Focusing on the universal multifractal model, we describe several techniques of analysis that will be used later in the study.

Chapter 6 describes the measurements of a shallow tidal flow which were taken near the bottom of a coastal zone in the Yellow Sea and obtained using an Acoustic Doppler Velocimeter (ADV). Furthermore, the data processing for

obtaining the turbulent energy dissipation rate, mean and small-scale values, is presented.

In Chapter 7 we show the results for internal intermittency of near-bottom turbulence. We present and compare the intermittent parameters estimated using the velocity field directly and using the dissipation rate field. Furthermore, the dependence of previous parameters on the internal flow parameters (turbulent Reynolds number) is discussed. The summary and conclusions are also given in Chapter 8. In Chapter 9 the bibliography used for our work is presented.

Complementary material is provided in the Appendixes: Appendix A is related to the basic aspects of turbulence and the estimation of turbulent kinetic energy rates and vertical diffusivities. In Appendix B we describe the basic properties of the log-normal distribution. Appendix C offers a review of different improvements made to several of the multiplicative energy cascade models described in the work. In Appendix D a basic description of the fractal dimension is given, while a description of the multifractal behavior is provided in Appendix E. General properties for the scaling exponent of the moments can be found in Appendix F. Finally, detailed descriptions of Lévy and log-Lévy distributions are presented in Appendix G.

2. Overview of External Intermittency: Patchiness in Stratified Flows

2.1. Stratified aquatic systems and turbulent patches

In aquatic systems, solar radiation creates the thermal stratification of the water column. On the other hand, wind and heat fluxes at the surface create water motion in the upper part which in turn produces energetic turbulence and reduces stratification that leads to quasi homogeneous mixed surface layers. Below the surface mixed layer, strong thermal and density gradients persist in the thermocline which separates the surface layer from the cold bottom layer , also weakly stratified. Thus, the presence of strongly stratified systems substantially affects the vertical motions and strongly influences the nature of turbulence and mixing (Peters et al., 1994; MacIntyre et al., 2006; Katsev et al., 2010).

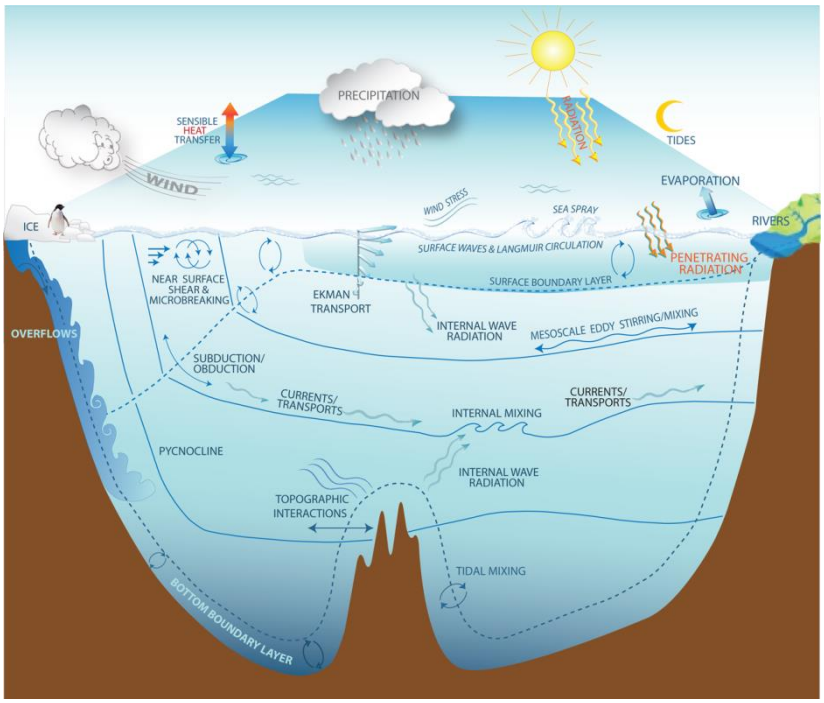

Fig. 2.1 Schematic plot of the mixing processes in natural waters. (from Geophysical Fluid Dynamics Laboratory, 2014).

Thermoclines play not only an essential role in the hydrodynamics, but also in the water quality of basins. Thermoclines are high stable regions that act as effective barriers resistant to any wind-induced mixing or exchange of water masses between upper and bottom layers. However, they are not complete barriers. Vertical mixing can occasionally occur due to the presence of velocity gradients (shear); usually related to the internal wave field forced by wind. These episodes are responsible for transferring dissolved gases, chemical compounds and suspended solids across the layer.

In lakes, wind excites standing waves (seiches) that can be traced for hours and even days after the wind dies down and finally ceases (Roget et al., 1997; Rueda et al., 2003; Valerio et al., 2012). So, although medium-sized and small lakes are exposed to low winds most of the time (Kocsis et al., 1998; Wüest et al., 2000; Gale et al., 2006) shear induced mixing at the thermocline owing to internal waves becomes relevant because of their persistence. Field measurements have shown that although the frequency of turbulence events in the thermocline is low they have a relevant impact on the lake, i.e. being substantially affected by sudden changes of wind velocity, such as storms and wind gusts (Hendelman, 2009; Wain and Rehmann, 2010; Cousins et al., 2010). This is why the analysis of turbulence is essential in quantifying the magnitude of the mixing as well as identifying which mechanisms control the generation, decay or enhancement of the turbulence (see in Fig. 2.1).

Observations carried out in the ocean thermocline also show that turbulence is extremely intermittent in time and space. Grant et al. (1968) reported for the first time the presence of 'well-bounded' turbulent regions close to the coast of British Columbia, which extend hundreds of meters on a horizontal scale and a few meters on a vertical scale. This was later corroborated by Nasmyth (1970) who detected thin, pancake-like layers ('patches') of only a few meters in size and separated by regions of strong density gradients. Nasmyth revealed that turbulence in stratified layers was confined to patches with small aspect ratios which could be caused by strong fluctuations of the vertical shear (stratified shear-induced turbulence).

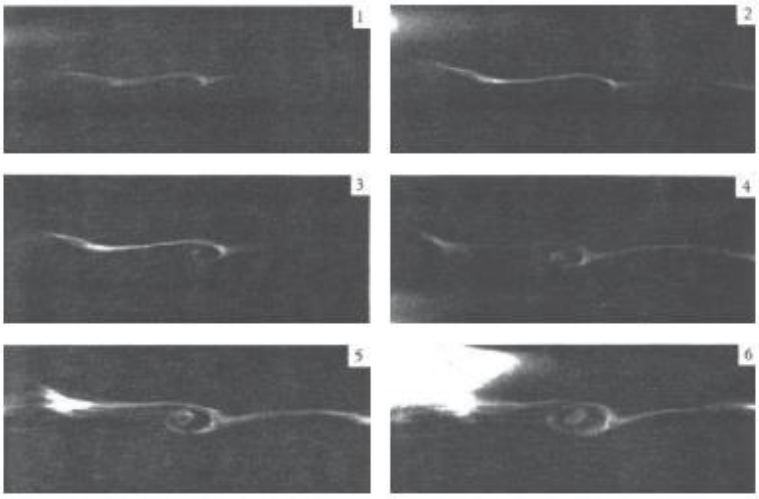

Fig. 2.2 Shear instabilities observed in the Mediterranean thermocline obtained using dye tracers and diving techniques (from Woods, 1968).

Mixing models have been used to simulate patch turbulence in the ocean thermocline (Dewitt et al., 1990; Hirabayashi and Sato, 2010; Mosaddad and Delphi, 2013). In these models, the passage of internal waves propagating along the thermocline produces shear perturbations within the layer. If the ratio between the inertia and buoyancy forces exceeds a critical value, these disturbances become unstable; they grow, sharpen, turn over and finally break creating a turbulent patch, as described in detail in Turner (1973). These disturbances intermittently appear in the layer. Woods (1968) was the first to produce evidence of this by photographing the breaking of internal waves in the summer thermocline in the Mediterranean Sea, near Malta (see images in Fig. 2.2). Later, flow observations have also corroborated this type of behaviour (Alford and Pinkel, 2000; Ledwell et al., 2004; Smyth and Thorpe, 2012).

As described above, experimental work shows that patchiness in the thermocline is produced by breaking internal waves. However, this is not the only factor and several studies have revealed that different types of local instabilities can also occur through other mechanisms, such as reflection on sloping boundaries (Lorke, 2007; Aghsaee et al., 2010; Bastida et al., 2012) and local topography radiating high frequency waves (Thorpe et al., 1996; Nikurashin and Ferrari, 2010; Venayagamoorthy and Fringer, 2012), among

others. However, when these kinds of internal waves interact with the background shear where they propagate, they can be amplified and favor shear instability as the primary breakdown mechanism (see Fig. 2.3).

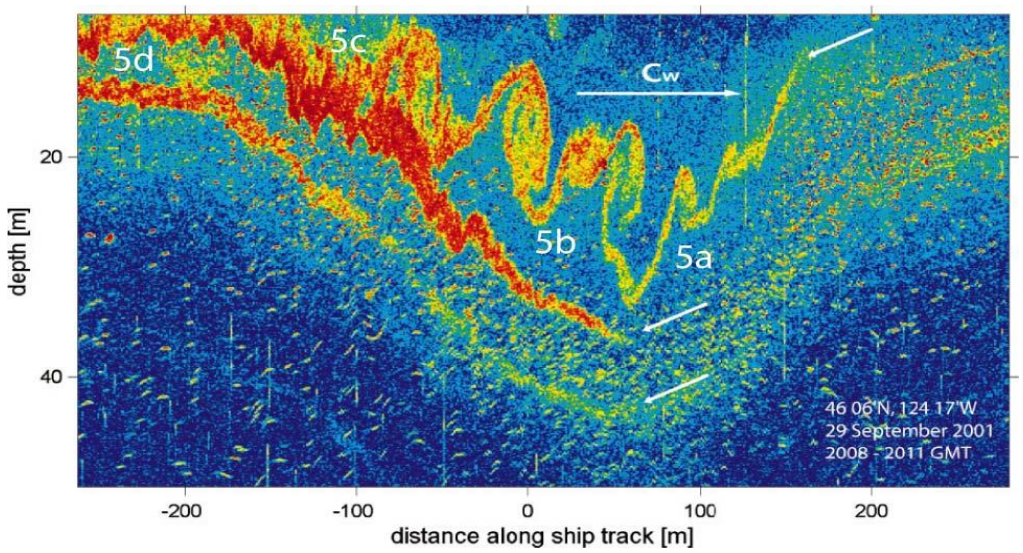

Fig. 2.3 Example of Kelvin-Helmholtz billows generated by current shear obtained close to the Oregon coast. **(**Moum et al.**,** 2003). Arrows indicate the phase speed of the train of solitary waves, c_w, and 5a and 5b depict the different stages of the Kelvin-Helmholtz billows.

Fernando (1991) pointed out that although different types of instabilities can form in sheared stratified layers, shear instabilities of the Kelvin-Helmholtz type are the most relevant ones. This concurs with theoretical analyses, numerical simulations and experimental research done in stratified shear-driven turbulence (Strang and Fernando, 2001; Patterson et al., 2006; Brucker and Sarkar, 2007; Smyth and Moum, 2012).

Observations in lakes (Imberger, 1994; Wüest and Lorke, 2003; Pannard et al., 2011) have also confirmed that local shear associated with the basin-scale seiche field can be strong enough to cause shear instabilities. Laboratory experiments show that energy can be transferred from large to small-scale mixing under different scenarios, such as solitons, bores and billows (Horn et al., 2001; Boegman et al., 2005; Fructus et al., 2009). However, strong shearing seiches generate shear-induced instabilities which lead to the formation of Kelvin-Helmholtz billows which in turn disintegrate into patches of high

dissipation and mixing (Cisneros-Aguirre et al., 2001; Troy and Koseff, 2005; Stashchuk et al., 2005).

2.2. Mixing in a turbulent patch

Estimates of mixing properties within a patch require not only knowledge of the breaking process itself, but also the evolution of the combined effect of different (possibly interacting) physical mechanisms in the mixing region of the system. In recent decades, laboratory experiments and numerical modeling have been used as helpful tools for understanding, simulating, testing and predicting vertical transport associated with isolated, intermittent patches. However, there is still much debate over whether or not these results can be extrapolated to field experiments.

Controlled laboratory experiments in stratified fluids have provided extensive information about the time-space features of velocity and temperature fields on a small-scale for an isolated overturning patch. Analysis of turbulence in a uniformly stratified flow, with and without background shears, was first reported in the pioneering works of Van Atta and co-workers (Rohr et al., 1984; Itsweire et al., 1986; Lienhard and Van Atta, 1995). Later, patch turbulence was studied in stratified flow containers and was induced by different external source mechanisms such as oscillating grids (Fernando, 2003; Qiu et al., 2009; Stretch et al., 2010) and rotating tanks (Wells and Helfrich, 2004; Praud et al., 2006; Sangrà et al., 2011) or by internal instability mechanisms such as breaking internal waves (Dauxois et al., 2004; Chen, 2012; Gorogetska et al., 2012) and intrusions (Lowe et al., 2002; Sutherland et al., 2004; Munroe et al., 2009).

The aforementioned experiments show that when background shear is present, a turbulent patch grows rapidly due to the inertia forces associated with the turbulent energy source and engulf non-turbulent parcels of fluid until be reaching a state of quasi-steady equilibrium (critical size of the patch). At this point the turbulence has destroyed the background stratification and the production of turbulent kinetic energy is balanced by the dissipation rate and

the rate of increase of potential energy: the turbulent patch is in an 'active' stage. Turbulent motions capture kinetic energy from the mean flow, which is responsible for sustaining turbulence. The evolution of a turbulent patch is shown in Fig. 2.4. In contrast, without any source of energy (shear free turbulence), the turbulent patch, affected by stratification, will, once a period of time has elapsed, quickly decay.

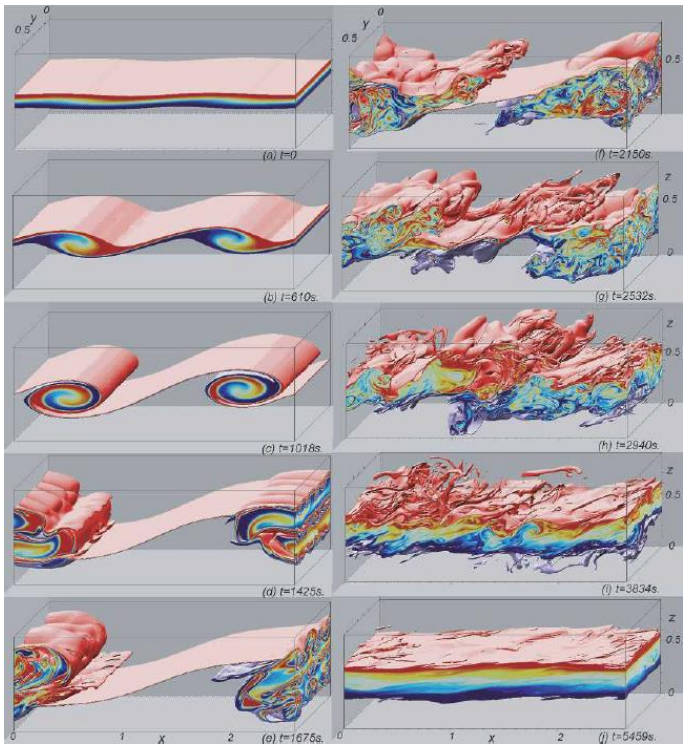

Fig. 2.4 Direct numerical simulation of the evolution of a turbulent patch (here salinity field is represented) across an interface in the ocean. Colors indicate intermediate values of salinity found in the interfacial layer (Smyth et al., 2005).

Numerical simulations of the evolution of turbulent patches show that they are bounded by thin interfaces of high stratification above and below and turbulence destroys the density gradients inside. Thus, their evolutionary state can be specified by the strength of the background (external) conditions and also by internal parameters which control the dynamics within the patches (Smyth et al., 2005; Inoue and Smyth, 2009; Rahmani et al., 2014).

Laboratory experiments have provided useful information about the evolution of a turbulent patch, but extrapolation to field measurements has

been controversial. The use of free-falling profilers introduces limitations to the vertical direction of the sampling process. Also, following the evolution of a single event just seems rather impossible timewise. With no knowledge of its three-dimensional structure and evolution stage it is thus necessary to make assumptions to correctly interpret the measurements. For example, some authors have argued that there is no necessary connection between geophysical flows and laboratory processes; the nature and intensities of the turbulent sources in environments are not known and could be quite different than the known energy sources in the laboratory (Gibson, 1980; Gibson et al., 2006; Leung, 2011). On the other hand, others believe that there is no reason not to apply the results obtained in laboratory experiments directly to the field (Gregg, 1980; Wijesekera and Dillon, 1997; Smyth et al., 2001).

A complete description of patch turbulence inferred from field measurements would require the ability of sampling the same patch in time and under the same conditions. Further, when detecting the patch for a second time, the effects of the stirring from the profiler during the first measurement could change these conditions (Dillon, 1982). However, this effect is expected to be local, as sampling exactly at the same place within the patch is highly improbable. Note that the abovementioned low aspect ratio of patches in stratified flows allows the same patch to be sampled at different locations. On the other hand, sampling a large number of patches which cover the different stages of evolution is also an alternative when studying the properties of turbulent patches.

2.3. Relevance of patch analysis

Given the fact that turbulent events do not fill the interior of natural water systems, turbulent patches become relevant in the study of mixing in these bodies. Accordingly, identifying turbulent patches and defining their statistics are the up and coming areas in the study of turbulence. Different methodologies have been proposed to identify turbulent patches from those

artificially created by noise. Further discussion on this topic is addressed in the following subsection.

Analysis of specific turbulent scales has been revealed as a useful tool to investigate mixing in a body of water. In fact, the energy dissipation rate ε and the vertical eddy diffusivities K_ρ, both of which are basic turbulent parameters, can be inferred from those scales obtained from standard finescale CTD profiles when microstructure measurements are not available and information about the velocity field is not known (Smyth et al., 2001; Cisewski et al., 2005; Frants et al., 2013). Evaluation of the turbulent scales has been traditionally done using fixed segmentation of the water column. However, given the intermittent character of patch turbulence, oriented analysis becomes a powerful alternative (Roget et al., 2006).

To estimate previous turbulent parameters, it is important to be familiar with three turbulent scales: the Thorpe L_T scale, the maximum Thorpe $L_{T,\max}$ scale and the Ozmidov L_O scale. For patch analysis, patch thickness h_p, which corresponds to the vertical extension of the turbulent patch, is also an important scale to take into account. The three turbulent scales are described below:

- *The Thorpe L_T scale* is defined as the root mean square of the Thorpe displacements $d'_T(z)$ within a depth range of the water column (Thorpe, 1977). Thorpe displacements $d'_T(z)$ correspond to the vertical distances that fluid particles need to be moved in order to obtain a stable density profile. Thus, it is expressed as

$$L_T = \left\langle \left(d'_T(z)\right)^2 \right\rangle^{\frac{1}{2}} \tag{2.1}$$

where angular brackets denote ensemble averaging.

In a general way, Thorpe displacements $d'_T(z)$ can be estimated from density profiles using a reordering routine which converts the density into a sorted profile. In this procedure, it is assumed that parcels of water have been displaced vertically by turbulence during the sampling. If salinity does not play a relevant role in the density

computation, temperature profiles can also range used instead of density profiles.

Thorpe displacements can be interpreted in energetic terms. The sorted profile corresponds to the minimum state of available potential energy which could be obtained from the rearrangement of the observed profile. Then, Thorpe displacements $d'_T(z)$ represent the distances travelled by water parcels to obtain a stable profile and can be related to the available turbulent potential energy, i. e. the energy released if a water parcel returns to its reference sate (Dillon, 1984).

An example of a turbulent patch detected in the pycnocline of the Mediterranean Sea is shown in Fig. 2.5. Measurements were taken during a field campaign in a coastal zone over the continental shelf close to the Ebro Delta in order to analyze mixing in that area and which has been discussed in Bastida et al. (2012).

- *The maximum $L_{T,max}$ Thorpe scale* corresponds to the maximum value of the Thorpe displacement $d'_T(z)$ observed within a segment or patch,

$$L_{T,max} = \max\left(d'_T(z)\right) \tag{2.2}$$

- *The Ozmidov L_O scale* is defined as

$$L_O = \left(\frac{\varepsilon}{N^3}\right)^{\frac{1}{2}} \tag{2.3}$$

where N is the buoyancy frequency, and ε the dissipation rate of turbulent kinetic energy (Ozmidov, 1965). The Ozmidov L_O scale indicates the vertical extension where turbulent eddies start to be affected by background stratification.

In fact, it has been found that L_T and L_O are highly correlated, being proportional, with $L_0 = c\,L_T$ and $c \sim 1$ (Dillon, 1982; Ferron et al., 1998; Fer et al., 2004).

Thus, we obtain

$$\varepsilon = \left(cL_T\right)^2 N^3 \qquad (2.4)$$

and considering that

$$K_\rho = \gamma\, \varepsilon / N^2$$

(Appendix A), thenSometimes the

$$K_\rho = \gamma\left(cL_T\right)^2 N \qquad (2.5)$$

maximum Thorpe $L_{T,\max}$ scale is considered instead of the Thorpe L_T scale (Gibson, 1999), because it represents the maximum displacement obtained in the patch or the segment being studied, its estimation does not depend on averages of vertical displacements. Several studies based on patch analysis show that both scales are also proportional and it has been stated that $L_{T,\max} \sim 2.5\, L_T$ (Moum, 1996; Lorke and Wüest, 2002). Based on measurements, when $L_{T,\max}$ and L_T are calculated at equal-distance segments (larger than $L_{T,\max}$) it is found that the linear regression becomes a power function similar to $L_{T,\max} \sim L_T^{0.85}$ (Lorke and Wüest, 2002). Our previous work also obtained similar results to these (Planella-Morato, 2007); as can be seen in Fig. 2.6a. However, when L_T is computed within each patch, the relation between $L_{T,\max}$ and L_T becomes almost linear with a constant factor of 2. This can be observed in Fig. 2.6.b where the dependence between $L_{T,\max}$ and L_T for all microstructure patches is presented on a logarithmic scale. From the regression shown in the plot, $L_{T,\max} / 0.93 L_T = 10^{0.32} = 2.1$ is obtained. This

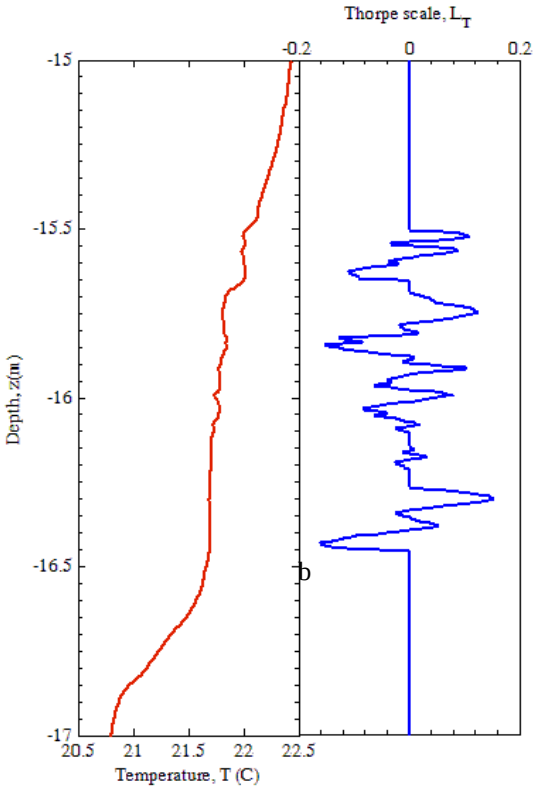

Fig. 2.5 An example of a turbulent patch detected in the pycnocline on the inner shelf of the Mediterranean Sea. Temperature signal is on the left and the Thorpe displacements are shown to the right.

indicates the relevance of addressing the analysis of patches in order not to introduce bias in the estimation of ε due to methodological procedures.

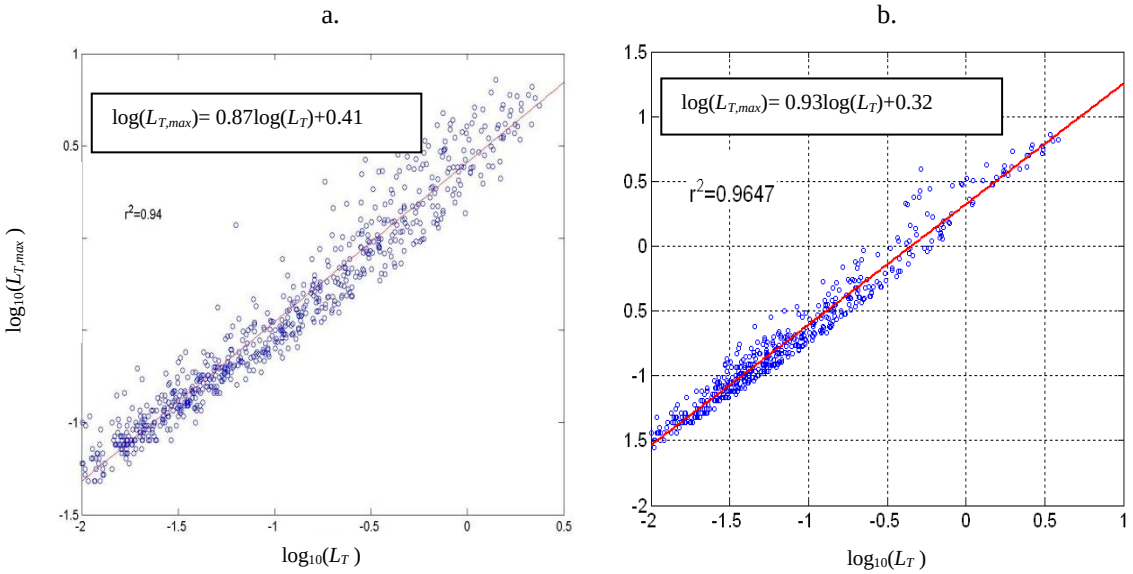

Fig. 2.6 Plots of the maximum Thorpe scale as a function of the Thorpe scale. Turbulent scales are calculated based on (a) fixed segmentation analysis and (b) patch analysis.

The analysis of normalized scales has also revealed interesting features of mixing in an isolated patch. This analysis has been performed based on laboratory experiments and numerical simulations (Smyth et al., 2001; Pham and Sharkar, 2010; Mater et al., 2013). They show that normalized turbulent scales look promising as age indicators of the patch, as is the case of the normalized Thorpe L_{Tp}/h_p scale. Although it is extremely difficult to follow the evolution of an isolated patch in the thermocline, the statistics of L_{Tp}/h_p provide information about the state of turbulence. It can help modelling the turbulent mixing in stratified flows which use empirical closures. Lozovatsky and Fernando (2002) suggest a parameterization of L_{Tp}/h_p based on a number of external and internal parameters which were successfully tested in the ocean. Here, we will test it in a stratified lake under low wind conditions.

2.4. Turbulent patch identification

A customary method to detect turbulent patches in the environment is based on the procedure as reported by Thorpe (1977). This compares the observed and the sorted profiles of density (temperature) and computes the Thorpe displacements $d'_T(z)$. Different methods based on Thorpe displacements have been used not only to identify turbulent patches in the ocean and lakes (Ferron et al., 1998; Piera et al., 2006; Gargett and Garner, 2008), but also in the atmosphere (Gavrilov et al., 2005; López et al., 2008; Wilson et al., 2011).

Initial studies on patch turbulence based on Thorpe analysis applied simple algorithms. That was the case of Dillon (1982) who isolated vertical overturns from surrounding regions with null displacements or by not exceeding a predetermined value. According to his definition, the patch thickness h_p was calculated as the difference between the upper and lower limits of the region wherein $\sum d'_T(z) = 0$.

Subsequent work has been focused more on dealing with noise. Noise can induce spurious overturns when a measured profile is analyzed, especially for weakly stratified layers, which in turn can lead a substantial increase in the percentage of turbulent events in the layer under study being obtained and consequently a considerable overestimation of the mixing. Dillon (1982) did not give any details about the noise threshold in his work, but Thorpe (1977) had set $d'_T(z)$=0 if Thorpe displacements had values less than or equal to noise resolution or noise standard deviation. Although subsequent studies have shown that this methodology is effective (Lorke and Wüest, 2002; Preusse et al., 2010; Coman and Wells, 2012), this constrain could be too restrictive and may eliminate valid displacements.

Moum (1996) developed a procedure to detect turbulent patches in stratified layers where turbulent patches were bounded by well-defined limits, and which requires $L_{T,max} < h_p$ and $\sum d'_T(z) = 0$. Furthermore, Ferron et al. (1998) and Gargett and Garner (2008) developed another approach to reduce the

effects of noise which consists of pre-processing the measured signal. Then, an intermediate density (temperature) profile is constructed so that the differences between the successive points in the profile are greater than a predefined noise threshold related to the accuracy or its standard deviation.

Instrumental noise and systematic errors have been also analyzed in the work of Galbraith and Kelley (1996) from measurements taken in the ocean. They estimate the minimum size of the turbulent patches which can be detected from profiles based on the instrumentation noise level and the density gradient. They suggest the minimum thickness of resolvable patches is

$$L_\rho = 2\frac{g}{N^2}\frac{\delta\rho}{\rho_0}, \tag{2.6}$$

where $\delta\rho$ is the density resolution and ρ_0 is the mean density. It can also be seen as a constraint on the Thorpe scale (Moum, 1996).

Galbraith and Kelley (1996) proposed two tests, the run length test and the water-mass test, to discriminate between real and artificial overturns from CTD density profiles. In the run-length, a 'run' was defined as the number of points (n) with consecutive positive values of $d_T'(z)$ in the patch. If patches are generated by an uncorrelated random series of displacements, the probability of observing positive and negative n values must be the same. Hence, the probability density function (pdf) of the run-length of a random variable n is

$$P(n) = 2^{-n} \tag{2.7}$$

(Larsen and Marx, 1986). The pdf of d_T' would be expected to follow (2.7), if noise were a source of inversion in temperature profiles. The test identifies a minimal acceptable run-length as the point where the experimental pdf of the run-length intersects double the pdf of the noise (i.e. (2.7)). Thus, a safety margin of $r = 2$ is taken for noise-induced overturns. Following this methodology, Timmermans et al. (2003) analyzed possible values of r by comparing their run-length to those expected from the Bernouilli trials described by (2.7). They found a slightly higher, value of r, $r \sim 2.45$, associated with the root mean square of the expected noise.

To detect statistically stationary segments Imberger and co-workers (Imberger and Ivey, 1991; Saggio and Imberger, 2001; Etemad-Sahidi and Imberger, 2006; Yeates et al., 2013) applied new segmentation algorithms to the temperature gradient signal. These algorithms include autoregressive models and thresholds to select only those segments that are stationary. After this, mean dissipation rates ε were then estimated for each segment and used to disregard those segments generated by temperature fluctuations below the temperature resolution.

Piera et al. (2002) showed that noise can be efficiently removed using wavelet denoising. In this technique, the measured signal is decomposed into frequency subbands and higher frequencies are smoothed out using a thresholding procedure (most of the information about noise is contained there). After wavelet denoising, the displacements were compared to the potential error, obtained from a theoretical model, and then validated if their value was smaller than this error. Next, the ratio of the validated displacements to the potential error is used as the acceptance index for turbulent patches. Although this method was only tested in freshwater, it has also been applied successfully in other environments and sometimes complemented by other tests which are described next (Peters and Johns, 2005; Piera et al., 2006; Evrendilek and Karakaya, 2014).

The work of Galbraith and Kelley (1996) also included a second test, the water-mass test, for those density overturns which have passed the run length test. These were once again inspected to eliminate those structures that could come from mismatches in time response of temperature and conductivity sensors. For each overturn, density points within each reordering region were fitted by linear regressions to those of temperature or salinity. The errors, defined as the normalized differences between the observed density profile ρ and the resulting values of the fitted densities against the respective Thorpe scales, were taken as a measure of the tightness of the T-S relationships. After visual inspection of the T-S plots, errors greater than 0.5 were required for any overturns to be accepted as turbulent patches. Gargett and Garner (2008)

introduced a more sophisticated two-parameter water test to avoid false overturns and salinity spikes in weakly stratified layers. Alford and Pinkel (2000) proposed a method based only on accepting as turbulent overturns those inversions present simultaneously in density, conductivity and temperature signals. However, Galbraith and Kelley tests, hereafter referred to as GK tests, have became popular among researchers as a useful tool in detecting turbulent patches in water bodies (Ullman et al., 2003; Martin and Rudnick, 2007; Thompson et al., 2007).

The previously described methods of patch identification are based on the fact that instrumental noise introduces random errors in the sorted signal. However, Johnson and Garret (2004) have shown that if noise is important in the profile, the Thorpe displacements do not display the same behavior as random series. Johnson and Garret (2004) analyzed the effect of noise in the run-length tests and concluded that they were dependent on two relevant parameters: the amplitude of the scaled amplitude Q of the noise over the turbulent patch and the number of data points n within it. The scaled amplitude Q of the noise is related to the background stratification and is defined as

$$Q = \frac{\delta\rho}{\left(\frac{d\rho}{dz}\right)h_p}, \tag{2.8}$$

where h_p is the patch height, $\delta\rho$ the accuracy of the density and $d\rho/dz$ the background stratification computed using the sorted density profile. Taking density profiles with added random and uncorrelated noise, Johnson and Garret (2004) plotted r for $d'_T(z)$ as a function of Q and n; hereafter referred to as JG plots. These plots show that Thorpe displacements do not behave as a random uncorrelated series. Thus, to specify a safety margin they suggested first finding the Q and n parameters from a set of experimental data and then using the JG plots to assess the noise threshold for the measured displacements.

3. Observations of External Intermittency: New Measurements in a Stratified Lake under Low Winds

3.1. Study site and experimental setup

Lake Banyoles (42º 7′N, 2º 45′E) is the largest of a series of five lakes (some intermittent) located in the same hydrographic karstic basin in Catalonia (North-eastern Spain), and the second largest natural lake in Spain. The area is very unstable and last lake was only formed in 1978.

The lake (Fig. 3.1) is a multi-basin water body, covering 1.12 km² and the maximum depth is 45 m (mean depth is ~15 m) with the surface located at 172 m above sea level. From the surface it appears to be formed by two main lobes, the northern and the southern lobes, which are connected by a narrow neck.

Planella-Morato et al. (2007) reviewed the extensive studies, which are related to its main features and hydrodynamics, about the lake. In terms of water inflows, seven streams come into the lake from its western zone, although most of its water enters the lake through twelve warm

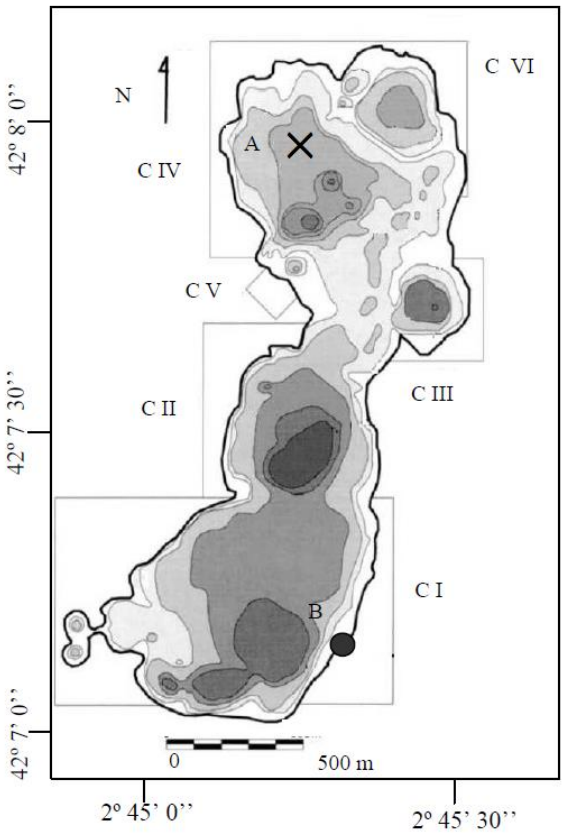

Fig. 3.1 Bathymetric map of Lake Banyoles (from Moreno-Amich and Garcia-Berthou, 1989). Distance between the isobaths is 5 m. The main basins (C-I to C-VI) are shown on the map. Point A indicates the measurement site and point B the location of the meteorological station.

underground springs (~95% of the total inflow). By considering their distribution the lake can be divided into six different subbasins (labeled as letter C in Fig. 3.1). Two of them are located at the southern lobe (mean depth of ~10 m) and the remainders are in the northern lobe (mean depth of ~18 m). About 95% of the total underground inflow enters the lake from the southern lobe (~90% through basin C-I) and a minimum quantity, less than 5% of the total inflow, comes from the northern lobe (Roget et al., 1994). The lake also has five outflow streams, located in the eastern part of the southern lobe and which cross the town of Banyoles before coalescing to form the Terri River.

The hydrodynamics of the lake includes several physical processes, of which the main mechanisms are shown in Fig. 3.2. Heat inflows, hydrodynamic plumes, baroclinic circulation and internal seiches are examples of these relevant processes, all of which have been analyzed in detail in different studies (Roget and Colomer, 1996; Colomer et al., 2001; Serra et al., 2005; Sanchez and Roget, 2007).

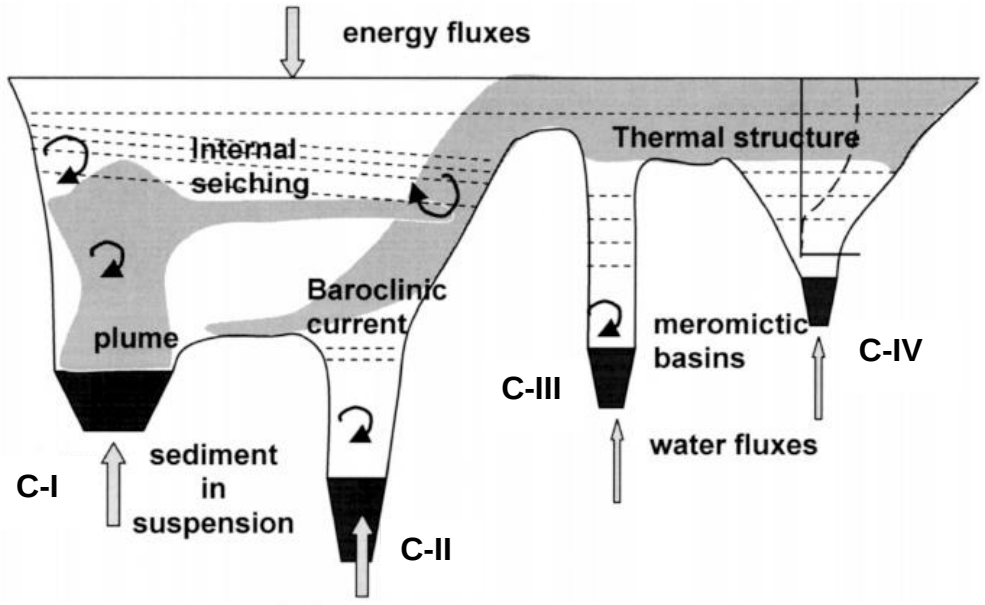

Fig. 3.2 Representation of the main physical processes present in Lake Banyoles (from Casamitjana et al.,2006).

Heavy stratification in Lake Banyoles occurs in late spring and at the beginning of summer, when weakly stratified surface (epilimnion) and bottom (hypolimnion) boundary layers are separated by a wide thermocline

(thermocline), which occupies about one third of the mean depth of the entire lake (Roget et al., 1997).

From April to October, mild winds with mean speeds below 2 $m \cdot s^{-1}$ are frequently observed over the lake area due to a sea breeze regime (the Mediterranean coast is about 30 km to the southeast). As a response to the breeze forcing, a quasi-stationary internal seiche field is established in the thermocline with wave amplitudes of about one meter or even higher (Roget et al., 1993). As described in Chapter 2, seiches influence vertical mixing and play an important role in transferring energy to the bottom layer, thereby influencing the transport of biological and chemical patterns (plankton, suspended sediments and nutrients among others), which are sensitive to small-scale patchiness.

Internal seiches in lakes are often dominated by high vertical modes (Perez-Losada et al., 2003). This is the case with Lake Banyoles, where a dominant second vertical first horizontal mode is easily excited (Roget et al., 1997).

In order to analyze shear-induced turbulence in a stratified system and under low winds, we planned the field campaign for summer. To clearly separate shear-induced turbulence mechanism from other possible mechanisms present in the lake, the experimental site was chosen in the western part of the northern lobe of the lake, far away from the main water inflows and outflows located in the southern lobe. Furthermore during the summer season the flow of surface streams is very low. The measurements were taken over four days in June-July 2009 (see Chapter 4, Table 4.1) at a gently sloping site, see point A located in the C-IV basin in Fig. 3.1. The test site (~ 12 m depth) was exposed to a south-easterly breeze with a fetch of ~ 2 km. The lake is surrounded by hills on all sides except the southeast, where a plain extends toward the Mediterranean Sea. Although the site is near to several underwater springs in basin C-IV, Casamitjana and Roget (1987) have shown that these inflows are small and drop to almost zero in summertime.

The wind was measured at a meteorological station (Davis Vantage Pro 6150C) located l km to the southeast of the test site (see point B in Fig. 3.1). The wind speed and wind direction were averaged over 30-minute periods. The atmospheric forcing over the lake during the observation period was dominated by north-westerly and south-easterly winds up to ~ 3 $m \cdot s^{-1}$. Irregular wind gusts (up to ~6-15 $m \cdot s^{-1}$) lasting only a few minutes originated episodically over the lake due to the uneven heating of the lake surface and surrounding mountains.

Microstructure and classical CTD data were recorded by profiling the measurements which were taken every day as soon as the breeze reached the test site (usually about 2 pm). We used the Sea and Sun Microstructure Turbulence system (MSS 90 Profiler) (Prandke and Stips, 1998) at a sinking speed of 0.85 $m \cdot s^{-1}$. The profiler was equipped with microstructure temperature and shear sensors. It had a fast response thermistor (FP07) with a sensitivity of 0.001°C and time response of 7 ms, leading to a vertical resolution of 0.6 cm. The resolution of the small-scale airfoil shear probe was 2 cm (Prandke et al., 2000). The conductivity, temperature, and depth (CTD) package contained a thermistor with a sensitivity of 0.001°C and a time response of 160 ms, a conductivity cell with a sensitivity of 0.001 $mS \cdot ms^{-1}$ and a time response of 100 ms, and a pressure gauge with a sensitivity of 100 Pa and a time response of 30 ms. Vertical resolution of the CTD profiles was ~ 14 cm.

The individual casts were launched from the lake surface to the very bottom of the lake approximately every two minutes for ~ 2 hours. Basic information about the measurements is given in Chapter 4, Table 4.1. The total number of profiles is 373. Reliable data were obtained from 2 m below the lake surface down to about 0.5 m from the bottom.

3.2. Data processing

Data obtained from meteorological station were used to compute the wind stress, τ_{10}, at 10 m above the surface level. This was calculated using the bulk formulas for light winds (Wu, 1994) and 30-minute averaged wind speed $\overline{U}_{10}$.

For the CTD datasets, an exponential recursive filter (Middleton and Foster, 1980; Fozdar et al., 1985; Lueck and Picklo, 1990) was applied to the conductivity signal to minimize spikes in salinity and density profiles caused by the different time responses of the temperature and conductivity sensors. Potential density was calculated based on the UNESCO routines (Chen and Millero, 1986). The equation of state for fresh water (Fofonoff and Millard, 1983; Chen and Millero, 1986) was used, taking the concentration of suspended solids into account (Sanchez and Roget, 2007). Since the vertical resolution of the CTD profiles was 14 cm at best, we averaged temperature T and potential density ρ_s to acquire a standard vertical resolution Δz = 0.2 m with which to analyze background stratification. The buoyancy frequency $N^2 = \frac{g}{\overline{\rho_s}} \frac{\Delta \rho_s}{\Delta z}$, where g is gravity, was calculated using sorted density profiles ρ_s (Thorpe, 1977).

A microstructure shear signal was used to estimate the turbulent kinetic energy (TKE) dissipation rate, ε. Empirical spectral densities of a small-scale shear signal were fitted to an analytical form of the transversal Panchev-Kesich shear spectrum along the lines of Roget et al. (2006) (Appendix A). The dissipation in patches was well resolved by the airfoil sensor (Wüest et al., 1996; Kocsis et al., 1999), at between 10^{-4} and 10^{-9} W·kg^{-1}.

We also calculated the patch buoyancy Reynolds number, $Re_b = \varepsilon / \nu N^2$, in order to evaluate turbulence activity in stratified layers. Gibson (1991a) argued that turbulence is active when Re_b > 30. Rohr et al. (1984) suggested critical Re_b = 10 – 16, which is in agreement with direct numerical simulations of homogeneous turbulence in stratified shear flows (Itsweire et al., 1993).

Analyzing data obtained in Knight Inlet (Vancouver, Canada), Gargett et al. (1984) proposed a wide range of critical Re_b from 18 to 165. Stillinger et al. (1983) noted that the high critical values of Re_b reported by Gargett et al. (1984) correspond to very active turbulent regions that are less influenced by regular internal waves but are associated with topographic lee waves accompanied by shear instabilities.

4. Results and Discussion on External Intermittency

4.1. Patch identification

In this work, we develop a new patch detection procedure using several tests (as described in in Chapter 2, subsection 2.4) combined with an inspection of the microstructure shear signal. This procedure was to be tested in Lake Banyoles; a shallow lake whose waters have very low conductivity. Since density in fresh water is almost completely determined by temperature, temperature profiles are commonly used to compute L_T in lakes (Piera et al., 2002; Lozovatsky et al., 2005; Lorke et al., 2008; Pernica et al., 2014). Then, individual temperature profiles are used to identify microstructure patches based on the computation of their respective Thorpe displacement profiles $d_T'(z)$.

4.1.1. New method for turbulent patch identification

The procedure of turbulent patch identification follows the procedure described in Galbraith and Kelley (1996) and introduces not only the corrections for the run-length as suggested by Johnson and Garrett (2004) (see in Chapter 2, subsection 2.4), but also the inspection of the microstructure shear signal. The proposed method has two basic steps: identify overturns and decide if they meet the requirements to be accepted as turbulent patches. These two steps are detailed below.

i. *Identification of overturns:* Temperature profiles are averaged over a specific distance to eliminate the smallest scales which are not resolved by the sensor. Then, in our work, complete microstructure overturns are identified automatically as segments with $d_T'(z) \neq 0$ and

$\sum d_T'(z) = 0$ (Dillon, 1982). Next, numerous pairs of small-scale shear $u_z'(z)$ and $d_T'(z)$ profiles will be visually inspected to determine whether different overturns belong to the same structure or not. Thus, a criterion based on microstructure signal is applied to combine segments into one overturn.

ii. *Acceptance criteria for turbulent patches:* To accept overturns as turbulent patches, we develop an algorithm which considers not only the nominal accuracy of the sensors, but also takes into account the actual noise level of the signal. In this way, overturns are accepted as turbulent patches based on two criteria: Firstly, since instrumental noise imposes a constraint on the thickness of detectable patches, the smallest sizes based on the value of the Thorpe scale within the patch are evaluated rewriting (2.6) in terms of the temperature

$$L_{Tp\min} = 2\frac{g\alpha\delta T}{N^2}, \tag{4.1}$$

where α is the thermal expansion coefficient. Here, the subscript '*p*' is introduced to indicate that turbulent scales will be evaluated inside the patches. Finally, we implement a statistical run-length test (Galbraith and Kelley, 1996; see Chapter 2, subsection 2.4) to differentiate turbulent patches and noise segments. Following Galbraith and Kelley (1996), we added the root mean square of the run-lengths of series *r* to (4.1) in order to accept a patch. However, to specify a safety margin we introduce the suggestions of Johnson and Garrett (2004) and inspect the plots of the scaled amplitude *Q* of the noise against the number of points n. Considering only temperature as a main contribution of density, the scaled amplitude *Q* of the noise can be expressed as

$$Q = \frac{\delta T}{\left(\frac{dT}{dz}\right)h_p}, \tag{4.2}$$

where h_p is the patch height, δT the resolution of the temperature sensor and dT/dz the background temperature gradient computed using the reordered temperature profile. Once the Q and n parameters of a set of experimental data are found, these plots will be used to assess the noise threshold r for the measured displacements. The maximum value of r is added as the cut-off value for the run-length test. Then, the results of the run-length impose another constraint for the Thorpe displacements to accept segments as microstructure patches.

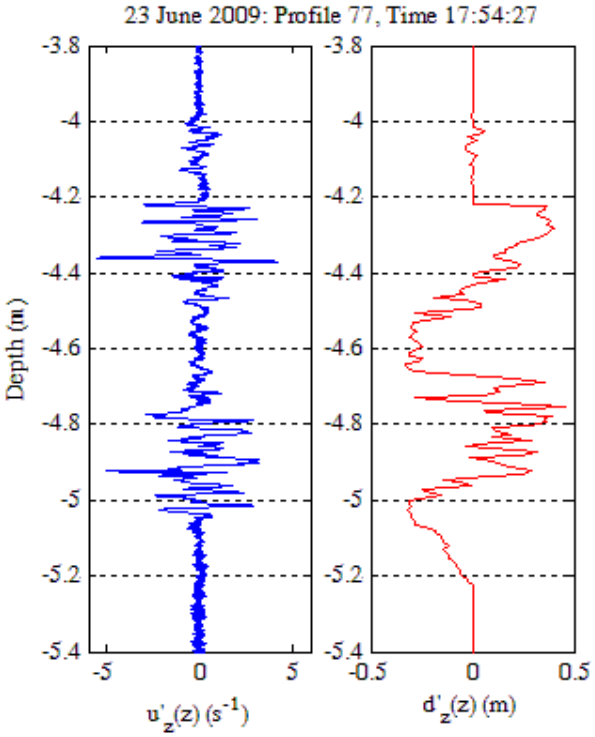

Fig. 4.1 Thorpe signal (on the left) and small-scale signal (on the right) obtained in the thermocline of Lake Banyoles on June 23. Note the difference of the microstructure signal within and outside the patch.

4.1.2. Application to our measurements

Following the methodology described above, the temperature profiles were first averaged over Δ = 0.8 cm to avoid false displacements resulting from noise. This averaging also eliminated scales that could not be resolved due to the time response of the temperature sensor. Then, complete microstructure overturns were detected automatically from Thorpe displacements $d_T'(z)$. After that, they were visually inspected together with the microstructure shear signal $u_z'(z)$ in order to check the criteria for patch identification. One such example is

shown in Fig. 4.1. Two segments corresponding to two independent overturns are clearly visible from the plots of $d_T'(z)$ profiles, between 3.8 and 5.4 m depth. First, one is found at depths between 3.90 and 4.17 m in the water column. The other is located 4 cm below with its upper boundary located at 4.21 m and the lower at 5.23 m. Small-shear signal also show signatures between 3.9 m and 5.2 m, which appear to be different from the signal outside this region. This indicates that they possibly belong to the same patch and they should be put together. After the inspection of the different pairs of Thorpe displacements $d_T'(z)$ and microstructure shear $u_z'(z)$ profiles, we concluded that segments separated by distances less than 6 cm could be combined into one single patch.

Selected patches of size h_p were used to evaluate the Thorpe scale L_{Tp}, defined as root-mean-square of d_T' (see Chapter 2, subsection 2.3). We implemented the statistical run-length test, to differentiate turbulent patches and noise segments. Following Galbraith and Kelley (1996), we added a safety margin *r* to the noise pdf (see (2.7)), evaluated from the plots suggested by Johnson and Garrett (2004). The non-dimensional parameter *Q* was calculated, plotted as a function of *n* and compared with the JG plots.The maximum *r* appeared to be 1.2, which is the factor to be added to the cut-off value. The result of the run-length test is given in Fig. 4.2 which shows *n* = 5 as an estimate of the cut-off run-length. Thus, the $d_T'(z)$ with $h_p <$ 5Δ = 4 cm segments were not accepted as microstructure patches.

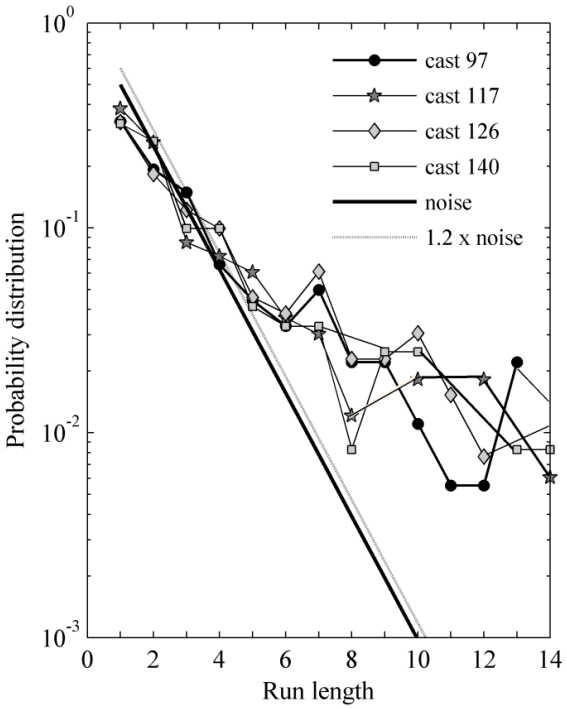

Fig. 4.2 The probability density functions of the Thorpe run-lengths for different profiles. The pdfs of random, uncorrelated noise (thick line) and of the noise factor 1.2 (dashed line). The intersection between the measured and noise pdfs indicates the cutoff run-length equals 5.

The resolution of the microstructure temperature sensor, $\delta T \sim 0.001^{o}$C, imposed an additional constraint on the smallest sizes of detectable patches based on the value of the Thorpe scale within the patch $L_{Tp\min}$. For N^2 in the range $5\times\left(10^{-3}-10^{-5}\right)$ s^{-2}, $L_{Tp\min}$ varies between ~ 1 and 7 cm. Combining the constraints imposed by vertical and temperature resolutions and following Lee et al. (2009), we used an intermediate condition for patch detection. As a result, no segments with h_p < 4 cm and $L_{Tp} < 4$ cm were considered as turbulent patches.

Table 4.1 summarizes the results of the displacement analysis including the number of detected and accepted patches and the number of patches with h_p > 25 cm, which were used to estimate the mean kinetic energy dissipation rate from a small-scale shear within the patch height.

Session	Time (h)	Number profiles	$\overline{U}_{10}$ (m s^{-1})	σ_U (m s^{-1})	$U_{\max}$ (m s^{-1})	$\tau_{10} \times 10^{-3}$ (N m^{-2})	Patches detected	Patches accept	Patches h_p > 25 cm
23 Jun 2009	1.71	81	0.77	0.42	4.03	0.94	659	373	196
25 Jun 2009	2.07	102	3.20	3.20	13.90	12.53	1005	448	326
27 Jun 2009	1.72	98	<0.50	no data	1.30	< 0.37	774	450	323
01 Jul 2009	1.80	92	0.60	2.20	4.47	0.54	880	512	283

Table 4.1 Characteristics of the field campaign, wind speed U_{10}, wind stress τ_{10}, and microstructure patches.

4.2. Patch location in the water column

The generation of turbulence in water's interior and boundary layers is usually governed by different processes. Roget et al. (2006), examining the

statistics of eddy diffusivities on a shallow shelf of the Black Sea, analyzed the importance of addressing processes orientated to domain averaging in order to interpret adequately the state of mixing in different layers. Then, previous to the analysis of patch turbulence, identifying the layers which divide the lake water column is indispensable. This allows characterizing which mechanisms are present in each layer and separately analyzing the statistics of patches.

4.2.1. Identification of layers in our measurements

To identify the layers in our measurements, the temperature, T (z,t), and squared buoyancy frequency, N^2 (z,t), have been analyzed. The corresponding contour plots are shown in Fig. 4.3 for the measurements taken under moderate winds conditions (June 25), and in Fig. 4.4 and Fig. 4.5 in light winds (June 27 and July 1, respectively). Based on the plots shown in Fig. 4.3 - Fig. 4.5, three major layers of the water column were specified.

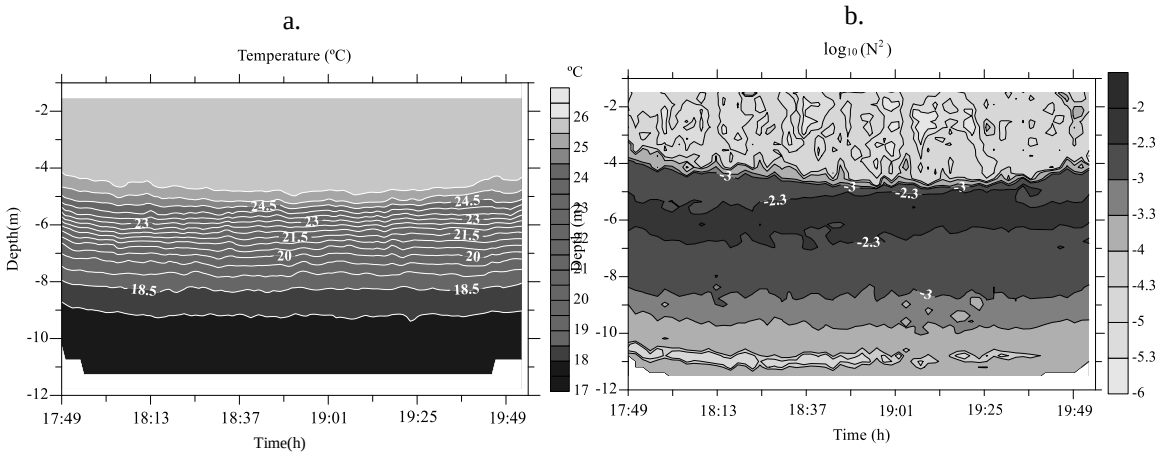

Fig. 4.3 The contour plot of temperature T (a) and the logarithm of squared buoyancy frequency $\log_{10}(N^2)$ (b) for June 25 (N is in s^{-1}).

We consider the surface layer (SL) , as the layer between the lake surface and the depth where N^2 sharply exceeds 10^{-3} s^{-2}. This layer was directly influenced by wind stress and heat fluxes. The depth of this layer varied between 2.5 and 4.5 m, depending on the atmospheric forcing prior to and during the observational periods. Stratification in the SL increased ($N^2 > 10^{-4}\,s^{-2}$) during periods of low winds ($\overline{U}_{10} < 0.5$ m s^{-1} on June 27 and July 1).

The thermocline (TH), starts immediately below the SL. It was strongly stratified (with a highest mean of $N^2 \sim 10^{-2}$ s^{-2}) and its thickness varied between 4 and 6 m in the depth range below the SL, with $z \sim 8.5$ m occupying ~ 35-55% of the water column.

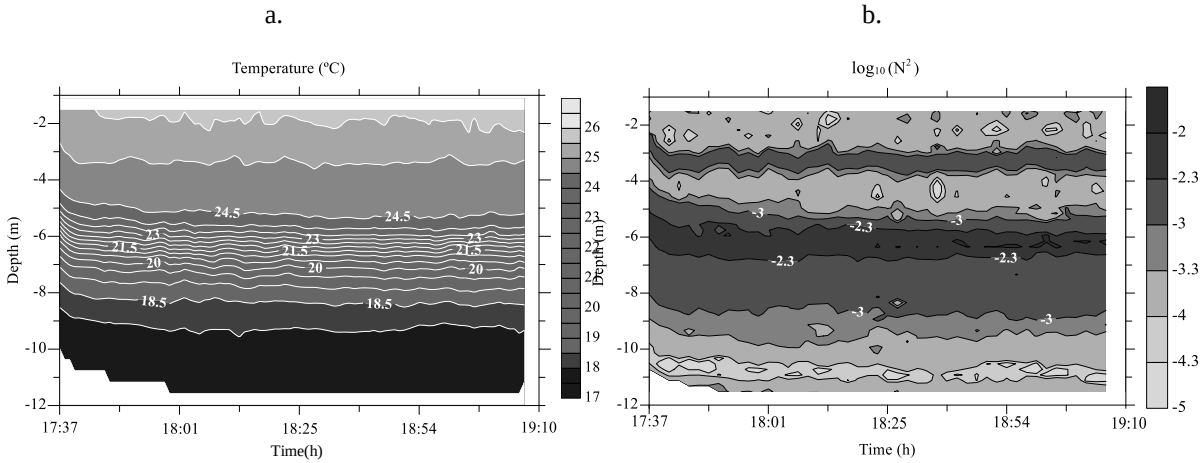

Fig. 4.4 The contour plot of temperature T (a) and the logarithm of squared buoyancy frequency $\log_{10}(N^2)$ (b) for June 27 (N is in s^{-1}).

Internal waves in the thermocline are easily recognizable in Fig. 4.5a. The opposite direction of the vertical displacements of the upper and lower boundaries of the thermocline (Fig. 4.5a, dashed lines) points to a dominant second mode of internal seiche. The direction for the horizontal velocity within each layer depends on the phase of the seiche oscillation, but the relative vertical structure of this horizontal velocity between layers remains the same. An example of horizontal velocities in each layer, identified by the white arrows, is shown in Fig. 4.5a. A two-dimensional three-layered hydrodynamic model (Münnich et al., 1992) was used to simulate the dynamics of internal seiches in the lake for the stratification observed on July 1. It was found that the period of the second vertical first horizontal internal mode (V2H1) was about 12 h, which is in agreement with the results obtained previously for similar atmospheric conditions and stratification in the lake (Roget et al., 1997). Field measurements on June 25 and 27 started two hours later than on July 1 and were therefore affected by a different phase shift in the V2H1 seiche mode, which followed from the time evolution of the isotherm depths shown in Fig. 4.3 and Fig. 4.4.

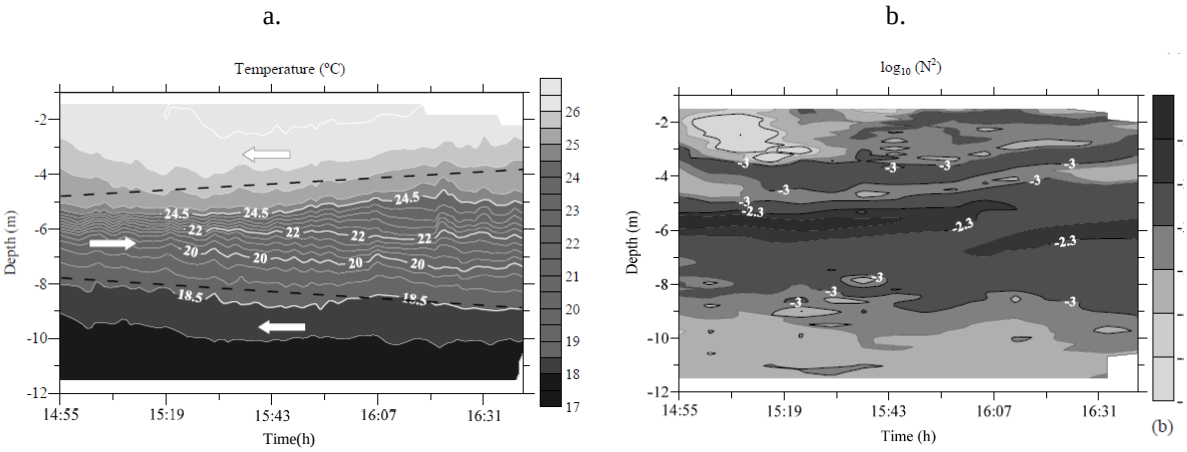

Fig. 4.5 The contour plot of temperature (a) and $\log_{10}(N^2)$ (b) for July 1. The opposite slopes of the upper and lower boundaries of the thermocline marked by dashed lines point to the dominant second mode of the internal seiche. The directions of flow in each layer are shown in panel (a) by white arrows.

The bottom layer (BL), extended from the base of the TH (z ~ 8.5 m) down to the bottom of the lake. The BL thickness was about 3 m with N^2 varying from 10^{-5} to 10^{-3} s^{-2}. A thin (~ 1 m wide) temporal weakly stratified ($N^2 < 5\times10^{-5}$ s^{-2}) sublayer was located at z ~ 10 m (Fig. 4.3b and Fig. 4.4b).

4.2.2. Stability of the water column

Shear flows in stratified systems are characterized by two relevant parameters: vertical shear Sh and buoyancy frequency N. Formally, vertical shear is defined as $Sh^2 = U_z^2 + V_z^2$, where $U_z = \partial U/\partial z$ and $V_z = \partial V/\partial z$ are the vertical gradients of the orthogonal components, U and V, of the horizontal velocity. On the other hand, the buoyancy frequency N corresponds to the frequency of oscillation at which a vertically displaced parcel will oscillate within a statically stable environment. The ratio between inertia (destabilizing) to buoyancy (stabilizing) forces is called the Richardson number Ri, i.e. $Ri = N^2/Sh^2$. In fact, it represents the capacity of the shear flow to destroy the density gradients. Large values of Ri indicate that the water column is very stable; high stratification suppresses turbulence. To the contrary, the water column is unstable for low values of Ri. The transition takes place at the critical

value of Ri_c ~1. It is usually accepted that the critical value for shear instability is $Ri_c = 0.25$.

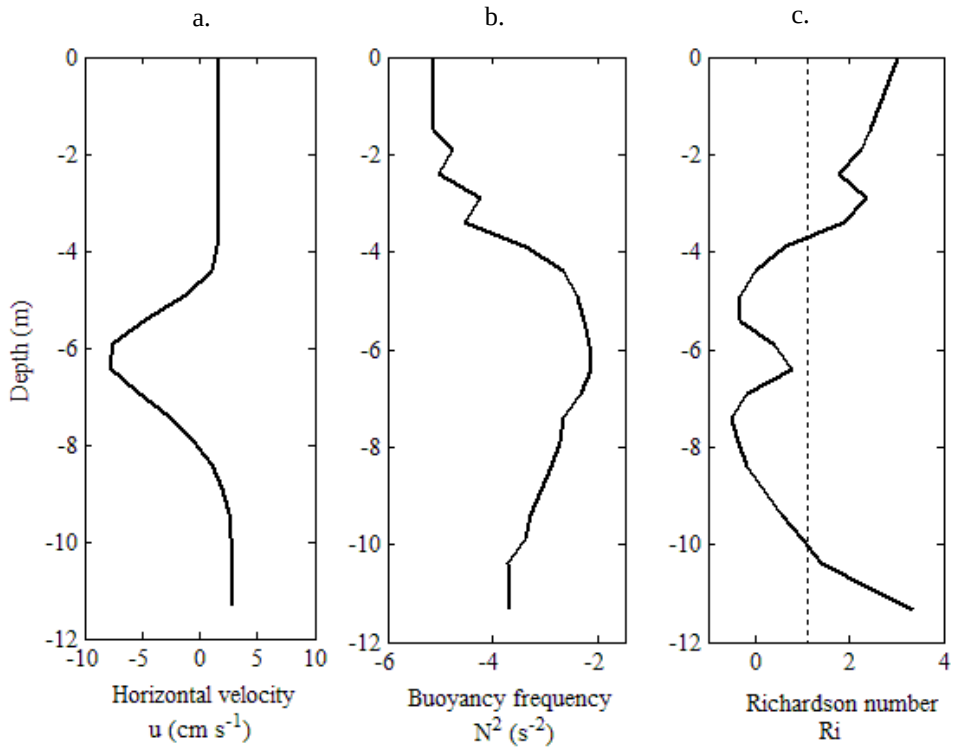

Fig. 4.6 The horizontal velocity profile of the second vertical mode of internal seiche u (a) calculated for a characteristic N^2 profile (b) and the resulting profile of $\log_{10}(Ri)$ (c).

To obtain a clearer view of the vertical structure of the horizontal velocity in the TH, we calculated the normal modes for a characteristic $N^2(z)$ profile shown in Fig. 4.6 (central panel) using a discretized version of the Taylor-Goldstein equations (Thorpe, 2005). The vertical profile of the horizontal velocity u of the dominant second vertical mode was used to estimate the shear profile of the internal seiche and the corresponding 'seiche Richardson number', with a vertical step Δz = 0.5 m. In Fig. 4.6, the horizontal velocity and the Richardson number are shown on the left and right panels, respectively. Low Ri values are concentrated near the upper and lower boundaries of the TH, where the internal-seiche shear is high (the value of Ri = 1 is indicated in Fig. 4.6 by a dashed line). Depending on the seiche phase and mode structure, turbulence in

the thermocline can be generated by seiche-induced shear instability (Münnich et al., 1992).

The calculation of *Ri* at 15 min time intervals throughout the entire period (12 h) of the seiche dominant V2H1 mode allowed for the simulation of the cumulative distribution function (CDF) of *Ri* in the thermocline, which is shown in Fig. 4.7.The Richardson number was less than critical for shear-induced turbulence ($Ri < 0.25$) approximately 25% of the time and in about 55% of cases it was below 1. It is important to emphasize that the vertical shear associated with the oppositely directed internal-seiche induced currents can episodically create shear instability in the thermocline and hence generate smaller scale internal waves and turbulent patches.

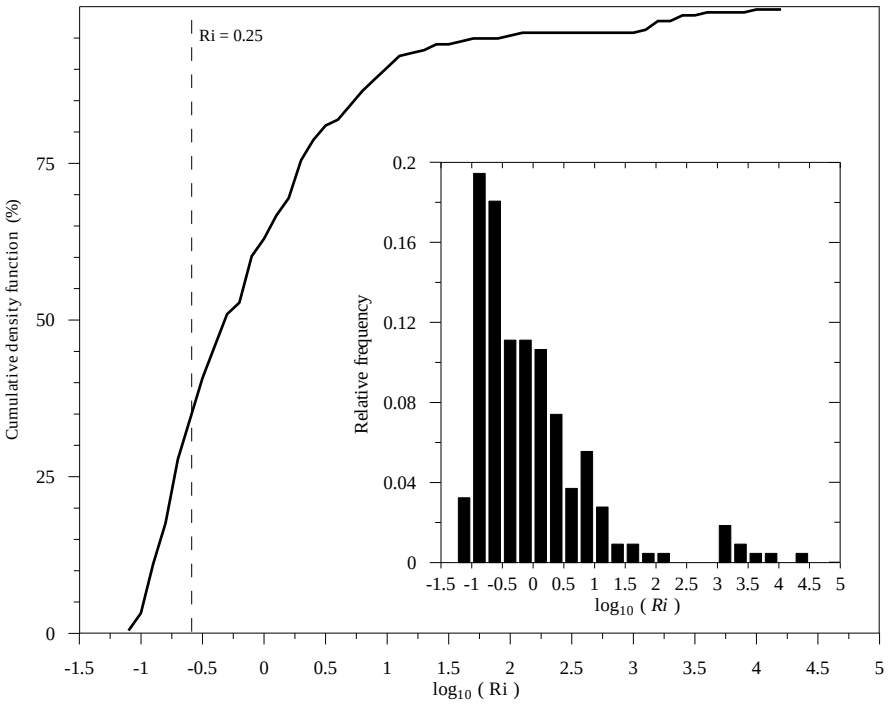

Fig. 4.7 The cumulative distribution function (CDF) of the simulated seiche Richardson numbers *Ri* in the thermocline. See insertion for the histogram of *Ri*.

It should be noted that the TH periodically contained several sublayers. For example, on June 27 when the wind speed was less than 0.5 m s^{-1} during the entire observational period, the TH (Δz = ~ 2.5 - 8.5 m) contained three definitive sublayers. A 1 m wide diurnal thermocline (Imberger, 1985) underlay

the SL where $N^2 \approx (1-5)\times 10^{-3}$ s^{-2}. Below it, a less stratified inner layer (N^2 < 10^{-3} s^{-2}) was observed down to z ~ 4.5 m. Finally, the most strongly stratified sublayer extends down to the lower boundary of the TH (Δz = ~ 4.5 - 8.5 m with $N^2 \approx 5\times 10^{-3}$ s^{-2}). The same sublayer structure in the TH was found on July 1 when the wind speed was also low (see Fig. 4.5b). The depths of the sublayers varied over time due to the influence of internal waves. In contrast, on June 25 when higher winds preceded the microstructure measurements, the TH did not contain any sublayers and the SL deepened to z ~ 4.5 m.

4.2.3. Patch location

The contour plots of the dissipation rate $\varepsilon(z,t)$ are shown in Fig. 4.8 together with the locations of turbulent patches with h_p > 25 cm (see subsection 4.1.2, Table 4.1).

It appears that the different patterns of the dissipation field generally correlate well with the locations and sizes of the microstructure patches. From these plots, it can be seen that wind forcing sustains turbulence in the SL and it is characterized by $\varepsilon > 5\cdot 10^{-8}$ W·kg^{-1}. In the TH, turbulence was patchy, with several episodes of large overturns. On June 27 and July 1, when three sublayers were clearly visible, the less stratified inner layer appears partially filled by turbulent patches; some with a height of $\varepsilon \approx 5\cdot 10^{-6}$ W· kg^{-1}. However, the majority were generally small and weak. Plots also reveal the existence of microstructure patches within the other sublayers, but of a lesser percentage and less energetic than before. Finally, in the BL several episodes of relatively strong turbulent events with $\varepsilon \geq 5\cdot 10^{-8}$ W·kg^{-1} were observed. The rest of the BL was filled with microstructure patches with a relatively low dissipation rate, some most probably associated with a slow moving intrusion from a remote region of the lake (Planella et al., 2009).

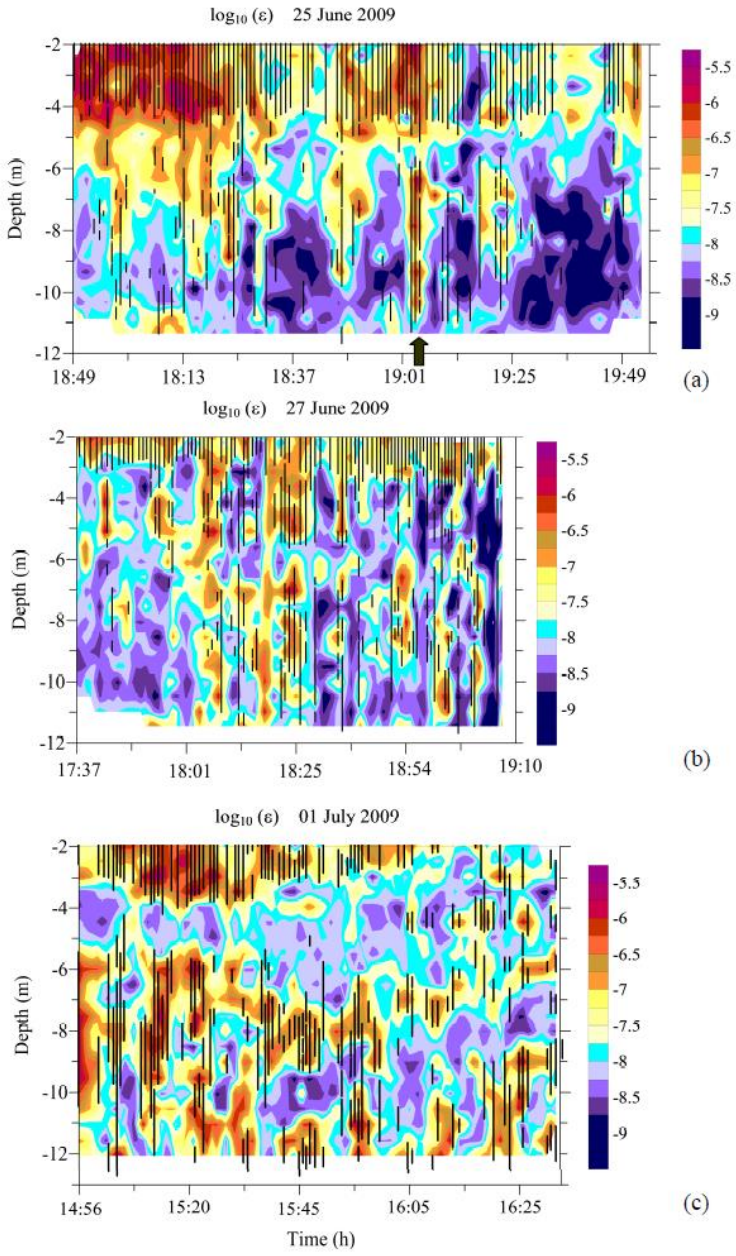

Fig. 4.8 Alignment of microstructure patches (vertical lines) in the background of $\log_{10}(\varepsilon)$ for June 25 (a), June 27 (b) and July 1 (c). The dissipation rate is in $W \cdot kg^{-1}$. The arrow in panel (a) points to the turbulent event induced by the wind gust.

4.2.4. Wind gusts and turbulent events

Powerful wind gusts lasting several minutes episodically passed over the lake in the late afternoon. We were lucky to measure a series of five consecutive

casts that embraced one of these events (marked by an arrow in Fig. 4.8a). Its evolution can be analyzed based on the Thorpe displacement $d_T'(z)$ and small-scale shear $u_z'(z)$ profiles; both of which are shown in Fig. 4.9. The event was captured on June 25 when a maximum wind speed of 7.7 m·s^{-1} was recorded during the meteorological data sampling time. The first cast in this series was taken at 19:00 and shows a weakly-turbulent SL 4.5 m in depth. The corresponding Thorpe displacements depict a classic Z-shape segment (Gibson, 1987). The averaged dissipation rate in the SL was relatively low, $\widetilde{\varepsilon}_{\mathrm{SL}} \approx 2.8 \cdot 10^{-8}$ W·kg^{-1}, and the corresponding buoyancy Reynolds number was $Re_b = \varepsilon / \nu N^2 \approx$ 900. No microstructure patches were detected in either the TH or BL during this cast.

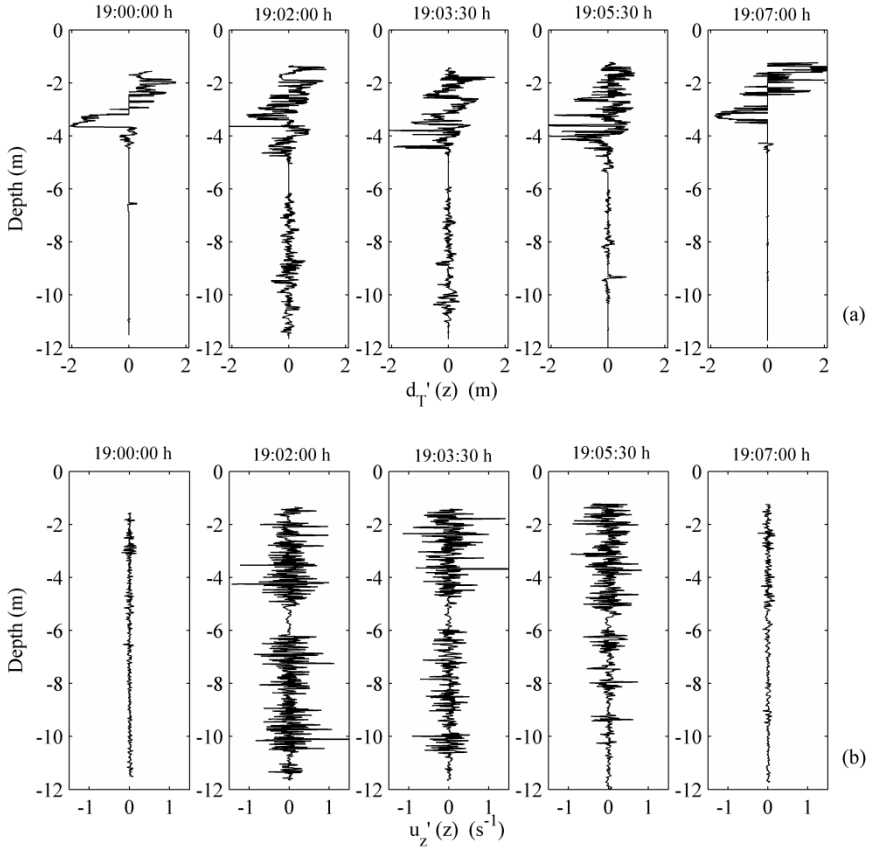

Fig. 4.9 A series of Thorpe displacements $d_T'(z)$ (a) and small-scale shear $u'_z(z)$ profiles (b) taken on June 25 during the passage of a wind gust (see text for details).

The thickness of the SL in the next profile (19:02 h) increased to z = 5 m and the averaged dissipation rate went up by about two orders of magnitude, $\tilde{\varepsilon}_{\mathrm{SL}} \approx 2.3 \cdot 10^{-6}$ W·kg^{-1} ($Re_b \approx 4800$). A large new turbulent patch emerged below z = 6.15 m, with $\tilde{\varepsilon}_{\mathrm{BP}} \approx 1.2 \cdot 10^{-6}$ W·kg^{-1} and $Re_b \approx 900$. The third profile in the series, taken at 19:03:30 h, shows that the thickness of the SL (4.7 m) and $\tilde{\varepsilon}_{\mathrm{SL}} \approx 2.2 \cdot 10^{-6}$ W·kg^{-1} was almost the same as during the second cast, but the amplitudes of Thorpe displacements and the dissipation within the large patch had decreased slightly ($\tilde{\varepsilon}_{\mathrm{BP}} \approx 7 \cdot 10^{-7}$ W·kg^{-1} and $Re_b \approx 450$). The following profile taken at 19:05:30 h demonstrates active turbulent mixing in the SL with a mean dissipation of $\tilde{\varepsilon}_{SL} \approx 10^{-6}$ W·kg^{-1} ($Re_b \approx 1500$) and the depth increased to ~ 5.5 m due to entrainment at the SL base. However, as the wind stress on the surface weakens, several microstructure patches still exist in the TH and BL, with $\tilde{\varepsilon}_{\mathrm{BP}} \approx 2 \cdot 10^{-7}$ W·kg^{-1} and $Re_b \approx 300$. One and a half minutes later, at 19:07 h, the fifth cast in the series shows a similar microstructure profile in the SL and no patches in the either TH or BL as observed in the first cast.

We also analyzed the evolution of turbulence in the surface layer based on the L_{Tp} / h_p ratio, which is supposed to decrease with time as turbulence ceases in a patch (Smyth et al., 2001). It was found that L_{Tp} / h_p decreased from ~ 0.2 to ~ 0.1 between 19:00 h and 19:02 h. Over the following three and a half minutes L_{Tp} / h_p decreased only slightly, remaining close to 0.1. The observed evolution of L_{Tp} / h_p is consistent with direct numerical simulations of a shear-driven overturn as it becomes turbulent (Smyth et al., 2001, their Fig. 4a).

4.3. Statistics of turbulent scales

In this subsection, results and discussion of the statistical analysis performed in the thermocline of the Lake Banyoles are presented. Our study analyzes the probability distribution function of the patch size h_p, the patch

Thorpe L_{Tp} scale and the normalized patch Thorpe L_{Tp}/h_p scale. Finally, a possible parameterization for L_{Tp}/h_p is also tested in the lake.

The total number of patches in the TH (subsection 4.1.2) was 315. Rare large turbulent events detected in the TH, generated mostly by short, powerful wind gusts (described in previous subsection), will belong to a different statistical population than the main population of regular sheared TH patches and were excluded from the analysis. In fact, the box plot distribution of h_p was inspected before performing the statistical analysis and these patches were identified as outliers. It was found that the outliers were outside the 2nd and 98th percentile, i.e. $h_p \in [0.10, 3.5]$ m, so we did not use these samples for any further analysis. The statistical independence of the remaining patches was analyzed for a complete set of the profiles as well as for the three subsets containing every second, third, and fourth profile. It appears that the complete dataset (315 patches) can be considered as a series of statistically independent samples.

4.3.1. The patch size

The cumulative distribution function (CDF) of the sizes of the microstructure patches h_p detected in the MT is shown in Fig. 4.10a. The plot shows that about 95% of the empirical cumulative distribution function $F(h_p = 0.14 - 2.15$ m) can be approximated by log-normal distribution

$$F(h_p) = \frac{1}{2} erfc\left[-\frac{\log(h_p) - \overline{\log(h_p)}}{\sigma\sqrt{2}} \right] \tag{4.3}$$

where *erfc* is the complimentary error function (Crow and Shimizu, 1988) and the parameters of the fit $\overline{\log(h_p)} = -0.65 \pm 0.08$ and $\sigma^2_{\log(h_p)} = 0.75 \pm 0.05$. The corresponding mean and median values are $\overline{h_p} = 0.69$ m, $med\ (h_p) = 0.50$ m. The Kolmogorov-Smirnov test (Ayyub and McCuen, 1996) of the goodness of the fit suggests that (4.3) cannot be rejected as a probability model for the empirical

CDF (p-value = 0.89; K-S statistics are 0.032, which is less than the K-S critical value of 0.076 at the 95% confidence level).

Log-normal distribution has been used as an approximation of patch sizes in various regions of ocean and coastal marine waters (Lozovatsky et al., 1993; Pozdynin, 2002). Stansfield et al. (2001) reported that the probability distribution of patch sizes in the ocean pycnocline can be considered as log-normal for 70% of their data (1 m < h_p < 15 m). Yamazaki and Lueck (1987) in turn suggested Gamma (or a simpler exponential) distribution as a possible approximation of $F(h_p)$. Our analysis of TH patches in Lake Banyoles confirms the log-normality of h_p distribution in the range ~ 0.14 m < h_p < 2.15 m.

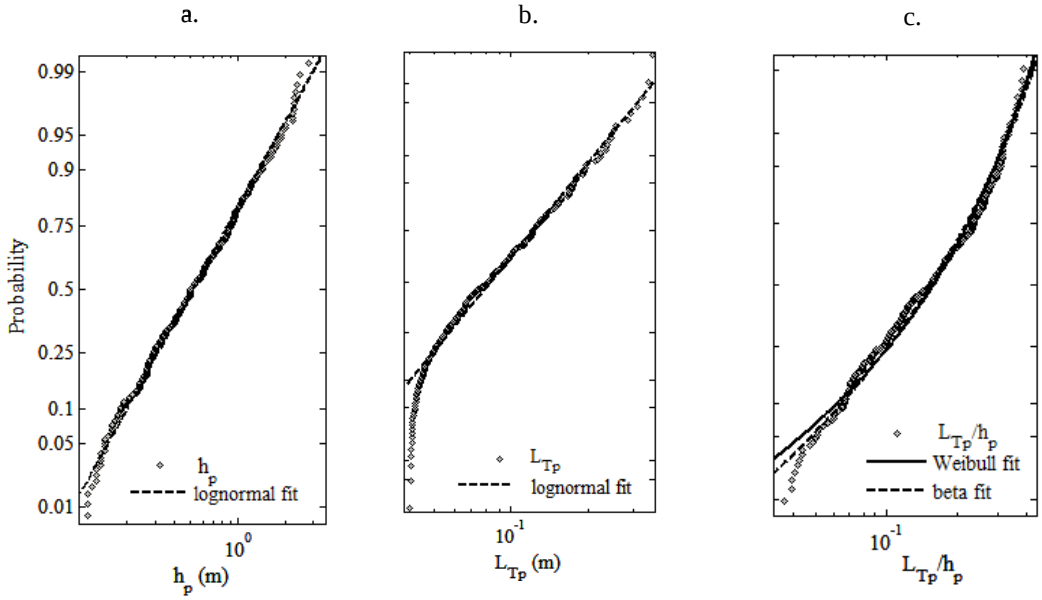

Fig. 4.10 The cumulative distribution functions (CDF) of the patch sizes h_p in the thermocline (a) and the patch Thorpe scale L_{Tp} (b) fitted by log-normal model (dashed lines). The CDF of the normalized patch Thorpe scale (c) is approximated by the Weibull (solid line), and beta (dashed line) distributions.

Lozovatsky and Fernando (2002) pointed out that the probability distributions of the sizes of turbulent regions as well as other properties of turbulence, such as turbulent scales and patch-averaged dissipation rates, are expected to be log-normal due to the similarity between the breakdown of turbulent eddies and the sizes of particles resulting from a series of successive statistically independent breakdowns, which is considered as asymptotically log-normal (Kolmogorov, 1941c).

4.3.2. The Thorpe scale within patches

The probability distribution of the Thorpe scale $F(L_T)$ has been analyzed in different aquatic environments mainly based on equal-distance segmentation of the Thorpe displacement profiles. Alford and Pinkel (2000) found that for $L_T \geq$ 1.5 m (CTD measurements in the thermocline of the Pacific Ocean) the tails of a log-normal distribution fit the empirical data well. Stansfield et al. (2001) also reported that based on CTD measurements the log-normal model to be an appropriate fit for $F(L_T)$ in the pycnocline of the Juan de Fuca Strait. Kitade et al. (2003) and Huzzey and Powell (2005) showed histograms of L_T that are clearly skewed to high values. The authors stated that the distributions were definitely not normal, but no formal approximation was suggested. All of these results were obtained for L_T larger than 0.4 m. It should be noted that the Thorpe scale in all the publications referred to was calculated at fixed, equally distant segments of the water column. For such L_T data, Lorke and Wüest (2002) found exponential rather than log-normal distribution to be the best fit for $F(L_T)$. Their measurements were taken in Lakes Baikal (Russia), Neuchâtel (Switzerland), and Müggelsee (Germany). The exponential model can be appropriate for $F(L_T)$ when L_T is calculated at the segments of $d_T'(z)$ profiles with arbitrary (usually equal) length and where the probability of zero L_T is not zero. For microstructure patches, however, the exponential model cannot be applied because $F(L_{Tp} = 0)$ must be zero, since $L_{Tp} = 0$ contradicts the definition of a patch.

In this study, we calculated the Thorpe L_{Tp} scales inside the microstructure patches. The CDF of the Thorpe scale for the TH patches $F(L_{Tp})$ shown in Fig. 4.10b can be fitted by log-normal distribution in the range 0.05 m < L_{Tp} < ~ 0.4 m, which covers ~ 85% of the data. The parameters of the distribution are $\overline{\log(L_{Tp})}$ = - 2.46 ± 0.05 and $\sigma_{L_{Tp}}$ = 0.52 ± 0.04. The mean value $\overline{L_{Tp}}$ = 0.10 m and the median value $med(L_{Tp})$ = 0.08 m. The K-S test for log-normal models,

however, is very close to its critical value at a level of 95%, and the goodness of the fit for L_{Tp} is lower than that for h_p.

4.3.3. The normalized Thorpe scale

The CDF of the normalized patch Thorpe L_{Tp}/h_p scale is plotted in Fig. 4.10c for the patches detected in the TH. Therefore, we explored several statistical models for the probability distribution of L_{Tp}/h_p. One such model is the Weibull (1951) distribution, which was suggested by Lozovatsky and Erofeev (1993) as a way of approximating the CDFs of the fine-structure inhomogeneities of N^2 on the assumption that stratification has the highest probability of being destroyed by turbulence in those layers of random thickness with the lowest N^2. Using the analogy between breaking events and turbulent overturns responsible for random generation of quasi-homogeneous (mixed) fine-structure layers and the generation of turbulent patches, we can apply this approach to the distribution of L_{Tp}/h_p.

The Weibull distribution

$$F\left(\frac{L_{Tp}}{h_p}\right)=1-exp\left[-\left(\frac{1}{\lambda_w}\left(\frac{L_{Tp}}{h_p}\right)\right)^{c_w}\right] \qquad 0<\frac{L_{Tp}}{h_p}<\infty \tag{4.4}$$

is specified by the scale λ_w and shape c_w parameters, which are related to the mean $\overline{L_{Tp}/h_p}$ and root mean square (rms) σ_{L_{Tp}/h_p} values of L_{Tp}/h_p through the Gamma function $\Gamma(x)=\int_0^\infty t^{x-1}e^{-t}\,dt$ as follows,

$$\overline{L_{Tp}/h_p}=\lambda_w\Gamma(\Phi), \qquad \text{where} \qquad \Phi\equiv 1+\frac{1}{c_w} \tag{4.5}$$

and

$$\sigma_{L_T/h_p}=\lambda_w{}^2\left[\Gamma(\Theta)-\Gamma^2(\Phi)\right], \qquad \text{where} \qquad \Theta\equiv 1+\frac{2}{c_w} \tag{4.6}$$

It should be noted that the Gamma function in (4.5) and (4.6) depends only on the shape parameter c_w.

The Weibull model fits the empirical $F(L_{Tp}/h_p)$ well in the range 0.07 < L_{Tp}/h_p < 0.5, which covers ~ 95% of the distribution, leaving out only 5% of the smallest L_{Tp}/h_p (Fig. 4.10c, solid line). The maximum likelihood estimates of the scale and shape parameters with 95% confidence intervals are λ_w = 0.21 ± 0.02 and c_w = 1.94 ± 0.16. It is evident that Weibull distribution is a good estimator of the normalized patch Thorpe scale in the thermocline.

The Weibull model has also been applied to the distribution of the Thorpe scale in a weakly stratified surface layer of the Boadella reservoir (Catalonia, Spain) during a period of wind-induced turbulence (Roget et al., 2006). Because the entire surface layer was turbulent during the period of measurements, its depth could be considered as h_p and it is therefore possible to compare the distributions of L_{Tp}/h_p in the Boadella reservoir and Lake Banyoles. Although the scale parameters of the corresponding Weibull approximations for Boadella and Banyoles are very different, the shape parameters c_w appear to be almost the same. In Boadella, c_w = 2.0 with a 95% confidence interval between 1.74 and 2.30; in Banyoles, c_w = 1.94 ± 0.16. This might be a coincidence, but it is also possible that the value c_w ~ 2 of the shape parameter is related to the nature of the turbulence, which is associated with shear instability in both cases. When L_T was analyzed in two double-diffusion convective layers with constant but different thicknesses h_p (Sanchez and Roget, 2007), it was found that the distributions of L_{Tp}/h_p could be approximated with a 95% confidence level by the Weibull model with c_w = 4.2 for both layers. This may indicate that the shape parameter of the Weibull distribution of the normalized patch Thorpe scale can characterize different mechanisms in the origin of the microstructure.

Since the patch Thorpe scale cannot exceed the size of a patch (specifically for turbulent events related to individual overturns) the probability distribution of L_{Tp}/h_p has to be defined on a finite domain [a, b], where a = 0 and b are its lower and upper boundaries. One of the continuous distributions that satisfy this condition is the beta distribution, whose principle features can be found in

many statistical books (Mood et al., 1974; Evans et al., 2000; Bean, 2001; Forbes et al., 2011). Its probability distribution function (pdf) is defined as follows

$$pdf_B(x) = \frac{x^{m-1}[b-x]^{q-1}}{B(m,q)\,b^{m+q-1}}, \qquad 0 < x < b, \tag{4.7}$$

where m and q are positive parameters of the beta function

$$B(m,q) = \int_0^1 t^{m-1}(1-t)^{q-1}dt\,. \tag{4.8}$$

The beta distribution fit shown in Fig. 4.10c coincides with the Weibull CDF for the upper 95% of the entire data set. Parameters of the model are m = 2.56 ± 0.47 and q = 10.65 ± 2.07 (b = 1), and the mean value $\overline{L_{Tp}/h_p}$ = 0.19.

The Weibull and beta approximations were tested using Kolmogorov-Smirnov statistics with a 95% confidence level. In the case of the Weibull distribution, the p-value, the K-S statistics and its critical value are 0.21, 0.060, and 0.076 respectively; while for the beta model they are 0.35, 0.052, and 0.076. In both cases, K-S statistics are less than the critical value, so neither distribution can be rejected as a probability model for the empirical CDF at the 95% confidence level. The p-value shows that the probability is higher for the beta model than for the Weibull distribution. If we run the test for an 80% confidence level then the Weibull model should be rejected, but the beta one should not. It should be noted that the upper limit of the random variable for the beta model is 1, although $max(L_{Tp}/h_p) < 1$.

4.3.4. Global statistics

Table 4.2 summarizes parameters of the probability distributions of h_p, L_{Tp}, and L_{Tp}/h_p separately for the entire set of patches (very small patches of L_{Tp} < 4 cm were not considered due to noise restrictions) and also for patches of h_p > 25 cm, where the calculation of ε was possible. The goodness of the fits and the appropriate range of the corresponding variables for the proposed CDFs are shown in Table 4.2.

For the entire dataset, the empirical CDF of patch sizes can be well fitted by a log-normal model deviating from log-normality by only CDF(h_p) < 0.03 and CDF(h_p) > 0.97. When small patches (h_p < 25 cm) are not included in the analysis of the CDF, the lower tail starts to deviate from the log-normal distribution at a much higher CDF(h_p) ≈ 0.15 (see Table 4.2).

A sharp cut in the lower tail of the L_{Tp} distribution is also observed for 15% of our data, which could be a result of the constraints of the patch identification method (L_{Tp} > 4 cm). When only patches with h_p > 25 cm were analyzed, the range of validity for the log-normal fit to the empirical CDF(L_{Tp}) extended from an initial 15% to 8%.

Based on the general results summarized in Table 4.2, it can be seen that the lack of vertical resolution, which prevents the identification of small patches, may explain the sharp cuts in the tails of the log-normal model for the patch size h_p as reported by several authors (Lozovatsky et al., 1993; Stansfield et al., 2001). Insufficient resolution of profiling measurements may also explain sharp tails at small scales of L_T probability plots (Alford and Pinkel, 2000; Stansfield et al., 2001) and the difficulties with fitting data to log-normal distribution reported by Kitade et al. (2003) and Huzzey and Powell (2005). It is worth noting, however, that small patches do not substantially modify the parameters of L_{Tp} distribution, because large eddies dominate the Thorpe scale values (Stansfield et al., 2001; Lorke and Wüest, 2002).

(a) Statistical parameters of the probability distribution of patch size h_p

	Log-normal distribution					K-S goodness-of-fit test	
Parameters CDF	$\overline{\log(h_p)}$	$\sigma_{\log(h_p)}$	*med(h_p)* (m)	$\overline{h_p}$ (m)	*p*-value	K-S statistics*	Range validity (m)
Entire data set (L_{Tp} > 4 cm)	-0.65	0.75	0.50	0.69	0.89	0.032 < 0.076	0.14 < h_p< 2.15 (3-97 % of data)
Patches with h_p > 25 cm	-0.42	0.60	0.62	0.78	0.19	0.066 < 0.083	0.35 < h_p < 2.00 (15-95 % of data)

(b) Statistical parameters of the probability distribution of the patch Thorpe L_{Tp} scale

	Log-normal distribution					K-S goodness-of-fit test	
Parameters CDF	$\overline{\log(L_{Tp})}$	$\sigma_{\log(L_{Tp})}$	*med(L_{Tp})* (m)	$\overline{L_{Tp}}$ (m)	*p*-value	K-S statistics*	Range of validity (m)
Entire data set (L_{Tp} > 4 cm)	-2.46	0.52	0.08	0.10	0.053	0.074 < 0.076	0.05 < L_{Tp} < 0.40 (15-99 % of data)
Patches with h_p > 25 cm	-2.39	0.51	0.09	0.11	0.51	0.051 < 0.083	0.044< L_{Tp} < 0.36 (8-99 % of data)

(c) Statistical parameters of the probability distribution of normalized Thorpe scale L_{Tp}/h_p

	Weibull distribution			K-S goodness-of-fit test	
Parameters CDF	λ_w	c_w	*p*-value	K-S statistics*	Range of validity
Entire data set (L_{Tp} > 4 cm)	0.21	1.94	0.21	0.060 < 0.076	0.07 < L_{Tp}/h_p < 0.5 (5-99 % of data)
Patches with h_p > 25 cm	0.19	1.99	0.21	0.065 < 0.083	0.05 < L_{Tp}/h_p < 0.4 (8-97 % of data)

	Beta distribution				K-S goodness-of-fit test	
Parameters CDF	*m*	*q*	*b*	*p*-value	K-S statistics*	Range of validity
Entire data set (L_{Tp} > 4 cm)	2.56	10.65	1	0.35	0.052 < 0.076	0.05< L_{Tp}/h_p< 0.5 (<5-99 % of data)
Patches with h_p > 25 cm	2.80	13.81	1	0.38	0.056 < 0.083	0.04< L_{Tp}/h_p < 0.4 (<5-97 % of data)

Table 4.2 Statistical parameters of log-normal distributions of h_p (a) and L_{Tp} (b), and the Weibull and beta distributions of L_{Tp}/h_p (c) in patches from the thermocline. *K-S statistics value is compared to the critical value of the test.

4.3.5. Parameterization of the normalized Thorpe scale

The Thorpe L_T scale, can serve as a good estimator of a characteristic turbulent scale that is used in semi-empirical closures of turbulent mixing in stratified flows. If L_T can be related to the patch size h_p, then the analysis of patch turbulence can be simplified by employing the algorithm of patch identification in a particular layer. As was shown in subsection 4.2.4, the ratio L_{Tp}/h_p varied in the SL depending on the state of turbulence, which is related to the age of the patch (Smyth and Moum, 2000; Smyth et al., 2001). The median value of L_{Tp}/h_p in the TH of Lake Banyoles was 0.18, which is more than twice the $med(L_{Tp}/h_p)$ = 0.07 reported by Moum (1996) for large ocean patches detected in the upper part of the thermocline. The size of the oceanic patches ranged between 3 and 15 m, while the lake patches detected in the TH are much smaller (the largest being h_p < 4 m). The background stratification in the ocean (a characteristic N ~ 0.005 s^{-1}) was much weaker than in the lake. Also, ocean patches selected for the analysis were large and not very energetic (with ε less than 10^{-8} $W \cdot kg^{-1}$ in more than 50% of cases). Therefore, the median of the ratio of L_{Tp}/h_p was small, suggesting that those patches were probably observed at a later stage of their evolution compared to the patches in the lake.

In general, the value of L_{Tp}/h_p is determined by a number of external and internal parameters, which include time at the initial stages of L_{Tp}/h_p evolution, but which could be governed by a balance between buoyancy and inertial forces if turbulence in a patch is sustained by, let us say, ambient shear. For such environments, Lozovatsky and Fernando (2002) introduced a parameterization of L_{Tp}/h_p taking into account its dependence on the so-called patch Richardson number, $Ri_p = N^2 h_p^4 / K_p^2$, and the patch mixing Reynolds number, $R_{mp} = K_p/\nu$, where the buoyancy frequency of the background

stratification is N^2, diffusivity is K_p, and molecular viscosity is ν. On physical grounds, the patch Richardson number reflects the balance between buoyancy and small-scale shear inside patches. This shear is an integral of the dissipation spectrum between the lowest wave number proportional to $2\pi/h_p$ and the highest possible wave number specified by the shear signal. The diffusivity K_p is a measure of this shear and the powers of N, K_p and h_p follow the requirement to make the combination non-dimensional. For geophysical flows (specifically the Black Sea coastal zone) it was found that

$$\frac{L_{Tp}}{h_p} = 1.5x + 0.03; \quad x = \frac{\left(L_{Tp}/h_p\right)^{\max}}{\left(1 + Ri_p/Ri_{pc}\right)^{1/4}\left(1 + R_{mpc}/R_{mp}\right)} \tag{4.9}$$

where x is the non-dimensional argument, $\left(L_{Tp}/h_p\right)^{\max}$ is an asymptotic constant that was estimated to be equal to 0.3, and Ri_{pc} and R_{mpc} are characteristic values of Ri_p and R_{mp} equal to 60 and 150, respectively. Note that the ratio L_{Tp}/h_p decreases with Ri_p, because the patch Richardson number is an analog of the inverse Ozmidov scale $L_O^{-1} \sim \left(N^3/\varepsilon\right)^{1/2}$.

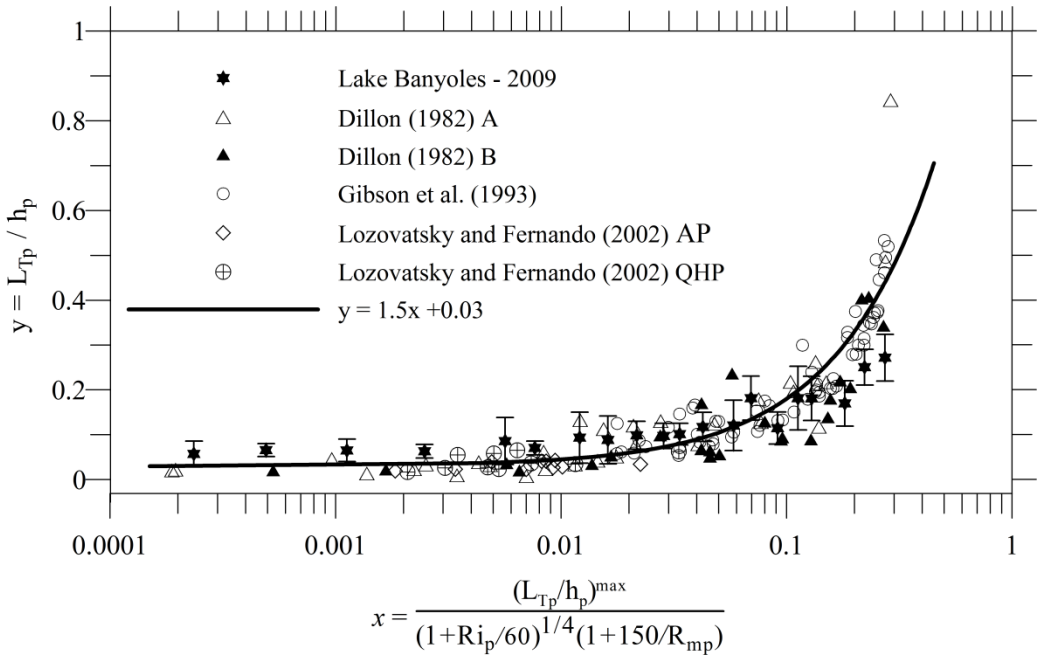

Fig. 4.11 The normalized patch Thorpe scale as a function of the patch Richardson and mixing Reynolds numbers (see text for details).

We tested (4.9) for TH turbulent patches in Lake Banyoles and only considered patches of h_p > 25 cm. The total number of such patches was 281. For about 90% of the patches, the buoyancy Reynolds number exceeded 30, signifying active turbulence. The bin-averaged values of L_{Tp}/h_p are shown in Fig. 4.11 and compared with (4.9) using $\left(L_{Tp}/h_p\right)^{\max}$ = 0.45 rather than the original 0.3 of Lozovatsky and Fernando (2002). Although the Banyoles samples sit slightly above the line specified by (4.9) for low values of the argument *x*, they are consistent with previous observations of patch turbulence in the ocean (Dillon, 1982; Gibson et al., 1993), and marine coastal waters (Lozovatsky and Fernando, 2002). It should noted that the modified value of $\left(L_{Tp}/h_p\right)^{\max}$ = 0.45 in (4.9) is close to $\left(L_{Tp}/h_p\right)^{\max}=1/\sqrt{3}$ = 0.57, which is the case for a single Z-shaped inviscid overturn without mixing (Gibson, 1987). Smyth et al. (2001) also indicated that $\left(L_{Tp}/h_p\right)^{\max}$ is close to 0.5 for a young overturn. Based on geometry, Gibson (1987) also proposed a slotted Z-model for an isolated turbulent mixing event where $\left(L_{Tp}/h_p\right)^{\max}$ = 0.41, but De Silva and Fernando (1992) argued that this model is only valid for the initial stages of mixing. Their laboratory experiments with sustained grid turbulence showed that L_{Tp}/h_p increases with time during the growing phase of a turbulent patch, which is consistent with the direct numerical simulations (DNS) of Smyth et al. (2001), but in this case $\left(L_{Tp}/h_p\right)^{\max}$ tends to a constant value ~ 0.27. A similar result, $\left(L_{Tp}/h_p\right)^{\max}$ ~ 0.29, was obtained by De Silva et al. (1996) when they were studying the cores of collapsed billows in a series of laboratory experiments. The asymptotic value of $\left(L_{Tp}/h_p\right)^{\max}$ may depend slightly on the turbulence generation mechanism, but it is safe to suggest that it is confined to between 0.25 and 0.5. For our data, the best estimate of $\left(L_{Tp}/h_p\right)^{\max}$ is 0.45. General dependence of the normalized Thorpe scale on the parameters of background stratification and patch turbulence, which is given by (4.9), agrees well with

microstructure measurements in deep and coastal oceans and is now also supported by the data obtained in a small lake.

4.4. Mean turbulent buoyancy fluxes by intermittent mixing

In this subsection we calculate the vertical mixing across the thermocline of the lake based on turbulent patchiness detected within the layer. Firstly, we evaluate the effects of the internal wave field across the thermocline. This is done through the computation of eddy diffusivities. Furthermore, the mixing effect of wind gustiness is also analyzed.

4.4.1. Diffusivities and buoyancy fluxes at the thermocline

The vertical mixing across the thermocline will be determined based on the diffusivity parameterization $K_p = \gamma \varepsilon / N^2$ (Osborn, 1980) in stratified lakes and by considering the dissipation rate ε and the buoyancy frequency *N*, which are calculated for individual patches (larger than 25 cm) rather than at equally segmented individual profiles. The mixing efficiency γ = 0.2 for active turbulence (Oakey, 1982) was used.

We calculated the averaged diffusivity $\overline{K}_{TH}^{i}$ for every i profile taking into account that intermittent mixing episodes occupied only a specific fraction of the thickness of the TH. By averaging a large number of turbulent patches over a specified domain (the TH in our case) during relatively long-standing stable background conditions (Nash and Moum, 2002) a representative estimate of $\overline{K}_{TH}$ can be deduced. In our case, a number of daily measured profiles were obtained under light breezy winds. Hence, the profile averaged diffusivity is calculated as follows,

$$\overline{K}_{TH}^{i} = \left(\sum_{j} h_p^j K_p^j + \left(\overline{H}_{TH}^{i} - \overline{H}_p^{i} \right) \times K_T \right) \Big/ \overline{H}_p^{i} , \tag{4.10}$$

where the superscript i represents the number of the profile, $\overline{H}_p^i$ is the fraction of the TH occupied by turbulent patches, $\overline{H}_{TH}^i$ is the mean thickness of the TH, h_p^j and K_p^j are the thickness and diffusivity of the individual patch j, and $K_T = 1.4 \times 10^{-7}$ m^2·s^{-1} is the molecular diffusivity.

Only patches with $h_p^j > 25$ cm were used due to the limitations of the ε calculation. It should be noted that large patches mostly contribute to the total mixing rate in pycnoclines (Gregg et al., 1986; Yamazaki and Lueck, 1987). The total number of TH patches with h_p > 25 cm was 281, which is ~ 90% of the total number of detected patches.

The state of turbulence in the patches was also evaluated using the buoyancy Reynolds number Re_b. It was found that for 90% of the patches Re_b > 30, which indicates active turbulence (see Chapter 3, subsection 3.2). The mean Re_b for all patches was 2400, and the median 645.

By averaging $\overline{K}_{TH}^i$ over the chosen number of profiles i = 2, 3, …281, a characteristic $\overline{K}_{TH}$ can be obtained for a specific time period. It is important to note that $\overline{K}_{TH}$ represents the mean vertical diffusivity across the TH only for relatively stable background conditions (light afternoon winds) observed in mid-summer during the period of field measurements. The histogram of the distribution of $\log_{10}(K_p)$ for all turbulent patches is shown in Fig. 4.12. The diffusivities ranged between $7.6 \cdot 10^{-7}$ and $1.4 \cdot 10^{-2}$ m^2·s^{-1} with a median value of $1.29 \cdot 10^{-4}$ m^2·s^{-1}. The distribution is slightly skewed towards high values, with the

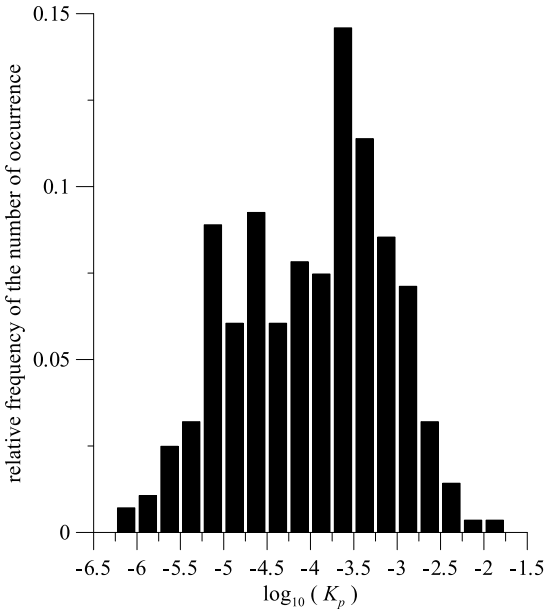

Fig. 4.12 The histogram of the logarithm of turbulent diffusivities in microstructure patches for the entire dataset of 281 patches.

skewness *S* equaling - 0.20. For approximately symmetric distributions (where the skewness is between - 0.5 and 0.5 (Bulmer, 1979) the mean value of K_p can be estimated as the geometric mean $\hat{K}_p$ (Borradaile, 2003). We calculated this value using the bootstrap method (Efron and Tibshirani, 1993). The bootstrap samples used for the averaging were ten times the actual number of samples. The campaign averaged $\hat{K}_p$ = $1.03 \cdot 10^{-4}$ $m^2 \cdot s^{-1}$ with 95% of bootstrapped confidence limits of 8.50×10^{-5} $m^2 \cdot s^{-1}$ and $1.22 \cdot 10^{-4}$ $m^2 \cdot s^{-1}$.

The estimate of effective mean diffusivity in the thermocline $\overline{K}_{TH}^{i}$ computed using (4.10) for the entire period of observations (i = 281 profiles) was $\overline{K}_{TH}$ = $7.03 \cdot 10^{-5}$ $m^2 \cdot s^{-1}$, which corresponds well to the averaged vertical diffusivities in stratified interiors of lakes and oceans (Ledwell and Watson, 1991; Alford and Pinkel, 2000; Sharples et al., 2001; Etemad-Sahidi and Imberger, 2006). Values ranging between 10^{-4} - 10^{-5} $m^2 \cdot s^{-1}$ were reported by Roget et al. (2006) for measurements on a shallow stratified shelf. The estimate of $\overline{K}_{TH}$ obtained, however, may be subject to relatively high variability considering the rather short period of our observations and temporal variations in the internal seiche characteristics in the lake.

In order to characterize vertical transport across the TH we first computed the buoyancy flux for each detected patch as $J_{bp} = K_p \, N_p^2$ and then averaged it over the entire dataset, in the same way as for K_p (4.10), to provide the buoyancy flux for non-turbulent segments $J_{bnt} = D_T N_{nt}^2$. The probability distribution of $\log_{10}$ (J_{bp}) can be considered approximately normal, with the skewness *S* equaling -0.38. The geometrically averaged $\hat{J}_{bp}$ was $(2.29 \pm 0.46) \cdot 10^{-7}$ $W \cdot kg^{-1}$. The effective mean buoyancy flux $\overline{J}_{TH}$ across the thermocline computed similarly to $\overline{K}_{TH}^{i}$ (4.10) and when averaged for the entire period of observations (i = 281) was found to be $1.90 \cdot 10^{-7}$ $W \cdot kg^{-1}$.

We analyzed the role of internal seiches as the major source of vertical mixing in the thermocline, comparing the distributions of K_p for June 25 and

July 1 when the measurement site was affected by internal seiches in different phases. The histograms of two distributions of $\log_{10}(K_p)$ are shown in Fig. 4.13. It should be noted that for July 1 the histogram is relatively symmetric, but not for June 25. About 60% of the data show $\log_{10}(K_p) < -4$, despite several large diffusivity values in the record. The number of turbulent patches detected on June 25 (55) was significantly fewer than on July 1 (87). Temporal variations in the thermocline displacements were small (of only a few centimeters) on June 25, but on July 1 they were large (maximum values of about ~ 0.5 m), as can be seen in Fig. 4.3 and Fig. 4.5. Note that large temporal variations in the vertical displacements correspond to a seiche phase with high horizontal velocities and maximum vertical shear. The seiche dynamics were similar on June 27. The mean patch diffusivities for June 25 and July 1 were estimated as $(4.58 \pm 1.71)\cdot10^{-5}$ and $(3.65 \pm 0.80)\cdot10^{-4}$ $m^2 \cdot s^{-1}$ respectively, with the diffusivities differing by an order of magnitude depending on the phase of the internal seiche. The values obtained on June 25 are close to those reported by Etemad-Sahidi and Imberger (2006) in Lake Biwa and Lake Kinneret.

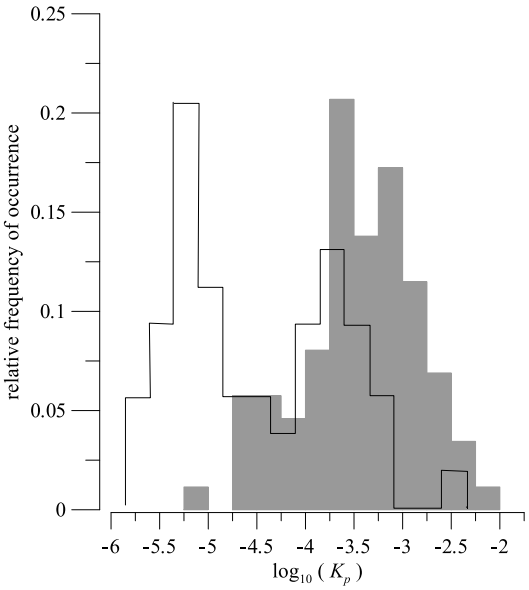

Fig. 4.13 The histogram of the logarithm of turbulent diffusivities in microstructure patches for July 1 (grey bars) and June 25 (open bars).

The mean diffusivities for June 25 and July 1 were computed using only turbulent fractions, which on July 1 occupied about 19% of the TH compared to 10% on June 25. The mean diffusivities across the TH were $1.61\cdot10^{-4}$ $m^2 \cdot s^{-1}$ and $5.73\cdot10^{-5}$ $m^2 \cdot s^{-1}$ respectively. Similar values were obtained for June 23 and June 27 (where the vertical displacements were small) with mean diffusivities of $5.57\cdot10^{-5}$ $m^2 \cdot s^{-1}$ and $8.1\cdot10^{-5}$ $m^2 \cdot s^{-1}$ respectively.

The effective buoyancy flux across the TH was ~ $1.72 \cdot 10^{-7}$ W·kg^{-1} on June 25, which is approximately half its estimate ($4 \cdot 10^{-7}$ W·kg^{-1}) for July 1. The difference is attributable to the variation in vertical shear in the TH, which is controlled by different phases of the internal seiche. The same conclusions can be drawn from June 23 and June 27 ($1.39 \cdot 10^{-7}$ W·kg^{-1} and $2.11 \cdot 10^{-7}$ W·kg^{-1}).

4.4.2. Impact of turbulent gusts on internal mixing

To evaluate the impact of wind gusts on internal mixing, the wind energy flux at 10 m above the lake's surface was calculated (Lombardo and Gregg, 1989),

$$P_{10} = \rho_{air} C_{10} U_{10}^3 \tag{4.11}$$

with the air density ρ_{air}, and the drag coefficient C_{10} computed following Wu et al. (1994). For U_{10} = 7.7 m·s^{-1}, P_{10} = 0.44 W·m^{-2}.

The integrated dissipation $\tilde{P}$ in a specific layer of the water column (between z_1 and z_2) can be evaluated (Wüest et al., 2000) as

$$\tilde{P} = \int_{z_1}^{z_2} \rho_w \, \bar{\varepsilon}(z) dz \,, \tag{4.12}$$

where $\bar{\varepsilon}(z)$ is zero for non-turbulent segments and equal to the mean dissipation for each patch within the layer. Since wind gusts directly influenced the second, the third and the fourth profiles shown in Fig. 4.9, we estimated $\tilde{P}$ in the SL, TH and BL by averaging the dissipation rate measured between 19:02:00 h and 19:05:30 h. In the SL, $\tilde{P}_{SL}$ = $7.1 \cdot 10^{-3}$ W·m^{-2}, which is about 1.6% of P_{10}. In the lake's interior, $\tilde{P}_{in}$ = $3.1 \cdot 10^{-3}$ W·m^{-2}, equal to ~ 0.7 % of P_{10}.

Wüest et al. (2000) reported that in Lake Alpnach about 1.5% of the wind energy dissipated in the surface layer and less than 0.7% in the stratified interior of the lake. The much lower values of $\tilde{P}_{SL}$ in lakes (Wüest and Lorke, 2003; Folkard et al., 2007) compared to the ocean, where Lozovatsky et al. (2005) found $\tilde{P}/P_{10} = 3-7$ % for moderately high winds, are related to wind work

lasting a short time during the passage of wind gusts. The transfer of potential energy from wind gusts to the SL and TH can increase the instabilities of the internal wave field, and pressure fluctuations could also transport energy to the interior of the water.

5. Overview of Internal Intermittency: Intermittency at Small Scales of Turbulence

5.1. Approach to internal intermittency

5.1.1. Kolmogorov's Similarity Hypothesis

Internal intermittency has its roots in the 1941 contributions of Kolmogorov to the classical theory of turbulence. At that time, Richardson (1922) had successfully introduced the 'energy cascade' model for turbulence. In that picture, energy was injected on the largest scales and it was transferred to successively smaller scales until being dissipated at the smallest ones, where turbulent energy was converted into heat by molecular viscosity.

Inspired by the Richardson's idea, Kolmogorov postulated the existence of an eddy hierarchy in any fully-developed turbulent flow with universal characteristics. As a new point of view, Kolmogorov (1941) assumed that information about the largest scales (*energy containing range*) is gradually lost as energy is transferred to the smaller scales. Then, there is a range of small scales at which turbulent motions are not dependent on the external forcing and can be considered in statistical equilibrium (*equilibrium range*). Consequently, this range of scales is isotropic, homogeneous and has a universal structure. Then, as Kolmogorov said in his first similarity hypothesis (Kolmogorov, 1941a; Kolmogorov, 1941b), turbulence in the equilibrium range is determined by the rate at which eddies receive energy from the larger scales and the energy dissipated in the eddies.

The Kolmogorov scales for time, length and velocity are indicators of the smallest scales at which the energy is dissipated. The Kolmogorov length scale is $\eta_K = \left(\nu^3/\tilde{\varepsilon}\right)^{\frac{1}{4}}$. Several works have shown that scales with the maximum of

dissipation are in a range of [5, 50]$\cdot\eta_K$ (Stewart and Grant, 1962; Panchev and Kesich, 1969; Monin and Yaglom, 1975; Arneodo et al., 1996; Roget, 2013). In Fig. 5.1 the maximum dissipation scale is shown for the Panchev and Kesich (1969) model which is located at a length scale of $50\eta_K$ (Appendix A). Therefore, it is also observed that scales of about ~ [3, 100]$\cdot\eta_K$ are responsible of the major part of the turbulent transport of particles in a flow (MacIntyre, 1993). In Fig. 5.1 the Batchelor microscale η_B which is an indicator of the smallest scales for scalar fluctuations until being dominated by molecular diffusion is also presented. Also, depending on ε, the scale where the variance of temperature fluctuations is higher according to the Batchelor model is shown.

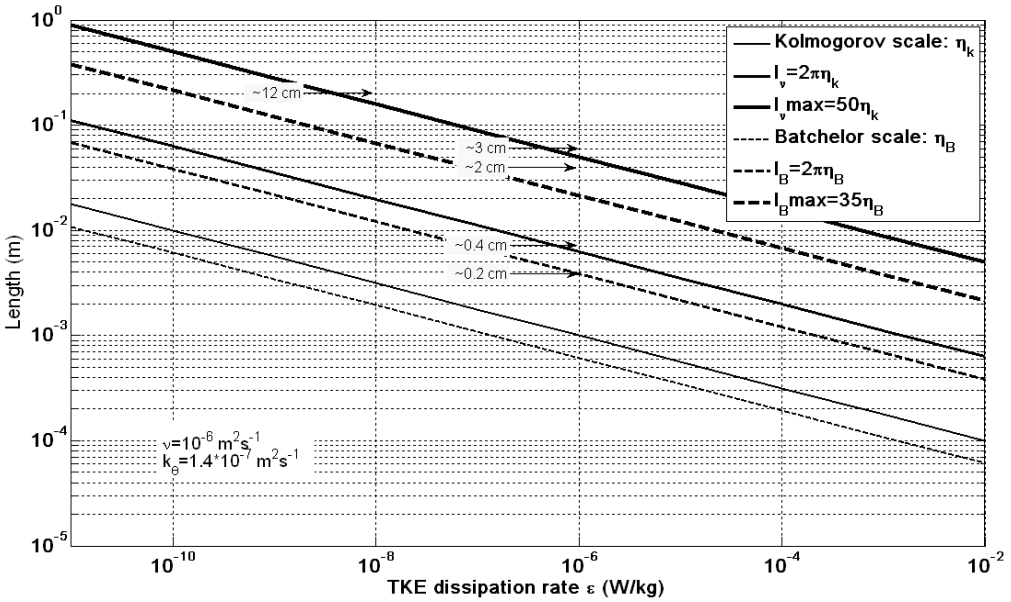

Fig. 5.1 Representation of Kolmogorov (solid line) and the Batchelor (dashed line) microscales, in logarithmic scale depending on ε, the rate of dissipation of the turbulent kinetic energy. The Batchelor microscale is an indicator of the smallest scales for scalar fluctuations until being dominated by molecular diffusion (Roget, 2013).

For fully-developed turbulence and within the equilibrium range the small-scale range of strong dissipation (*dissipation subrange*) is expected to be well away from the larger scales. This leads to the development of a transitional region, the *inertial subrange*, where dissipation will be neglected if compared to the energy transferred through smaller scales, as shown in Fig. 5.2.

In the inertial subrange, processes of turbulence production and dissipation are not important and there is a balance between the rate at which

energy is transferred and the rate at which it is dissipated at smallest scales. Hence, the energy spectrum in the inertial subrange will be independent of ν and only have dependence on ε, which was postulated by Kolmogorov (1941) in his second hypothesis. Since energy spectrum $E(k)$ has units of $[L]^3 \cdot [T]^{-2}$, dimensional analysis shows that, in the inertial subrange, it can be expressed as

$$E(k) = C_K \varepsilon^{\frac{2}{3}} k^{-\frac{5}{3}} \tag{5.1}$$

where C_K is a constant with a value of $C_K = 18/55\, C_\varepsilon$ for the longitudinal velocity component and $C_K = 24/55\, C_\varepsilon$ for the transversal one, and $C_\varepsilon = 1.6$ is the Kolmogorov constant (Srenivasan, 1995). The equation (5.1) is usually known as the Kolmogorov's *'five-thirds law'*.

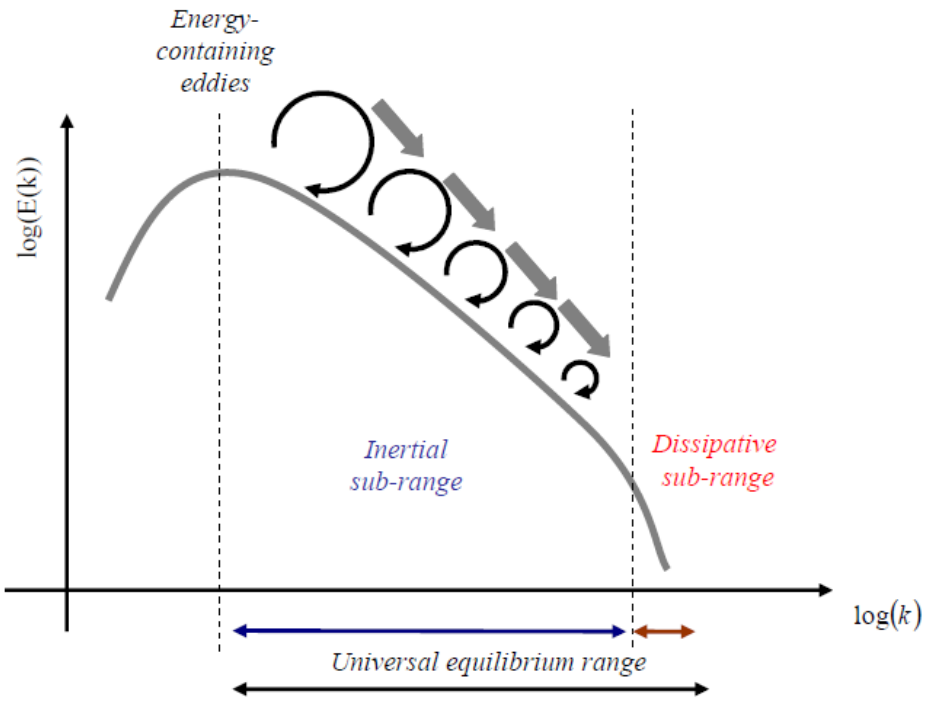

Fig. 5.2 Representative scheme of the energy spectrum of turbulence in a logarithmic scale. The inertial subrange is delimited by vertical dotted lines (adapted from Seuront et al., 1999).

Another consequence of the second self-similarity hypothesis is that, under assumptions of local homogeneity and isotropy, the velocity differences $\Delta\vec{v}$ at two neighbouring points located at $\vec{r}_1$ and $\vec{r}_2$ respectively, i.e. $\Delta\vec{v} = \vec{v}(\vec{r}_1, t) - \vec{v}(\vec{r}_2, t)$, are invariant under rotations and reflections. Including also

stationarity, the velocity differences only depend on $\vec{r}$, with $\vec{r} = \vec{r}_2 - \vec{r}_1$. Also, under these assumptions the Navier-Stokes equations are invariant to scaling transformations in the inertial subrange (Frisch and Parisi, 1985).

The fluctuations of any component of the velocity field Δv (longitudinal, and transverse direction as seen in Fig. 5.3), can be written as

$$\Delta v(r) = v(x+r) - v(x) \equiv \Delta v_r \tag{5.2}$$

with x indicating the spatial direction chosen and r the distance between the two points.

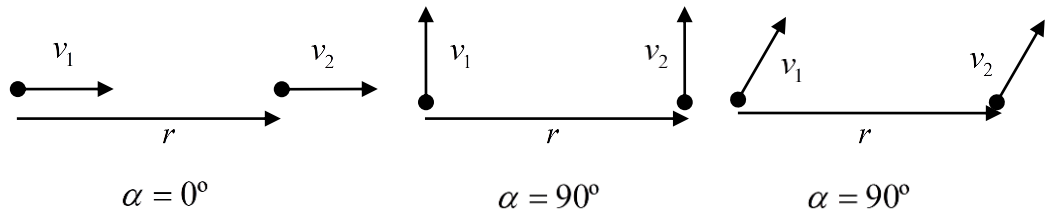

Fig. 5.3 Geometries of the components of the velocity field: longitudinal (left) and transverse (middle and right) directions.

The *p*-order moments, usually called *velocity structure functions of order p*, for any component of the velocity field $\Delta\vec{v}$ (Fig. 5.3) are defined as

$$s_p(r) = \left\langle \Delta v_r^p \right\rangle \tag{5.3}$$

The angular brackets indicate an average over the distance x.

According to Kolmogorov's second hypothesis, the form of $s_p(r)$ in the inertial subrange must be of the form

$$s_p(r) \sim (\varepsilon r)^{\frac{p}{3}} \tag{5.4}$$

because the only possibility of removing the viscosity parameter ν is if $s_p(r) \sim r^{p/3}$ (Pope, 2000; Hinze, 1975). Note that for p = 2, the expression of $s_2(r) \sim r^{2/3}$, known as the Kolmogorov's *'two-thirds law'* for isotropic turbulence. If this expression is transformed in the Fourier space, the *'five-thirds law'* for the energy spectrum is recovered (Tennekes and Lumley, 1972).

In a general form, the equation (5.4) is usually written as a function of *the scaling exponents* $\zeta(p)$

$$s_p(r) = \left\langle \Delta v_r^p \right\rangle \propto r^{\zeta(p)} \tag{5.5}$$

with $\zeta(p) = p/3$, which is known as Kolmogorov's scaling.

Experimental values obtained for the second order structure function follow the 2/3 value predicted by Kolmogorov scaling theory well (i.e. $s_2(r) \approx r^{2/3}$). It was successfully tested for the first time by Grant et al. (1962) based on turbulence generated in a tidal stream between Vancouver and the Quadra Islands, in British Columbia (Canada). Although initial work confirmed this scaling in laboratory and field experiments (Gibson, 1963; Sanborn and Marshall, 1965; Kistler and Vrebalovich, 1966; Uberoi and Freymuth, 1969), subsequent work has shown discrepancies between the Kolmogorov prediction and the scaling exponents for higher order structure functions (Van Atta and Chen, 1970; Anselmet et al., 1984; Meneveau and Sreenivasan, 1991; Benzi et al., 1995; Zhou et al., 2005). This is the so-called '*anomalous scaling*': as the higher the scaling exponent, the greater the deviation is.

5.1.2. The Refined Similarity Hypothesis

Previous results show that something was going wrong in the Kolmogorov theory of 1941. In fact, Kolmogorov had assumed in his theory that the energy dissipation rate ε was uniform in the space and constant in time, i.e. $\varepsilon \equiv \tilde{\varepsilon}$, with $\tilde{\varepsilon}$ the mean dissipation rate. Soon he received several comments and evidences that questioned this idea. For example, Batchelor and Townsend (1949) found that turbulence tends to form isolated regions of concentrated vorticity showing intermittent character. Also Landau had objected that theory, as Kolmogorov noted in the famous International Turbulence Colloquium held in Marseille in 1961, and pointed out that ε is a function of position and time with $\varepsilon = \varepsilon(\vec{r},t)$: in regions where $\varepsilon(\vec{r},t) > \tilde{\varepsilon}$, the energy cascade would proceed

more vigorously, and an intermittent distribution of $\varepsilon(\vec{r},t)$ should be expected (internal intermittency). As Moffatt (1981) said in his article, there was 'a problem that was to seriously affect the credibility of Kolmogorov's theory; this was the problem of intermittency. […]. Gone was the beautiful simplicity of the earlier theory: from 1961 on, no aspect of turbulence would be simple'.

In the Marseille meeting in 1961, Kolmogorov argued during his presentation that $\varepsilon(\vec{r},t)$ would be log-normally distributed and showed that, although the effect on the energy spectrum should be small, the higher orders could be seriously affected by small-scale intermittency. One year later, Kolmogorov (1962) and Obukhov (1962) suggested the Refined Similarity Hypothesis (RSH) according to which the velocity increment Δv_r over a separation distance *r* is specified not by the mean dissipation rate $\tilde{\varepsilon}$ but rather by the dissipation rate ε_r averaged over a specific volume of radius $r < L$ and defined by

$$\varepsilon_r = \frac{3}{4\pi r^3}\int_V \varepsilon(\vec{x}+\vec{y},t)\,dV(y) \tag{5.6}$$

which, instead of (5.4) and (5.5), leads to the following scaling relation

$$s_p(r) = \left\langle \Delta v_r^p \right\rangle \sim (\varepsilon_r r)^{p/3} \tag{5.7}$$

where the dissipation rate ε_r can be also understood as the energy flux between eddies.

If ε_r is log-normally distributed, they showed that the moments of ε_r scale as (Appendix B)

$$\frac{\left\langle \varepsilon_r^{\,p} \right\rangle}{\tilde{\varepsilon}^{\,p}} \sim \left(\frac{L}{r}\right)^{\mu p(p-1)/2} \qquad \eta_K << r << \ell \tag{5.8}$$

with μ a positive constant. And for $p = 2$ we obtain

$$\left\langle \varepsilon_r^2 \right\rangle = A \cdot \tilde{\varepsilon}^2 \left(\frac{L}{r}\right)^{\mu} \tag{5.9}$$

The variance of ε_r can be also expressed as

$$\sigma^2_{\log \varepsilon_r} = A_\varepsilon + \mu \log\left(\frac{L}{r}\right) \tag{5.10}$$

where A_ε depends on the large-scale motions and μ is the so-called *intermittency exponent*, which accounts for the intermittency effects (Monin and Yaglom, 1975; Frisch, 1995).

The RSH leads to the question about the statistics of ε_r, which is assumed to be log-normal without any theoretical considerations. However, this has opened the door to allow turbulence to be interpreted from a different perspective, one where ε_r the key descriptor is associated with a random variable and has specific characteristics. In the following subsections the fundamentals of the turbulent energy cascade models are detailed.

5.1.3. Multiplicative energy cascades

The starting point of most energy cascade models developed until now is that proposed by Gurvich and Yaglom (1967) who theoretically derived an explicit cascade model to take intermittency into account. They introduced a discrete procedure in scale wherein the transfer of kinetic energy down the cascade occurs with the breakdown of turbulent eddies. Since their basic idea of breakage is the same as for the other models presented in the section, it is worthwhile describing them next.

The model begins by considering a domain Q with energy-containing eddies of size L ($Q \propto L^3$) that will be successively divided into subdomains q_i of characteristic length r_i ($q_i \propto r_i^3$). Let us consider $\varepsilon(x)$ as a non-negative quantity defined only by local properties and which represents the dissipation rate on the smallest scales, i.e. the rate of energy transfer on those scales. The energy dissipation rate ε_i and the volume q_i is given by

$$\varepsilon_i = \frac{\int_{q_i} \varepsilon(x) dx}{q_i} \tag{5.11}$$

Here, the quantity ε_i is a random variable that represents an average in the volume q_i, associated with the eddy of size r_i. Consider the fact that it breaks

down successively into a smaller volume q_{i+1} and is characterized by the length scale r_{i+1}. The scale ratio λ_b between two successive breakages is a constant, $\lambda_b = \frac{r_i}{r_{i+1}}$. Then, the values of ε_i are related through the random breakage coefficient

$$W_{i+1} = \frac{\varepsilon_{i+1}}{\varepsilon_i}, \qquad i=1,2,\ldots,K \tag{5.12}$$

and up to some stage *K*; the number of breakage processes where the values of ε_i do not fluctuate anymore. Therefore, the average value $\varepsilon(x)$ in the entire volume which contains the breakage process Q is

$$\tilde{\varepsilon} = \frac{\int_Q \varepsilon(x)dx}{Q} \tag{5.13}$$

and the scale ratio λ after i iterations is defined as

$$\lambda = \frac{L}{r_i} = \lambda_b^i \tag{5.14}$$

Considering that the random variables ε_i are mutually independent and identically distributed, then the value of ε_λ in any specific volume at resolution scale λ can be determined by the density function W (Seuront et al., 2005)

$$\varepsilon_\lambda = \tilde{\varepsilon} \cdot \prod_{j=1}^{i} W_j \tag{5.15}$$

The expression is transformed into

$$\log(\varepsilon_\lambda) = \log(\tilde{\varepsilon}) + \sum_{j=1}^{i} \log(W_j) \tag{5.16}$$

The moment of the dissipation rate ε_j after *j* steps can be written as

$$\left\langle \varepsilon_\lambda^p \right\rangle = \tilde{\varepsilon}^p \cdot \left\langle \left(\prod_{j=1}^{i} W_j \right)^p \right\rangle = \tilde{\varepsilon}^p \cdot \prod_{j=1}^{i} \left\langle (W_j)^p \right\rangle = \tilde{\varepsilon}^p \cdot \left\langle W^p \right\rangle^i \tag{5.17}$$

because they are independent variables.

On the other hand, $\left\langle (\varepsilon_r)^p \right\rangle$ scale as $\left\langle (\varepsilon_r)^p \right\rangle \sim (L/r)^{K(p)}$ (see (5.8) for example), then (5.17) can be expressed as

$$\left\langle \varepsilon_\lambda^p \right\rangle \sim \lambda^{K(p)} \tag{5.18}$$

where $K(p)$ is *the scaling exponent of the moments of order p* for the energy dissipation rate and so, using (5.14)

$$K(p) = log_{\lambda_b}\left(\langle W\rangle^p\right) \tag{5.19}$$

The conservation of the energy implies that $\langle W\rangle = 1$, and then $K(1) = 0$.

According to the RSH, the structure function can be rewritten in terms of ε_λ for any step of the cascade

$$\left\langle (\Delta v_\lambda)^p \right\rangle \sim \left\langle (\varepsilon_\lambda)^{p/3} \right\rangle \cdot \lambda^{-p/3} \tag{5.20}$$

where now $\Delta v_\lambda = \left|v(x+r) - v(x)\right|$ with $\lambda = L/r$ so values of are always positive.

Because the velocities' differences are defined positive, now the structure functions can be calculated for orders either fractional or integer and they are defined as[1]

$$S_p(r) = \left\langle \left|v(x+r) - v(x)\right|^p \right\rangle \propto r^{\zeta(p)} \propto \lambda^{-\zeta(p)} \tag{5.21}$$

where $\zeta(p)$ is the same as (5.5).

Considering (5.5), (5.10) and (5.20), the relation between the scaling exponents of the structure functions of order *p*, $\zeta(p)$ and the moment function of the energy dissipation rate, $K(p)$ is

$$\zeta(p) = \frac{p}{3} - K\left(\frac{p}{3}\right) \tag{5.22}$$

Following (5.1), the energy spectrum $E_v(k)$ of the velocity fluctuations in the *k*-space is

$$E_v(k) \approx \varepsilon^{\frac{2}{3}} \cdot k^{-B} \tag{5.23}$$

and by definition (Monin and Yaglom, 1975) it can be obtained as an integration of the second-order structure function $S_2(r)$ in the *k*-space (see (5.22)). Then, it is found that

[1] Experimental data shows that scaling exponents for the structure functions $s_p(r)$ can be estimated for those obtained from the absolute values, $S_p(r)$ (Benzi et al., 1984).

$$B = 1 + \zeta(2) \tag{5.24}$$

Note that for Kolmogorov scaling shown in (5.4) $\zeta(2) = 2/3$ and then $B = 5/3$, which is the five-thirds Kolmogorov law.

5.1.4. The log-normal model

The works of Gurvich and Yaglom detailed above assumed that the distribution of $\log(W)$ was normal, i.e. the logarithms of the dissipation rate were also normal distributed. In fact, if η_K and L are the smallest and the largest scales for which W follows the breakage model, the ratio η_K / L is large enough that the sum in (5.16) can be approximated to a Gaussian distribution according to the Central Limit Theorem (Evans and Rosenthal, 2003). In this case, W obeys a log-normal law and the expression of the scaling exponents of the *p*-order moments $K(p)$ in (5.18) is quadratic in form, i.e.

$$K(p) = \mu p(p-1)/2, \tag{5.25}$$

(see also (5.8)), giving the intermittency exponent $\mu = K(2)$.

As a first approach, the intermittency exponent μ is considered as universal, but there is considerable uncertainty about its value. This value of μ, which has been reported in several works, varies depending on the type of the flow. For example, Monin and Yaglom (1975) reported a value of $\mu \approx 0.5$. However, for well-developed turbulence in the laboratory it has been found that $\mu = 0.25$ (Sreenivasan and Kailasnath, 1993). In atmospheric turbulence, μ ranges between 0.2 and 0.5 (Anselmet et al., 1984; Schmitt et al., 1992; Chiriginskaya et al., 1994).

The scaling exponents $\zeta(p)$ for the log-normal model are calculated using (5.22) and (5.25)

$$\zeta(p) = \frac{p}{3} + \frac{\mu}{18} p(3-p) \tag{5.26}$$

so that internal intermittency account for a departure $\Delta\zeta(p) = \mu p(3-p)/18$ from the Kolmogorov scaling.

Using the expression (5.24) the exponent of the spectrum, *B*, is

$$B = 1 + \zeta(2) = 1 + (2/3 + \mu/9) = 5/3 + \mu/9 \quad (5.27)$$

which is slightly steeper ($\Delta B = \mu/9$) than Kolmogorov's 5/3 law.

Although log-normal approximation was proposed as a good solution for the problem of intermittency, several works have questioned its application. Then, some attempts to improve the log-normal model have been suggested to take into account the weight of the outliers in the distribution of ε_r, i.e. the relevance of strong fluctuations in the dissipation field; as in the case of the Yamazaki model (Appendix C). However, the application of the multifractal theory was the next step in understanding and quantifying the phenomenon of internal intermittency (Novikov, 1971; Schertzer and Lovejoy, 1987; Schmitt et al., 1994). Its description and application to different turbulence models is analyzed in the following subsection.

5.2. Fractal modeling for turbulence

5.2.1. General description of fractals

The word 'fractal' (from the Latin 'fractus' or broken) was introduced by Mandelbrot (1975) to describe complicated geometric shapes which cannot be represented by classical geometry. These kinds of objects are characterized by the repetition of geometric structures at ever smaller levels of resolution. Their general description has been reviewed in many books on fractals (Feder, 1988; Barnsley, 1988; Falconer, 1990; Solé and Bascompte, 2006) and some of them are detailed below.

The basic property of fractals is that they exhibit the same shape when the scale is changed (*scale-invariance*). Following Mandelbrot (1982), a fractal is defined as 'a rough or fragmented geometric shape that can be split into parts, each of which is a reduced-size copy of the whole'. From this definition two more properties can be drawn: first, they have *fine structure*, with their details present on small scales; second, they are *self-similar* being exactly, approximately or statistically similar to a part of itself.

Self-similarity allows classified fractals to be categorized into two types depending on their construction (Falconer, 1990). If these rules of construction are deterministic, they are called *deterministic fractals;* if their construction is related to a random variable, they are called *stochastic fractals*. If all the pieces are identical, the fractal is considered as a *monofractal*. On the other hand, if the pieces are not identical then it is a *multifractal*.

Fractals are also characterized by their *fractal dimension* (Mandelbrot, 1967), which represents a measure of how the fractal fills the embedded space just as it is re-scaled to smaller and smaller scales. In contrast with the integer values of the dimensional topological dimensions (i.e. lines, areas and volumes), fractal dimensions are fractional (Appendix D). If the fractal is scaled successively with a scale ratio λ', then the number of copies n that an object contains of itself can be related to its fractal dimension D through the power law

$$n = (\lambda')^{-D} \tag{5.28}$$

and the fractal dimension is

$$D = \frac{\log(n)}{\log\left(\frac{1}{\lambda'}\right)} \tag{5.29}$$

Note that it also works for any of the topological dimensions. For example, if the scale ratio λ' is $1/2$, a cube can be cut into 8 half-sized cells. Using (5.29) it gives $D = 3$ (Appendix D).

5.2.2. The monofractal case: The β-model

Fractal structures, defined by their fractal dimension, are scalar-invariant and exhibit power-law behavior. For turbulence, the equations of Navier-Stokes are scale-invariant in the inertial subrange (Frisch and Parisi, 1985) and this suggests that fractal framework can be appropriate for modeling that process. Thus, it is expected that if eddies can be described as fractal objects, their statistical properties will depend on the scale ratio by a power law.

The first (and also the simplest) model of multiplicative process based on fractal considerations was the β-model. Introduced by Frisch et al. (1978), but previously presented by Mandelbrot (1974) as a 'black and white' model, it follows an original scheme proposed by Novikov and Stewart (1964).

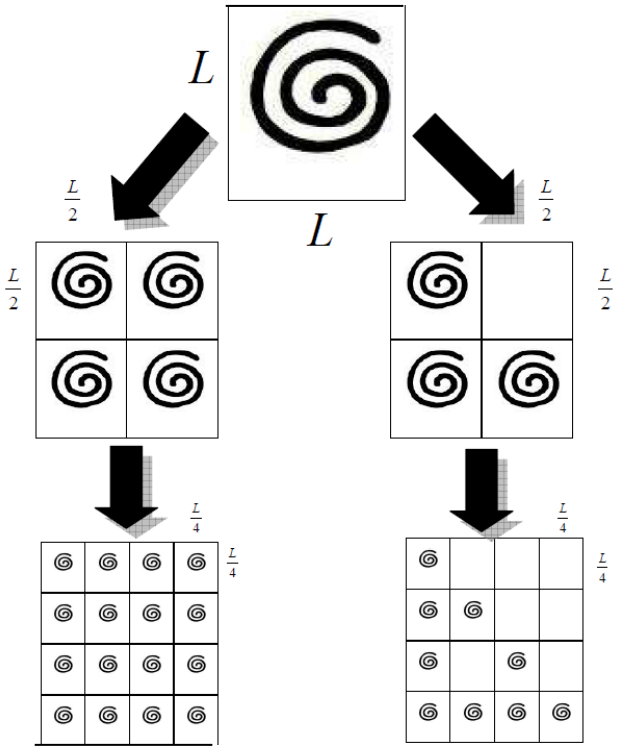

Fig. 5.4 Examples of isotropic turbulent cascades. On the left, the homogeneous case (i.e. non-intermittent cascade process). On the right, the 'β-model' (monofractal case) represented by subeddies that do not fill the whole space. In this latter case, the fractal dimension D = log(3)/log(2) ~ 1.58 (Seuront et al., 1999)

The basic idea of the model is that at each stage of the energy cascade turbulent eddies occupy only a fraction of the available volume. Thus, intermittency is considered leaving eddies to be either *'alive'* (active) or *'dead'* (inactive). Turbulent activity is controlled by a factor $\beta \in [0,1]$, which determines the fraction of available volume occupied by 'alive' eddies from one generation to the next and is an adjustable value of the model. Since at any stage of the cascade eddies have the same intensity, the β-model is a monofractal model, see in Fig. 5.4.

To describe the model and the parameters involved, consider the (i+1)-*th* step of the cascade. In the model the factor β can be expressed as

$$\beta = \frac{n \cdot r_{i+1}^3}{r_i^3} \tag{5.30}$$

where n is associated with the space filled by active eddies of size r_{i+1} at the considered step of the cascade. The breakage coefficient $\lambda_b = r_i / r_{i+1}$ can be also related to the fractal dimension D using (5.28) and $n = \lambda_b^D$, with $\lambda_b = 1/\lambda'$

The codimension c represents the non-turbulent region present in the available space and is defined as

$$c = d - D \tag{5.31}$$

where d is the dimension of the embedding space d and D the fractal dimension. This is a measure of the sparseness of the fractal set. Then, the factor β can be rewritten using the codimension c as

$$\beta = \frac{n}{\lambda_b{}^d} = \frac{\lambda_b{}^D}{\lambda_b{}^d} = \lambda_b{}^{-(d-D)} = \lambda_b{}^{-c} \tag{5.32}$$

From (5.30), the fraction p_i of the whole space occupied active eddies is

$$p_i = \prod_{j=1}^{i} (\beta)^j = \lambda^{-c} \tag{5.33}$$

and λ is the scale ratio defined by (5.14). The random breakage coefficient W_i in (5.12) can be written as

$$\begin{cases} Pr(W = \dfrac{1}{\beta}) = \beta & \text{'alive' subeddy} \\ Pr(W = 0) = 1 - \beta & \text{'dead' subeddy} \end{cases} \tag{5.34}$$

Note that the active region is decreasing by a factor β ($\varepsilon_{i+1} = \beta \cdot \varepsilon_i$) at each stage of the breakage process. Since the mean value of the energy is conserved, this represents that the value of the energy in the active cells is increasing by a factor $1/\beta$.

Recalling that $\lambda = \lambda_b^i$ and using (5.33) the probability of the two possible values of the normalized dissipation rate $\varepsilon_\lambda^* = \varepsilon_\lambda / \tilde{\varepsilon}$ at scale ratio λ can be expressed as

$$\begin{cases} Pr(\varepsilon_\lambda^* = \lambda^c) = \lambda^{-c} & \text{'alive' subeddy} \\ Pr(\varepsilon_\lambda^* = 0) = 1 - \lambda^{-c} & \text{'dead' subeddy} \end{cases} \tag{5.35}$$

In this expression we have used a normalized quantity, hereafter symbolized by a star superscript, to better indicate fluctuations above and below the mean $\tilde{\varepsilon}$. For a non-normalized quantity, the same expression is valid but $\varepsilon_\lambda^* = \lambda^c$ must be replaced by $\varepsilon_\lambda = \tilde{\varepsilon} \lambda^c$.

Equation (5.35) shows that the conservation of the energy is respected ($\langle \varepsilon_\lambda^* \rangle = 1$), with $\varepsilon_\lambda^* = \lambda^c$ which corresponds to a boost ($\varepsilon_\lambda^* > 1$).

Because normalization does not affect the scaling exponents of the *p*-moments $K(p)$ of the dissipation rate, they can be calculated as

$$\left\langle \left(\varepsilon_\lambda^*\right)^p \right\rangle = \sum_{k=1}^{2} \left(\varepsilon_{\lambda,k}^*\right)^p \cdot p\left(\varepsilon_{\lambda,k}^*\right) = (\lambda^c)^p \cdot \lambda^{-c} = \lambda^{c(p-1)} \tag{5.36}$$

Using (5.18) we obtain the scaling exponent of the *p*-order moment of ε_λ

$$K(p) = c(p-1) \tag{5.37}$$

If the intermittency exponent μ is determined as $\mu = K(2)$, see in (5.25), then (5.40) gives that μ is equal to the codimension c. Thus,

$$K(p) = \mu(p-1) \tag{5.38}$$

From (5.22) the scaling exponent of the *p*-order structure function $S_p(r)$

$$\zeta(p) = \frac{p}{3} - \mu\left(\frac{p}{3} - 1\right) \tag{5.39}$$

According to (5.24), the power-spectrum exponent δ has the value of

$$B = 1 + \zeta(2) = \frac{5}{3} + \frac{\mu}{3} \tag{5.40}$$

The experimental results for high orders of $\zeta(p)$ reported by Anselmet et al. (1984), concluded that the model was not satisfactory as a model for turbulence because experimental scaling exponents did not exhibit a linear behavior, as theoretically predicted in the β-model. Consequently, several corrections to the β-model were suggested, such as the random β-model or the bifractal model, until the multifractal formalism was introduced (see details in Appendix C).

5.2.3. Multifractals

Fluctuations of turbulent quantities generally span a wide range of scales and exhibit different levels of intensity. Thus, it seems reasonable to think that

the previous monofractal description based only on one single fractal dimension, i.e. the trivial 'dead' or 'alive' event choice, should not be the general case. In the multifractal framework, turbulent eddies can be described as a set of local fractals, each of which is associated to the different levels of intensity. While the multifractal term was introduced by Frisch and Parisi (1985), the same idea had been analyzed previously in other works (Hentschel and Procaccia, 1983; Grassberger, 1983; Schertzer and Lovejoy, 1984). In this case, the multifractal theory does not work with only one scaling exponent as a monofractal does, but rather with *multiple scaling*.

Extending the monofractal formalism to the multifractal theory, the whole space is covered by an infinite number of sets, namely S_j ($j = 1,...,\infty$). In each of these sets, the (normalized) dissipation rate $\varepsilon^*_{\lambda,j}$ will scale as (Schertzer and Lovejoy, 1987)

$$\varepsilon^*_{\lambda,j} \sim \lambda^{\gamma_j} \tag{5.41}$$

and the exponent is knows as the *singularity* γ_j of the set S_j.

The value of the singularities γ represents the intensity level of turbulence on the scale of observation λ. In fact, as is described in Tessier et al. (1993), when λ increases, larger values of ε^*_λ appear (higher activity) and these are also concentrated in smaller and smaller regions.

If a set S_j has a fractal dimension $D(\gamma_j)$, the codimension of the set $c(\gamma_j)$ can be defined following (5.31) as

$$c(\gamma_j) = d - D(\gamma_j) \tag{5.42}$$

The probability distribution of the dissipation rate $\varepsilon^*_{\lambda,j}$ can be expressed as $\lambda^{-c(\gamma_j)}$, see (5.33). To calculate the scaling exponents for the *p*-order moments of the dissipation rate $\left\langle \left(\varepsilon^*_\lambda\right)^p \right\rangle$, the contribution of the each set c_j must be multiplied by their probability $\lambda^{-c(\gamma_j)}$, and finally add up to all the sets

$$\left\langle \left(\varepsilon^*_\lambda\right)^p \right\rangle = \sum_j \lambda^{\gamma_j p} \lambda^{-c(\gamma_j)} = \sum_j \lambda^{\gamma_j p - c(\gamma_j)} \tag{5.43}$$

These basic ideas of the multifractal theory are explored in the next subsection, where the α-model, a multifractal model, is described in detail.

5.2.3.1. The α-model

The α-model (Schertzer and Lovejoy, 1983) overcomes the dichotomy of 'dead' or 'alive' present in the β-model, thus allowing the eddies to be either 'more active' (strong) or 'less active' (weak) by being associated with the values γ^+ and γ^- respectively. This is controlled by a random variable W according to the binomial distribution proposed in (5.34) for the β-model

$$\begin{cases} Pr(W = \lambda_b^{\gamma^+}) = \beta & \text{'strong' subeddy} \\ Pr(W = \lambda_b^{\gamma^-}) = 1-\beta & \text{'weak' subeddy} \end{cases}$$

where $\beta = \lambda_b^{-c}$, as is shown in (5.32).

At any stage of the cascade, different sets exhibit activity whose intensity is modulated by the random multiplicative factor λ_b^{-c}, as it is shown in Fig. 5.5 in comparison with the monofractal model.

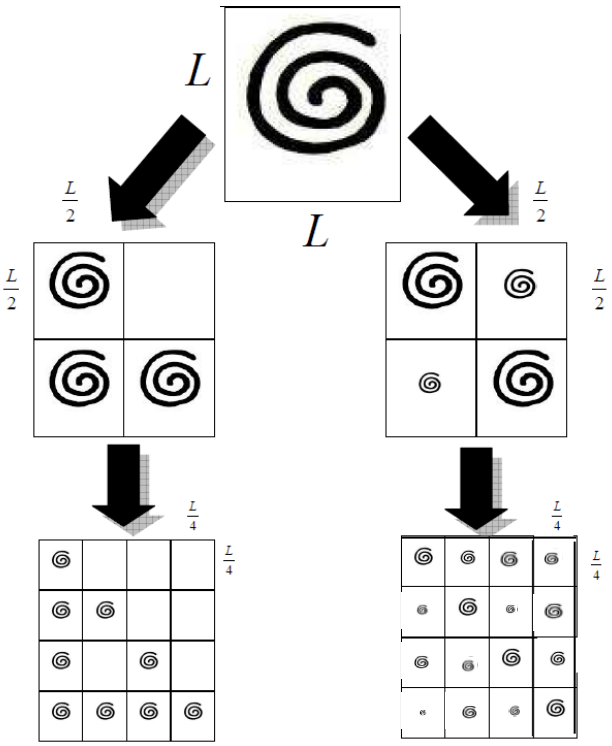

Fig. 5.5 On the left, the monofractal 'β - model', which allows eddies to be 'alive' or 'dead'. On the right, the 'α - model', which allows eddies to be 'more active' or 'less active' (Seuront et al., 1999).

Here, the singularities γ^+, γ^- (Fig. 5.6) can be rewritten as a function of the codimension of the fractal set c and other parameters α, α' such that

$$\gamma^+ = \frac{c}{\alpha};\ \gamma^- = -\frac{c}{\alpha'} \tag{5.45}$$

with $c > 0, \alpha > 0$ and $\alpha' > 0$.

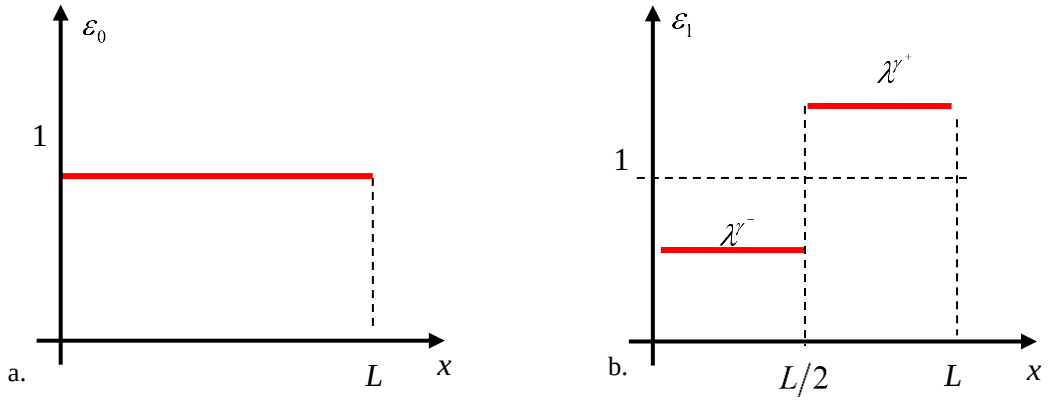

Fig. 5.6 Example of 'α-model' cascade, (a) the first step and (b) the second step generated by a 'strong' subeddy associated with a singularity $\gamma^+ > 0$ and a 'weak' subeddy associated with a singularity $\gamma^- < 0$ (Schertzer and Lovejoy, 1996).

The conservation of the energy at each step forces one of these parameters to be dependent on the other two because

$$\left\langle \varepsilon_\lambda^* \right\rangle = 1 = \lambda_b^{-c} \cdot \lambda_b^{\gamma^+} + \left(1 - \lambda_b^{-c}\right) \cdot \lambda_b^{\gamma^-} \tag{5.46}$$

The moments of the dissipation rate ε_λ are obtained from (5.18) and (5.19) as

$$K(p) = \log_{\lambda_b}\left[\lambda_b^{-c} \cdot \lambda_b^{p\gamma^+} + \left(1 - \lambda_b^{-c}\right) \cdot \lambda_b^{p\gamma^-}\right] \tag{5.47}$$

For the scaling exponent for the structure functions $S_p(r)$ (see in (5.22))

$$\zeta(p) = \frac{p}{3} - \log_{\lambda_b}\left[\lambda_b^{-c} \cdot \lambda_b^{\left(\frac{p}{3}\right)\gamma^+} + \left(1 - \lambda_b^{-c}\right) \cdot \lambda_b^{\left(\frac{p}{3}\right)\gamma^-}\right] \tag{5.48}$$

A detailed description about multifractal behavior for the α-model is provided in Appendix E. It can be seen that for a discrete cascade and after *n* steps *n* >> 1, the probability of the intensity level, i.e. singularity γ_i, depends on its codimension c_i of the set as

$$Pr\left(\varepsilon_n^* = \lambda^{\gamma_i}\right) = \lambda^{-c_i} \tag{5.49}$$

For a fully developed turbulence, i.e. $\lambda \to \infty$, the codimension can be considered a continuous function $c(\gamma)$, and the discrete model is transformed into a *continuous cascade model*.

For continuous cascade models, a fundamental multifractal relation exists (Schertzer and Lovejoy, 1987)

$$Pr\left(\varepsilon_\lambda^* \geq \lambda^\gamma\right) \approx \lambda^{-c} \tag{5.50}$$

For a multifractal cascade model, this expression links the function $c(\gamma)$ to the intensity levels ε_λ ($\varepsilon_\lambda = \widetilde{\varepsilon} \cdot \varepsilon_\lambda^*$) at scale ratio λ through the singularities γ.

5.2.3.2. Scaling exponent and codimension functions

Multifractal processes are usually determined by the scaling exponents of the statistical moments, which can be expressed as functions for fully-developed cascades. In this latter case, interesting one-to-one correspondence can be established between moments, *p*, and the singularities, γ. However, before delving deeper into this, it is important to describe the general properties of the scaling exponent function of the moments $K(p)$ and the codimension function $c(\gamma)$.

The basic properties for the scaling exponent function $K(p)$ are:

- $K(0) = 0$: In multifractals the available space is filled by turbulent events associated with different intensities. On the contrary, for monofractals, $K(0) = -c \neq 0$ and $K(p)$ is a straight line.
- $K(1) = 0$: This is a direct consequence of the conservation of the energy (subsection 5.1.3).
- $K(p)$ is a convex function: For the case $0 < p < 1$, the values of $\left\langle \left(\varepsilon_\lambda^*\right)^p \right\rangle$ decrease; then, $K(p) < 0$. On the other hand, for $p > 1$ those values increase; this implies that $K(p) > 0$.
- When $\lambda \to \infty$: $\left\langle \varepsilon_\lambda^p \right\rangle \to \infty$ when $K(p) > 0$, which occurs for $p > 1$: If the scale of resolution increases, it is possible to find larger and larger values of ε_λ concentrated in smaller and smaller regions. The extreme case corresponds to a set formed by only a delta function $\delta(\vec{r})$ randomly

localized in a region A of volume V of the d-dimensional space. Then, $\lim_{\lambda\to\infty}\varepsilon_\lambda = \tilde{\varepsilon}\cdot\delta(\vec{r})$ and

$$\varepsilon_{\lambda,\vec{r}}\begin{cases}\tilde{\varepsilon}\cdot\lambda^d & \vec{r}\in A\\ 0 & \vec{r}\notin A\end{cases} \tag{5.51}$$

If it is distributed uniformly in the whole space, the moment of order p is calculated as

$$\left\langle \varepsilon_\lambda^p \right\rangle = \tilde{\varepsilon}\,\lambda^{dp}\lambda^d \approx \lambda^{d(p-1)}; \tag{5.52}$$

$$K(p) = d(p-1) \Rightarrow \lim_{\lambda\to\infty}\left\langle \varepsilon_\lambda^p \right\rangle \to \infty \quad \text{if } p>1 \tag{5.53}$$

which is known as the *divergence of the moments.*

For the codimension function $c(\gamma)$, the most relevant are:

- $c(\gamma)\geq 0$: This is trivial from (5.50).
- $c(\gamma)$ is an increasing function of γ and must be convex: If γ increases, then the volume occupied by these active eddies decreases, and so the corresponding fractal dimension also decreases. From (5.42), its codimension increases.

Schematic graphs for both functions are shown in Fig. 5.7 and Fig. 5.8.

The Legendre transformations (Appendix F) indicate that there is a value of the singularity γ_p associated with each value of the moment p which maximizes the function $p\gamma - c(\gamma)$ (Lovejoy and Schertzer, 1990)

$$K(p) = max_\gamma\left(p\gamma - c(\gamma)\right) \Leftrightarrow c(\gamma) = max_p\left(p\gamma - K(p)\right) \tag{5.54}$$

Using the definition of a maximum of a function we obtain from $c(\gamma)$

$$\left.\frac{d}{d\gamma}\left(p\gamma - c(\gamma)\right)\right|_{\gamma_p} = 0 \quad\Rightarrow\quad p_\gamma = \left.\frac{dc}{d\gamma}\right|_{\gamma_p} \tag{5.55}$$

and from $K(p)$

$$\left.\frac{d}{dp}\left(p\gamma - K(p)\right)\right|_{p_\gamma} = 0 \quad\Rightarrow\quad \gamma_p = \left.\frac{dK}{dp}\right|_{p_\gamma} \tag{5.56}$$

From the dual Legendre transforms the basic properties of $K(p)$ define other properties for the $c(\gamma)$ function and vice versa (Tessier et al., 1993). These are given below and shown in Fig. 5.7 and Fig. 5.8

- The y-intercept of the tangent line of the function $c(\gamma)$ (or $K(p)$) at each value γ_p (or p_γ) corresponds to the absolute value of the scaling exponent $K(p)$ (or $c(\gamma)$). The slope of the tangent line of the function $c(\gamma)$ (or $K(p)$) at each value γ_p (or p_γ) corresponds to the order of the moments p (or γ_p).

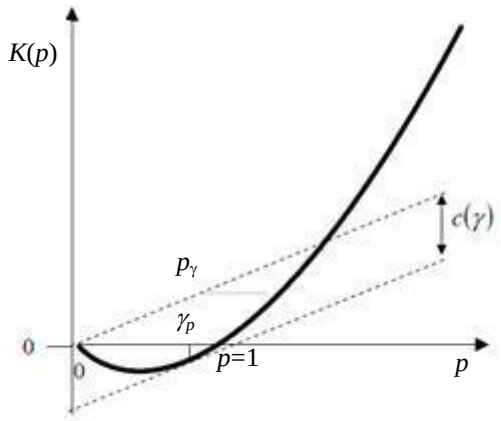

Fig. 5.7 Schematic plot $K(p)$ vs. p. Properties detailed in the text are shown in the figure: $K(1)=0$ and $K'(p)=\gamma_p$ (Tessier et al., 1993).

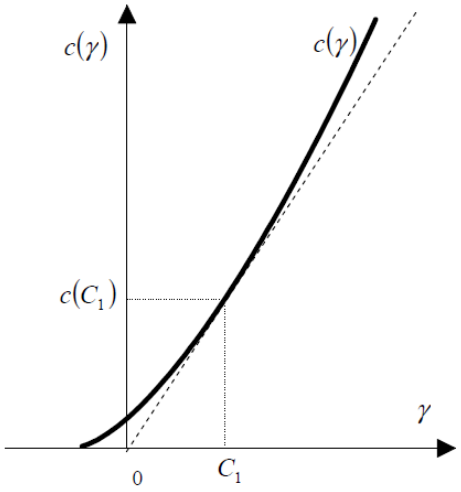

Fig. 5.8 Schematic plot of $c(\gamma)$ properties where they can be showed: 1) $c(C_1) = C_1$,2) $c'(C_1) = 1$. Note that the function is convex (Tessier et al., 1993).

- A value of $\gamma = C_1$ exists and is known as the *codimension of the mean process* (see in Fig. 5.8) which in turn verifies $c(C_1) = C_1$. This is derived from the energy conservation, i.e. $K(1) = 0$, and from (5.55) there is a value of γ that satisfies $c'(\gamma) = 1$. Then, the tangent of the function $c(\gamma)$ at a value $\gamma = C_1$ is the bisecting line on the first quadrant, i.e. $c(C_1) = C_1$.

5.2.3.3. Bare and dressed quantities

The quantities involved in a real multiplicative cascade process go down to a scale resolution λ and are known as 'bare' quantities. However, in

experimental work, one is forced to use probes of a finite size and which is usually larger than the Kolmogorov scale η_K. These collect averaged data (in space or in time) for a quantity at the scale of device resolution λ, which is less than the 'inner' scale of the process Λ associated with the Kolmogorov scale η_K. These averaged quantities are called 'dressed' quantities because they contain information about the small scales and, in some way, are dressed by them (Schertzer et al., 1993; Schmitt et al., 1994). Instrumentation usually measures dressed quantities (for microstructure probes for example they resolve scales of ~ cm and η_K is of ~ mm). In general, dressed quantities are related to the resolution scale and their moments can diverge statistically. It will not happen with bare quantities whose moments can be calculated at each step of the cascade. Moreover, experimental datasets are finite and this constrains the number of turbulent events that can be explored, thus introducing an upper bound for the singularities. Both limitations, sample size and instrument resolution, influence the statistics of dressed quantities: bare and dressed quantities will be similar but not equivalent.

Characteristic behavior of the scaling exponents $K_d(p)$ of the dressed moments and the dressed codimension $c_d(\gamma)$ are known as multifractal phase transitions, in a similar manner to statistical thermodynamics (Schertzer and Lovejoy, 1994; Schmitt et al., 1994). The subscript 'd' indicates that they come from dressed quantities and should not be confused with the embedding dimension d (see for instance from (5.31) to (5.33)). Multifractal phase transitions are related to the combined effect of the instrument resolution and the sample size. The two possible cases, first and second order phase transitions, are described below.

i. Second order multifractal transitions:

Second order multifractal transitions are associated with the size of the sample. If all the realizations of the process are available, the whole set of the singularities γ can be determined, but in nature samples are in fact finite. Then, it is only possible to observe singularities up to a maximum value $\gamma_{\max}$

. This is known as the *undersampling* effect. In this case, for $\gamma \le \gamma_{\max}$ the values of empirical (dressed) and theoretical (bare) codimension functions are equal. Then, $c_d(\gamma) = c(\gamma)$ for $\gamma \le \gamma_{\max}$.

Using the Legendre transform (5.54), the critical order of the moments p_s is given by $p_s = c'(\gamma_{\max})$ and

$$K_d(p) = \gamma_{max} \cdot p - c(\gamma_{max}) \tag{5.57}$$

And the continuity condition at $p = p_s$ yields

$$K_d(p) = \gamma_{\max} \cdot (p - p_s) + K(p_s) \tag{5.58}$$

The scaling exponent of the dressed moments for a finite number of realizations is

$$K_d(p) = \begin{cases} K(p) & p \le p_s \\ \gamma_{\max} \cdot (p - p_s) + K(p_s) & p > p_s \end{cases} \tag{5.59}$$

which leads to the well-known spurious *linear behavior* for $p > p_s$.Note that the slope of the line for $p > p_s$ corresponds to the value of $\gamma_{\max}$ and the *y*-intercept is $-c(\gamma_{max})$.

If the number of samples (or sampling size) increases, high values of γ can be observed. Then, the dressed codimension $c_d(\gamma)$ becomes larger and the critical value of $p_s = c'(\gamma_{\max})$ increases. Hence, in the linear part of the graph of $K_d(p)$, its slope increases. In the case of undersampling, the first derivative is constant at $p = p_s$ whereas the second derivative is not, and this is known as a second order multifractal phase transition.

Second order multifractal phase transitions verify that:

$$K'(p_s) = \gamma_{\max} \tag{5.60}$$

ii. First order multifractal transitions

Dressed quantities can also diverge statistically due to the scale resolution. Following (5.52) and (5.53), there will be a critical order p_D that

satisfies the condition $K(p_D) = d \cdot (p_D - 1)$; that is the condition of divergence of the moments. However for finite samples, we have also discussed the existence of a maximum accessible value of γ, $\gamma_{\max}$.

Using the restriction for singularities in the Legendre transformations we obtain,

$$K_d(p) = \gamma_{\max} \cdot p - c(\gamma_{\max}) \tag{5.61}$$

And the continuity condition at $p = p_D$ yields

$$K_d(p) = \gamma_{\max} \cdot (p - p_D) + K(p_D) \tag{5.62}$$

which also leads to a spurious *linear behavior* for $p > p_D$. Then, the scaling exponent of the dressed moments for a finite number of realizations is

$$K_d(p) = \begin{cases} K(p) & p \le p_D \\ \gamma_{\max} \cdot (p - p_D) + K(p_D) & p > p_D \end{cases} \tag{5.63}$$

However, the critical order p_D also defines a critical value for the singularities, namely γ_D. The case $\gamma_D \ge \gamma_{\max}$ corresponds to the case described earlier for the second order multifractal transitions. On the other hand, if $\gamma_D < \gamma_{\max}$, then the Legendre transformations (5.54) and (5.56) yield

$$K'(p_D) = \gamma_D \tag{5.64}$$

Thus, the dressed codimension function $c_d(\gamma)$ takes a linear form, as can be seen in (5.54)

$$c_d(\gamma) = p_D \cdot \gamma - K(p_D) \tag{5.65}$$

and

$$c_d(\gamma) = p_D(\gamma - \gamma_D) + c_d(\gamma_D) \tag{5.66}$$

Then,

$$c_d(\gamma) = \begin{cases} c(\gamma) & \gamma \le \gamma_D \\ p_D(\gamma - \gamma_D) + c(\gamma_D) & \gamma > \gamma_D \end{cases} \tag{5.67}$$

Here the slope of the line for $\gamma > \gamma_D$ is p_D and the *y*-intercept is $-K(p_D)$. Note that if the number of realizations increases, it is possible to find higher

values of γ. If so, the linear range of $c_d(\gamma)$ becomes larger but its slope does not change. On the contrary, the graph of $K_d(p)$ shows that although the critical order moment p_D remains constant, the slope in the linear part increases. It also indicates that the moment function $K_d(p)$ is not derivable at $p = p_D$, then it is known as a first order multifractal phase transition.

Using the continuity condition, first order multifractal phase transitions verify

$$D(p_D - 1) = K(p_D) \tag{5.68}$$

and

$$K'(p_D) \neq \gamma_{\max} \tag{5.69}$$

Note that when the number of samples is large enough, then divergence of the moments is observed and the limitation for the critical order will be p_D instead of p_s.

The divergence of the moments can be also analyzed based on probability distributions, as detailed in Appendix F.

5.2.4. Universal multifractals: The log-Lévy model

Multifractal framework leads to scaling exponent $K(p)$ and codimension $c(\gamma)$ functions that must be increasing and convex. Because so many functions that fulfill these requisites exist, an infinite number of parameters are necessary to almost determine them. However, Schertzer and Lovejoy (1987) overcome this problem by suggesting the existence of 'universal' multifractals. In their work, Schertzer and Lovejoy (1987) assumed that for a given process there is a set of initial conditions (i.e. different realizations), also known as a *basin of attraction*, which will converge towards the same limit (*stable attractor*). This basic idea is illustrated in

Fig. 5.9. The existence of universal multifractals has been tested in a great many different geophysical fields which have in turn reported empirical

evidence of this behavior (Pandey et al., 1998; Finn et al., 2001; Watson et al., 2009; Gires et al., 2013).

In the universal multiplicative cascade models, the probability distribution of the sum of n independent and identically distributed random variables belong to a family of probability distributions which are stable and possess a domain of attraction. Then, the logarithms of W_i, $\log(W_i)$, tend to a *stable distribution*, also known as *Lévy distributions*. For log-additive processes, this distribution is the *log-Lévy (log-stable) distribution*. We have described in detail the properties of Lévy and log-Lévy distributions in Appendix G.

Log-Lévy distributions are characterized by four parameters: the index parameter, the skewness parameter, the scaling parameter and the location parameter. When the skewness parameter is -1, the moments of W_i are finite i.e. it ensures that the moments of all orders for ε_λ exist.

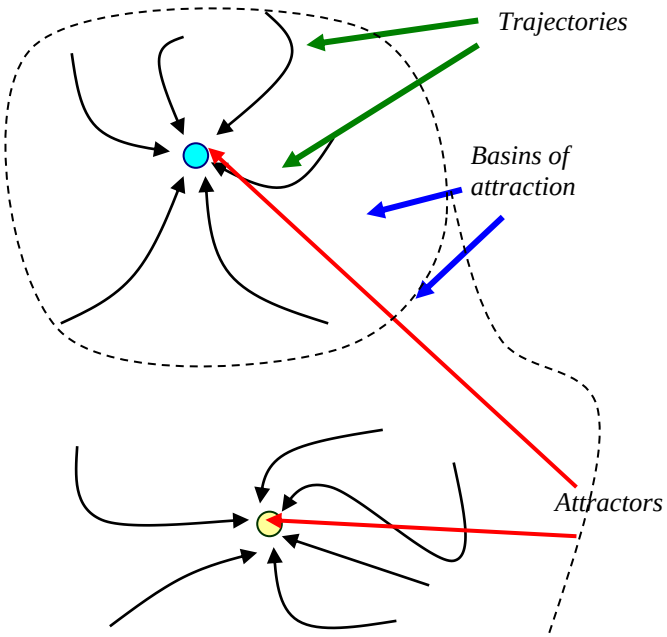

Fig. 5.9 Schematic plot of basins of attraction with their corresponding attractors. Possible trajectories for the processes are shown in the figure.

The moment scaling exponent $K(p)$ for the universal and conservative multifractal model is (Appendix G)

$$K(p)=\begin{cases}\dfrac{C_1}{\alpha-1}\left(p^\alpha-p\right) & \alpha\neq 1\\ C_1 p\log(p) & \alpha=1\end{cases} \tag{5.70}$$

Using the Legendre transform we can derive the 'universal' expression for the codimension function as is shown next

$$c(\gamma)=\max_p\left(p\gamma-K(p)\right)\Rightarrow\exists p^*\,|\,c(\gamma)=p^*\gamma-K\left(p^*\right) \tag{5.71}$$

$$c(\gamma) = p^* \gamma - \frac{C_1}{\alpha - 1}\left(\left(p^*\right)^{\alpha} - p^*\right) \tag{5.72}$$

Knowing the expression of the derivative of $K(p)$ we can obtain the value of γ as

$$K'\left(p^*\right) = \gamma \tag{5.73}$$

$$\gamma = \frac{C_1}{\alpha - 1}\left(\alpha\left(p^*\right)^{\alpha - 1} - 1\right) \tag{5.74}$$

Substituting γ in (5.71)

$$c(\gamma) = p^* \frac{C_1}{\alpha - 1}\left(\alpha\left(p^*\right)^{\alpha - 1} - 1\right) - \frac{C_1}{\alpha - 1}\left(\left(p^*\right)^{\alpha} - p^*\right) = C_1\left(p^*\right)^{\alpha} \tag{5.75}$$

Isolating p^* from (5.74) and replacing it in (5.75)

$$p^* = \left(\frac{\alpha - 1}{\alpha C_1}\gamma + \frac{1}{\alpha}\right)^{\frac{1}{\alpha - 1}} \tag{5.76}$$

$$c(\gamma) = C_1\left(\frac{\alpha - 1}{\alpha C_1}\gamma + \frac{1}{\alpha}\right)^{\frac{\alpha}{\alpha - 1}} \Rightarrow c(\gamma) = C_1\left(\frac{\gamma}{C_1 \alpha'} + \frac{1}{\alpha}\right)^{\alpha'} \tag{5.77}$$

where $\frac{1}{\alpha} + \frac{1}{\alpha'} = 1$.The same process can be done for $\alpha = 1$. Then, the parameterized form for the codimension function $c(\gamma)$ is

$$c(\gamma) = \begin{cases} C_1\left(\frac{\gamma}{C_1 \alpha'} + \frac{1}{\alpha}\right)^{\alpha'} & \alpha \neq 1 \\ C_1 \exp\left(\frac{\gamma}{C_1} - 1\right) & \alpha = 1 \end{cases} \tag{5.78}$$

As can be observed for both functions, log-Lévy distributions for conservative fields are parameterized by only two parameters, α and C_1, which characterizes the intermittency of the field. As a summary, the parameters α and C_1 are described next,

- The *mean codimension C_1 of process*: It can be understood as a measure of the 'sparseness' (inhomogeneity) of a given field. High values of C_1 indicate that the energy is concentrated in small volumes; the field is more intermittent. For $C_1 = 0$, the turbulent field becomes isotropic over

the whole space and then the turbulent field is non-intermittent; in other words, it is the homogeneous case.

- The *degree of multifractality* α: This is associated to the multifractal behavior of the cascade, i.e. how intense the fluctuations are that fill the available space. The multifractality parameter α is the Lévy index of the log-stable distribution of ε_λ and indicates the class to which the probability distribution belongs (Appendix G):
  - α = 2: Log-normal multifractal. This is obtained for the maximum value for α.
  - $1<\alpha<2$: log-Lévy processes with unbounded singularities.
  - α = 1: log-Cauchy multifractals.
  - $0<\alpha<1$: log-Lévy processes with bounded singularities.
  - α = 0 corresponds to the monofractal β-model process. In this case, only one singularity exists and the β-model is recovered.

According to (5.22) the log-Lévy model derives that the scaling exponents $\zeta(p)$ of the structure function $S_p(r)$ should be

$$\zeta(p)=\frac{p}{3}-\frac{C_1}{\alpha-1}\left[\left(\frac{p}{3}\right)^{\alpha}-\frac{p}{3}\right] \tag{5.79}$$

Seuront et al. (2005) suggested that C_1 and α have universal values close to 0.15 and 1.5, respectively, for very high Reynolds numbers.

Using the (5.24) the power spectrum *B* is

$$B=1+\zeta(2)=\frac{5}{3}-\frac{C_1}{\alpha-1}\left[\left(\frac{2}{3}\right)^{\alpha}-\frac{2}{3}\right] \tag{5.80}$$

The intermittency parameter μ, which corresponds to $\mu=K(2)$ from (5.25), gives an intermittency parameter $\mu=2C_1$ for log-normal distribution ($\alpha=2$) and $\mu\approx 1.65C_1$ for log-Lévy distribution with $\alpha=1.5$.

Critical orders for multifractal transitions can be also expressed in terms of C_1 and α following (5.70) and (5.78)

- For first-order multifractal transitions, from (5.68), we can calculate the critical order p_D associated to the divergence of the moments as

$$K(p_D) = D \cdot (p_D - 1) \Rightarrow D = \frac{K(p_D)}{p_D - 1} \tag{5.81}$$

- For second order multifractal transitions, the critical order p_s related to the finiteness of the sample can be obtained from

$$p_s = c'(\gamma)\big|_{\gamma=\gamma_{\max}} = \left(\frac{\gamma_{\max}}{C_1\alpha'} + \frac{1}{\alpha}\right)^{\alpha'-1} = \left[\frac{c(\gamma_{\max})}{C_1}\right]^{\frac{\alpha'-1}{\alpha'}} \quad \alpha \neq 1 \tag{5.82}$$

$$p_s = c'(\gamma)\big|_{\gamma=\gamma_{\max}} = \exp\left(\frac{\gamma}{C_1} - 1\right) = \frac{c(\gamma_{\max})}{C_1} \quad \alpha = 1 \tag{5.83}$$

5.3. Tools for multifractal analysis

There are several techniques for analyzing the multifractal behavior of the field under study. In our work, we focus on three of these methods: the structure-function (SF) method, the Trace Moment (TM) method and the Double Trace Moment (DTM) method, which have been widely used by scientists. The first one deals directly with the calculation of the structure functions of the measured field. The other two methods work on the scaling exponents of a conservative field which is derived from the measured field.

Next we describe in detail the three proposed methods. A summary of the steps for their application can be also found at the end of each subsection.

5.3.1. The structure-function (SF) method

The SF method consists of computing the statistical moments of the fluctuations Δv_r of any component of the turbulent field $\vec{v}$ and determining the scaling exponents $\zeta(p)$ according to the power law shown in (5.5)

$$s_p(r) \equiv \left\langle \Delta v_r^p \right\rangle \propto r^{\zeta(p)} \tag{5.84}$$

Straight lines at any order *p* are expected for the logarithmic plots of $s_p(r)$ as a function of *r* and their slopes correspond to the scaling exponents $\zeta(p)$. The intermittency parameters are found by fitting $\zeta(p)$ to a theoretical model, for example μ in the log-normal model or C_1 and α for log-Lévy model (recall that log-normal is a particular case of the log-Lévy model with μ=2).

Previous to the application of the method, it is necessary to check if the presence of a *power-law* in the original records has been observed ($E(f) \sim f^{-B}$). For turbulent flows this range is associated with the inertial subrange ($B = -5/3$) which will be found at scales below the outer (integral) scale L_0 and down to the Kolmogorov scale η_K. Taking v' as the fluctuations of the velocity component v, the integral scale L_0 may be estimated (Tennekes and Lumley, 1972) as

$$L_0 = c_0 \left[rms(v') \right]^3 / \tilde{\varepsilon} \tag{5.85}$$

where $rms(v')$ is the root-mean-square of v', $\tilde{\varepsilon}$ the mean dissipation rate of the velocity record and c_0 is a constant near unity.

Usually inertial subrange is difficult to define exactly (Sreenivasan and Dhurva, 1998). Further, depending on the Reynolds number, the inertial subrange can expand only (roughly) one order of magnitude and sometimes less. Because short and inaccurate ranges can introduce uncertainties into the estimations of the exponents, Benzi et al. (1993) introduced the Extended Self-Similarity (ESS) method to improve the quality of this scaling range.

The ESS method consists of widening the region of scaling using the SF plots of any order against a structure function of another one. The relative scaling exponent $\zeta(p,q) = \zeta(p)/\zeta(q)$ is obtained. Since the shape of all structure functions is quite similar, the relative exponent $\zeta(p,q)$ remains constant for a larger range and the scaling observed in the plots is much wider, regardless of the Reynolds Re number (self-similarity can be extended); several examples of ESS applications are shown in Fig. 5.10, which was extracted from Benzi et al. (1993). Taking as a reference the third-order $s_3(r)$ structure function and also

recalling that $s_3(r) \propto r$, (5.84) can be written as

$$s_p(r) = A_p [s_3(r)]^{\frac{\zeta(p)}{\zeta(3)}} \Rightarrow s_p(r) \propto [s_3(r)]^{\zeta(p)} \tag{5.86}$$

and the scaling exponents $\zeta(p)$ can be inferred, with A_p being a set of constants. Note that although the ESS method extends the scaling range, its bounds should be properly analyzed to reduce possible errors in the estimations of $\zeta(p)$.

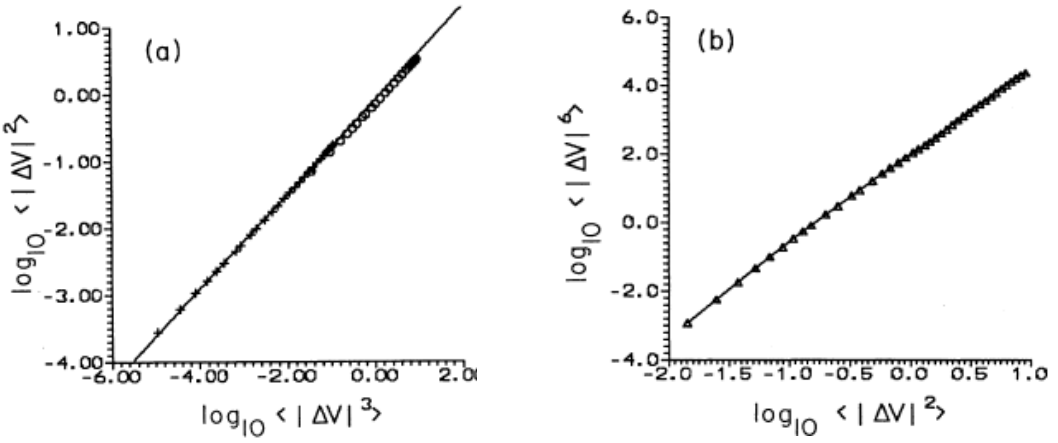

Fig. 5.10 Extended Self-Similarity applied to (a) $<\Delta v(r)^2>$ as a function of $<|\Delta v(r)|^3>$ and (b) $<|\Delta v(r)|^6>$ as a function of $<|\Delta v(r)|^2>$. The plots show a good linear fit between both functions and it is valid for a wide range of scales (Benzi et al., 1993).

The ESS methodology being works well if the absolute velocity increments $S_p(r)$ are considered instead of $s_p(r)$ (Benzi et al., 1993; Sreenivasan and Dhruva, 1998). Thus, for the structure functions $S_p(r)$ it is possible to write

$$S_p(r) = B_p [S_3(r)]^{\zeta(p)} \tag{5.87}$$

and the behavior of $S_p(r)$ and $|s_p(r)|$ scales with the same power law.

Next we summarize the steps for the application of the SF method:

1) Determine the integral scale L_0 to define the possible range of scales to perform the analysis.
2) Compute the velocity differences of the given velocity component field Δv_r for different values of the separation scale r. Calculate the structure

functions $S_p(r)$ of different orders p for the absolute value of the Δv_r of the velocity field.

3) Generate the logarithmic plots $S_p(r)$ as a function of $S_3(r)$ after inspection of the scaling range up to L_0 in the logarithmic plots of $S_p(r)$ against r, and obtain the scaling exponents $\zeta(p)$ as slopes of the plot.
4) Fit the empirical values of $\zeta(p)$ to the log-Lévy model (log-normal model if $\alpha = 2$) in order to obtain the intermittency parameters C_1 and α. Then, estimate the intermittency exponent μ: $\mu = K(2)$, see (5.25).

5.3.2. The Trace Moment (TM) Method

The TM method (Schertzer and Lovejoy, 1987) allows the intermittency parameters (μ, C_1 and α) to be estimated using the scaling exponent $K(p)$ function of the *p*-order moments of a scalar field, which are evaluated at different scales of resolution. This has been successfully tested in different geophysical fields (Schmitt et al., 1992; Rodriguez-Iturbe and Rinaldo, 1997; Bernardara et al., 2007).

As in the case of the SF method, the first step is to determine a suitable range of scales for the inertial subrange, which will be inside the interval defined by L_0 (integral scale) and η_K (Kolmogorov scale). However, if the highest achievable spatial resolution after data processing is r_0, the analysis will be performed over a range of scales of size $r \in [r_0, L_0]$ (Lovejoy and Schertzer, 2010).

The so-called small-scale dissipation field, i.e. a *conservative field*, is estimated from the data series of one component of the turbulent velocity field $v = \{v_i\}, i = 1,2,....N$, with N being the number of points of the series according to the isotropic formula $\varepsilon = 7.5\nu(dw/dz)^2$ (Appendix A).

The small-scale dissipation field is split up into subrecords A of length Λ, where Λ is the lower power of 2 closest to the value of the ratio L_0/r_0. For

each subrecord, the field is normalized by the mean value in order to reconstruct the cascade. Normalizations can be performed over all the subrecords or over each subrecord in particular (Schmitt et al., 1994; Finn et al., 2001). However, the former procedure allows for an estimation of the outer scale L_0 to be obtained (Lovejoy and Schertzer, 2013). The normalized field is marked with a star, i.e. $\varepsilon_{\Lambda}^{*}$, as -introduced in subsection 5.2.2. As a result, we obtain a set of N_{Λ} subrecords $\{A_i\}$ for the field $\varepsilon_{\Lambda}^{*}$, with $i = 1,2,...N_{\Lambda}$ and $N_{\Lambda} = N/\Lambda$.

The next step consists of estimating the dissipation field in *coarser scales* λ. Then, each subrecord A_i is *degraded* from the finest resolution scale $\lambda = \Lambda$ to $\lambda = 1$. Intermediate scales λ can be easily obtained taking all the powers of 2 and satisfying $1 \le \lambda \le \Lambda$ (i.e., $r_0 \le r \le L_0$).

That is, starting from $\lambda = \Lambda$, this process is carried out by dividing each subrecord A_i into n_{λ} successive disjoint intervals B_{λ,A_i}, which contain Λ/λ points, with $n_{\lambda} = \lambda$. This defines a subset of intervals $\{B_{\lambda,A_i}(j)\}$ with $j = 1,2,....N_{\Lambda} \times n_{\lambda}$ covering the subrecords A, where the small-scale dissipation rates $\varepsilon_{\Lambda}^{*}$ are averaged. Thus, at scale ratio λ, the new field $\varepsilon_{\lambda}^{*}(j)$ for a particular interval $B_{\lambda,A_i}(j)$ of a subrecord A_i can be expressed (Lovejoy and Schertzer, 2010) as

$$\varepsilon_{\lambda}^{*}(j) = \frac{1}{N_{\Lambda} \times n_{\lambda}} \sum_{k=1}^{n_{\lambda}} \varepsilon_{\Lambda}^{*}(n_{\lambda} \cdot (j-1) + k) \tag{5.88}$$

Note the resulting dissipation field $\varepsilon_{\lambda}^{*}$ represents the dressed (averaged) field at resolution scale λ.

To determine the moments of order p, the values of dressed field $\varepsilon_{\lambda}^{*}$ are raised to powers p and then ensemble averaged at different scales over the set $\{A_i\}$, i.e.

$$M_p(\lambda) = \left\langle \left(\varepsilon_{\lambda}^{*}\right)^p \right\rangle \tag{5.89}$$

The multifractality of the process is investigated by plotting each of moments $M_p(\lambda)$ as a function of λ. This allows the scaling regime to be identified: it is the range of scales $\lambda \in [1, \Lambda]$ at which moments fit well to a power law, i.e. a straight line in a logarithmic plot. Thus, the slopes of the logarithmic graphs in the scaling range are estimations of $K(p)$ (note that it corresponds to dressed moments, symbolized previously as $K_d(p)$). If $K(p)$ is a linear function of p and has $K(0) \neq 0$, the process will be a monofractal process. From (5.37) $K(p) = -c$ with $c = C_1$, this is the codimension of the process. In contrast, for multifractals the graph of the function will be convex with $K(0) = 0$. Also, the curve displays a linear part related to a critical value p_{crit} (p_D or p_s) which is associated with multifractal phase transitions.

Finally, to estimate the multifractal parameters, C_1 and α, several procedures exist and two of them are detailed next:

- Fit $K(p)$ to the theoretical expression given in (5.70) with non-linear regression (usual methodology). The critical moment p_{crit} is estimated from the regression.
- Using the first and second derivatives of $K(p)$ for $p = 1$ they can be easily related to the multifractal parameters as follows:

$$K'(p) = \frac{dK(p)}{dp} = \frac{C_1}{\alpha - 1}\left(\alpha p^{\alpha-1} - 1\right) \Rightarrow C_1 = K'(p=1) \tag{5.90}$$

$$K''(p) = \frac{d^2K(p)}{dp^2} = \frac{C_1}{\alpha - 1}\alpha(\alpha - 1)p^{\alpha-2} \Rightarrow K''(p=1) = C_1\alpha \tag{5.91}$$

and

$$\alpha = \frac{K''(p=1)}{C_1} \tag{5.92}$$

The intermittency exponent μ is estimated as $\mu = K(2)$ from (5.70).

In conclusion, we summarize the steps of the TM method which need to be applied to the turbulent field in order to obtain the parameters of the universal multifractal model (a schematic of the method is shown in Fig. 5.11).

1) Determine the integral scale L_0 and highest available resolution scale. This defines a suitable range of scales $r \in [r_0, L_0]$ with which to perform the analysis.
2) Estimate the small-scale dissipation rate at the highest available resolution scale r_0.
3) Split the small-scale dissipation field into subrecords A of length Λ, where Λ is the power of 2 closest to the ratio of L_0/r_0 and normalized by the mean. The resulting field is symbolized by ε_Λ^*.
4) Degrade ε_Λ^* to lower resolutions. To do this divide each subrecord A_i into disjoint intervals B_{λ,A_i} which contain Λ/λ points, with λ a power of 2 between 1 and Λ. The resulting field at a particular scale λ is symbolized by ε_λ^*. Start the process with λ=1, obtain the moments of order p of ε_λ^*, $M_p(\lambda)$, for λ=1 by ensemble averaging and then continue the degradation process up to $\lambda = \Lambda$.
5) Evaluate $K(p)$ from the slopes of the straight line region (power-law fitting) present in the logarithmic plots of $M_p(\lambda)$ against λ.
6) Estimate the intermittent parameters C_1 and α (non-linear regression or derivative method) and the intermittency exponent as $\mu = K(2)$.

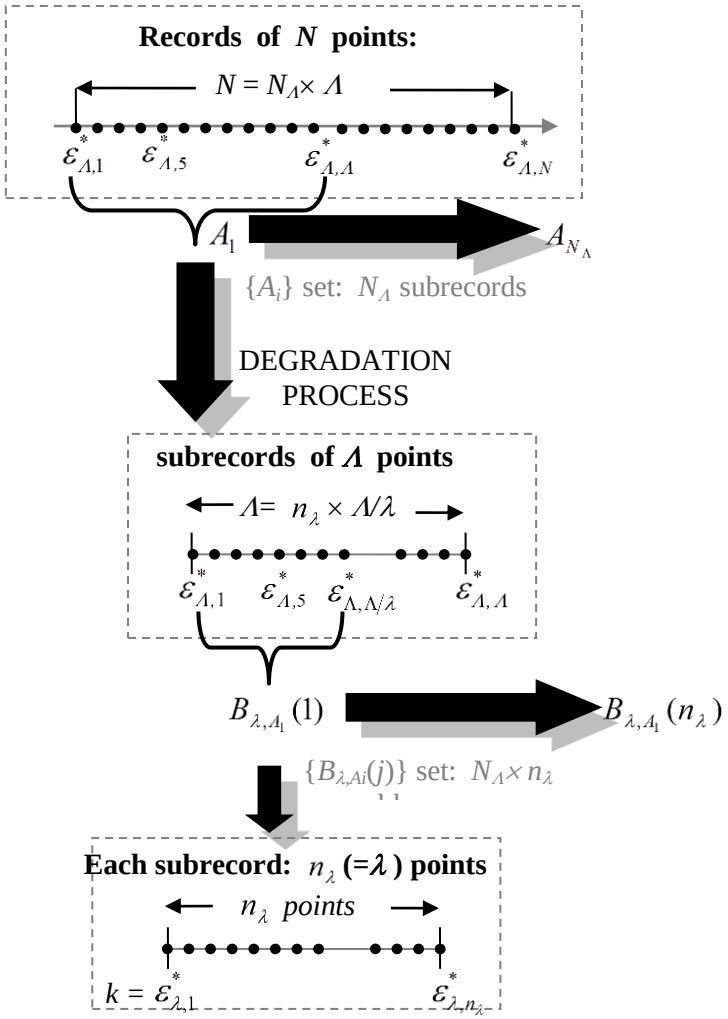

for N_Λ subrecords (whole sample):

Series of $\{n_\lambda(k)\}$ $k = 1, 2 \ldots N_\Lambda$

Estimation of *p*-order moments

(ensemble average):

$$M_p(\lambda) = \left\langle \left(\varepsilon_\lambda^*\right)^p \right\rangle$$

Fig. 5.11 Schematic application of the TM method for a specific value of λ. A similar procedure is applied to the field for the double trace moments (DTM method). Repeat degradation process for λ up to Λ.

5.3.3. Double Trace Moment (DTM) Method

Using the TM method the intermittency parameters simultaneously fit the scaling exponent $K(p)$ function by two parameters, which are correlated. The Double Trace Moment (DTM) method (Lavallée, 1991), which is a generalization of the Trace Moment (TM) method, allows the multifractal parameter α and then C_1 to be determined independently.

The DTM technique consists of the introduction of a second moment η in order to estimate the parameter α. Firstly, the small-scale dissipation field ε_Λ at the finest resolution scale Λ is raised to powers η, ε_Λ^η. Then, following the same procedure as in the TM method, the new field is degraded on different scales λ using a set of intervals $\{B_{\lambda,A}(j)\}$ for covering each subrecord A resulting in a new field $\varepsilon_\lambda^\eta = (\varepsilon_\Lambda^\eta)_\lambda$ being obtained. After this, ε_λ^η is normalized.

The moments of order p for the new field $\varepsilon_\lambda^{*\eta}$ are ensemble averaged over the set $\{A_i\}$, i.e.:

$$M_{\eta,p}(\lambda) = \left\langle \left(\varepsilon_\lambda^{\eta^*}\right)^p \right\rangle \tag{5.93}$$

which have the scaling property,

$$\left\langle \left(\varepsilon_\lambda^{\eta^*}\right)^p \right\rangle \approx \lambda^{K(p,\eta)} \tag{5.94}$$

Considering that the expression (5.93) can be expressed as

$$M_{\eta,p}(\lambda) = \left\langle \left(\varepsilon_\lambda^{\eta^*}\right)^p \right\rangle = \left\langle \frac{\left(\varepsilon_\lambda^{\eta}\right)^p}{\left\langle \varepsilon_\lambda^{\eta} \right\rangle^p} \right\rangle = \frac{\lambda^{K(p\eta)}}{\lambda^{pK(\eta)}} = \lambda^{K(p\eta)-pK(\eta)} \tag{5.95}$$

then,

$$K(p,\eta) = K(p\eta) - \eta K(p) \tag{5.96}$$

In the case of universality,

$$K(p,\eta) = \eta^\alpha K(p) \tag{5.97}$$

which can be trivially deduced by substituting (5.70) in (5.96).

To determine the multifractal parameters, each value of the scaling exponents of the double trace moments $K(p,\eta)$ is calculated from the slope of the straight-lined part (power-law fitting) of the logarithmic graph of $M_{\eta,p}(\lambda)$ against λ. By applying logarithms to (5.97) this is transformed into:

$$\log(|K(p,\eta)|) = \alpha \log(\eta) + \log(|K(p)|) \tag{5.98}$$

and the parameter α can be directly obtained by linear regression in the corresponding logarithmic plot for each moment p, as shown in Fig. 5.12.

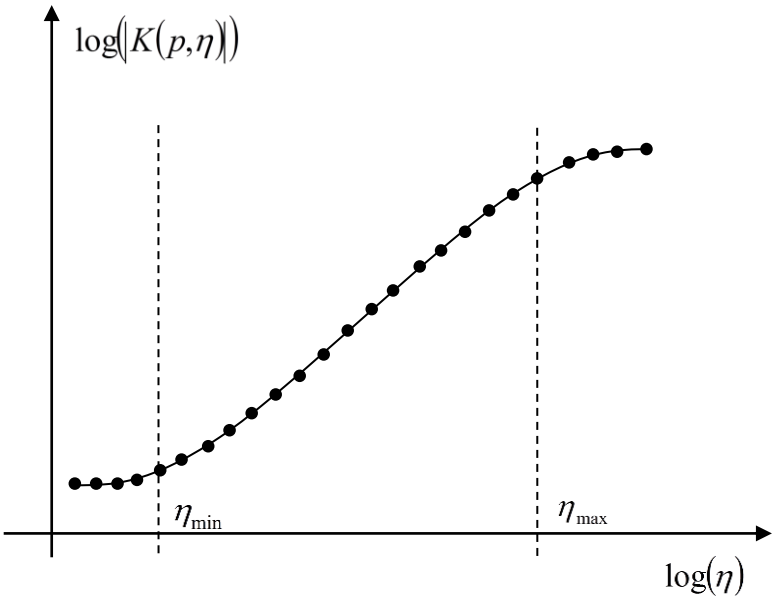

Fig. 5.12 Graph of log($K(p,\eta)$) vs. log(η) for the DTM analysis. Determination of the intermittency parameter α is obtained based on the slope of the linear part of the logarithmic graphs between η_{min} and η_{max} at which the function flattens (marked by dotted lines). Only points inside the interval [η_{min}, η_{max}] are considered for the analysis.

Breaks in the linearity, observed in Fig. 5.12, lead to the characteristic 'S'-shaped graph. For high values of η the break in linearity is caused by the divergence of the moments (p_D) or the sampling size (p_s) of the datasets. On the other hand, for low values of η the sensor resolution and noise will also affect the signal. Furthermore, it breaks the linearity of the plot. Although the latter can be removed by data filtering, this should be done with caution because it could smooth the real structure of the signal.The range of η for the power-law fit to $|K(p,\eta)|$ is done by detecting the two regions in which the

function $|K(p,\eta)|$ is practically constant, when it is plotted in logarithmic scale. Thus, the bounds for the range of $\eta \in [\eta_{\min}, \eta_{\max}]$ correspond to those values of η associated with lower and upper empirical values of $|K(p,\eta)|$ and denoted by $|K(p,\eta_{\min})|$ and $|K(p,\eta_{\max})|$. Once the interval is selected, parameter α is usually determined from a particular point $\eta^* \in [\eta_{\min}, \eta_{\max}]$ choosing one of three options: An intermediate point $\overline{\eta}$ whose ordinate corresponds to the mean value of the lower and upper values of $|K(p,\eta)|$, that is

$$K(p,\overline{\eta}) = \left(|K(p,\eta)|_{\min} \cdot |K(p,\eta)|_{\max}\right)^{\frac{1}{2}} \tag{5.99}$$

- The inflexion point η_{IP} of $\log|K(p,\eta)|$ vs. $\log(\eta)$.
- The point of abscissa $\eta_a = 1$.

After the point has been selected, the intermittency parameter α is estimated by evaluating the slope at this point using a given number *n* of nearest discretized η values. This number *n* of points is obtained by adding and/or removing nearest points until the goodness of the fit R^2 is less than a fixed threshold.

The parameter C_1 can be estimated with the help of the *y*-intercept in (5.98), i.e. $\log(\eta) = 0$. Then, the fit should include the point of abscissa $\eta = 1$ to get reliable estimations of this parameter. For a conservative field and assuming the universal multifractal model the parameter C_1 is

$$C_1 = \frac{|K(p,\eta)|(\alpha - 1)}{p^{\alpha} - p} \tag{5.100}$$

Finally, as we have also done in the previous methods, the intermittency exponent μ is estimated as $\mu = K(2)$ from (5.70).

The DTM is a generalization of the TM method and some of the steps in both procedures are equal. Taking this in account, the basic steps of application of the DTM method are listed below:

1) Proceed in the same way as described in the TM method up to estimating the small-scale dissipation rate at the highest available resolution scale r_0.
2) Raise the small-scale dissipation field to powers η.
3) Split it into subrecords A of length Λ, where Λ is the power of 2 close to L_0/r_0 The resulting field is symbolized by ε_Λ^η.
4) Degrade the new field ε_Λ^η to lower resolutions by following the TM method: use disjoint interval B_{λ,A_i}, which contains Λ/λ points, to cover the set of subrecords $\{A_i\}$, with λ a power of 2 between 1 and Λ. For each value λ the resulting field is normalized by the mean and symbolized by $\varepsilon_\lambda^{\eta^*}$.
5) Obtain the moments of order *p* for $\varepsilon_\lambda^{\eta^*}$, i.e. the double trace moments $M_{\eta,p}(\lambda)$, by ensemble averaging for each step (each λ) of the degradation process.
6) Evaluate the scaling exponent $|K(p,\eta)|$ from the slopes of the linear region present in the logarithmic plots of $M_{\eta,p}(\lambda)$ against λ.
7) Estimate the intermittency parameter α in the following way:
   i. Determine an appropriate range for $\eta \in [\eta_{\min}, \eta_{\max}]$. The bounds are those values of η associated with the upper and lower values of the plateaus observed in the logarithmic plot of the function $|K(p,\eta)|$ vs η.
   ii. Calculate $\eta^* \in [\eta_{\min}, \eta_{\max}]$ using one of three options: the intermediate point $\overline{\eta}$ whose ordinate corresponds to the mean value of the lower and upper values of $|K(p,\eta)|$, the inflexion point η_{IP} or the point of abscissa $\eta_a = 1$
   iii. Estimate α by evaluating the slope at η^* and adding and/or removing nearest points until the goodness of the fit R^2 is less than a fixed threshold.

8) Estimate C_1 by using the *y*-intercept of the logarithmic graph of $|K(p,\eta)|$ as a function of η and the expression of the scaling exponent $K(p,1)=K(p)$ for the universal multifractal model.

9) Evaluate the intermittency exponent as $\mu = K(2)$.

6. Observations of Internal Intermittency: Measurements in a Tidal Flow

6.1. Study site and experimental set up

The northern part of the East China Sea (ECS), also known as the Yellow Sea (Fig. 6.1), is a partially enclosed sea bounded by the Chinese mainland to the west and north and by the Korean Peninsula to the east. The south is delimited by an imaginary line which connects the mouth of the Changjiang (Yangtze) river and the South Korean Cheju Island. Covering a total area of ~ 295.000 km^2, it is one of the largest continental shelves in the world.

The Yellow Sea is quite a shallow basin (a mean depth of ~45 m) with a maximum depth of ~150 m. While slopes are gentle along the Chinese coast they increase sharply on the Korean Peninsula. Deep waters are mainly found in a narrow central region, increasing in depth from north to south through the long axis of the sea which extends from the ECS inland.

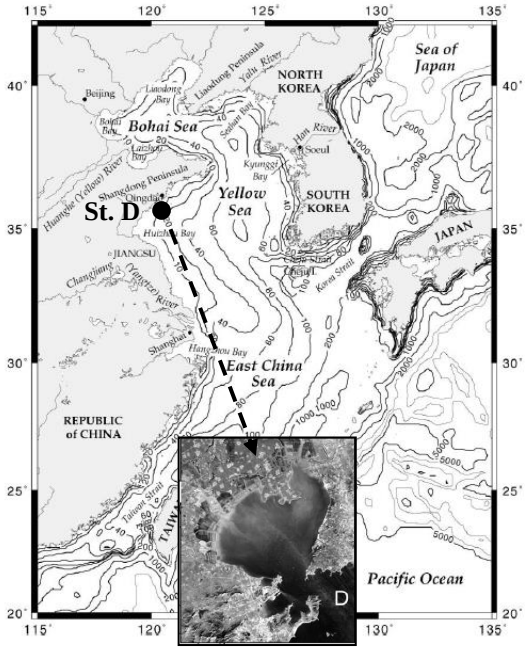

Fig. 6.1 Bathymetric map of the Yellow Sea, located at the northwestern part of the East China Sea with the location of the mooring station (St. D). The surrounding area is enlarged in the insertion showing Jiaozhou Bay on the Chinese coastline. St. D was set up about 2 km to the east of the mouth of the bay and 1.2 km south of the northern coastline (adapted from Lozovatsky et al., 2008a).

The hydrodynamics of the Yellow Sea is governed by different processes such as atmospheric forcing, tides, freshwater discharges and

currents. Overviews of such processes can be found in Zhou et al.'s book (1994) and have also recently been analyzed in a number of different works (Ichikawa and Beardsley, 2002; Lozovatsky et al., 2008a; Lozovatsky et al., 2008b; Xu et al., 2009; Xing et al., 2012).

Tide forcing is a relevant factor in the dynamics of the sea. Despite high spatial and temporal variability of tides, they greatly impact the basin, prevailing over other currents in the absence of monsoons (Liu et al., 2007; Moon et al., 2009). Tides are mixed, with semidiurnal and diurnal constituents both being important, show complex spatial structure and are dominated by semidiurnal tides (Bao et al., 2001; Cui and Yanagi, 2007). They are particularly strong on the Korean coast, where the tidal range oscillates between 4 m and 8 m; along the Chinese coast, ranges are from 1 to 3 m (Uda, 1966; Yanagi et al., 1997). Tidal currents generated by tides are strong at the tip of the Korean Peninsula, reaching maximum speeds of ~5.5 $m \cdot s^{-1}$ (King et al., 2001). However, their characteristic maximum speeds are about 1 - 1.5 $m \cdot s^{-1}$ near the coastlines and ~ 0.5 $m \cdot s^{-1}$ in the central basin (Teague et al., 1998; Zhao et al., 2011). Tidal flows can be also affected by the topography of the sea-floor or by coastal features: specifically, bays and narrow straits that force currents to flow in a rather directional direction, leading to the formation of reversible tidal flows which in turn can interact with other mechanisms (Xiaohui et al., 2004).

The extensive work of Lozovatsky et al. (2008), shows that the dynamics of the shallow waters in the northwestern part of the Yellow Sea is mainly driven by tidal flows. In order to analyze the internal intermittency of turbulence in such conditions, we used the velocity time series obtained from a bottom-mounted Nortek 6 MHz 'Vector' Acoustic Doppler Velocimeter (ADV) deployed in the area during their field campaign. Measurements were conducted on December 14, 2005, about 1.2 km offs the northeastern coast of China (36.04°N, 120.32°E) at a water depth of 19 m. The measurement site (St. D in Fig. 6.1) is located 2 km from the mouth Jiaozhou Bay. The ADV was mounted looking down in order to measure at a height of 0.45 m above the

bottom (mab). Velocity data were recorded during 25 hours in a shallow-water tidal current and covered two complete semidiurnal tidal cycles. The ADV sampling rate was 16 Hz and data were recorded continuously during the observational period.

A nearly unidirectional reversible tidal flow dominated the mesoscale dynamics at the test site; see Fig. 6.2 (adapted from Lozovatsky et al., 2008a). The amplitude of the west-directed flood current of ~ 0.35 - 0.42 m·s^{-1} was twice that of the eastern ebb current. The amplitude of the transversal horizontal component was much smaller at ~ 0.05 m·s^{-1}. Strong winds blew in the area during the measurements, exciting seiche modes in the bay (Zhao et al., 2011). From the analysis of the flow dynamics, Lozovatsky et al. (2008a) showed that the reversing tidal flow was affected by seiches of a ~ 2.3 h period. The seiching modulation of zonal velocity during the ebb tide was comparable with the tidal magnitude. The shallow water column was well mixed due to winter cooling from the sea surface and tidal mixing in the bottom boundary layer (BBL).

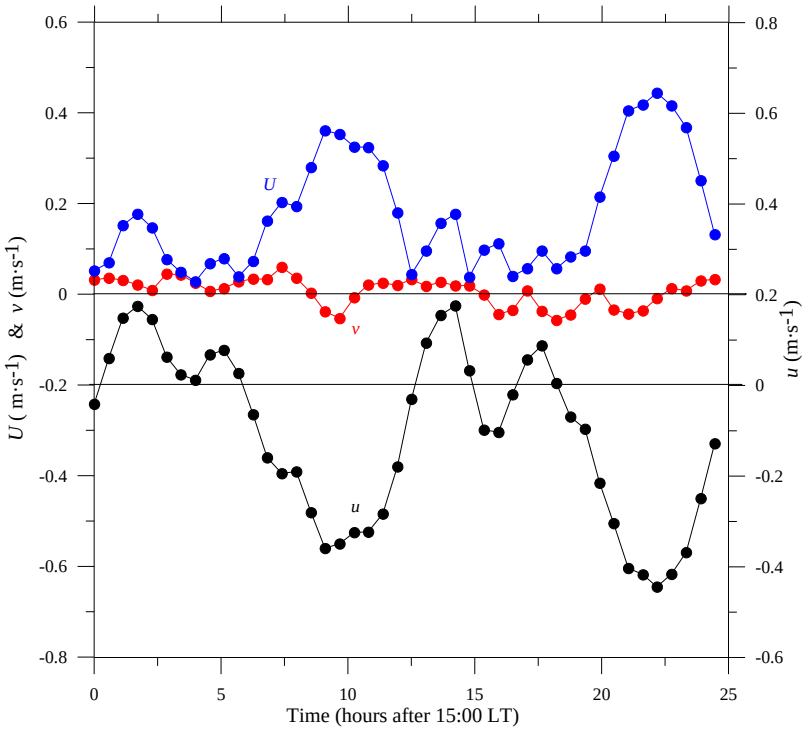

Fig. 6.2 Two ADV velocity current components, *u* (alongshore) and *v* (cross-shore), and the magnitude of the tidal current *U* observed at St. D at a height of 0.45 meters above the bottom (depth 18.5 m) observed during the observational period (25 h). Note that, most of the period the flow is driven by the alongshore component *u* with maximum *U* speeds of ~0.45 m·s^{-1}.

6.2. Data processing

To analyze the internal intermittency of turbulence in a near-bottom tidal flow, the 25-hour velocity record was subdivided into 44 segments. Each segment contained 2^{15}=32628 individual samples, which corresponds to a time interval of ~ 34 min. Thus, such segments are long enough to allow sufficient multiplicative assembly averaging to calculate the structure functions with an acceptable level of error. On the other hand, turbulent fluctuations in the segments should be relatively stationary to yield reliable spectra and structure functions, and to assume a turbulent frozen field which is measured during its advection. Our tests showed that a 34 minute segment is a good compromise between the two factors above which require opposite criteria.

6.2.1. Velocity spectra and the mean turbulent energy dissipation rate

Spectral analysis of the ADV data enables estimations of the dissipation rate to be obtained. However, the sensor geometry of ADV probes introduces noise into those components of the velocity normal to the transmitter beam. This is due to the fact that ADV velocity measurements are referred to as bistatic axes which are slanted away from the beam transmitter (angle $\alpha < 15^{o}$) with the motion parallel being more sensitive to the transmitter axis than to the transversal ones (Roget, 2013). Several studies have been shown that sensor noise follows a white-noise type behavior, flattening the velocity data at high frequencies (Nikora and Goring, 1998; Voulgaris and Trowbridge, 1998; Hendricks, 2001). These features were also observed in our measurements of the horizontal components along and across the mean flow; as shown in the previous work of Lozovatsky et al. (2008b). However, analysis of $w(t)$, the velocity component along the transmitter beam, revealed that for this component most of segments were not affected by noise. If affected, $w(t)$ data

were less noisy than the horizontal velocity components whose spectra flattened above low frequencies $f > 2-3$ Hz. So, only the $w(t)$ records were used for further analysis.

The mean dissipation rate $\tilde{\varepsilon}$ is evaluated through the spectrum of the transverse velocity component fluctuations , $E_w(k)$, with k the wave number expressed in cpm (Appendix A). Thus, $w(t)$ at each segment is transformed into the respective spatial series $w(x)$ using the Taylor's 'frozen turbulence' hypothesis (Monin and Yaglom, 1975). Turbulent velocity, w', corresponds to the fluctuations about the mean. In this case, averaging over time is equivalent to averaging over the segments sampled with the moving sensor. Taylor's hypothesis can be used if the rate of change in eddies is small compared to the time that it takes to pass the sensor and so the turbulence field can be thought of as frozen. Considering that eddies will evolve faster in a more intense turbulent field, Taylor's frozen hypothesis is roughly tested by the ratio between the standard deviation of the turbulent velocity, $rms(u')$, and the sensor velocity V. If the ratio $rms(u')/V < 0.025$, the turbulent field is considered as frozen. In the case presented here, the applicability of Taylor's hypothesis was tested by calculating the ratio $rms(w')/U$ for each segment and this never exceeded 2.5% at segments close to high and low tides (minimum advecting velocity) and mostly took values below 1%.

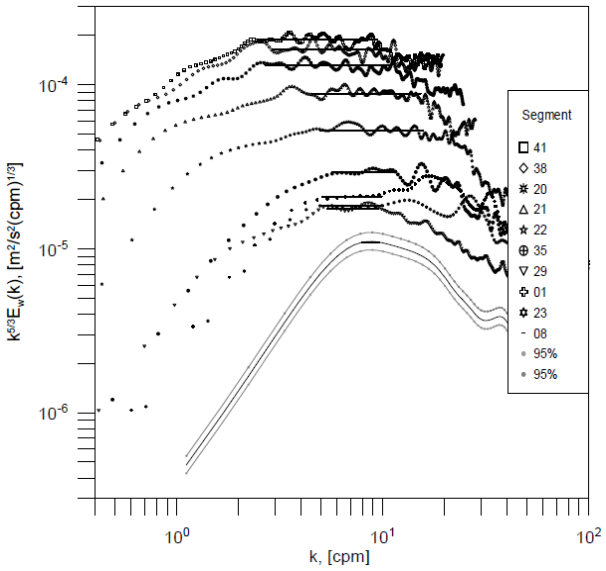

Fig. 6.3 Examples of compensated spectral densities $k^{-5/3}E_w(k)$. Horizontal lines depict inertial subranges. The 95% confident bounds (valid for every spectrum) are shown for the spectrum 8.

Fig. 6.3 shows the compensated spectrum $k^{-5/3}E_w(k)$ plotted as a function of the wave number k for each segment (Appendix A). Data were of high quality; thus, a despiking procedure was not applied and they were only detrended. The mean dissipation rate $\tilde{\varepsilon}$ was evaluated in the inertial subrange, which corresponds to the horizontal plateau in the graph. Four segments were excluded from the subsequent analysis because the inertial subrange was not clearly visible in the power spectral density plots (one of these is shown in Fig. 6.3).

6.2.2. The small-scale dissipation field

Estimations of the small-scale dissipation rate are required to resolve the small scales of turbulence (see Fig. 5.1). As ADVs sample small volumes, they are able to resolve small scales of turbulence under specific conditions (Durgesh et al., 2014), then, the first step is to investigate such conditions in our case. Taking in account that the Nyquist frequency of the ADV is f_N = 8 Hz, this is able to resolve small scales of about ~2 cm for slow currents of ~ 20 cm·s^{-1}. However, if the speed increases, the minimum spatial scale resolved by the ADV will also increase. Thus, this limits the range of the observed inertial subrange and then the calculation of the small-scale dissipation field.

In our measurements, the magnitude of the tidal current U varies over a range of between 3 and 45 cm·s^{-1} (see in Fig. 6.2) and ~ 60 % of the segments (28 segments) have speeds < 20 cm·s^{-1}. Based on this criterion, a set of 28 segments was accepted for continuing the analysis with.

The next step was to select those segments that allowed the small-scale dissipation rate field to be properly estimated. To do this, the peak of the maximum dissipation $\ell_{\nu\max}$ evaluated from the PK69 spectrum (Appendix A) was compared to the minimum length scale r_0 resolved by the ADV. $\ell_{\nu\max}$ was calculated from the Kolmogorov scale η_K using the mean dissipation rate $\tilde{\varepsilon}$ obtained in the previous subsection. Then, for values of $r_0 < \ell_{\nu\max}$ estimations

of $\tilde{\varepsilon}$ using the variance method do not require corrections for variance loss (Roget et al., 2006) and the small dissipation rate can be directly estimated from the velocity gradients. Based on this criteria, we accepted only those segments which had smallest spatial scales r_0 beyond the peak of maximum resolution $\ell_{\nu\max}$.

Analysis of our data shows that values of the mean dissipation rate $\tilde{\varepsilon}$ vary in a range of between 10^{-7} - 10^{-4} W·kg^{-1}. For values of $\tilde{\varepsilon}$ ~ 10^{-6} W·kg^{-1} and tidal currents of ~ 0.2 m·s^{-1}, the Kolmogorov scale η_K was about ~ 1.4 mm and $\ell_{\nu\max}$ ~ 6.5 cm. The Nyquist length scale resolved by the ADV was $k_{\min}$ ~ 2.5 cm (f_N = 8 Hz), which is about 2 - 3 times smaller than the spatial scale $\ell_{\nu\max}$. Then, if there is no noise at high frequencies, the instrument will resolve the small scales of turbulence beyond the peak of the spectrum. After inspecting the segment set, 26 segments were accepted so as to calculate the small-scale dissipation field.

Finally, we estimated the small-scale dissipation field as described in Appendix A. Briefly, ε was calculated from the small-scale gradients of the vertical velocity component as

$$\varepsilon = 7.5\nu\left(\frac{\Delta w}{\Delta x}\right)^2 = \frac{7.5\nu}{U^2}\left(\frac{\Delta w}{\Delta t}\right)^2 \tag{6.1}$$

Note that the assumption of Taylor's frozen hypothesis is required and which was satisfactorily tested previously in subsection 6.2.1. For those segments affected by noise data we averaged and resampled pairs of data points taken previous to application of (6.1).

6.2.3. Taylor microscale and microscale Reynolds turbulent number

The microscale λ_w and the turbulent Reynolds numbers $R_{\lambda w}$ are important parameters in order to characterize turbulence in the inertial subrange. The Taylor microscale λ_w is an intermediate length scale associated to the size of

the eddies in the inertial subrange, i.e. in which viscous forces affect the dynamics of the turbulent eddies in the flow. It is defined (Tennekes and Lumley, 1972) as

$$\lambda = \sqrt{\frac{\overline{(w')^2}}{\overline{(dw'/dx)^2}}} \tag{6.2}$$

Where $\overline{(w')^2}$ and $\overline{(dw'/dx)^2}$ are the variances of the velocities and the velocity gradients, respectively. If $rms(w')$ is the root-mean-square of the vertical velocity fluctuations, the turbulent Reynolds numbers $R_{\lambda w}$ is defined (Pope, 2000) as

$$R_\lambda = \frac{rms(w')\lambda}{\nu} \tag{6.3}$$

For the present measurements λ_w is of about ~ 2 - 4 cm and $R_{\lambda w}$ at the height of the boundary layer exhibit variations between ~ 50 and ~ 1100. Segments accepted after small-scale dissipation rate analysis are in a range of $R_{\lambda w} \in (80,310)$.

7. Results and Discussion on Internal Intermittency

7.1. Multifractal analysis based on the velocity field

7.1.1. Calculation of the structure functions

The structure function of the vertical velocity, also called transverse structure function (TSF), is calculated using (5.3) as

$$s^p(r) \equiv \left\langle \Delta w_r^p \right\rangle = \overline{[w(x+r)-w(x)]^p} \tag{7.1}$$

, where x is the along-flow distance and $r = n(U/f)$ the sampling interval in the x direction, U is the magnitude of the mean velocity in every segment, f the ADV sampling rate and n = 1, 2,… 32 determines the sampling interval r.

To study the segments, the Reynolds number was calculated using two definitions: the near-bottom Reynolds number Re_{nb} and the integral turbulent Reynolds number R_{int}. The near-bottom Reynolds Re_{nb} was calculated (Lozovatsky et al., 2008b) as

$$Re_{nb} = \frac{(\Delta U/h)\cdot L^2}{\nu} \tag{7.2}$$

, with ΔU the ADV velocity at h = 0.45 mab and L the characteristic scale in the layer ($L = \kappa d$ where d the thickness of the layer and κ the Von-Karman constant). Because it is specified by the mean flow velocity U, this allows periods of tidal flooding (high Re_{nb}) and ebbing (low Re_{nb}) to be identified. On the other hand, the integral Reynolds number R_{int} was determined with reference to the integral scale L_{int} (Chapter 6, see subsection 6.2.3) as

$$R_{int} = \frac{rms(w')L_{int}}{\nu} \tag{7.3}$$

where w' represents the fluctuations of the vertical velocity field. This is related to the energetics of tidal flow: high energetic tidal flow phases corresponds to

high R_{int} . Both Reynolds numbers exhibit almost the same behavior during the time period analyzed (as is shown in the global analysis presented in Fig. 7.1).

For the evaluation of $\zeta(p)$ (see (5.84)) the ESS method described in Chapter 5, subsection 5.3.1 has been used. Examples of $log\,S^3(r)$ against $log(r)$ (plotted in Fig. 7.1) allow the "+ 1" subrange to be identified, which is larger for segments where Reynolds numbers (Re_{nb} and Re_{int}) are also larger.

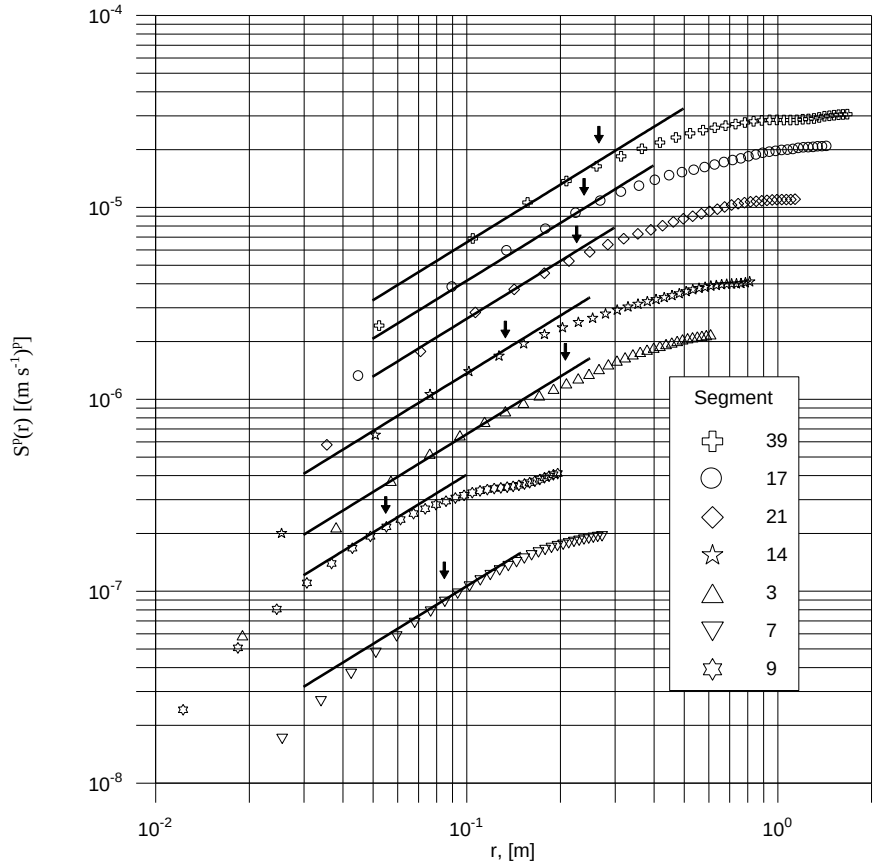

Fig. 7.1 The third-order transverse structure functions for several segments. The '+1' subranges are highlighted by bold lines. The arrows correspond to the turbulent integral scale $L_{int.}$

The scaling of $S^p(r)$ vs. $S^3(r)$ instead of *r*, was applied in the range $L_{\text{int}} > r > L_K$, where L_{int} is the integral turbulent scale and $L_K = c_{ds}\eta_K$ is the scale where the maximum rate of dissipation is reached (see in Chapter 5, 5.1.1).

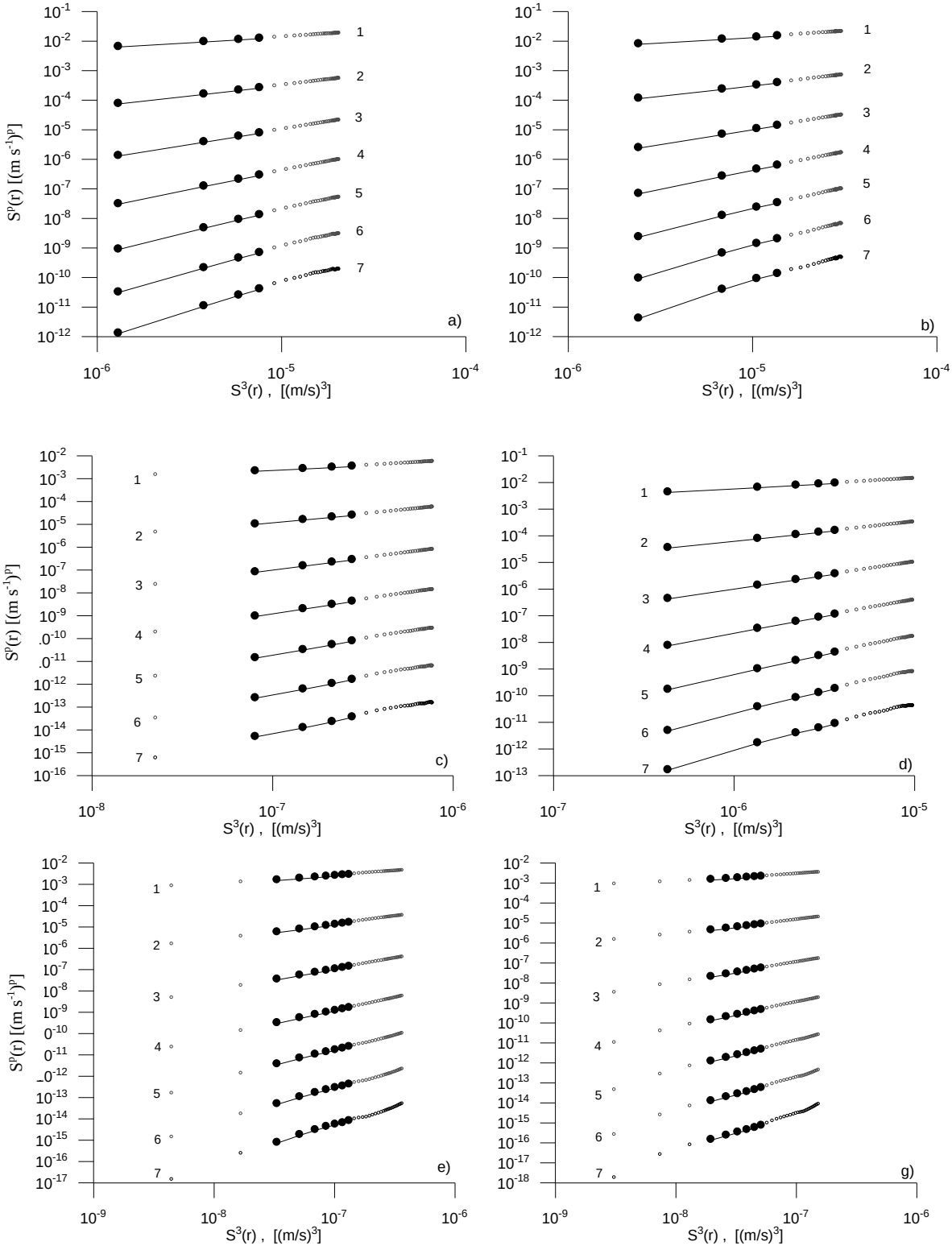

Fig. 7.2 Examples of TSF logarithmic plots showing $S^p(r)$ vs. $S^3(r)$ for high (a) 17 and (b) 39, (b) moderate (c) 35 and (d) 43 and low (e) 23 and (g) 33 Reynolds numbers . The well-fitted linear sections coincide with $L_{int} > r > L_K$ range, highlighted by solid circles.

An approximate match between L_{int} and the low-wave number end of the inertial subrange was attained with c_o = 0.6. In our case, we took an intermediate value of c_{ds} = 15 (Monin and Yaglom, 1975) to fit the $log\,S^p\left(log\,S^3\right)$ inside the inertial subrange (not necessarily covering all the scales r).

Our tests with high-order $S^p(r)$ ($p_{\max}$ = 14; $r_{\max}$ = $32\times U/\Delta f$) showed that a confident linear fit in the range $L_{int} > r > L_K$ can be applied to the plots of S^p vs. S^3 functions at almost all observational segments and bearing in mind that $p < 7 - 8$, see Fig. 7.2. Accordingly, to obtain confident scaling functions $\zeta(p)$ for different tidal phases, S^p for all segments were calculated using the absolute values of increments of vertical velocity $\left\langle\left|\Delta w_r^p\right|\right\rangle$ for $p = 1 - 7$. In

Fig. 7.2, solid dots indicate the range where the linear fit was adjusted in order to obtain the scaling exponents $\zeta(p)$. Note that final estimates of $S^p(r)$ at the largest separation scale $r_{\max}$ were obtained by averaging more than 1000 individual samples of Δw_r, ensuring a minimal statistical error of $S^p(r)$. Indeed, the error of the 7th order SF after averaging is equal to the error σ_w of an individual original sample of *w*, namely $7\sigma_w\sqrt{2/10^3} \approx \sigma_w$.

7.1.2. Intermittency parameters

After determination of the scaling exponents $\zeta(p)$, intermittency parameters from the best fit are estimated to intermittency models. Several examples of $\zeta(p)$ and their corresponding fits to multifractal and log-normal models (upper and lower panels, respectively) are shown in Fig. 7.3. The right panel represents those segments with the highest Re_{nb}. It can be seen that high orders $\zeta(p)>3$ are below the expected values without intermittency, i.e. $p/3$. For values of $\zeta(p)<3$, these are above the value of $p/3$. Curves cross the

value $\zeta(3)=1$. If Re_{nb} decreases, graphs also show a more pronounced departure from the classical value of $p/3$.

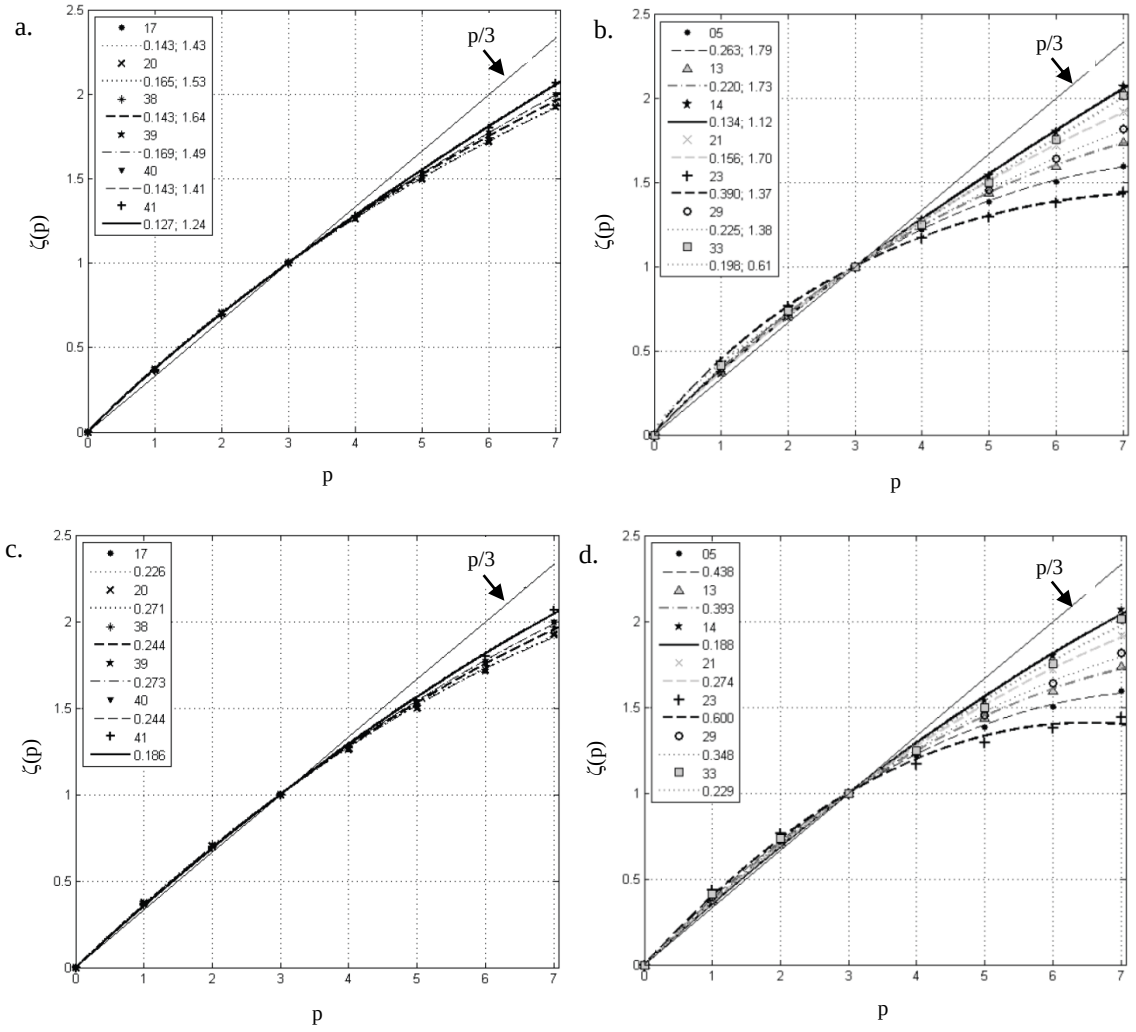

Fig. 7.3 Examples of the empirical scaling exponents for orders from 1 up to 7 in several segments (numbered in the inset) and their approximations with the multifractal (a,c) and the log-normal (b,d) models. The symbols show empirical results and the lines the fits to the model predictions. Best-fit values of models are given also in the insets.

The intermittent parameters C_1, α and μ are represented for the whole period of the experiments, in Fig. 7.4. Also in this same figure the near bottom and integral turbulent Reynolds numbers are presented. The intermittency parameters in the figure are shown with 95% confidence bounds. As observed in Fig. 7.4, the Reynolds numbers are mainly in phase with α and out of phase with C_1 and μ.

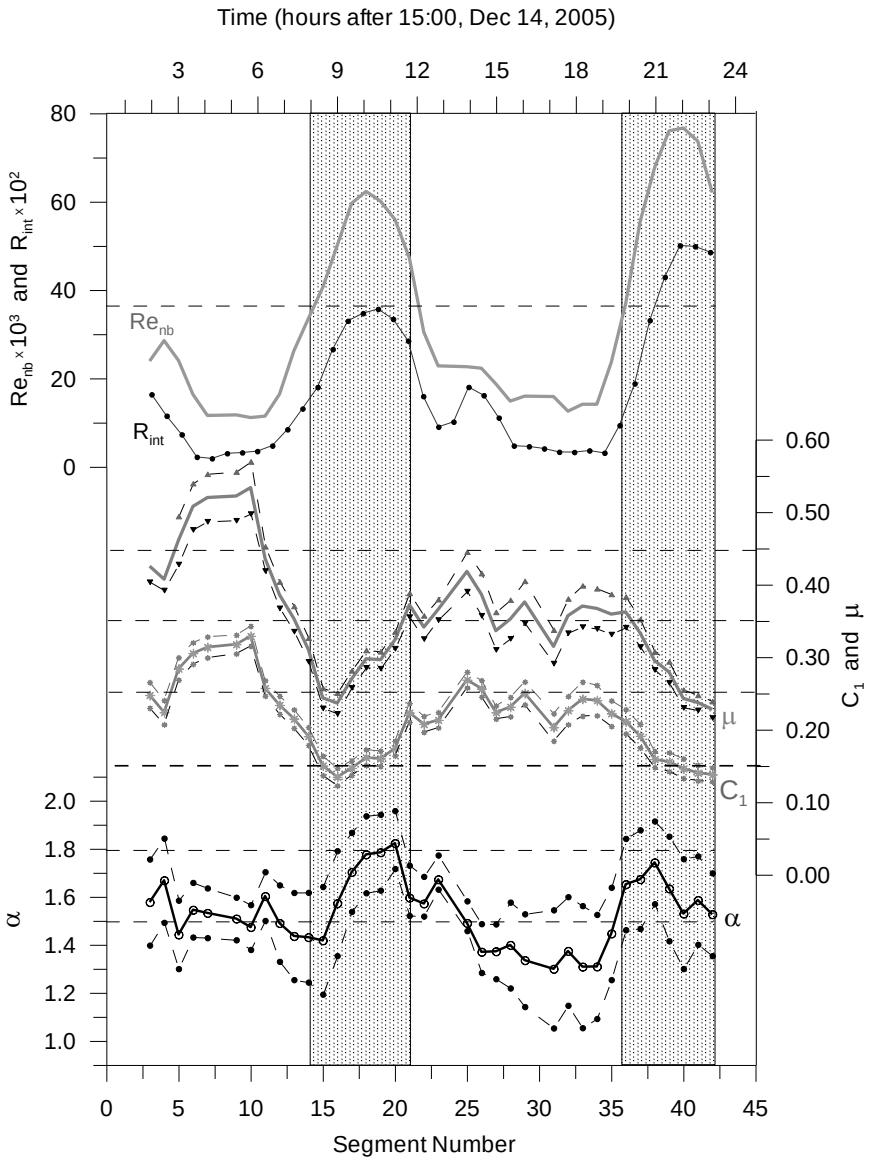

Fig. 7.4 Intermittency parameters obtained from multifractal model. The Reynolds numbers are in phase with α and out of phase with C_1 and μ. The intermittency parameters are shown with 95% of confidence bounds. Two periods of flooding along with highest Reynolds numbers recorded are highlighted.

7.1.3. Interpretation of the results

According to previous results, during energetic flooding tidal phases (high Reynolds numbers), the parameters of the intermittency models approached the mean values of $\tilde{\mu} \approx 0.24$, $\tilde{C}_1 \approx 0.15$, and $\tilde{\alpha} \approx 1.5$; all of which are close to those that have been obtained in the laboratory and are accepted as the

universal values for fully-developed turbulence, $\hat{C}_1 = 0.15$, $\hat{\alpha} = 1.5$ and $\hat{\mu} = 0.25$ (Sreenivasan and Kailasnath, 1993). With the decrease of advection velocity, μ and C_1 increased up to $\mu \approx 0.5$ - 0.6 and $C_1 \approx 0.25$ - 0.35, but α decreased to about 1.4.

These results can explain the reported disparities between the smaller universal values of the intermittency parameters μ and C_1 (mostly measured in laboratory and atmospheric high-Reynolds number flows) and those (μ = 0.4 - 0.5) reported for oceanic stratified turbulence in the pycnocline and which is associated with relatively low local Reynolds numbers.

7.2. Multifractal analysis based on trace moments

Determination of the intermittency parameters based on the multifractal analysis of ε is based on the 26 segments accepted (from the original 44) after the inspection of the small-scale dissipation rate described in Chapter 6, subsection 6.2.2.

7.2.1. Calculation of the trace moments

As described in the procedure detailed in Section 5.3, the trace moments of ε at its maximum achievable resolution r_0 should be computed in a predefined range, i.e. $r \in [r_0, L_0]$. A possible choice of L_0 is the integral scale L_{int} (see Fig. 7.3), which, as mentioned, is an estimation of the size of the largest turbulent eddies in the inertial subrange. The plots of the spectral densities shown in Fig. 6.3 support this option as commented below.

From the previous computation of the trace moments (as discussed in Chapter 5, subsection 5.3.2), we normalize the dissipation field using the average over all the subrecords. Then, we degrade (average) ε_λ^* to lower length r scales, i.e. $r_0 \le r \le L$ ($L_{\text{int}} \le L$).

In Fig. 7.5, the moments $M_p(r)$ for different values of p (p = 0.8, 0.9, 1.1 and 1.2) were calculated for moderate (Segment 44) and low (Segment 34) Re_{nb} and plotted as a function of r in a double logarithmic plot. They exhibit a good linear trend in a logarithmic scale for small values of r, while the slopes become flatter for larger scales thus, showing the possible presence of another scaling regime (energy-containing subrange). Similar behavior was also found by Lauren et al. (2001) in their work on multifractality for turbulent atmospheric surface-layer winds. Excluding the larger scales on the estimation of the scaling exponents, the corresponding linear regressions are drawn in Fig. 7.6.

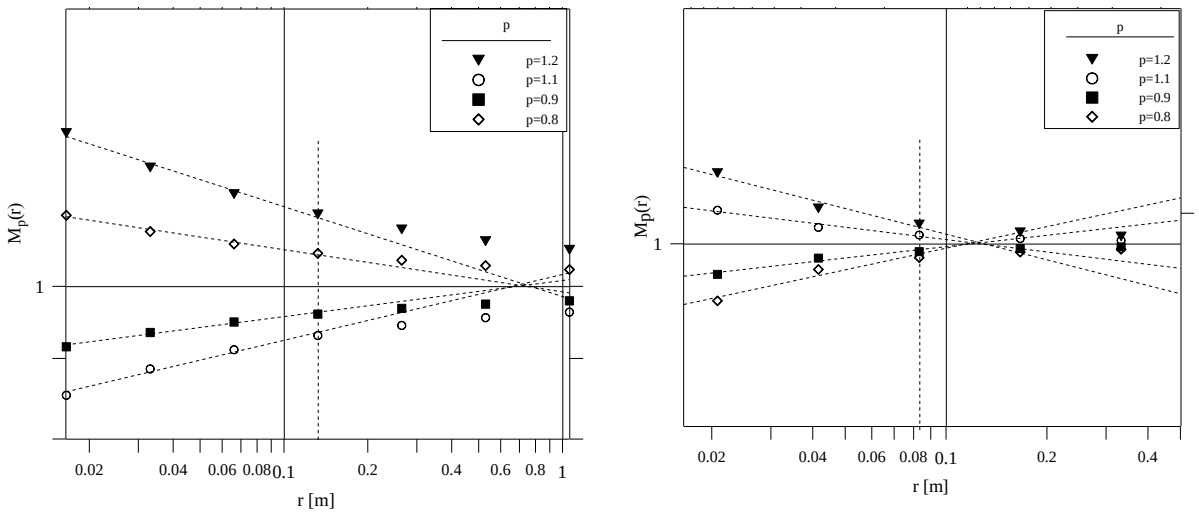

Fig. 7.5 Plots of the trace moments $M_p(r)$ of the normalized energy dissipation rate as a function of r for (a) Segment 44 and (b) Segment 34, and for p = 0.8, 0.9, 1.1 and 1.2. The scaling range is marked by a dotted vertical line. Best fitting lines in the scaling range are indicated by dashed lines.

For Segment 44 (Fig. 7.6a), the fitting range goes up to r_{max}=13.2 cm with R^2-values higher than 0.98. In Fig. 7.6b, the fitting range is very narrow (only three points), and moves up to 8.3 cm. In this case, R^2 > 0.95 and so, the estimations of the slopes would be subject to higher uncertainty. Adding one more point to the fit the value of R^2 substantially decreases, reaching close to 0.9, which could be indicative of a possible break in the scaling range. Values of

r_{max} are quite close to L_{int} as assumed at the beginning of this subsection. They also coincide with the upper bound observed in the velocity spectra shown in Fig. 6.3.

Length scales shown in Fig. 7.6, indicate that ranges normalized by the Kolmogorov scale η_K, $r^* = r/\eta_K$ extend over a range of $20 \le r^* \le 165$ and $20 \le r^* \le 82$ for segments 44 and 34, respectively. They agree well with the small scaling ranges found in different works on intermittency for relatively low Reynolds numbers and based on experimental data and numerical simulations (Watanabe and Gotoh, 2004; Zhou et al., 2005; Hao et al., 2008; Almalkie and Bruyn Kops, 2012). Meneveau and Sreevinasan (1991) reported larger scale ratios of r^* (from $r^* \sim 30$ up to $r^* \sim 300$) for higher Reynolds numbers in the atmospheric surface layer.

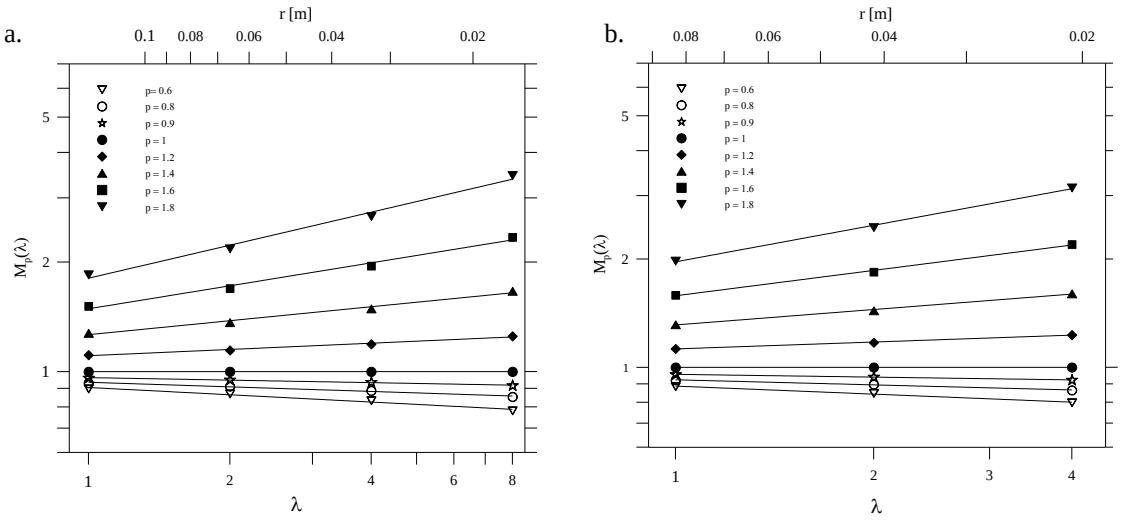

Fig. 7.6 Logarithmic plots of the trace moments $M_p(\lambda)$ against the scale ratio λ (lower panel; horizontal axis) and within the scaling range for λ. Also the scaling range r in meters is presented in upper horizontal axis. The trace moments $M_p(\lambda)$ have been plotted for (a) Segment 44 and (b) Segment 34, and for p = 0.6, 0.8, 0.9, 1, 1.2, 1.4, 1.6 and 1.8. Best power-law fittings are indicated by solid lines.

Although the small number of points in the scaling range of our data, there are several works which successfully apply the trace moment techniques with the same number of points in the scale as we do in our work (Pecknold et al., 2001; Vidal-Vazquez et al., 2010; Gheidari et al., 2011). Further, in our case

data series are averaged over quite a large number of ensembles (~ 8000 points for $r_{\max}$) and we can be confident about the estimations of the scaling exponents $K(p)$.

Small scaling ranges impose a critical limitation on the multifractal analysis of turbulence. This can be improved by averaging over a large number of ensembles. Also in Sanchez-Martin et al. (2014, submitted) we have suggested the possibility of using overlapping subsegments. This is another possible option to increase the number of points in the fitting as the range over scales would not vary so much and in turn the value of the slope obtained from both cases, would not differ substantially.

According to previous discussion, we applied the TM and DTM methods to the range $r \in [r_0, L_{\text{int}}]$. Fig. 7.6 shows several examples of trace moments of ε_λ^* in the range $r_0 \le r \le L_{\text{int}}$ for segments 44 and 34. The field is degraded within subrecords A of length Λ over λ, varying from $\lambda = 1$ to $\lambda = \Lambda$, i.e. $r_0 \le r \le L_{\text{int}}$. In the upper axis we have represented the length scaling range r (in meters) and the lower axis is the corresponding scale ratio λ. They have both been plotted for eight different values of p, with p being between 0.4 to 2. For all the segments the scaling ranges are small. They typically have four points, with $1 \le \lambda \le 8$, but even fewer, only three points, with $1 \le \lambda \le 4$, in several cases. This is the case for Segment 34 for example, which has a maximum value of r of ~ 8.5 cm.

In the Fig. 7.7 and following the same criteria for the range (see Chapter 5, subsection 5.3.2), the double-traced moments $M_{p,\eta}(\lambda)$ are plotted vs. the corresponding scales r or λ (upper or lower x-axis), in the same interval as the trace moments $M_p(\lambda)$. Note that unique trace moments correspond to $M_{p,\eta}(\lambda)$ for $\eta = 1$. We show the power-law fits for $\eta = 0.8$ and $\eta = 1.2$, for segments 44 (Fig. 7.7 a, b) and 34 (Fig. 7.7 c, d). The values of the first-order moment p are included in the top left-hand corner of the graph. Both fits have $R^2 > 0.98$.

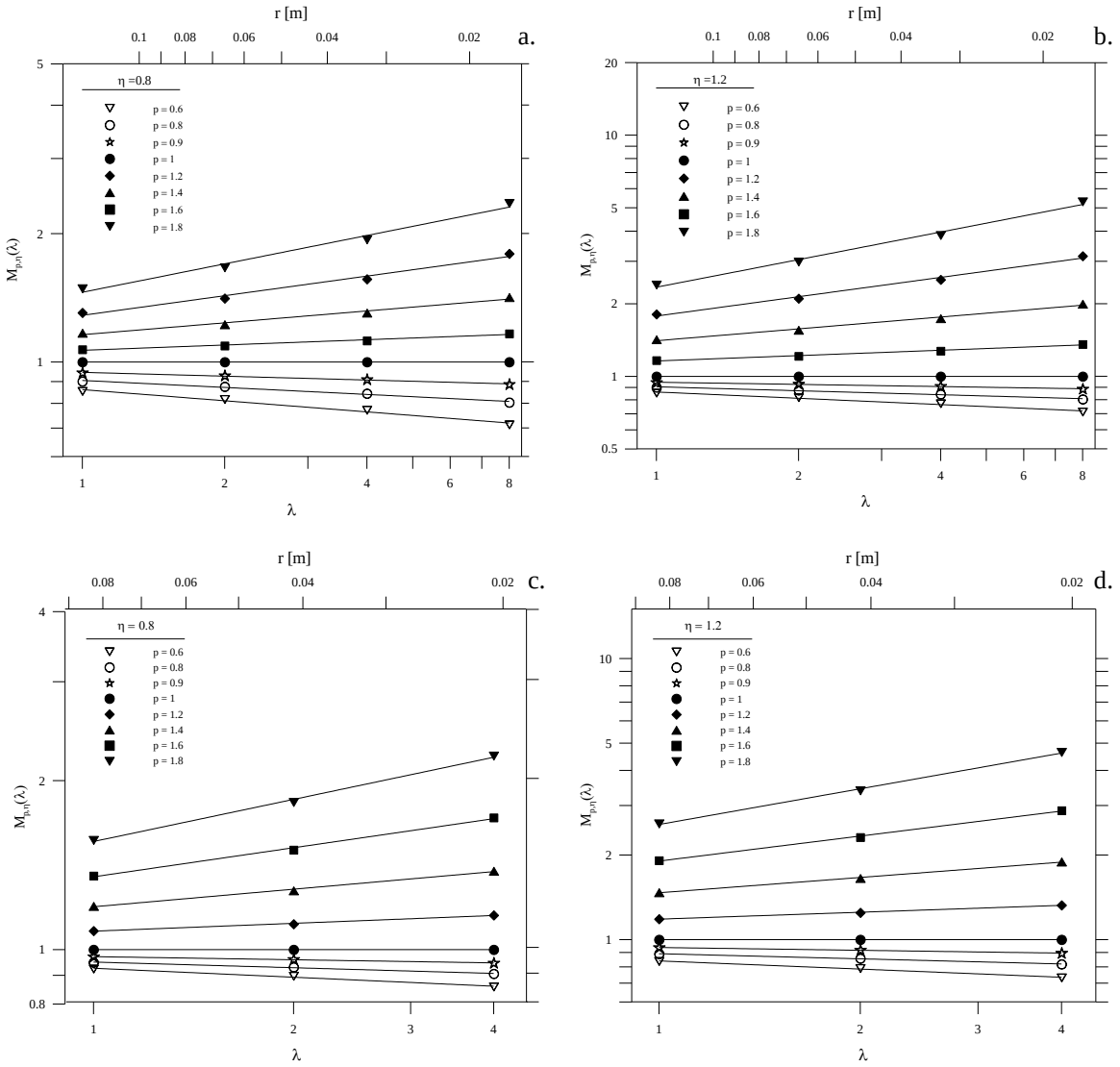

Fig. 7.7 Logarithmic plots of $M_{p,\eta}(\lambda)$ against the scale ratio λ (lower panel; horizontal axis) and within the scaling range for λ . Also the scaling range r (in m) is presented on the upper horizontal axis (upper panel). The trace moments $M_{p,\eta}(\lambda)$ has been plotted for (a,b) Segment 44 and (c,d) Segment 34, for different values of η = 0.8 and 1.2 (indicated on the left side of each figure) and also for p = 0.6, 0.8, 0.9, 1, 1.2, 1.4, 1.6 and 1.8. Best power-law fittings are indicated by solid lines.

7.2.2. Intermittency parameters

The empirical functions obtained for $K(p)$ in previous sections, are plotted in Fig. 7.8 and fitted to the best linear curve using the toolbox available on Matlab software. The functions exhibit a non-linear behavior up to critical values of $p_{crit} \sim 2-2.5$; for segment 44, $p_{crit} = 2.5$ and for segment 34, $p_{crit} = 2.1$. This critical value indicates the existence of multifractal phase transitions (p_s or

p_D) as it was described in Chapter 5, subsection 5.2.3.3; it is addressed in the next subsection.

Best fittings to a universal multifractal model allow intermittency parameters C_1 and α to be estimated; the goodness-of-fit has values of R^2 > 0.999. Taking all the selected segments, the mean value of the intermittency parameters and its root-mean-square boundaries are $\widetilde{C}_1 = 0.26 \pm 0.02$, $\widetilde{\alpha} = 1.46 \pm 0.05$ and $\widetilde{\mu} = 0.42 \pm 0.03$. Although $\widetilde{\alpha}$ is slightly lower than that obtained using the SF method, the obtained values of $\widetilde{C}_1$ and $\widetilde{\mu}$ are higher than those predicted for the multifractal model. However, it is important to recall here that we have analyzed not all the set of subsegments available, just only those with $R_{\lambda w} \in (80,310)$.

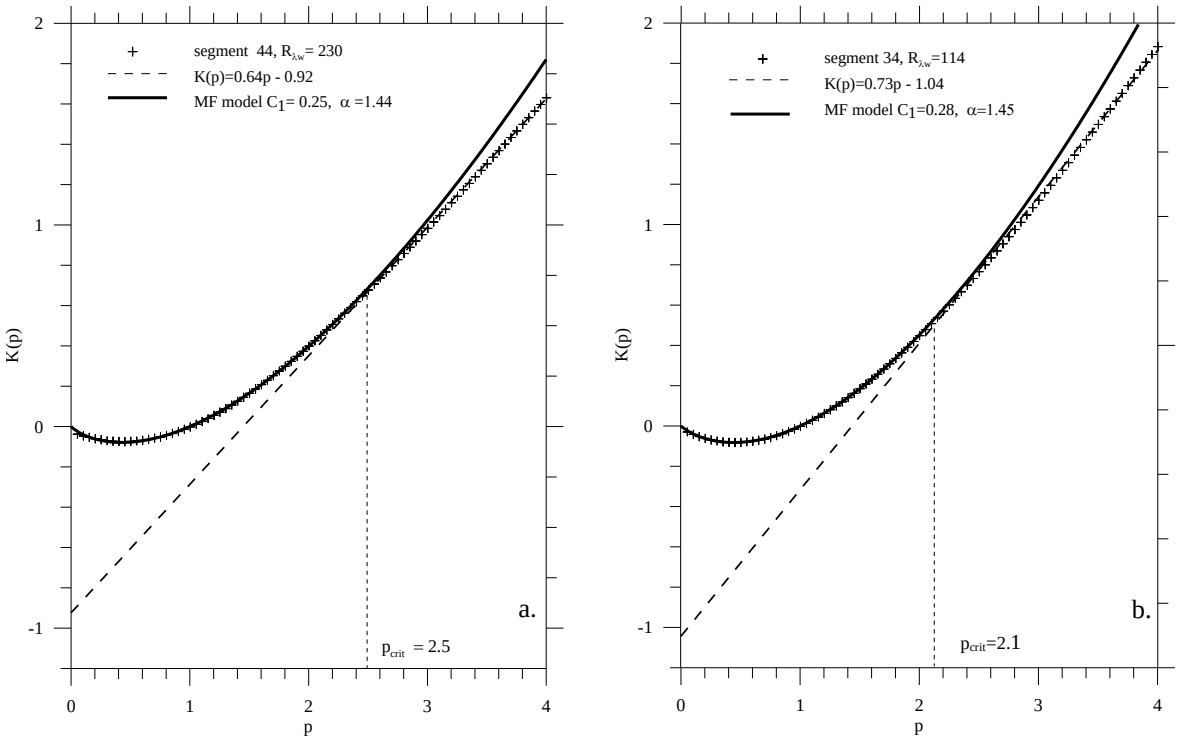

Fig. 7.8 Scaling exponents $K(p)$ function for $M_p(\lambda)$ (a) for moderate (44) and (b) low (34) values of $R_{\lambda w}$ .Best fits to the multifractal model are displayed at the top. Theoretical and empirical curves are in agreement up to $p = p_{crit}$. For larger moments, spurious linear behavior for $K(p)$ is observed (multifractal phase transitions).

Alternatively, the values of the intermittency parameters are also evaluated using the DTM method. We chose the same values of p (first-order moment) as those used in the TM method and $\eta \in [0.2,3]$ for that of the second-order. For each segment, the scaling exponents $|K(p,\eta)|$ of $M_{p,\eta}(\lambda)$ are represented in a logarithmic plot as a function of η. Plots in Fig. 7.9 display the characteristic 'S' shape described in Chapter 5 (subsection 5.3.2): for each value of p, the functions of the scaling exponents flatten out for small and high values of η.

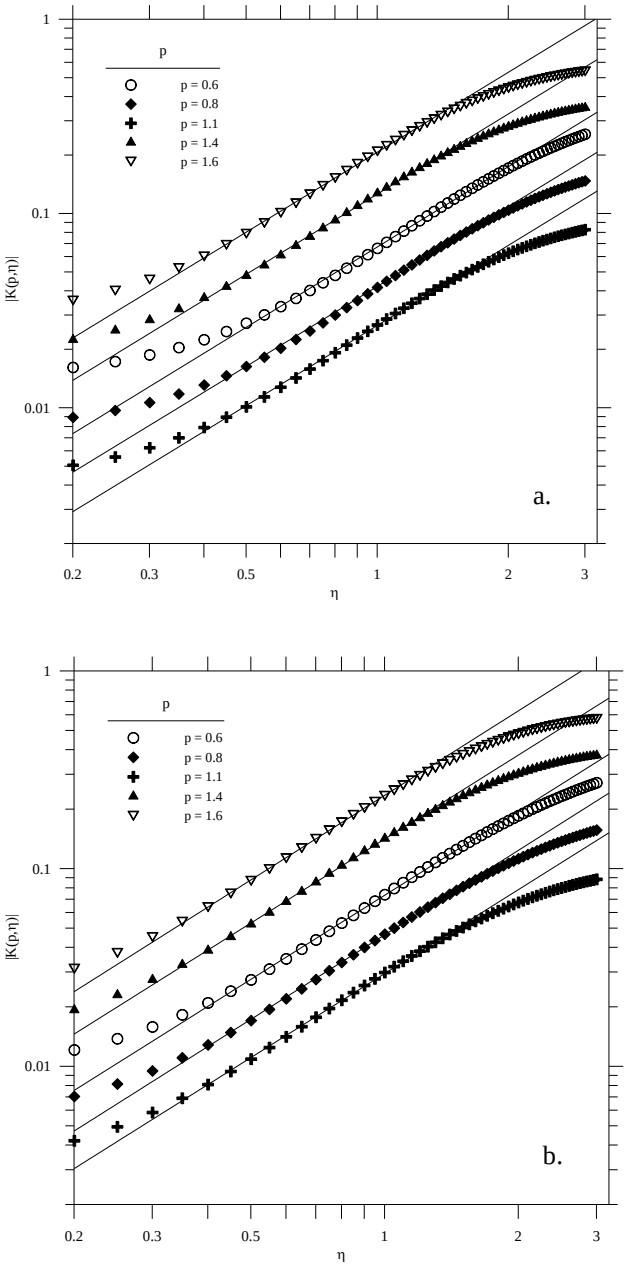

Fig. 7.9 Scaling exponents of the double-traced moments $K(p,\eta)$ against η for p = 0.6, 0.8, 1.1, 1.4 and 1.6. Note the flattening for high and low η. Power-law fits are shown in the figure.

The break in the linearity for small η can be explained by the influence of noise: recall that the original data series has only been resampled in pairs when high-frequency noise was clearly visible. Thus, it is most likely that the presence of noise at highest frequencies affects the non-filtered original records and also those others which resampling failed to eliminate. On the other hand, the

deviation of the scaling exponents $|K_d(p,\eta)|$ observed at high η are related to multifractal transitions.

The central sections of the plots show linear trends, which are almost parallels and can be expressed as (5.98)

$$\log|K(p,\eta)| = \alpha \log(\eta) + \log|K(p)| \tag{7.4}$$

Previous to power-law fitting (that it is linear in logarithmic scale), we exclude high and small η where the behavior is non linear and then evaluate the slopes at $\eta_{p=1}$ in a large enough segment of nearest discretized η values with $R^2 > 0.999$ (we take 10 points for the fitting). The set of slopes gives the mean value and rms boundaries of the parameter α. For the examples given in Fig. 7.9, we obtain $\alpha = 1.46 \pm 0.02$ for Segment 44 and $\alpha = 1.47 \pm 0.02$ for Segment 34. Note that these values are practically the same, albeit a little bit higher, as obtained with the TM method and they fall within the interval defined by the standard deviation.

To estimate the value of the codimension parameter C_1, we compute the *y*-intercept for each of the fits with

$$C_1 = \frac{|K(p,\eta)|(\alpha - 1)}{p^{\alpha} - p} \tag{7.5}$$

As an example, for Segment 44 we obtain $C_1 = 0.25 \pm 0.02$ and for Segment 34, $C_1 = 0.28 \pm 0.02$. The mean value of the intermittency parameters for all the possible subrecords is $\tilde{C}_1 \approx 0.26 \pm 0.02$, $\tilde{\alpha} \approx 1.45 \pm 0.05$ and $\tilde{\mu} \approx 0.43 \pm 0.04$. These values agree very well with those obtained the TM method, which indicates their robustness.

For atmospheric flows, Sreenivasan and Kailashnath (1993) also analyzed the intermittency of the turbulent dissipation field. Data were obtained from high-frequency anemometers, which were able to capture most of the small-scale velocity fluctuations. At high R_λ (between 1500-2000), they suggested a universal value of $\hat{\mu} = 0.25 \pm 0.05$ and which has been corroborated by results obtained in laboratory experiments and numerical simulations (Chen et al.,

1997, Cleve et al., 2004, Zhou et al., 2005). Our results for $\widetilde{C}_1$ and $\tilde{\mu}$ depart considerably from the expected universal intermittency exponent $\hat{\mu}$. However, in stratified ocean turbulence, R_λ are mostly less than those found in the atmosphere and this could affect the value of $\hat{\mu}$. In fact, several works have reported higher values of μ, μ ~0.4-0.5 in the ocean (e.g. Wijesekera et al., 1993; Gibson, 1998).

7.2.3. Multifractal phase transitions

As it has been described previously, the linear behavior exhibited by $K(p)$ for $p > p_{crit}$ in Fig. 7.8, indicates the presence of multifractal phase transitions. In that case, Then, the value of the critical order p_{crit} (p_s or p_D) is the order at which $K(p)$ shows a spurious linear behavior. Best fits for the $K(p)$ curve in Fig. 7.8 give critical points $(p_{crit}, K(p_{crit}))$ for segments 44 and 34 of (2.5, 0.68) and (2.1, 0.51), respectively.

The slopes of the linear section of $K(p)$ allow the value of the singularity γ_{crit} associated with $\gamma_{\max}$ (second-order phase transition) or γ_D (first-order phase transition) to be estimated. The *y*-intercept of the line is related to its codimension, i.e. $-c(\gamma_{crit})$. Linear fit equations, with their R^2-value, are shown in the graphs (Fig. 7.8). We obtain values for the maximum singularities γ_{crit} of ~ 0.64 and ~ 0.73 and for their respective codimensions $c(\gamma_{crit})$ ~ 0.92 and ~ 1.04. Note the values of $c(\gamma_{crit})$ are very close to the topological dimension of the space, which is one-dimensional, indicating that energy is concentrated in very small regions, i.e. the fractal dimension is $D \approx 0$ and codimension $c \approx 1$.

In our case small scales have been resolved and it seems reasonable to think that the only restriction for γ_{crit} is the sampling size of the sample. To corroborate this assumption we have estimated the values of p_{crit} in the case of sample size limitations (p_s, second-order phase transition) or divergence of the

moments (p_D , first-order phase transition). The maximum reachable critical orders p_s and p_D for phase transitions (see Chapter 5, subsection 5.2.3.3) are

$$p_s = \left(\frac{c(\gamma_{\max})}{C_1} \right)^{\frac{1}{\alpha}} \tag{7.6}$$

and

$$D = \frac{K(p_D)}{p_D - 1} \tag{7.7}$$

which gives p_s ~ 2.6, p_D ~ 8.06 for Segment 44 and p_s ~ 2.4, p_D ~ 6.57 for Segment 34. Note that, estimations of p_s are in agreement with those obtained from the best fitting curve of the scaling exponents $K(p)$. These values are smaller than the moment critical orders p_D . Thus, we conclude that the linear behavior of the moment scaling function can be explained by the finite size of the sample.

7.3. Dependence on the turbulent Reynolds number

The data contains turbulent episodes with different intensity depending on in the phase of tidal flow. This allows to analyze the variability of the intermittency parameters, depending on the characteristics of the flow instead of using their mean values. The parameters of μ , C_1 and α will be plotted as a function of the turbulent Reynolds number $R_{\lambda w}$. Recall that for the estimations using structure functions, the analysis is directly applied to the transverse velocity field; for trace moment methods, it is applied to the dissipation field constructed from the transverse velocity component under isotropy assumption. To facilitate further discussion, plots have been shown in two separate figures, Fig. 7.10 (SF method) and Fig. 7.11 (DTM method). In Fig. 7.10, the range of $R_{\lambda w}$ is large, up to values of $R_{\lambda w}$ ~1000; whereas this is not the case of Fig. 7.11, with maximum values of $R_{\lambda w}$ of about ~300.

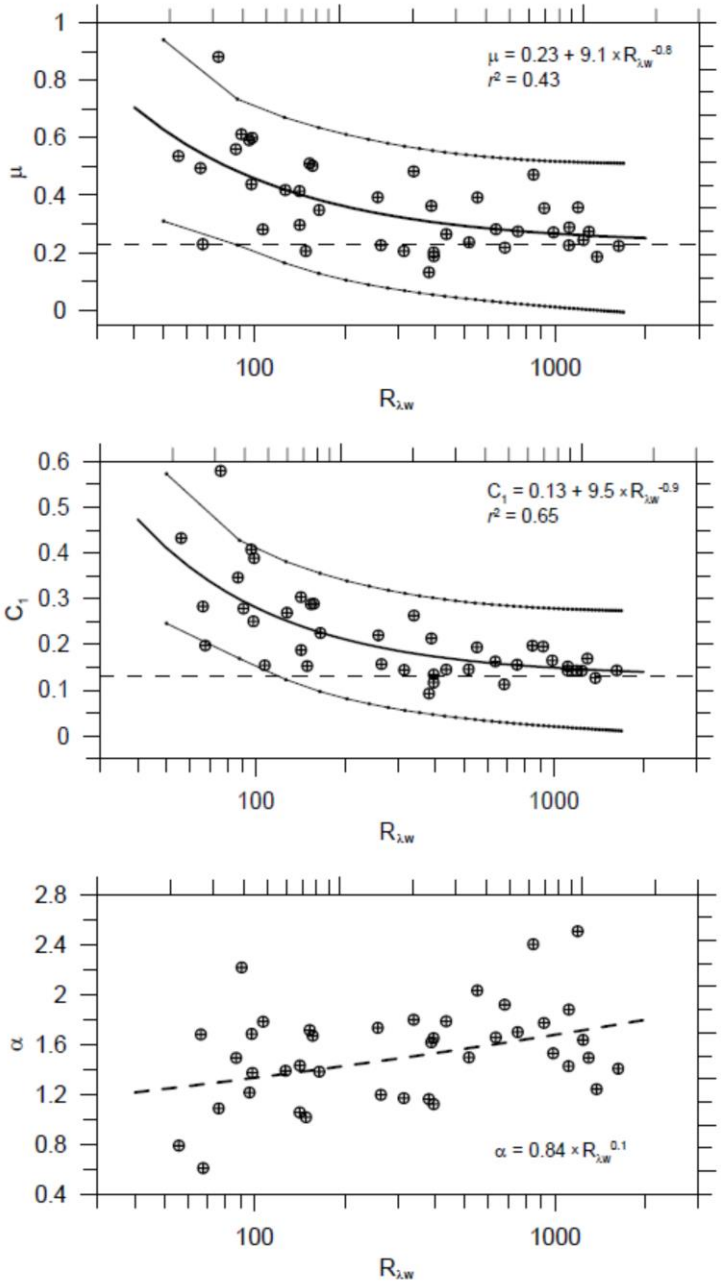

Fig. 7.10 The dependencies of intermittency parameters μ, C_1 and α on the local turbulent Reynolds number $R_{\lambda w}$. The least-squared fits with 95% lower and upper confident bounds for μ and C_1 are shown.

From the plots, μ and C_1 show a tendency to increase as $R_{\lambda w}$ decreases. Points have been fitted to power functions with corresponding equations and R^2-values inserted in the plot. In Fig. 7.11 the values of $R_{\lambda w}$ are not high, but the points fit well to a power law with high correlation between intermittency parameters and $R_{\lambda w}$. Thus, we assume that the same trend holds for high values

of $R_{\lambda w}$ (>300). The dotted lines marked in Fig 7.10a,b and Fig. 7.11a,b indicate the asymptotic values for $\mu(R_{\lambda w})$ and $C_1(R_{\lambda w})$ dependencies.

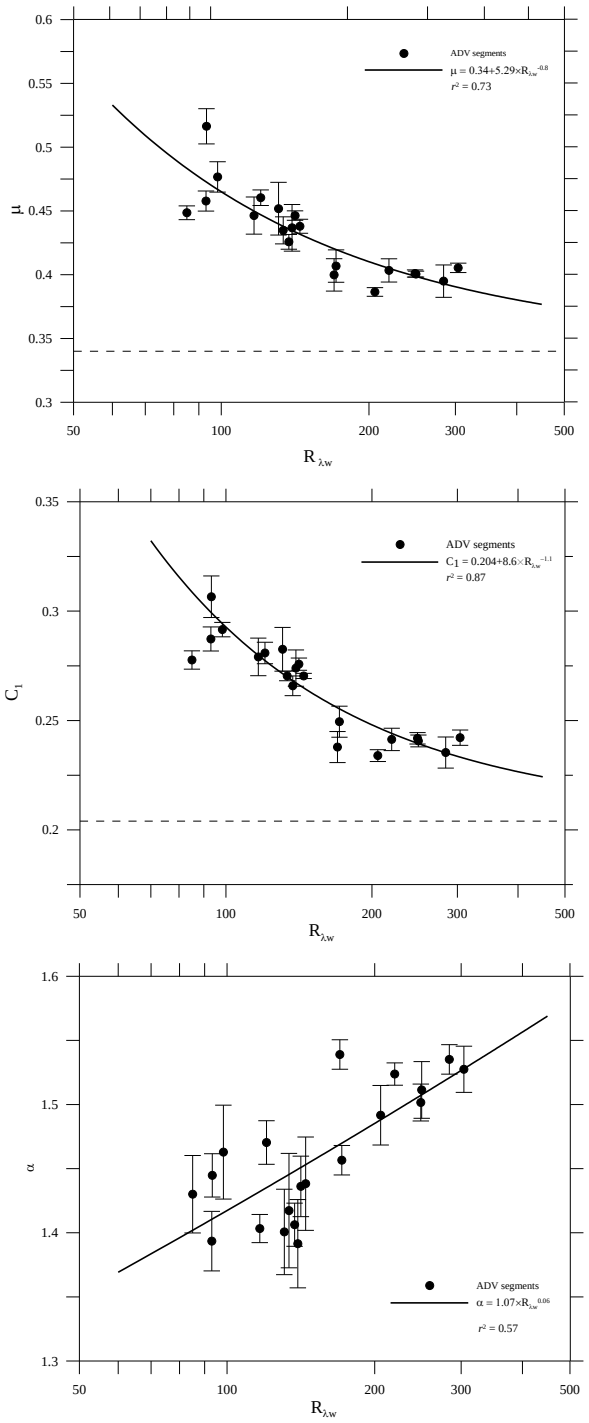

Fig. 7.11 The dependencies of intermittency parameters μ, C_1 and α on the local turbulent Reynolds number $R_{\lambda w}$ based on the multifractal analysis (DTM method) of the dissipation field, under isotropic assumptions.. Best curve (linear) fits are shown (solid lines) and their equations are given in the figure. Error bars correspond to the rms boundaries for each value.

The best fitted curves for empirical data obtained from SF analysis is shown next

$$C_1 = 0.13 + 9.1 \cdot R_{\lambda w}^{-0.9},\ \alpha = 0.84 \cdot R_{\lambda w}^{0.08} \text{ and } \mu = 0.23 + 9.05 \cdot R_{\lambda w}^{-0.8} \quad (7.8)$$

,while those obtained from DTM method are

$$C_1 = 0.20 + 8.6 \cdot R_{\lambda w}^{-1.1},\ \alpha = 1.07 \cdot R_{\lambda w}^{0.06} \text{ and } \mu = 0.34 + 5.29 \cdot R_{\lambda w}^{-0.8} \quad (7.9)$$

Moreover, the exponents of the power laws for μ, C_1 and α obtained from (7.8) and (7.9) are similar for both the SF and DTM methods. Thus, these results suggest a possible influence of the turbulent Reynolds number on C_1 and μ.

From , it can be seen that asymptotic values of the curves are attained for $R_{\lambda w}$>500-700 with $\mu^0 = 0.23$ and $C_1^0 = 0.13$. Both curves show a dependence of μ and C_1 on $R_{\lambda w}$, but it is statistically insignificant for α. The obtained estimates are close to the expected universal values $\hat{C}_1$ and $\hat{\mu}$. The value of α^0 was estimated as ~1.5 (Seuront et al., 2005), which approximates well to the mean value of $\tilde{\alpha}$ for high energetic segments. On the other hand, in Fig. 7.11, asymptotic values can be approximated by their values $C_{1\varepsilon}^0 = 0.20$ and $\mu_\varepsilon^0 = 0.34$, which are higher than those obtained from the analysis with structure functions. Lauren et al., (2001) found that $\alpha \approx 2$, $C_1 \approx 0.15$, $\mu \approx 0.3$ when analyzing the dissipation field ε from the isotropic approximation. However, these differ from other values obtained for the analysis of ε for well developed turbulence in the atmosphere (Schmitt et al., 1992, Schmitt,t et al., 1993, Chiriginskaya et al., 1994) and they gave $C_1 \approx 0.25-0.3$, $\alpha \approx 1.35-1.5$ and $\mu \approx 0.4-0.5$. Discrepancies may be related to the method used to reconstruct the field. In this latter case, these works reconstruct the turbulent dissipation field using fractional derivatives and taking absolute values (because the data had coarse spatial resolution) instead of using squares of the velocity gradients, as we did. Furthermore, Lauren et al. (2001) uses the squares ($\varepsilon \sim (\partial u/\partial x)^2$) in their estimations of the small-scale dissipation field and so the differences observed in our results may be attributed to small range in $R_{\lambda w}$. Note also that

ocean turbulence is usually not completely developed and consequently it is difficult to achieve very high values of $R_{\lambda w}$.

In order to compare intermittency parameters found in our study, we address to Hao et al. (2008), who extensively analyzed the scaling exponents for transverse and longitudinal structure and also for the energy dissipation field using different assumptions. The authors analyzed the turbulent velocity field in the centerline of a wake generated by a cylinder in a wind tunnel for different R_λ between 120 and 320. Hao et al. (2008) showed that the scaling exponents $K(p)$ of the moments calculated using the full expression of the dissipation field ε_0 are nearly constant ($\mu \sim 0.18$). However, a decreasing trend of $K(p)$ with the increase in R_λ was observed for the dissipation rate calculated using isotropic approximation; the authors found μ_ε~0.3 at R_λ~300 which is consistent with previous results from Zhou et al. (2005). In our case, we observe a similar trend for μ as Hao et al. (2008), but with values a little bit higher (μ_ε ~0.4 at R_λ~300). The decrease of μ with the increase of R_λ has been also found in the work of Almalkie and Bruyn Kops (2012) who analyzed intermittency using numerical simulation of ε_0. For low R_λ, the behavior of the intermittent exponent was $\mu_\varepsilon \sim 0.5$ for R_λ~250, in other words, close to that obtained in our work. It appears that transverse velocity component is more intermittent than longitudinal velocity.

We have also analyzed the intermittency of the dissipation field estimated from the transverse shear in Sanchez-Martin et al. (2014, submitted), with an ascending microstructure profiler in upper ocean. The results also suggested a possible dependency of the intermittent parameters on R_λ. In Fig. 7.12, we have plotted their bin-averaged results of $\mu_\varepsilon(R_{\lambda w})$ and their rms boundaries jointly with our results. Despite the high scatter of the data, the values of μ_ε fit quite well to our results and also agree with the characteristic values for ocean turbulence.

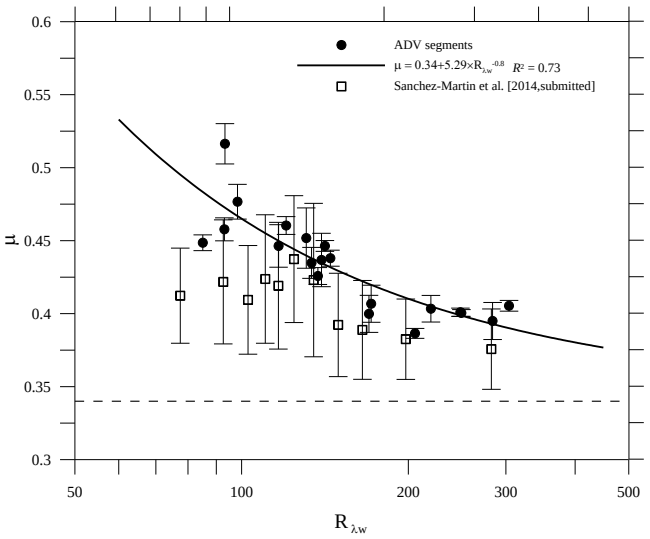

Fig. 7.12 Comparison of the results for the intermittency parameter μ obtained from ADV and a vertical microstructure profiler. Best curve fit of the results for our work is also plotted in the figure and its equation and R^2-value shown on the top. For microstructure profiler results, error bars indicate the rms boundaries of the values of the bin-averaged value of μ.

8. Conclusions

The aim of this work has been to investigate the intermittent behavior of turbulence in natural waters and is based on measurements obtained in two specific geophysical environments: the thermocline of a small stratified lake and the bottom boundary layer in a tidal flow. By using these two datasets, it has been possible to describe the phenomenon in its global sense, which includes the two different views of intermittency, i.e. external and internal intermittency.

This chapter summarizes the main points from our study and concludes the work. Possible future research directions are also presented in the final subsection of the chapter.

8.1. Analysis of external intermittency

- External intermittency has been analyzed in a stratified shear flow under low winds. We carried out a field campaign in Lake Banyoles using a microstructure free-falling profiler equipped with precision and fast response CTD sensors and a small-scale shear probe. The water column shows the characteristic three-layered profile where there is the: surface layer in the upper part, which extended from the surface to a maximum depth at which N^2, sharply exceeds 10^{-3} s^{-2} and, depending on the atmospheric forcing prior to and during the observations, results in a thickness of ~2.5 - 4.5 m. Below this is the thermocline, a strongly stratified layer ($N^2 \sim 10^{-2}$ s^{-2}) which occupies ~35 % - 55% of the water column. Finally, in the deepest part, there was the bottom layer, which was a weakly-stratified layer ($10^{-5} \leq N^2 \leq 10^{-3}$ s^{-2}).

- An internal seiche field with a dominant second vertical mode was identified in the lake. Vertical displacements of the thermocline showed that this mode oscillated in different phases depending on the day of

measurements. This mode was also reproduced using a numerical model.

- The 'seiche Richardson number' Ri has been computed at 15-min time intervals using the vertical profiles of the simulated horizontal velocity and the background stratification. The results have shown that the local vertical shear of the seiche field in the upper and lower part of the boundaries of the thermocline was strong enough to cause instabilities and generate turbulent patches.

- A new methodology to identify turbulent patches was adopted. Patches were detected based on the standard computation of the Thorpe displacements profiles and also by monitoring the microstructure shear signal. Initially, profiles of small-scale shear were visually inspected together with the corresponding Thorpe displacement profiles to determine whether the consecutive overturns belong to the same structure or not. In our study, we concluded that segments separated by distances less than 6 cm formed part of the same patch.

  To avoid any noise effects when detecting the real overturns, a run-length test was implemented in the Thorpe displacements profiles. The root-mean-square (rms) of the run length r of Thorpe displacements obtained from linear profiles with added random noise is used as a safety margin in the PDFs of experimental run-lengths to be accepted as patches. The value of r was obtained from the plots of the scaled noise amplitude Q, defined as $Q = \delta T / (dT/dz) h_p$, as a function of the number of points n in each overturn. The r value was determined to be of r=1.2 and was used to estimate the smallest thickness of detectable patches.

  Instrumental resolution also imposes a constraint on the identification of turbulent patches. Consequently, segments with $L_{Tp\min} > 2g\alpha\delta T / N^2$ were selected as real overturns. In our analysis, and due to limitations in

the vertical and temperature resolutions, only those patches with a thickness of h_p > 4 cm and Thorpe scales L_{Tp} > 4 cm were accepted as turbulent patches.

The method detected 880 patches with 512 of them being considered acceptable. From the total number of accepted patches, 283 patches had a thickness of h_p > 25 cm, which is the minimum width needed to estimate the turbulent energy dissipation rate in a patch.

- Locations and sizes of turbulent patches correlated well with the patterns of the dissipation rate ε evaluated in 0.5-m segments during the observation period. Highly energetic turbulent regions with highest $\varepsilon \approx 10^{-6}$ W·kg^{-1} were observed in the interior across almost the entire water column. Although the field campaign was performed under light winds (breeze regime), these events were associated with episodic powerful wind gusts lasting only a few minutes (speeds exceeding 6 m·s^{-1} and up to 15 m·s^{-1}). These gusts transferred ~ 1.6% of the wind energy to the surface mixed layer and ~ 0.7% to the stratified water interior, generating large (with h_p sometimes reaching several meters) but rare microstructure patches in the bottom layer. Wind gusting possibly generates strong horizontal fluctuations of pressure that induce short-lived strong horizontal and vertical shear instabilities that stir and mix the water interior. However, gust events have been disregarded for the patch analysis of turbulence under a low wind regime.

- Microstructure patches were detected across the entire water column. However, statistical analysis has been focused on the thermocline far from the boundaries, where turbulence generated by seiche-induced shear was usually patchy. The number of patches accepted in this layer was 315. As mentioned above, large rare turbulent events detected in the layer and generated mostly by wind gusts were excluded because they

belong to a different statistical population rather than from regular patches. The patch size h_p, the corresponding Thorpe L_{Tp} scale and the normalized Thorpe L_{Tp}/h_p scale have been analyzed. Analysis has been performed for the entire data excluding the small patches (h_p < 25 cm). The main findings for the statistical analysis are as detailed below:

1) The empirical CDF of patch sizes h_p has been fitted well by a log-normal model with mean and median values of 0.69 m and 0.5 m, respectively. It deviates from log-normality by only CDF(h_p) < 0.03 and CDF(h_p) > 0.97. When small patches (h_p < 25 cm) have not been included in the analysis, the lower tail has deviated from the log-normal distribution at a much higher CDF(h_p) $\approx$ 0.15. The lack of vertical resolution has been suggested as a possible explanation to the sharp cuts observed in the tails of the log-normal model found in the relevant literature.

2) The empirical CDF of the Thorpe L_{Tp} scale inside the patches $F(L_{Tp})$ have been well approximated by the log-normal distribution for $L_{Tp} \in [0.05, 0.4]$ m, and which covers ~ 85 % of the data. The sharp cut in the lower tail of L_{Tp} can be attributed to the constraint in the patch identification method (L_{Tp} < 4 cm). If only patches h_p > 25 cm are analyzed, the fitting to the log-normal model extends to ~ 92 % of the data. However, that the parameters of the log-normal distribution for both cases are shown to be practically the same. This would indicate that the statistics are not substantially affected by small patches. Finally, the presence of sharp tails at small scales of L_{Tp} probability plots and the difficulties in fitting the experimental data to the log-normal model as reported by various authors can be also associated with the insufficient vertical resolution of the measurements. In general these results are in accordance with the

log-normal distribution proposed by other authors, although none of the previous works were focused on low wind forcing in stratified lakes.

3) The empirical CDF of L_{Tp}/h_p has been fitted well to the Weibull and beta distributions in a range covering about 95% of the data. The median value of L_{Tp}/h_p (0.17) appears to be about two times larger than that reported by Moum (1996) for a series of ocean patches detected in the main pycnocline of the North Atlantic ($med(L_{Tp}/h_p)$ = 0.07). A possible cause of this discrepancy is the different evolutionary state of the patches: microstructure patches in the lake were possibly observed at an earlier stage of their evolution compared to the ocean patches.

4) The parameterization of the normalized Thorpe L_{Tp}/h_p scale proposed by Lozovatsky and Fernando (2002) for deep and coastal waters has been successfully tested for a small lake. In their parameterization, the normalized Thorpe L_{Tp}/h_p scale depends on the parameters of background stratification and patch turbulence, both of which can be combined into two non-dimensional numbers: the patch Richardson number $Ri_p = N^2 h_p^4 / K_T^2$ and the patch mixing Reynolds number $R_{mp} = K_T/\nu$ (the frequency of the background stratification is N^2, diffusivity is K_T, and molecular viscosity is ν. Then, it can be expressed as

$$\frac{L_{Tp}}{h_p} = 1.5\,x + 0.03; \quad x = \frac{\left(L_{Tp}/h_p\right)^{\max}}{\left(1 + Ri_p/Ri_{pc}\right)^{1/4}\left(1 + R_{mpc}/R_{mp}\right)}$$

where Ri_{pc} and R_{mpc} are characteristic values of Ri_p and R_{mp} equal to 60 and 150, respectively. The asymptotic value $\left(L_{Tp}/h_p\right)^{\max}$ is found to be 0.45, somewhat higher than the value obtained from Lozovatsky and Fernando (2002) for patches detected in ocean and marine coastal waters under moderate and strong winds (from 3 $m \cdot s^{-1}$ up to 15 $m \cdot s^{-1}$).

- Different phases of the oscillation cycle of internal seiches in the lake affected the vertical shear in the thermocline and, as the result, the generation of turbulent patches. The temporal variability of vertical mixing was analyzed based on the averaged vertical diffusivities estimated from the microstructure patches. When large vertical displacements of the isotherms (i.e. maximum vertical shear) were observed (July 1), we obtained an averaged diffusivity of $(3.65 \pm 0.80) \cdot 10^{-4}$ $m^2 \cdot s^{-1}$, higher than that in the phase of very low internal seiche amplitude (June 25), with its value of $(4.58 \pm 1.71) \cdot 10^{-5}$ $m^2 \cdot s^{-1}$. This correlated well with the turbulent fraction of the thermocline observed for those days (19% on July 1 and 10 % on June 25). Buoyancy fluxes were estimated as $4 \cdot 10^{-7}$ $W \cdot kg^{-1}$ for July 1 and $1.72 \cdot 10^{-7}$ $W \cdot kg^{-1}$ on June 25. Our results are close to the average diffusivities across the thermocline reported by Etemad-Shadidi and Imberger (2006) in Lake Biwa and Lake Kineret. We conclude that even under low wind, mixing across the thermocline in a lake is not negligible.

8.2. Analysis of internal intermittency

- Internal intermittency was analyzed in a shallow tidal flow and based on velocity data recorded by an ADV deployed close to the bottom boundary layer. Their analysis has shown that measurements of the vertical velocity component *w* were high quality and barely affected by noise. Mean dissipation rate was evaluated using the compensated

spectra of the fluctuations of the vertical velocity and gave estimations of $\tilde{\varepsilon} \sim 10^{-7} - 10^{-5}$ W·kg^{-1}.

- Under several flow conditions, the instrumentation was able to resolve small spatial scales beyond the peak of the maximum dissipation, evaluated from the Panchev-Kesich spectrum. It allows to estimate the the small-scale dissipation field has been calculated assuming isotropy and using the gradients of *w*.

- The structure functions of the vertical velocity *w* (TSF) were computed in order to estimate their scaling exponents $\zeta(p)$. It has been observed that for relatively low Reynolds numbers, $\zeta(p)$ progressively deviate from the Kolmogorov scaling, i.e. $\zeta(p) = p/3$. It is suggested that this can be attributed to the higher intermittency of underdeveloped turbulence.

- The log-Lévy and log-normal multifractal models were applied for the scaling of the structure function exponents (SF method). The results have shown that for very high energetic segments, i.e. turbulent Reynolds number $R_{\lambda w} > 500\text{-}700$ which corresponds to high-speed flooding phases of tidal flow, the values of intermittency parameters are $\tilde{\mu} \approx 0.24$, $\tilde{C}_1 \approx 0.15$, and $\tilde{\alpha} \approx 1.5$. These are close to the expected universal values obtained for fully developed turbulent flows at high Reynolds number in the atmosphere and in laboratory experiments. However, for relatively low turbulent Reynolds numbers $R_{\lambda w}$, the intermittency parameters C_1 and μ deviate from the previous classical values, increasing their values up to $C_1 \sim 0.25 - 0.35$ and $\mu \sim 0.5 - 0.6$ when $R_{\lambda w}$ drops below ~ 100.
- The analysis of the scaling exponents $K(p)$ of the *p*-order moments of the small dissipation field ε have supported the earlier results obtained with the SF method: Although it was only possible to evaluate segments with

$R_{\lambda w}$ up to ~310, the same tendency of C_1 to increase and μ to decrease for decreasing values of $R_{\lambda w}$ has been observed. In fact, turbulence in the ocean is usually characterized by relatively low Reynolds numbers, i.e. not sufficiently developed with no clear cuts between ranges; contrary to what is found in the atmosphere where scaling ranges are easily identifiable and extend over a wide range of scales. Then, this could explain the fact that reported values of μ for ocean turbulence are usually higher than those obtained in atmospheric turbulence, with values of μ ~0.4-0.5 (Gibson, 1998).

- The relationships between α, C_1 and μ and $R_{\lambda w}$ were approximated by power law functions. Their asymptotic values represent the expected values attained at very high Reynolds numbers. Concretely, it is found that:

  1) The multifractal analysis using the SF method gives a result of $\alpha^0 = 1.5$, $C_1^0 = 0.13$ and $\mu^0 = 0.23$, which are in agreement with the expected values of $\alpha \approx 1.5$, $C_1 \approx 0.15$ and $\mu \approx 0.25$ for fully developed turbulence as reported by different authors for other scalar fields (Schertzer et al., 1995; Seuront et al., 2005).

  2) The multifractal analysis for the small-scale dissipation field ε calculated by its isotropic formula gives asymptotic values of $\alpha_\varepsilon^0 =$ 1.6, $C_{1\varepsilon}^0 = 0.20$ and $\mu_\varepsilon^0 = 0.34$. These are close to the values reported by Lauren et al., (2001), who found $\alpha \approx 2$, $C_1 \approx 0.15$, $\mu \approx 0.3$ when analyzing the small-scale dissipation field obtained from surface layer turbulent winds at high Reynolds numbers. However, previous results differ from the values of $C_1 \approx 0.25 - 0.3$, $\alpha \approx 1.35 - 1.5$ and $\mu \approx 0.4 - 0.5$ obtained by other authors for well-developed turbulence

in the atmosphere (Schmitt et al., 1992; Chigirinskaya et al., 1994). A possible explanation of this discrepancy may be related to the method of reconstructing the field as in this latter case the turbulent dissipation field is reconstructed using fractional derivatives and taking the cube of the absolute values (data have coarse spatial resolution) instead of using squares of the velocity gradients as we did (see also Lauren et al., 2001).

3) The trend of the intermittency parameters C_1 and μ to increase for low $R_{\lambda w}$ observed from the multifractal analysis of ε (μ_ε ~0.3 at R_λ ~300) is consistent with other results obtained in laboratory and numerical simulations. In particular, the dependence of the intermittency exponent μ on $R_{\lambda w}$ obtained in the laboratory experiments of Hao et al. (2008) has shown that μ tends to increase in R_λ when obtained from the analysis of ε is calculated assuming isotropy. They found $\mu_\varepsilon \sim 0.3$ at $R_\lambda \sim 300$ which in turn is consistent with the previous results of Zhou et al. (2005). From numerical simulations, Almalkie and Bruyn Kops (2012) also obtained an increasing trend for μ ($\mu_\varepsilon \sim 0.5$ for R_λ ~250).

- Our results are in accordance with the behavior of the distribution of patchiness of small-scale phytoplankton for a tidal current as reported by Seuront and Schmitt (2005) who found increasing phytoplankton patchiness distributions when turbulence decreased along with variations related to the phase of the tidal cycle. These are directly consistent with the findings presented in this work.

8.3. Suggestions for future work

The analysis of intermittency carried out in this study provides many opportunities for extending this work in future research. Some of these directions are described next.

A natural extension for the analysis of patch turbulence would be to implement our methodology in sea waters. As salinity can be a significant parameter in determining density profiles (intrusions, water of different origins etc.) the procedure presented in this work should be applied to the density profile. In this case, with the introduction of other tests to our methodology, spurious density overturns caused by mismatches in time response of sensors may well be eliminated . For example, the T-S plots described by Galbraith and Kelley (1996) would be useful in avoiding these false overturns. The statistics of turbulent scales and mixing across different layers can help to corroborate the results of our study. Furthermore, the probability distributions of other turbulent scales, such as the distance between patches or the Thorpe displacements inside the patches, could be interesting variables to be analyzed.

Large but rare turbulent events (we observed only ten of them) have been observed in the interior of the Lake Banyoles. These patches have been supposed to belong to a different statistical population from the regular patches observed in the thermocline and thus governed by different statistical probability distribution functions. Having a long series of wind induced large patches would make it possible to obtain valuable statistical characteristics of these rare events by analyzing their CDF and comparing it with the extreme value distribution model. In addition, a possible correlation between those large episodic events and a suitable parameter which could characterize the gustiness of the wind should also be analyzed in order to quantify the mixing caused by such gusts. Then this could be compared to the mixing generated by the shear of the internal seiche field analyzed in this work. Special long-term field measurements will be needed to shed light on this problem.

Another interesting line of research would be tot take measurements along horizontal transects using microstructure instrumentation. This would allow a complete description (vertical and horizontal) of turbulent patches to be made and their characteristics to be analyzed. Furthermore, from these data it may also be possible to study the influence of the turbulent Reynolds number on the scaling exponents for the small-scale dissipation field, which is expected to depend on the nature of the flow and anisotropy of turbulence. Further experiments to study these effects and even the effect of the use of different components of the velocity field to compute the turbulent kinetic energy rate on the intermittency parameters would be also interesting.

9. Bibliography

Aghsaee, P., L. Boegman, and K. G. Lamb (2010), Breaking of shoaling internal solitary waves, *J. Fluid Mech.,* 659, 289-317.

Alford, M. H., and R. Pinkel (2000), Observations of overturning in the thermocline: the context of ocean mixing, *J. Phys. Oceanogr., 30*, 805–832.

Almalkie, S., S. M. de Bruyn-Kops (2012), Energy dissipation rate surrogates in incompressible Navier-Stokes turbulence, *J. Fluid Mech., 697*, 204-236.

Anselmet, F., Y. Gagne, E. J. Hopfinger, and R. A. Antonia (1984), High-order velocity structure functions in turbulent shear flow, *J. Fluid Mech., 140*, 63–89.

Arneodo, A., C. Baudet, and F. Belin (1996), Structure functions in turbulence, in various flow configurations, at Reynolds number between 30 and 5000, using extended self-similarity, *Europhys. Lett. 34,* 411–416.

Ayyub, B. M., and M. H. McCuen (1996), *Numerical methods for engineers*, Prentice Hall, Upper Saddle River, New Jersey.

Baird, E. (2011), *Alt. Fractals:A visual guide to fractal geometry and design*, 232 pp., Chocolate Tree Books, U.K.

Baker, M. A. and C. H. Gibson (1987), Sampling turbulence in the stratified ocean: statistical consequences of strong intermittency. *J. Phys. Oceanogr.*, *17*(10), 1817-1837.

Bao, X., G. Gao, and J. Yan (2001), Three dimensional simulation of tide and tidal current characteristics in the East China Sea, *Oceanol. acta*, *24*(2), 135-149.

Barnsley, M. (1988), *Fractals Everywhere*, 531 pp, Academic Press Inc., Boston, Mas.

Bastida, I., J. Planella, E. Roget, J. Guillén, P. Puig, and X. Sánchez (2012), Mixing dynamics on the inner shelf of the Ebro Delta, *Sci. Mar.*, 76(S1), 31-43.

Batchelor, G. K., and A. A. Townsend (1949), The nature of turbulent motion at large wave-numbers, *Proc. R. Soc. Lond. A*, *199,* 238–255.

Bean, M. A. (2001), *Probability: the science of uncertainty with applications to investments, insurance, and engineering* (Vol. 6), 428 pp, American Mathematical Soc., Providence, Rhode Island.

Benzi, R., G. Paladin, G. Parisi and A. Vulpiani (1984), On the multifractal nature of fully developed turbulence and chaotic systems. *J. Phys. A*, 17, 3521–3531.

Benzi, R., S. Ciliberto, R. Tripiccione, C. Baudet, F. Massaioli, and S. Succi (1993), Extended self similarity in turbulent flows, *Phys. Rev. E*, *48*, R29-R32.

Benzi, R., S. Ciliberto, C. Baudet, and G. Ruiz-Chavarria (1995), On the scaling of three-dimensional homogeneous and isotropic turbulence, *Physica D*, *80*, 385-398, doi: 10.1016/0167-2789(94)00190-2.

Bernardara, P., M. Lang, E. Sauquet, D. Schertzer, and I. Tchiguirinskaya (2007), *Multifractal analysis in hydrology. Application to time series*, 62 pp, Editions Quae, Paris, France.

Boegman, L., G. N. Ivey, and J. Imberger, (2005), The energetics of large-scale internal wave degeneration in lakes. *J. Fluid Mech.*, 531, 159-180.

Borak, S., W. Hardle, and R. Weron (2005), Stable distributions, In P. Cizek, W. Hardle, and R. Weron, eds., *Statistical tools for finance and insurance*, Springer-Verlag, Leipzig, Germany, 21-44.

Borradaile, G. (2003), *Statistics of earth science data*, 351 pp., Springer-Verlag, Berlin, Germany.

Brucker, K. A., and S. Sarkar (2007), Evolution of an initially turbulent stratified shear layer, *Phys. Fluids*, 19(10), 105105.

Bulmer, M. G. (1979), *Principles of Statistics*, 252 pp., Dover Publications Inc., Mineola, NY.

Casamitjana, X., and E. Roget (1987), Behavior of the 10 natural fluidized beds in Lake Banyoles (In Catalan), *Scientia Gerundensis*, *13,* 187-199.

Casamitjana, X., J. Colomer, E. Roget, and T. Serra (2006), Physical limnology in Lake Banyoles. *Limnetica, 25***,** 181-188.

Cava, D., and G. G. Katul (2009), The effects of thermal stratification on clustering properties of canopy turbulence, *Boundary-layer meteorol.*, *130*(3), 307-325.

Chen A. Ch., and F. J. Millero (1986), Precise thermodynamics properties for natural waters covering only the limnological range . *Limnol. Oceanogr.,* 31, 657-662.

Chen, S., K. R. Sreenivasan, and M. Nelkin (1997), Inertial range scaling of dissipation and enstrophy in isotropic turbulence, *Phys. Rev. E*, 56, 4928-4930.

Chen, C. Y. (2012), A critical review of internal wave dynamics. Part 2: Laboratory experiments and theoretical physics, *J. Vib. Control*, 18(7), 983-1008.

Chiriginskaya, Y., D. Schertzer, S. Lovejoy, and A. Lazarev (1994), Unified multifractal atmospheric dynamics tested in the tropics: part I, horizontal scaling and self organized criticality, *Nonlin. Proc. Geophys.*, *1*, 105-114.

Cisneros-Aguirre, J., J. L. Pelegrí, and P. Sangrà (2001), Experiments on layer formation in stratified shear flow. *Sci. Mar.*, 65(S1), 117-126.

Cisewski, B., V. H. Strass, and H. Prandke (2005), Upper-ocean vertical mixing in the Antarctic Polar Front Zone. *Deep-Sea Res. Pt. II, 52*(9), 1087-1108.

Cleve, J. , M. Greiner, B. R. Pearson, and K. R. Sreenivasan (2004), Intermittency exponent of the turbulent energy cascade, *Phys. Rev. E*, *69*, 066316.

Coman, M. A., and M. G. Wells (2012), Temperature variability in the nearshore benthic boundary layer of Lake Opeongo is due to wind-driven upwelling events. *Can. J. Fish. Aquat. Sci.*, 69(2), 282-296.

Colomer, J., T. Serra, J. Piera, E. Roget and X. Casamitjana (2001), Observations of a hydrothermal plume in a karstic lake, *Limnol. Oceanogr.,* 46 (1), 197-203.

Colosi, J. A., et al. (1999), A review of recent results in ocean acoustic wave propagation in random media: Basin scales, *IEEE J. Oceanic Eng.,* 24, 138-155, doi: 10.1109/48/48.757267.

Cousins, M., M. T. Stacey, and J. L. Drake (2010), Effects of seasonal stratification on turbulent mixing in a hypereutrophic coastal lagoon. *Limn. Oceanogr.*, 55(1), 172.

Crow, E., and K. Shimizu (1988), *Log-normal Distributions: Theory and applications*. Marcel Dekker, New York.

Cui, G., and T. Yanagi (2007), Dispersion of suspended sediment originated from the Yellow River in the Bohai Sea, *Coastal Mar. Sci., 31*(1), 9-18.

Dauxois, T., A. Didier, and E. Falcon (2004), Observation of near-critical reflection of internal waves in a stably stratified fluid, *Phys. Fluids,* 16(6), 1936-1941.

De Silva, I. P. D., and H. J. S. Fernando (1992), Some aspects of mixing in a stratified turbulent patch, *J. Fluid Mech., 240*, 601-625, doi:10.1017/S0022112092000223.

De Silva, I. P. D., H. J. S. Fernando, F. Eaton, and D. Hebert (1996), Evolution of Kelvin-Helmholtz billows in nature and laboratory, *Earth Planet. Sci. Lett., 143*, 217-231, doi: 10.1016/0012-821X(96)00129-X.

Delaney, M. P. (2003), Effects of temperature and turbulence on the predator–prey interactions between a heterotrophic flagellate and a marine bacterium, *Microb. Ecol., 45*, 218–225, doi: 10.1007/s00248-002-1058-4.

Dewitt, R. J., F. S. Henyey, and J. A. Wright (1990), The geometry of turbulent patches from a numerical simulation of internal wave critical layer events. *J. Geophys. Res.*, *95*(C6), 9731-9737.

Dillon, T. M. (1982), Vertical overturns: A comparison of Thorpe and Ozmidov length scales, *J. Geophys. Res., 87*, 9601–9613.

Dillon, T. M. (1984), The energetics of overturning structures: Implications for the theory of fossil turbulence, *J. Phys. Oceanogr.*, *14*(3), 541-549.

Druet, C. (2003), The fine structure of marine hydrophysical fields and its influence on the behavior of plankton: An overview of some experimental and theoretical investigations, *Oceanologia*, *45*(4), 517-555.

Durgesh, V., J. Thomson, M. C. Richmond, B. L. Polagye (2014), Noise correction of turbulent spectra obtained from acoustic Doppler velocimeters, *Flow Meas. Instrum.*, *27*, 39-41, doi: 10.1016/j.flowmeasinst.2014.03.001.

Efron, B., and R. Tibshirani (1993), An introduction to the bootstrap, In D. R. Cox et al., eds., *Monographs on Sstatistics and Applied Probability*, *57*, Chapman & Hall/CRC, Boca Raton, Florida.

Etemad-Sahidi, A., and J. Imberger (2006), Diapycnal mixing in the thermocline of lakes: Estimations by different methods, *Environ. Fluid Mech., 6*, 227-240.

Evans, M., N. Hastings, and B. Peacock (2000), Beta distribution, In A.C. Noel et al., eds., *Statistical Distributions*, Wiley, New York, NY, 34-42,Wiley.

Evans, J. M., and J. S. Rosenthal, (2003), *Probability and Statistics: The Science of Uncertainty*, 760 pp, W. H. Freeman and Company, New York, NY.

Evans, C., B. Reynolds, C. Hinton, S. Hughes, D. Norris, G. Grant, and B. Williams (2008), Effects of decreasing acid deposition and climate change on acid extremes in an upland stream, *Hydrol. Earth Syst. Sci., 12*, 337-351.

Evrendilek, F., and N. Karakaya (2014), Monitoring diel dissolved oxygen dynamics through integrating wavelet denoising and temporal neural networks, *Environ. Monit. Assess.*, *186*(3), 1583-1591.

Falconer, K. J. (1990), *Fractal geometry: mathematical foundations and applications*, 288 pp, John Wiley and Sons, Chichester, U.K.

Feder, J. (1988), *Fractals*, 283 pp, Plenum Press, New York, NY.

Feller, W. (1971), *An introduction to probability theory and its applications*, Vol.2, 670 pp., Wiley and sons, New York, NY.

Fer, I., R. Skogseth, and P. M. Haugan (2004), Mixing of the Storfjorden overflow (Swalbard Archipielago) inferred from density overturns, *J. Geophys. Res.*, *109*, C01005, doi: 10.1029/2003JC001968.

Fer, I., M. B. Paskyabi (2014), Autonomous Ocean Turbulence Measurements Using Shear Probes on a Moored Instrument. *J. Atmos. Ocean. Tech.*,, *31*(2), 474-490.

Fernando, H. J. S. (1991), Turbulent mixing in stratified flows, *Ann. Rev. Fluid Mech.* , 23, 455-493.

Fernando, H. J. S. (2003), Turbulent patches in a stratified shear flow, *Phys.f Fluids*, 3164-3169.

Ferron, B., H. Mercier, K. Speer, A. Gargett, and K. Polzin (1998), Mixing in the Romanche Fracture Zone, *J. Phys. Oceanogr., 28*, 1929–1945.

Finn D., B. Lamb, M. Y. Leclerc, S. Lovejoy, S. Pecknold, D. Schertzer (2001), Multifractal analysis of plume concentration fluctuations in surface layer flows, *J. Appl. Meteorol*., *40*, 229–245.

Flajolet, P., and R. Sedgewick (1995), Mellin transforms and asymptotics: finite differences and Rice's integrals, *Theor. Comput. Sci*., 144, 101-124.

Fofonoff, N. P., and R. C. Millard Jr. (1983), Algorithms for computation of fundamental properties of seawater, UNESCO technical papers in marine science, 44, UNESCO, Paris.

Folkard, A. M., Sherborne, A. J., and Coates, M. J (2007), Turbulence and stratification in Priest Pot, a productive pond in a sheltered environment, *Limnology*, *8(2)*, 113-120, doi: 10.1007/s10201-007-0207-3.

Forbes, C., M. Evans, N. Hastings, and B. Peacock (2011), 212 pp., *Statistical distributions*. John Wiley & Sons.New Jersey, NJ,

Fozdar, F., J. Parker, and J. Imberger (1985), Matching temperature and conductivity sensor response characteristics, *J. Phys. Oceanogr., 15*, 1557-1570.

Frants, M., et al. (2013), An Assessment of Density-Based Finescale Methods for Estimating Diapycnal Diffusivity in the Southern Ocean, *J. Atmos. Ocean Tech., 30*(11), 2647-2661.

Frisch, U., P. L. Sulem, and M. Nelkin (1978), A simple dynamical model of intermittent fully developed turbulence, *J. Fluid Mech*., *87*,719-736.

Frisch, U., and G. Parisi (1985), Fully developed turbulence and intermittency. In M. Ghil, R. Benzi, and G. Parisi, eds., *Turbulence and predicability in geophysical fluid dynamics and climate dynamics,* Proceedings of the International School of Physics "Enrico Fermi", Course LXXXVUI, Italian Physical Society, North-Holland, Amsterdam, 84-87.

Frisch, U. (1995), *Turbulence: The Legacy of A. N. Kolmogorov*, 296 pp, Cambridge, Cambridge Univ. Press, Cambridge, U.K.

Fructus, D., M. Carr, J. Grue, A. Jensen, and P. A. Davies, (2009), Shear-induced breaking of large internal solitary waves. *J. Fluid Mech.*, *620*, 1-29.

Galbraith, P. S., and D. E. Kelley (1996), Identifying overturns in CTD profiles, *J. Atmos. Oceanic Technol., 13*, 688-702.

Gale E.; C. Pattiaratchi, and R. Ranasinghe (2006), Vertical mixing processes in Intermittently Closed and Open Lakes and Lagoons, and the dissolved oxygen response, *Estuar. Coast. Shelf Sci.*, *69*, 205-216.

Gargett, A., and Garner, T. (2008), Determining Thorpe scales from ship-lowered CTD density profile, *J. Atmos. Ocean. Tech., 25*(9), 1657-1670.

Gargett, A. E., T. R. Osborn, and P. W. Nasmyth (1984), Local isotropy and the decay of turbulence in a stratified fluid, *J. Fluid Mech., 144*, 231-280.

Gavrilov, N. M., H. Luce, M. Crochet, F. Dalaudier, and S. Fukao (2005), Turbulence parameter estimations from high-resolution balloon temperature measurements of the MUTSI-2000 campaign, *Ann. Geophys.*, 23(7), 2401-2413.

Geophysical Fluid Dynamics Laboratory (2014), *Ocean Mixing*, available from: http://www.gfdl.noaa.gov/ocean-mixing [03 July 2014]

Gheidari, M. H. N., A. Telvari, H. Babazadeh, and M. Manshouri (2011), Estimating design probable maximum precipitation using multifractal methods and comparison with statistical and synoptically methods case study: basin of Bakhtiari Dam, *Water Resour.*, *38*(4), 484-493.

Gibson, M. (1963), Spectra of turbulence in a round jet, *J. Fluid Mech.*, 15, 161-173.

Gibson, C. H. (1980), Fossil temperature, salinity, and vorticity turbulence in *Marine Turbulence*, vol. 28, edited by Jacques J. C. Nihoul, pp. 221-257, Elsevier Oceanographic Series, Elselvier, Amsterdam.

Gibson, C. H. (1987), Fossil turbulence and intermittency in sampling oceanic mixing processes, *J. Geophys. Res., 92*, 5383-5404, doi: 10.1029/JC092iC05p05383.

Gibson, C. H. (1991a), Laboratory, numerical, and oceanic fossil turbulence in rotating and stratified fluid*, J. Geophys. Res., 96*, 12549-12566.

Gibson, C. H. (1991b), Turbulence, mixing and heat flux in the ocean main thermocline, *J. Geophys. Res., 96,* 20403-20420.

Gibson, C. H., V. N. Nabatov, and R. V. Ozmidov (1993), Measurements of turbulence and fossil turbulence near Ampere Seamount, *Dyn. Atmos. Oceans, 19*, 175-204.

Gibson, C. H. (1998), Intermittency of internal wave shear and turbulence dissipation. In J. Imberger, ed., *Physical Processes in Lakes and Oceans*, Coastal Estuarine Stud., vol. 54, AGU, Washington, DC,363-376.

Gibson, C. H. (1999), Fossil turbulence revisited, *J. Mar. Sys.*, 21, 1-4, 147-167.

Gibson, C. H., V. G. Bondur, R. N. Keeler, and P. T. Leung (2006), Remote sensing of submerged oceanic turbulence and fossil turbulence, *International Journal of Fluid Dynamics*, *2*(2), 111-135.

Gires, A., I. Tchiguirinskaia, D. Schertzer, S. Lovejoy (2013), Influence of the zero-rainfall on the assessment of the multifractal parameters, *Adv. Water Resour.*, 45, 13–25.

Gorogetska, N., V. Nikishov, and K. Hutter (2012), Laboratory modeling on transformation of large-amplitude internal waves by topographic obstructions, In K. Hutter ed., *Nonlinear Internal Waves in Lakes,* Springer Berlin Heidelberg, Germany, 105-191.

Grant, H.L., R.W. Stewart and A. Moilliet (1962), Turbulence spectra from a tidal channel, *J. Fluid Mech.*, 12, 241-268.

Grassberger, P. (1983), Generalized dimensions of strange attractors, *Phys. Lett. A*, *97*, 227-230.

Gregg, M. C. (1980), Microstructure patches in the thermocline, *J. Phys. Oceanogr.*, 10, 915–943.

Gregg, M. C., E. A. D'Asaro, T. J. Shay, and N. Larson (1986), Observations of persistent mixing and near-inertial internal waves, *J. Phys. Oceanogr., 16*, 856–885.

Gurvich, A., and M. A. Yaglom (1967), Breakdown of eddies and probability distributions for small-scale turbulence, boundary layers and turbulence, *Phys. Fluids Suppl.*, 10, S59-65.

Hao, Z., T. Zhou, Y. Zhou, and J. Mi (2008), Reynolds number dependence of the inertial range scaling of energy dissipation rate and enstrophy in a cylinder wake, *Exp. Fluids*, *44*, 279-289, doi: 10.1007/s00348-007-0400-5.

Hendelman, N. (2009), The frequency of turbulence in the thermocline of Opeongo Lake, *University of Toronto Journal of Undergraduate Life Science*, *3*(1).

Hendricks, P. J. (2001), Comparison of turbulence measurements from a SonTek ADV and a nobska MAVS, In *OCEANS, 2001, MTS/IEEE Conference and Exhibition*, Vol. 3, 1860-1866.

Hentschel, H.G. E., and I. Procaccia (1983), The infinite number of generalized dimensions of fractals and strange attractors, *Physica D*, *8*, 435-444.

Hinze, J. O. (1975), *Turbulence*, 790 pp., Mc Graw-Hill, New York, NY.

Hirabayashi, S., and T. Sato (2010), Scaling of mixing parameters in stationary, homogeneous, and stratified turbulence, *J. Geophys. Res.*, *115*(C9).

Horn, D. A., J. Imberger, J., G. N. Ivey (2001), The degeneration of large-scale interfacial gravity waves in lakes, *J. Fluid Mech.*, *434*, 181-207.

Hood, M., et al.(2010), Ship-based repeat hydrography: A strategy for a sustained global program, In Hall et al., ed., *Proceedings of OceanObs'09: Sustained Ocean Observations and Information for Society*, vol. 2, ESA Publication WPP-306, Venice, doi: 10.5270/OceanObs09.cwp.44.

Huzzey, L. M., and T.M. Powell (2005), Tidal variation in turbulent eddy sizes in an stuary, available from: www.dtic.mil/get-tr-doc/pdf?AD=ADA573634 [31 July 2014]

Ichikawa, H., and R. C. Beardsley (2002), The current system in the Yellow and East China Seas, *J. Oceanogr.*, *58*(1), 77-92.

Imberger, J. (1985), The diurnal mixed layer, *Limnol. Oceanogr., 30*, 737-770.

Imberger, J., and J. C. Patterson (1990), Physical Limnology, In T. Wu, ed., *Advances in Applied Mechanics*, Academic Press, Boston, Mas., 303-475.

Imberger, J., and G. N. Ivey (1991), On the nature of turbulence in a stratified fluid. Part II: Application to lakes, *J. Phys. Oceanogr.*, *21*(5), 659-680.

Imberger, J. (1994), Transport processes in lakes: a review, In R. Margalef, ed., *Limnology Now: A Paradigm of Planetary Problems*, Elselvier Sci., new York, NY, pp. 99-191.

Imberger, J. (1998), Flux paths in a stratified lake: A review in *Physical processes in lakes and oceans*, edited by J. Imberger, pp. 1-18, Coastal and Estuarine Studies AGU, Washington DC.

Inoue, R. and W. D. Smyth (2009),: Efficiency of mixing forced by unsteady shear flow. *J., Phys. Oceangr.*, 39, 1150–1166.

Itsweire, E. C., K. N. Helland, and C. W. Van Atta (1986), The evolution of grid-generated turbulence in a stably stratified fluid, *J. Fluid Mech., 162,* 299-338, doi:10.1017/S0022112086002069.

Itsweire, E. C., J. R. Koseff, D. A. Briggs, and J. H. Ferzinger (1993), Turbulence in stratified shear flows: Implications for interpreting shear-induced mixing in the ocean, *J. Phys. Oceanogr., 23*, 1508-1522.

Ivey, G. N., and J. Imberger (1991), On the nature of turbulence in a stratified fluid, part I: the energetics of mixing, *J. Phys. Oceanogr*., 21, 650–658.

Jago C. F., S. E. Jones, P. Sykes, and T. Rippeth (2006), Temporal variation of suspended particulate matter and turbulence in a high energy, tide-stirred, coastal sea: Relative contributions of resuspension and disaggregation, *Cont. Shelf Res., 26,* 2019–2028.

Johnson, H. L., and C. Garrett (2004), Effects of noise on Thorpe scales and run lengths*, J. Phys. Oceanogr.*, *34*, 2359–2372.

Katsev, S. et al. (2010), Mixing and its effects on biogeochemistry in the persistently stratified, deep, tropical Lake Matano, Indonesia, *Limnol. Oceanogr., 55*(2), 763-776.

King, M. J., W. J. Kim, and C. Y. Cho (2001), In C. Das Parag, D. M. Frangopol and A. S. Nowak, eds., *Bridge, Design, Construction and Maintenance*, The Institution of Civil Engineers, 565 pp, Hong Kong, 175-186.

Kistler, A. L., and T. Vrebalovich (1966), Grid turbulence at large Reynolds numbers*, J. Fluid. Mech.*, 26, 37-47.

Kitade Y., M. Matsuyama, and J. Yoshida (2003), Distribution of overturn induced by internal tides and Thorpe scale in Uchiura Bay, *J. Oceanogr., 59*, 845-850.

Klymak, J. M., S. Legg, and R. Pinkel (2010), A simple parameterization of turbulent tidal mixing near supercritical topography, *J. Phys. Oceanogr., 40*(9), 2059-2074.

Kocsis, O., B. Mathis, M. Gloor, M. Schurter, and A. Wüest (1998), Enhanced mixing in narrows: a case study at the Minau sill (Lake Constance), *Aquat. Sci.*, *60*, 236-252.

Kocsis, O., H. Prandke, A. Stips, A. Simon, and A. Wüest (1999), Comparison of dissipation of turbulent kinetic energy determined from shear and temperature microstructure, *J. Mar. Sys., 21*, 67-84.

Kolmogorov, A. N. (1941a), The local structure of turbulence in incompressible fluid for very large Reynolds numbers, *Dokl. USSR Acad. Sci*., 39, 301–305.

Kolmogorov, A.N. (1941b), On decay of isotropic turbulence in incompressible viscid fluid, *Dokl. Acad. Sci. USSR*, 31(6), 538-541.

Kolmogorov, A. N. (1941c), On log-normal distribution of the sizes of particle in the course of breakdown, *Dokl. Akad. Sci., 31*, 99–101.

Kolmogorov, A.N. (1962), A refinement of previous hypotheses concerning the local structure of turbulence in a viscous incompressible fluid at high Reynolds number, *J. Fluid Mech*., *13,* 82–85.

Kuo, A. Y. C., and S. Corrsin (1971), Experiments on internal intermittency and fine-structure distribution functions in fully turbulent fluid, *J. Fluid. Mech.*, *502*(2), 285-319, doi: 10.1017/S0022112071002581.

Kundu, P. K. (1990), *Fluid mechani*cs, 638 pp., Academic Press, San Diego, Calif.

Laha, R. G., and V. K. Rohatgi (1979), *Probability Theory*, 557 pp, Wiley, New York, NY.

Lande, R., and M. R. Lewis (1989), Models of photoadaptation and pthotosynthesis by algal cells in a turbulent mixing layer, *Deep Sea Res., 36*, 1161-1175.

Larsen, R. J., and M. L. Marx (1986), An introduction to mathematical statistics and its applications, Prentice-Hall, Englewood Cliffs, New Jersey.

Lauren, M. K., M. Menabde, and G. L. Austin (2001), Analysis and simulation of surface-layer winds using multiplicative cascade models with self-similar probability densities, *Boundary-Layer Meteorol.*, *100*, 263-286.

Lavallée, D. (1991), *Multifractal techniques: analysis and simulation of turbulent fields,* Ph.D. thesis, 144 pp, McGill University, Montreal, Canada.

Ledwell, J. R., and A. J. Watson (1991), The Santa Monica basin tracer experiment: A study of diapycnical and isopycnical mixing, *J. Geophys. Res.*, *96*, 8695-8718.

Ledwell, J. R., T. F. Duda, M. A. Sundermeyer, and H. E. Seim (2004), Mixing in a coastal environment: 1. A view from dye dispersion. *J. Geophys. Res.*, *109*(C10).

Lee, I., R. C. Lien, J. T. Liu, and W. S. Chuang (2009), Turbulent mixing and internal tides in Gaoping (Kaoping) submarine canyon, Taiwan. *J. Mar. Sys.*, *76*(4), 383-396.

Leung, P. T. (2011), *Coastal microstructure: From active overturn to fossil turbulence,* Ph.D. thesis, Texas A&M University.

Lienhard, J. H., and C. W. Van Atta (1990), The decay of turbulence in thermally stratified flow, *J. Fluid Mech.*, 210, 57-112.

Liu, J., Y. Saito, H. Wang, Z. Yang, and R. Nakashima (2007), Sedimentary evolution of the Holocene subaqueous clinoform off the Shandong

Lombardo, C. P., and M. C. Gregg (1989), Similarity scaling of viscous and thermal dissipation in a convecting surface boundary layer, *J. Geophys. Res., 94*, 6273–6284.

López, P., J. Cano, D. Cano, and M. Tijera (2008), Time evolution of Thorpe profiles corresponding to atmospheric soundings, *Geophys. Res. Abstracts*, 10.

Lorke, A. (2007), Boundary mixing in the thermocline of a large lake. *J. Geophys. Res., 112*(C9).

Lorke, A., and A. Wüest (2002), Probability density of displacement and overturning length scales under diverse stratification, *J. Geophys. Res., 107*, 3214, doi:10.1029/2001JC001154.

Lorke, A., L. Umlauf, and V. Mohrholz (2008), Stratification and mixing on sloping boundaries, *Geophys. Res. Lett., 35*(14).

Lovejoy, S., and D. Schertzer (1986), Scale invariance, symmetries, fractals, and stochastic simulations of atmospheric phenomena, *Bulletin of the American meteorological society*, *67*(1), 21-32.

Lovejoy, S., and D. Schertzer (1990), *Our multifractal atmosphere: a unique laboratory for nonlinear dynamics*, Physics in Canada, *46*, 62-71.

Lovejoy, S., and D. Schertzer (2007), Scaling and multifractal fields in the solid earth and topography, *Nonlin. Proc. Geophys.*, 14, 1–38.

Lovejoy, S., and D. Schertzer (2010), On the simulation of continuous in scale universal multifractals, part I: Spatially continuous processes, *Comput. and Geosci.*, 36, 1393-1403, doi:10.1016/j.cageo.2010.04.010

Lovejoy, S., and D. Schertzer (2013), *Emergent Laws and Multifractal Cascades*, 475 pp, Cambridge, Cambridge University Press, New York, NY.

Lowe, R. J., P. F. Linden, and J. W. Rottman (2002), A laboratory study of the velocity structure in an intrusive gravity current, *J. Fluid Mech.*, *456*, 33–48.

Lozovatsky, I. D., A. S. Ksenofontov, A. Y. Erofeev, and C. H. Gibson (1993), Modeling of the evolution of vertical structure in the upper ocean by atmospheric forcing and intermittent turbulence in the pycnocline, *J. Mar. Sys.*, *4*, 263-273.

Lozovatsky, I. D., and A. Y. Erofeev (1993), Statistical approach to eddy viscosity simulation for numerical models of the upper turbulent layer, *J. Mar. Sys.*, *5*, 391-399.

Lozovatsky, I. D., and H. J. S. Fernando (2002), Mixing on a shallow shelf of the Black Sea, *J. Phys. Oceanogr., 32*, 945–956.

Lozovatsky, I. D., E. G. Morozov, and H. J. S. Fernando (2003), Spatial decay of energy density of tidal internal waves, *J. Geophys. Res.*, *108*(C6).

Lozovatsky, I., E. Roget, and H. J. S. Fernando (2005), Mixing in shallow waters: measurements, processing and applications, *J. Ocean Univ. China, 4*, 293-305, doi:10.1007/s11802-005-0050-2.

Lozovatsky, I. D., Z.Liu, H. Wei, and H. J. S. Fernando (2008a), Tides and mixing in the northwestern East China Sea. Part I: Rotating and reversing tidal flows, *Cont. Shelf Res.*, 28, 318-337. Doi: 10.1016/j.csr.2007.08.006.

Lozovatsky, I. D., Z.Liu, H. Wei, and H. J. S. Fernando (2008b), Tides and mixing in the northwestern East China Sea. Part II: The near-bottom turbulence, *Cont. Shelf Res.*, 28, 338-350, doi: 10.1016/j.csr.2007.08.007.

Lozovatsky, I. D., H. S. J. Fernando, and S. M. Shapovalov (2008c), Deep-ocean mixing on the basin scale: Inference from North Atlantic transects, *Deep Sea Res. I, 55*(9), 1075-1089.

Lueck, R. G., and J. J. Picklo (1990), Thermal inertia of conductivity cells: Observations with a Sea-Bird Cell, *J. Atmosf. Oceanic Technol., 7*, 756-768.

MacIntyre S. (1993), Vertical mixing in a shallow, eutrophic lake: Possible consequences for the light climate of phytoplankton, *Limn. Oceanogr.*, *34*, No 4, 798-817.

MacIntyre, S., J. O. Sickman, S. A. Goldthwait, and G. W. Kling (2006), Physical pathways of nutrient supply in a small, ultraoligotrophic arctic lake during summer stratification, *Limnol. Oceanogr., 51*(2), 1107-1124.

MacIntyre, S., J. F. Clark, R. Jellison, and J. P. Fram (2009), Turbulent mixing induced by nonlinear internal waves in Mono Lake, California. *Limnol. and Oceanogr.*, *54*(6), 2255-2272.

Mahrt, L. (1989), Intermittent of atmospheric turbulence, *J. Atmos. Sci.*, *46*, 79-95.

Mandelbrot, B. (1967), How long is the coast of Britain? Statistical self-similarity and fractional dimension, *Science*, *156*, 3775, 636-638, doi: 10.1126/science.156.3775.636.

Mandelbrot, B. (1974), Intermittent turbulence in self-similar cascades: divergence of high moments and dimension of the carrier. *J. Fluid Mech.*, *62*, 331-358.

Mandelbrot, B. (1975), *Les objects fractals: forme, hasard et dimension*, 196 pp, Flammarion, Paris, France.

Mandelbrot, B. B. (1982), *The fractal geometry of nature,* 461 pp, Freeman and Co, New York, NY.

Margalef, R. (1987), *Our Biosphere*, 176 pp., Ecol. Inst., Luhe, Germany.

Martin, J. P., and D. L. Rudnick (2007), Inferences and observations of turbulent dissipation and mixing in the upper ocean at the Hawaiian Ridge, *J. Phys. Oceanogr.*, *37*(3), 476-494.

Mater, B. D., S. M. Schaad, and S. K. Venayagamoorthy (2013), Relevance of the Thorpe length scale in stably stratified turbulence, *Phys. Fluids, 25*(7), 076604. doi: 10.1063/1.4813809

Meneveau, C. and K. Sreenivasan (1987), Simple multifractal cascade model for fully developed turbulence, *Phys. Rev. Lett*., 59, 1424-1427.

Meneveau, C., and K. Sreenivasan (1991), The multifractal nature of turbulent energy dissipation, *J. Fluid Mech*., *224*, 429-484.

Middleton, J. H., and T. D. Foster (1980), Fine structure measurements in a temperature-compensated halocline, *J. Geophys. Res., 85*, 1107–1122.

Moffatt, H.K. (1981), Some developments in the theory of turbulence, *J. Fluid Mech*., *106*, 2747.

Monin, A. S., and A. M. Yaglom (1975), Statistical Fluid Mechanics: Mechanics of Turbulence, vol.2, 874 pp., MIT Press, Cambridge, Mass.

Mood, A. M., F. A. Graybill, and D. C. Boes (1974), *Introduction to the theory of statistics*, McGraw Hill, New York, NY.

Moon, J. H., N. Hirose, and J. H. Yoon (2009), Comparison of wind and tidal contributions to seasonal circulation of the Yellow Sea, *J. Geophys. Res*., *114*(C8), doi:10.1029/2009JC005314, 2009

Moreno-Amich, R., and E. Garcia Berthou (1989), A new bathymetric map based on echo-sounding and morphometrical characterization of the Lake of Banyoles, *Hydrobiologia, 185*, 83-90.

Moreno-Ostos, E., L. Cruz-Pizzaro, A. Basanta-Alvés, C. Escot, and D.G. George (2006), Algae in the motion: Spatial distribution of phytoplanktonin thermally stratified reservoirs, *Limnetica*, 25(1-2), 205-216.

Mosaddad, S. M., and M. Delphi (2013), Numerical Simulation of Turbulence in Northern Part of the PG, *World Applied Sciences Journal*, *21*(11), 1577-1582.

Monin, A. S. and Yaglom, 1967,A. M., *Statistical Hydromechanics, Part 2*, 8Nauka, Moscow, Russia.

Moum, J. N. (1996), Energy-containing scales of turbulence in the ocean thermocline, *J. Geophys. Res .*, 101, 14095-14109.

Moum, J. N., D. M. Farmer, W. D. Smyth,, L. Armi, and S. Vagle (2003), Structure and generation of turbulence at interfaces strained by internal solitary waves propagating shoreward over the continental shelf, *J. Phys. Oceanogr., 33*(10), 2093-2112.

Münnich, M., A. Wüest, and D. M. Imboden (1992), Observations of the second vertical mode of the internal seiche in an alpine lake, *Limnol. Oceanogr., 37*, 1705-1719.

Munroe, J. R., C. Voegeli, B. R. Sutherland, V. Birman, and E. H. Meiburg (2009), Intrusive gravity currents from finite-length locks in a uniformly stratified fluid, *J. Fluid Mech.*, *635*, 245-273.

Nasmyth, P. (1970), *Oceanic turbulence*, Ph.D. thesis, University of British Columbia, 69 pp.

Nash, J. D., and J. N. Moum (2002), Microstructure estimates of turbulent salinity flux and the dissipation spectrum of salinity, *J. Phys. Oceanogr.*, *32*, 2312-2333, doi: 10.1175/1520-0485(2002)032<2312:MEOTSF>2.0.CO;2.

Nikora, V. I., and D. G. Goring (1998), ADV measurements of turbulence: Can we improve their interpretation?, *J. Hydraul. Eng.g*, *124*(6), 630-634.

Nikurashin, M., and R. Ferrari (2010), Radiation and dissipation of internal waves generated by geostrophic motions impinging on small-scale topography: Theory. *J. Phys. Oceanogr.*, *40*(5), 1055-1074.

Nishri, A., J. Imberger, W. Eckert, I. Ostrovsky, and Y. Geifman (2000), The physical regime and the respective biogeochemical processes in the lower water mass of Lake Kinneret, *Limnol. Oceanogr., 45*, 972-981.

Novikov, E. A., and R. Stewart (1964), Intermittency of turbulence and spectrum of fluctuations in energy dissipation, *Izv. Akad. Nauk. SSSR Ser. Geofiz*., *3*, 408-412.

Novikov, E. (1971), Intermittency and scale similarity in the structure of a turbulent flow, *Prikl. Mat. Mech*., 35, 266-277.

Oakey, N. (1982), Determination of the rate of dissipation of turbulent energy from simultaneous temperature and velocity shear microstructure measurements, *J. Phys. Oceanogr., 12*, 256–271.

Obukhov A. M. (1962),Some specific features of atmospheric turbulence, *J. Fluid Mech.*, *13*, 77–81.

Osborn, T. R. (1980), Estimates of the local rate of vertical diffusion from dissipation measurements, *J. Phys. Oceanogr.*, *10*(1), 83-89.

Ozmidov, R. V. (1965), On the turbulent exchange in a stably stratified ocean, *Atmos. Ocean Phys*., 8, 853–860.

Paka, V., V. Zhurbas, B. Rudels, and D. Quadfasel, (2013), Turbulence measurements and estimates of entrainment in the Denmark Strait overflow plume, *Ocean Sci., 9*, 1003-1014.

Panchev, S., and D. Kesich (1969), Energy spectrum of isotropic turbulence at large wavenumbers, *C.R. Acad. Bulg. Sci., 22*, 627–630.

Pandey, G., S. Lovejoy, and D. Schertzer (1998), Multifractal Analysis Including Extremes of Daily River Flow Series for Basins one to a million square kilometers, *J. Hydrology*, *208*, 62-81.

Pannard, A., B. E. Beisner, D. F. Bird, J. Braun, D. Planas, and M. Bormans (2011), Recurrent internal waves in a small lake: Potential ecological consequences for metalimnetic phytoplankton populations, *Limnol. Oceanogr., 1*, 91-109.

Patterson, M. D., C. P. Caulfield, J. N. McElwaine, and S. B. Dalziel (2006), Time-dependent mixing in stratified Kelvin-Helmholtz billows: Experimental observations, *Geophys. Res. Lett.*, *33*(15).

Pecknold, S., S. Lovejoy, and D. Schertzer (2001), Stratified multifractal magnetization and surface geometric fields, part 2: multifractal analysis and simulation, *Geophys. Int. J.*, *145*, 127-144.

Perez-Losada, J., E. Roget, and X. Casamitjana (2003), Evidence of high vertical wave-number behaviour in a continuously stratified reservoir, *J. Hydrol. Eng., 129*, 734-737.

Pernica, P., M. G. Wells, and S. MacIntyre (2014), Persistent weak thermal stratification inhibits mixing in the epilimnion of north-temperate Lake Opeongo, Canada, *Aquat. Sci.*, *76*(2), 187-201.

Peters, H., M.C. Gregg and T. B. Sanford (1994), The diurnal cycle of the upper equatorial ocean: Turbulence, fine-scale shear and mean shear. *J. Geophys. Res.*, 99, 7707-7723.

Peters, F., and C. Marrase (2000), Effects of turbulence on plankton: an overview of experimental evidence and some theoretical considerations, *Mar. Ecol. Prog. Ser., 205*, 291-306, doi:10.3354/meps205291.

Peters, H., and W. E. Johns (2005), Mixing and entrainment in the Red Sea outflow plume. Part II: Turbulence characteristics, *J. Phys. Oceanogr.*, *35*(5), 584-600.

Pham, H. T., ans S. Sharkar (2010), Transport and mixing of density in a continuously stratified shear layer, *Journal of Turbulence*, *11*, 1-23.

Piera, J., E. Roget, and J. Catalan (2002), Turbulent patch identification in microstructure profiles: A method based on wavelet denoising and Thorpe displacement analysis, *J. Atmos. Oceanic Technol., 19*, 1390–1402.

Piera, J., R. Quesada, R., and J. Catalan (2006), Estimation of nonlocal turbulent mixing parameters derived from microstructure profiles, *J. Mar. Res.*, *64*(1), 123-145.

Planella-Morato, J. (2007), *Mixing processes and hydrodynamic diagrams* (In Catalan), Minor thesis, University of Girona, 124 pp.

Planella, J., X. Sanchez, and E. Roget (2009), Delving deeper into the hydrodynamics of karstic lakes: One more step to improve environmental management and ecohydrology, in *WMHE2009, Proceedings International Symposium on Water Management and Hydraulic Engineering*, edited by C. Popovska and M. Jovanovski, pp.815-826, Faculty of Civil Engineering Ss. Cyril and Methodius Univ. , Skopje.

Pope, S. B. (2000), *Turbulent flows*, 771 pp, Cambridge, Cambridge Univ. Press, Cambridge, U.K.

Pozdynin, V.D. (2002), Small-scale turbulence in the ocean, Nauka Publ., Moscow (in Russian).

Prandke, H., and A. Stips (1998), Test measurements with an operational microstructure turbulence profiler: detection limit of dissipations rates, *Aquat. Sci., 60*.191-209.

Prandke, H., K. Holtsth, and A. Stips (2000), *MITEC technology development: the microstructure-turbulence measuring system MSS, EUR 19733 EN*, Ispra Joint Research Center, European Commission.

Praud, O., J. Sommeria, and A. M. Fincham (2006), Decaying grid turbulence in a rotating stratified fluid, *J. Fluid Mech.*, *547*, 389-412.

Preusse, M., F. Peeters, and A. Lorke (2010), Internal waves and the generation of turbulence in the thermocline of a large lake, *Limnol. Oceanogr., 55*(6), 2353-2365.

Qiu, X., D. X. Zhang, Z. M. Lu, and Y. L. Liu (2009), Turbulent mixing and evolution in a stably stratified flow with a temperature step, *J. Hydrodyn. Ser. B, 21*(1), 84-92.

Rahmani, M., B. Seymour, and G. Lawrence (2014), The evolution of large and small-scale structures in Kelvin–Helmholtz instabilities, *Environ. Fluid Mech.*, 1-27.

Rhodes, C. J., and A. M. Reynolds (2007), The influence of search strategies and homogeneous isotropic turbulence on planktonic contact rates, *Europhys. Lett., 80*, 60003-60008, doi: 10.1209/0295-5075/80/60003.

Richardson, L.F. (1922), *Weather prediction by numerical process*, 152 pp, Cambridge Univ. Press, Cambridge, U.K.

Rodriguez-Iturbe, I., and A. Rinaldo (1997), *Fractal river basins: Chance and self-organization*, 564 pp, Cambridge University Press, Cambridge, U.K.

Roget, E., G. Salvadé, F. Zamboni, and J. E. Llebot (1993), Internal waves in a small lake with a thick metalimnion, *Verh. Internat. Verein. Limnol., 25*, 91-99.

Roget, E., X. Casamitjana, and J. E. Llebot (1994), Calculation of the flow into a lake through the underground springs with suspensions, *Netherlands Journal of Aquatic Ecology,* 28, 135-141.

Roget, E., and J. Colomer (1996), Flow characteristics of a gravity current induced by differential cooling in a small lake, *Aquat. Sci.,* 58(4), 367-377.

Roget, E., G. Salvadé, and F. Zamboni (1997), Internal seiche climatology in a small lake where transversal and second vertical modes are usually observed, *Limmol. Oceanogr., 42*, 663-673.

Roget, E., I. Lozovatsky, X. Sanchez, and M. Figueroa (2006), Microstructure measurements in natural waters: Methodology and applications, *Progr. Oceanogr., 70,* 126-148, doi:10.1016/j.pocean.2006.07.003.

Roget, E., I. Lozovatsky, X. Sanchez, M. Figueroa (2007), Corrigendum to microstructure measurements in natural waters: Methodology and applications [Progress in Oceanography 70(2006) 126-148], *Progr. Ocanogr., 72*, 114.

Roget, E. (2013), Hydrophysical Measurements in Natural Waters. In H. J. S. Fernando, ed., *Handbook of Environmental Fluid Dynamics, Vol 2,*. CRC Press/Taylor & Francis Group, Boca Raton, Florida, 497-509.

Rohr, J. J., E. C. Itsweire, and C. W. Van Atta (1984), Mixing efficiency in stably stratified decaying turbulence, *J. Geophys. Astrophys. Fluid Dyn., 29*, 221-236.

Rosenblum, L. J., and G. O. Marmorino (1990), Statistics of mixing patches observed in the Sargasso Sea, *J. Geophys. Res*, *95*(C4), 5349-5357.

Ruddick, B., A. Anis, and K. Thompson (2000), Maximum likelihood spectral fitting: The Batchelor spectrum, *J. Atmos. Ocean. Tech.*, *17*(11), 1541-1555.

Rueda, F. J., S. G. Schladow, S. G. Monismith, and M. T. Stacey (2003), Dynamics of large polymictic lake I: Field observations, *J. Hydraul. Eng.*, *129*(2), 82-91.

Saggio, A., and J. Imberger (2001), Mixing and turbulent fluxes in the metalimnion of a stratified lake, *Limnol. Oceanogr., 46*, 392-409.

Saiz, E., A. Calbet, and E. Broglio (2003), Effects of small-scale turbulence on coperpods: The case of *Oithona davisae*, *Limnol. Oceanogr., 48*, 1304-1311.

Sanchez, X., and E. Roget (2007), Microstructure measurements and heat flux calculations of a triple-diffusive process in a lake within the diffusive layer convection regime, *J. Geophys. Res., 112*, 181-188, C02012, doi:10.1029/2006JC003750.

Sanchez, X., E. Roget, J. Planella, and F. Forcat (2011), Small-scale spectrum of a scalar field in water: The Batchelor and Kraichnan models. *J. Phys. Oceanogr., 41*(11), 2155-2167.

Sanchez-Martin, X., G. Sutherland, J. Planella-Morató, J. M. Lilly, and B. Ward (2014), Inermittency measurements in the ocean with a microstructure profiler: multi-fractal nature of the dissipation field, Phys. Fluids, submitted.

Sanborn, V. A., and R. D. Marshall (1965), Local isotropy in wind tunnel turbulence, Colorado State, Uaiu. Rep. CER, 65, UAS-RDM71.

Sangrà, P. et al. (2011), The Bransfield current system, *Deep-Sea Res. I, 58*(4), 390-402.

Schertzer, D., and S. Lovejoy (1983), The dimension of the atmospheric motions, Turbul. Chaotic Phenomena Fluids, IUTAM Symp., Kyoto U.K., Japan, 141-144.

Schertzer, D., and S. Lovejoy (1984), On the dimension of atmospheric motions, In T. Tatsumi, ed., *Turbulence and Chaotic Phenomena in Fluids*, Amsterdam, Elselvier, 505-512.

Schertzer, D., and S. Lovejoy (1987), Physical modeling and analysis of rain clouds by anisotropic scaling multiplicative processes, *J. Geophys. Res*., *92*, 9693-9714, doi: 10.1029/JD92iD08p09693.

Schertzer, D., S. Lovejoy, and D. Lavallée (1993), Generic multifractal phase transitions and self-organized critically, In J.M. Perdang and A: . Lejeune, eds., *Cellular automata: prospects in astrophysical applications*, World Scientific, Singapore.

Schertzer, D., S. Lovejoy (1994), Multifractal generation of self-organized critically, In M. Novak, *Fractals in Natural and Applied Sciences,* Elselvier, The Netherlands, 325-339.

Schertzer, D., and S. Lovejoy, S. (1995), From scalar cascades to Lie cascades: joint multifractal analysis of rain and cloud processes, In R. A. Feddes, ed.,

Space/time variability and interdependence for various hydrological processes, Cambridge University Press, Cambridge, U.K., 153-173.

Schertzer, D., and S. Lovejoy (1996), Resolution dependence and multifractals in remote sensing and geographical information systems, Lecture Notes, McGill University, Montreal, Canada.

Schmitt, F., D. Lavallée, D. Schertzer, and S. Lovejoy (1992), Empirical determination of universal multifractal exponents in turbulent velocity fields, *Phys. Rev. Lett.*, *68*, 305-308.

Schmitt, F., D. Schertzer, S. Lovejoy, and Y. Brunet (1993), Estimation of universal multifractal indices for atmospheric turbulent velocity fields,, *Fractals*, 1, 568-575.

Schmitt, F., D. Schertzer, S. Lovejoy, and Y. Brunet (1994), Empirical study of multifractal phase transitions in atmospheric turbulence, *Nonlin. Proc. Geophys.*, *1*, 95-104, doi:10.5194/npg-1-95-1994.

Schernewski, G., V. Podsetchine, and T. Huttula (2005), Effects of the flow field on small scale phytoplankton patchiness, *Nord. hydrol., 36*, 85-98.

Serra, T., J. Colomer, M. Soler, R. Julia, and X. Casamitjana (2005), Behaviour and dynamics of a hydrothermal plume in Lake Banyoles, Catalonia,NE Spain. *Sedimentology,* 52 (4), 795-808.

Seuront, L., F. Schmitt, Y. Lagadeuc, D. Schertzer, and S. Lovejoy (1999), Multifractal as a tool to characterize multiscale inhomogeneous patterns: Example of phytoplankton distribution in turbulent coastal waters, *J. Plankton Res., 21*, 877-922.

Seuront, L., F. Schmitt, and Y. Lagadeuc (2001), Turbulence intermittency, small-scale phytoplankton patchiness and encounter rates in plankton: where do we go from here?, *Deep-Sea Res. I, 48*, 1199-1215.

Seuront, L., and F.G. Schmitt (2005), Multiscaling statistical procedures for the exploration of biophyisical couplings intermittent turbulence. Part II. Applications, *Deep Sea Res. II*, *52*, 1325-1343, doi: intermi10.1016/j.dsr2.2005.01.005.

Seuront, L., H. Yamazaki, and F. G. Schmitt (2005), Intermittency, In H. Baumert, J. Sündermann, and J. Simpson, eds., *Marine Turbulence: Theories, Observations and Models,* Cambridge, U. K.,66-78.

Shimeta, J., P. A. Jumars, and E. J. Lessard (1995), Influences of turbulence on suspension feeding by planktonic protozoa; experiments in laminar shear fields, *Limnol. Oceanogr., 40*, 845-859.

Sharples, J., C. M. Moore, and E. R. Abraham (2001), Internal tide dissipation, mixing, and vertical nitrate flux at the shelf edge of NE New Zealand. *J. Geophys. Res., 106*(C7), 14069-14081.

Smyth, W. D., and J. N. Moum (2000), Length scales of turbulence in stably stratified mixing layers, *Phys. Fluids, 12*, 1327-1342, doi:10.1063/1.870385.

Smyth, W. D., J. N. Moum, and D.R. Caldwell (2001), The efficiency of mixing in turbulent patches: inferences from direct numerical simulations and microstructure observations, *J. Phys. Oceanogr., 31*, 1969-1992.

Smyth, W. D., J. D. Nash, and J. N. Moum (2005), Differential diffusion in breaking Kelvin-Helmholtz billows, *J. Phys. Oceanogr*., 35, 1004–1022.

Smyth, W. D., and J. N. Moum (2012), Ocean mixing by Kelvin-Helmholtz instability, *Oceanography*, *25*(2), 140-149.

Smyth, W. D., and S. A. Thorpe (2012), Glider measurements of overturning in a Kelvin-Helmholtz billow train, *J. Mar. Res.*, *70*(1), 119-140.

Solé, R. V., and J. Bascompte (2006), *Self-Organization in Complex Ecosystems (MPB-42),* 373 pp, Princeton University Press, Princeton, NJ.

Spiegel, M. R. (1982), *Mathematical Handbook of Formulas and Tables*, 271 pp., McGraw Hill, New York, NY.

Squires, K.D., and H. Yamazaki (1995), Preferential concentration of marine particles in isotropic turbulence, *Deep Sea Res*., *42*, 1989-2004, doi: 10.1016/0967-0637(95)00079-8.

Sreenivasan, K. R., and P. Kailasnath (1993), An update on the intermittency exponent in turbulence, *Phys. Fluids A*, 5, 512-514, doi: 10.1023/B: APPL.0000044408.46141.026.

Sreenivasan, K. R. (1995), On the universality of the Kolmogorov constant, *Phys. Fluids, 7*(11), 2778-2784.

Sreenivasan, K. R., and R. A. Antonia (1997), The phenomenology of small-scale turbulence, *Annu. Rev. Fluid Mech*., *29*, 435-472, doi: 10.1146/annurev.fluid.29.1.435.

Sreenivasan, K. R., and B. Dhruva (1998), Is there scaling in high-Reynolds-number turbulence?, *Prog. Theoret. Phys. Supp*., *130*, 103-120.

Staquet, C., and P. Bouruet-Aubertot (2001), Mixing in weakly turbulent stably stratified flows, *Dyn. Atmos. Oceans, 34*, 81-102, doi. 10.1016/S0377-0265(01)00062-8.

Stansfield, K., C. Garrett, and R. Dewey (2001),The probability distribution of the Thorpe displacement within overturns in Juan de Fuca Strait, *J. Phys. Oceanogr., 31*, 3421-3434.

Stashchuk, N., V. Vlasenko, and K. Hutter (2005), Numerical modelling of disintegration of basin-scale internal waves in a tank filled with stratified water, *Nonlin. Proc. Geophys., 12*(6), 955-964.

Stewart R. W., and H. L. Grant (1962), Determination of the rate of dissipation of turbulent energy near the sea surface in the presence of waves, *J. Geophys. Res*., 67(8), 3177-3180.

Stillinger, D. C., K. N. Helland, and C. W. Van Atta (1983), Experiments on the transition of homogeneous turbulence to internal waves in a stratified fluid, *J. Fluid Mech., 131*, 91-122.

Strang, E. J., and H. J. S. Fernando (2001), Entrainment and mixing in stratified shear flows, *J. Fluid Mech.*, *428*, 349-386.

Stretch, D. D., J. W. Rottman, S. K. Venayagamoorthy, K. K. Nomura, and C. R. Rehmann (2010), Mixing efficiency in decaying stably stratified turbulence. *Dyn. Atmos. Oceans*, *49*(1), 25-36.

Strikwerda, J. (2004), *Finite differences schemes and partial differential equations,* SIAM Editions, Pacific Groove, CA.

Sutherland, J., D. J. R. Walstra, T. J. Chesher, L. C. Van Rijn, and H. N. Southgate (2004), Evaluation of coastal area modelling systems at an estuary mouth, *Coastal Eng.*, 51, 119–142.

Tennekes, H., and J. L. Lumley (1972), *A First Course in Turbulence*, 300 pp., MIT Press, Cambridge, Mass.

Teague, W. J., H. T. Perkins, Z. R. Hallock, and G. A. Jacobs (1998), Current and tide observations in the southern Yellow Sea. *J. Geophys. Res.*, *103*(C12), 27783-27793.

Tessier Y., S. Lovejoy, and D. Schertzer (1993), Universal multifractals in rain and clouds: theory and observations, *J. Appl. Meteor., 32*, 223-250.

Thompson, A. F., S. T. Gille, J. A. MacKinnon, and J. Sprintall (2007), Spatial and temporal patterns of small-scale mixing in Drake Passage, *J. Phys. Oceanogr.*, *37*(3), 572-592.

Thorpe, S. A. (1977), Turbulence and mixing in a Scottish loch, *Philos. Trans. Roy. Soc. London, 286A*, 125-181.

Thorpe, S. A., J. M. Keen, R. Jian, and U. Lemmin (1996), High-frequency internal waves in Lake Geneva, Philos. Trans. R. Soc. Lond. A, 354, 237–257.

Thorpe, S. A. (2005), *The Turbulent Ocean*, 439 pp, Cambridge University Press, Cambridge, U.K.

Timmermans, M. L., C. Garrett, and E. Carmack (2003), The thermohaline structure and evolution of the deep waters in the Canada Basin, Arctic Ocean, *Deep-Sea Res. I, 50*, 1305-1321.

Troy, C. D., and J. R. Koseff (2005), The instability and breaking of long internal waves, *J. Fluid Mech.*, *543*, 107-136.

Turner, J. S. (1973), *Buoyancy effects in fluids*, 368 pp, Cambridge University Press, Cambridge, New York,NY.

Tyson, R. K. (1991), *Principles of Adaptative Optics*, 298 pp., Academic, San Diego, Calif.

Tweddle, J. F., J. Sharples, M. R. Palmer, K. Davidson, and S. McNeill (2013), Enhanced nutrient fluxes at the shelf sea seasonal thermocline caused by stratified flow over a bank, *Progr. Oceanogr.*, *117*, 37-47.

Uberoi, M. S., and P. Freymuth (1969), Spectra of turbulence in wakes behind circular cylinders, *Phys. Fluids A*, *12*, 1359-1363.

Uchaikin, V. M., and V. M. Zolotarev (1999), *Chance and stability: stable distributions and their applications*, VSP BV, Zeist, The Netherlands.

Uda, M. (1966), Yellow Sea, In K. W. Fairbridge, ed., *Encyclopedia of Oceanography*, 1021 pp, Van Nostrand and Reinhold, New York, NY.

Ullman, D. S., A. C. Dale, D. Hebert, and J. A. Barth (2003), The front on the Northern Flank of Georges Bank in spring: 2. Cross‐frontal fluxes and mixing. *J. Geophys. Res., 108*(C11), 8010, doi:10.1029/2002JC001328, 2003

Valerio, G., M. Pilotti, C. Luisa Marti, and J. Imberger (2012), The structure of basin-scale internal waves in a stratified lake in response to lake bathymetry and wind spatial and temporal distribution: Lake Iseo, Italy, *Limnol. Oceanogr.*, *57*(3), 772.

Van Atta, C. W., and W. Y. Chen (1970), Structure functions of turbulence in the atmospheric boundary layer over the ocean, *J. Fluid Mech.*, *44*, 145–159.

Venayagamoorthy, S. K., and O. B. Fringer (2012), Examining breaking internal waves on a shelf slope using numerical simulations, *Oceanography*, 25(2), 132–139, doi: 10.5670/oceanog.2012.48

Veneziano, D., and A. Langousis (2010), Scaling and fractals in hydrology, In B. Sivakumar and R. Berndtsson, *Advances in data-based approaches for hydrologic modeling and forecasting*, 145 pp, World Scientific, Singapore.

Vidal-Vazquez, E., J. G. V. Miranda, and J. Paz-Ferreiro (2010), A multifractal approach to characterize cumulative rainfall and tillage effects on soil surface micro-topography and to predict depression storage, *Biogeosciences*, *7*, 2989-3004.

Voulgaris, G., and J. H. Trowbridge (1998), Evaluation of the Acoustic Doppler Velocimeter (ADV) for turbulence measurements, *Journal of Atmos. Ocean. Tech.*, *15*(1), 272-289.

Wain, D. J., and C. R. Rehmann (2010), Transport by an intrusion generated by boundary mixing in a lake, *Water Resour. Res.*, *46*, W08517, doi:10.1029/2009WR00839.

Washburn, L., and C. H. Gibson (1984), Horizontal variability of temperature microstructure at the base of a mixed layer during MILE, *J. Geophys. Res.*, *89*(C3), 3507-3522.

Watanabe, T., and T. Gotoh (2004), Statistics of a passive scalar in homogeneous turbulence, *New J. of Phys.*, *6*, 40.

Watson, B. P., S. Lovejoy, Y. Grosdidier, and D. Schertzer (2009), Scattering in thick multifractal clouds. Part I: overview and single scattering, *Physica A*, *388*, 3695-3710.

Weibull, W. (1951), A statistical distribution function of wide applicability, *Journal of Appl. Mech., 18*, 293-297.

Wells, J. R., and K. R. Helfrich (2004), A laboratory study of localized boundary mixing in a rotating stratified fluid, *J. Fluid Mech.*, *516*, 83–113.

Wijesekera, H. W., T. M. Dillon, and L. Padman (1993), Some statistical and dynamical properties of turbulence in the ocean pycnocline, *J. Geophys. Res.*, *C12*, 22665-22679.

Wijesekera, H. W., and T. M. Dillon (1997), Shannon entropy as an indicator of age for turbulent overturns in the oceanic thermocline, *J. Geophys. Res.*, 102 (C2), 3279-3291.

Wilson, R., F. Dalaudier, and H. Luce (2011), Can one detect small-scale turbulence from standard meteorological radiosondes?, *Atmospheric Measurement Techniques Discussions*, *4*(1), 969-1000.

Woods, J. D. (1968), Wave-induced shear instability in the summer thermocline. *J. Fluid Mech.*, *32*(04), 791-800.

Wu, J. (1994), Altimeter wind and wind-stress algorithms: further refinement and validation, *J. Atmos. Oceanic Technol., 11*, 210–215.

Wüest, A., D. C. Van Senden, J. Imberger, G. Priepke, and M. Gloor (1996), Comparison of diapycnal diffusivity measured by tracer and microstructure techniques, *Dyn. Atmos. Oceans, 24*, 27-39, doi: 10.1016/0377-0265(95)00408-4.

Wüest, A., G. Priepke, and D. C. Van Senden (2000), Turbulent kinetic energy balance as a tool for estimating vertical diffusivity in wind-forced stratified waters, *Limnol. Oceanogr., 45*, 1388-1400.

Wüest, A., and A. Lorke (2003), Small-scale hydrodynamics in lakes, *Annu. Rev. Fluid Mech., 35*, 373-412, doi:10.1146/annurev.fluid.35.101101.161220.

Xiaohui, T., W. Fan, C. Yongli, B. Hong, B., and H. Dunxin (2004), Current observations in the southern Yellow Sea in summer, *Chin. J. Oceanol. Limn.*, *22*(3), 217-223.

Xing, F., Y. P. Wang, and H. V. Wang (2012), Tidal hydrodynamics and fine-grained sediment transport on the radial sand ridge system in the southern Yellow Sea, *Mar. Geol.*, *291*, 192-210.

Xu, L. L., D. X. Wu, X. P. Lin, and C. Ma (2009), The study of the Yellow Sea Warm Current and its seasonal variability, *Journal of Hydrodyn. Ser. B*, *21*(2), 159-165.

Yaglom, A.M. (1966), The influence of fluctuations in energy dissipation on the shape of turbulent characteristics in the inertial interval, *Sov. Phys. Dokl.*, 2, 26.

Yamazaki, H., and R. Lueck (1987), Turbulence in the California Undercurrent, *J. Phys. Oceanogr., 17*, 1378–1396.

Yamazaki, H. (1990), Breakage models: Intermittency and log-normality, *J. Fluid Mech., 219*, 181-193, doi:10.1017/S0022112090002907.

Yamazaki, H., and D. Kamykowski (1991), The vertical trajectories of motile phytoplankton in a wind-mixed water column, *Deep-Sea Res., 38*, 219-248.

Yanagi, T., A. Morimoto, and K. Ichikawa (1997), Seasonal variation in surface circulation of the East China Sea and the Yellow Sea derived from satellite altimetric data, *Cont. Shelf Res.*, *17*(6), 655-664.

Yeates, P. S., A. Gómez-Giraldo, and J. Imberger (2013), Observed relationships between microstructure patches and the gradient Richardson number in a thermally stratified lake, *Env. Fluid Mech., 13*(3), 205-226.

Zhao, Z., M. H. Alford, J. Girton, T. M. S. Johnston, and G.S. Carter. (2011), Internal tides around the Hawaiian Ridge estimated from multisatelliate altimetry.*J.Geophys.Res.41*,JC12041,doi: 10.1029/2011JC007045.

Zhou, D., Y. B. Liang, C.K. Tseng (1994), *Oceanology of China Seas,* Vol.1, 565 pp, Kluivert Academic Publishers, Dordrecht, The Netherlands.

Zhou, T., Z. Hao, L. P. Chua, S. C. M. Yu (2005), Scaling of longitudinal and transverse velocity increments in a cylinder wake, *Phys. Rev. E, 71*, 066307.

Zhou, T., Z. Hao, L. P. Chua, Y. Zhou (2006), Comparisons between different approximations to energy dissipation rate in a self-preserving far wake, Phys. Rev. E, 74, 0560308.

Appendixes

A. Turbulent kinetic energy budget and calculations of the energy dissipation rate

A.1. Navier-Stokes equations and turbulent kinetic energy budget

The movement of any arbitrary parcel of water in a flow is governed by the Navier-Stokes equations, which takes into account three basic principles:

- Newton's second law.
- The constitutive law (Newton's law of viscosity), which relates the shear stress in a fluid to the rate of change of its deformation over time.
- The conservation of mass (continuity equation).

The Navier-Stokes equation for the velocity field $\vec{u}$ of an incompressible flow is expressed as (Kundu, 1990):

$$\frac{\partial \vec{u}}{\partial t} + \vec{u} \cdot \nabla \vec{u} = -\frac{\nabla P}{\rho} + \nu \nabla^2 \vec{u} + \vec{F} \tag{A.1}$$

where P is the pressure, ρ is the density, $\vec{F}$ is the external force and ν the kinematic viscosity.

The presence of non-linear terms in the equation is responsible for turbulence. The transition from a 'laminar' to 'turbulent' regime is governed by a dimensionless parameter, called the Reynolds number, which measures the ratio between the inertial forces (non-linear advective term) to the viscous forces (linear viscous damping), i.e.

$$\mathrm{Re} = \frac{u \cdot L}{\nu} \tag{A.2}$$

with u and L being the characteristic length scale and velocity of the fluid. Although some exact solutions of the equations of the Navier-Stokes do exist (Poiseuille flow for example), they are very difficult to solve at high Reynolds numbers (fully developed turbulence) because of the large number of scales involved.

Turbulence can be also analyzed from a statistical approach. Considering the turbulent quantities as random variables, instantaneous values of these quantities are decomposed into their mean part and the fluctuations around the mean, the so-called Reynolds decomposition. Using this decomposition it is possible to obtain equations for the mean quantities and also for their fluctuations (variances).

Following previous discussion, any component of the velocity field $\tilde{u}_i$ can be written using the Reynolds decomposition as $\tilde{u}_i = U_i + u_i$, with $i = 1,2,3$ being any of the space coordinates. Combining the resulting equations, a general balance for the turbulent kinetic energy (*TKE*), defined as $TKE = 1/2\sum_i \overline{u_i^2}$, is obtained. The *TKE* budget of a turbulent flow is expressed as

$$\frac{\partial}{\partial t}\left(\frac{1}{2}\overline{u_i^2}\right) = -\frac{\partial}{\partial x_j}\underbrace{\left(\frac{1}{\rho}\overline{p'u_j} + \overline{\frac{1}{2}u_i^2 u_j} - 2\nu\overline{u_i e_{ij}}\right)}_{A} - \underbrace{\overline{u_i u_j}\frac{\partial U_i}{\partial x_j}}_{B} - \underbrace{\rho' u_i \frac{g_i}{\rho}}_{C} - \underbrace{2\nu\overline{e_{ij}e_{ij}}}_{D} \qquad \text{(A.3)}$$

with $e_{ij} = 1/2 \cdot \left(\partial u_i/\partial x_j + \partial u_j/\partial x_i\right)$, known as the strain rate vector, U_i and u_i are, respectively, the mean velocity and its corresponding fluctuation for the component i (i.e. also j); $\vec{g}$ is the gravity vector, p' the pressure fluctuations and ρ and ρ' are, respectively, the mean value of the density and its fluctuation.

The physical meaning of each term is described next (Kundu, 1990):

- *Transport term* (A): Three first terms are divergences (spatial gradients). They are neither sources nor sinks and represent the spatial transport of turbulent kinetic energy. If *TKE* is locally produced and dissipated, they can be neglected.
- *Shear production* (B): This represents the loss of mean kinetic energy, i.e. the gain of turbulent kinetic energy due to the interaction of the Reynolds stress ($\overline{u_i u_j}$) and the mean shear $\partial U_i/\partial x_j$.

- *Buoyant production* (C): This represents the loss of turbulent kinetic energy working against a stable stratification. However, in unstable conditions, this term also becomes a production term.
- *Kinetic energy dissipation rate* (D): Symbolized by ε, it accounts for that part of the *TKE* which is converted into heat due to the viscous forces. It is of the order of the turbulent production terms and can be estimated by different direct or indirect methods.

A.2. The kinetic energy dissipation rate

Equation (A.3) of the *TKE* describes the balance between the terms of production, transport and destruction of *TKE.* Specifically, the instantaneous rate of the energy dissipation ε_0 of the *TKE* is defined as (Zhou et al., 2006)

$$\varepsilon_0 = 2\nu e_{ij} e_{ij} = -\frac{\nu}{2}\sum_{i,j=1}^{3}\left(\frac{\partial u_i}{\partial x_j} - \frac{\partial u_j}{\partial x_i}\right) \tag{A.4}$$

where $i, j = 1,2,3$ represents the coordinate axes, u_i the velocity components of the velocity field, i.e. u,v and w, and x_i the respective spatial coordinates. The instantaneous dissipation rate ε_0 is generally decomposed into longitudinal, transversal and asymmetric components, which can be directly measured by instruments

$$\varepsilon_0 = \nu\sum_{i,j=1}^{3}\left[2\left(\frac{\partial u_i}{\partial x_i}\right) + \left(\frac{\partial u_i}{\partial x_j}\right) - \frac{\partial u_i}{\partial x_j}\cdot\frac{\partial u_j}{\partial x_i}\right] \tag{A.5}$$

For a practical point of view we are interested in the mean energy dissipation rate $\tilde{\varepsilon}$, which is the average of the instantaneous energy dissipation rate, i. e. $\tilde{\varepsilon} \equiv \bar{\varepsilon}_0$. In the experiments conducted in the field, determining the instantaneous dissipation rate ε_0 is a very complicated matter, because it is difficult to measure all the derivatives simultaneously. In fact, instruments allow derivatives to be obtained along a specific direction of the flow. For example, in aquatic systems, it is possible to compute longitudinal velocity

gradients with the help of hotwire and transverse probes, such as ADVs and vertical microstructure profilers. In this latter case, profilers include shear airfoil sensors which directly measure small-scale shear. Also, in the atmosphere, hotwire and sonic anemometers have been used to calculate the gradients of any component of the velocity field along the streamwise direction of the wind.

The traditional way of estimating ε_0 is using only one derivative, which assumes homogenous isotropic turbulence. Then, the equation (A.5) for ε_0 can be expressed (Hinze, 1975) as

$$\varepsilon_{iso} = 7.5\nu\left(\frac{\partial u_i}{\partial x_j}\right)^2 \tag{A.6}$$

where u_i represents any component of the velocity and x_j a direction normal to it. Only if the distance between the points is small can the derivatives $\partial u_i/\partial x_j$ be approximated by their gradients, $\Delta u_i/\Delta x_j$, and the expression (A.6) is called for different authors as the small-scale energy dissipation field (Meneveau and Sreenivasan, 1991; Lauren et al., 2001; Zhou et al., 2006). Then, the mean dissipation rate $\tilde{\varepsilon}$ for a segment of interest corresponds to the variance of the velocity derivatives

$$\tilde{\varepsilon} = \tilde{\varepsilon}_{iso} = 7.5\nu\overline{\left(\frac{\partial u_i}{\partial x_j}\right)^2} \tag{A.7}$$

In addition, the variance can also be computed by integrating the measured transverse-shear spectrum:

$$\tilde{\varepsilon} = 7.5\cdot\nu\int_{\tilde{k}_0}^{\tilde{k}_{max}} E_{sh}\left(\tilde{k}\right)d\tilde{k} \tag{A.8}$$

where the shear spectrum $E_{sh}\left(\tilde{k}\right)$ is expressed as a function of the wave number $\tilde{k}$ with $\tilde{k} = 2\pi/\ell$ (rad·m^{-1}) and ℓ the wavelength, the representative measure of the size of the turbulent eddies. The upper and the lower integration limits correspond to the highest wave number not contaminated by noise and the upper limit for the inertial subrange (i.e. the external wave number),

respectively. This method is usually known as *the variance method*. However, if scales are far from the Kolmogorov scale, which is the case of very energetic segments or signals contaminated by noise on small scales, part of the total variance is lost. Therefore, different methodologies must be applied to properly estimate the value of the dissipation rate $\tilde{\varepsilon}$ (Prandke and Stips, 1998; Fer and Paskyabi, 2014).

Another procedure to estimate the mean dissipation rate in a specific segment, widely used in oceanography, consists of obtaining the best fit of the measured shear spectrum to one of the universal forms derived theoretically (Panchev and Kesich, 1969, abbreviated as PK69) or analytically (Nasmyth, 1970). During the last decade, our research group has been working on spectrum techniques, offering new formulas and improving fitting methods, which have been tested on field using microstructure profilers, in order to estimate $\tilde{\varepsilon}$ accurately (Roget et al., 2006; Sanchez et al., 2011; Roget, 2013). In this way, we have discussed several options to evaluate $\tilde{\varepsilon}$, using not only shear spectra, but also different temperature (scalar) ones (i.e. the Batchelor and Kraichnan spectra), as is detailed in Sanchez et al. (2011). In this latter case, the temperature spectra depend on two parameters, the temperature variance χ_T and the dissipation rate ε, which are required to estimate χ_T in order to obtain ε. Next, we describe the method to directly obtain $\tilde{\varepsilon}$ from fitting the small-scale shear to fitting the PK69 spectrum, developed by our group and as described in Sanchez et al. (2011). In the article, this procedure is also proposed in order to obtain $\tilde{\varepsilon}$ from the other spectra.

Values of mean dissipation rate are estimated by fitting the measured shear spectrum $E_{sh}\left(\tilde{k}\right)$ to the analytical form of the one-dimensional PK69 transverse spectrum $E_{sh}^{PK}\left(\tilde{k}\right)$, as given by Roget et al. (2006). Panchev and Kesich (1969) theoretically derived the expression for the three-dimensional spectrum of the velocity field in the equilibrium range (i.e. inertial and viscous subranges), but no analytical solution was possible for the one-dimensional

case. Thus, Roget et al. (2006) numerically integrated the three-dimensional PK69 spectrum and from the results they proposed the following formula for the one-dimensional case,

$$E_{sh}^{PK}\left(\tilde{k}\right) = 0.9372\,\tilde{k}^{0.3748}\exp\left(-6.011\tilde{k}^{1.548}\right) \tag{A.9}$$

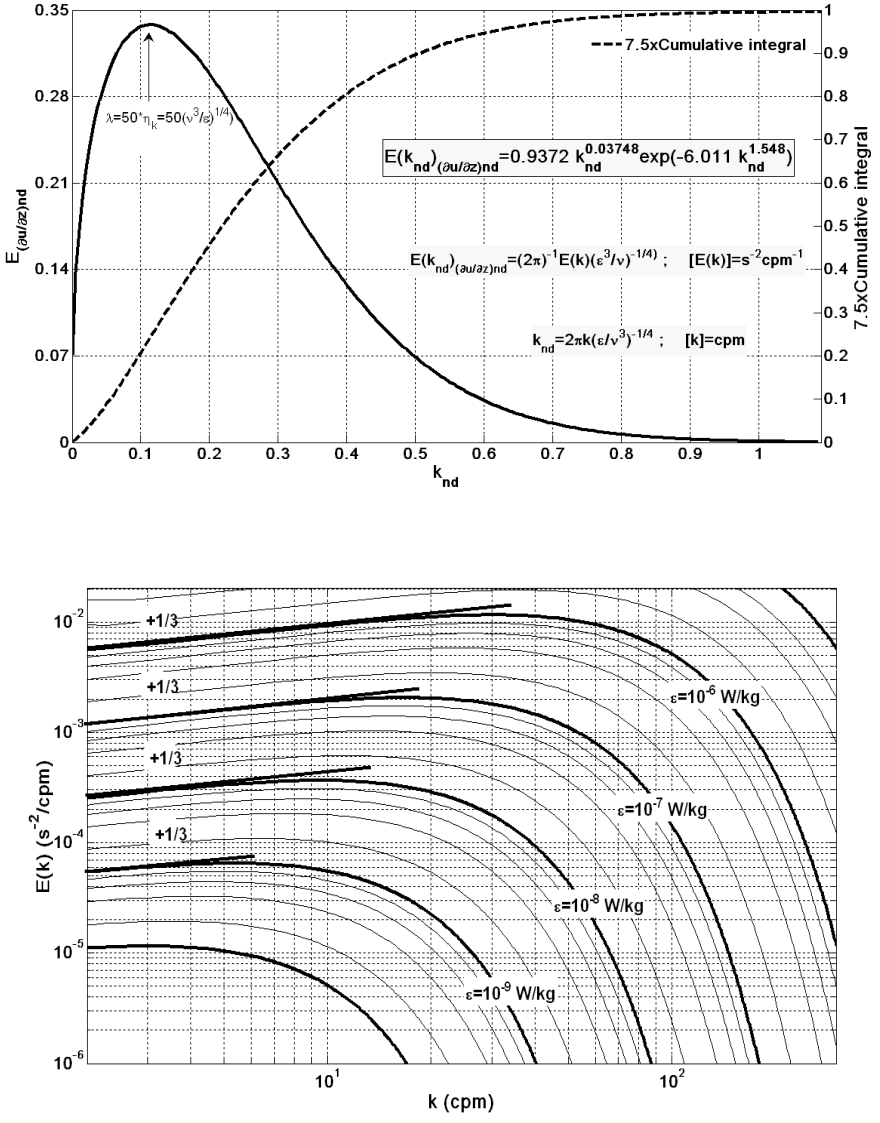

Fig. A.1 (a) Non-dimensional 1D Panchev–Kesich transversal shear spectra and its cumulative integral, which is normalized along the lines of $\varepsilon = 1$, plotted as a function of the non-dimensional wave number k_{nd} . See the maximum of dissipation of ~ $50\eta_K$ (b) Several dimensional 1D Panchev–Kesich transversal shear spectra. Straight lines with 1/3 slopes corresponding to the inertial subrange are also indicated in the plot (extracted from Roget, 2013).

In this expression, the constant values are given by Roget et al. (2006) and Roget et al. (2007). Higher precision coefficient are given by Sanchez et al.

(2011), see in Fig. A.1a. In oceanographic units, $k = \tilde{k}/2\pi$ (cpm = m^{-1}) and the spectrum is expressed as $E_{sh}^{PK}(k) = 2\pi E_{sh}^{PK}(\tilde{k})$. Different energetic levels for the theoretical one-dimensional spectrum $E_{sh}^{PK}(k)$ are shown in Fig. A.1b.

The 1D spectrum $E_{sh}^{PK}(k)$ presents the following characteristics, which are also shown in Fig. A.1a:

- It has a maximum of dissipation near the wave number $k = 1/\ell_{\nu\max}$ with $\ell_{\nu\max} = (2\pi/0.13)\eta_K \sim 50\eta_K$. At this wave number the spectrum drops because of the molecular viscosity effects, which become important.
- The integral of $E_{sh}^{PK}(k)$ up to wave number $k_c = 0.513/\eta_K$ accounts for 90% of the total variance. If this is extended to the Kolmogorov wave number $k_K = 1/\eta_K$, the integral accounts for 99.8% of the total variance.

The fitting of the measured shear spectrum to the model given by (A.9) is performed in a range of $k \in [k_{min}, k_{max}]$. The lowest wave number $k_{\min}$ corresponds to the smallest value that we could obtain from the size of the window used to compute the spectrum. On the other hand, the highest wave number $k_{\max}$ is usually determined at the intersection point between $E_{sh}(k)$ and the proposed noise model. However, it is also possible to define $k_{\max}$ as the critical value at which the deviation of $E_{sh}(k)$ from noise exceeds a predefined threshold. Then, the lowest wave number is taken as the cut-off wave number to compute the best fit. The fitting is performed using the *method of the maximum likelihood*, as proposed by Ruddick et al. (2000). The method introduces the likelihood function which depends on the measured shear spectrum and parameter ε. From this function the value of the parameter has to be estimated. Specifically, the value of ε that maximizes the likelihood function corresponds to the value that gives the best fit to the model. Then, an iteration algorithm allows ε to be determined accurately. As the likelihood function tends to the normal distribution, the error associated with ε can be estimated from the standard deviation.

The goodness of the fit is tested using three parameters: First, the *mean absolute deviation* (*MAD*), defined as the ratio between the experimental and the theoretical spectrum evaluated for a range of k where the noise is lower than the signal. Second, the *signal noise ratio* (*SNR*) which is the ratio between measured and noise signal. Finally, the *likelihood ratio* (*LHR*), defined as a parameter which evaluates whether the experimental spectrum better fits the PK69 model or a potential law. Based on measurements obtained from free-falling microstructure profilers, we have proposed values of $MAD \leq 0.3$, $SNR \leq 1.3$ and $LHR \geq 2$ for the acceptance of the fit. Specifically, the value of MAD is more restrictive than the value suggested by Ruddick et al. (2000). This allows a more precise fit to be obtained and thus, a more accurate value of ε.

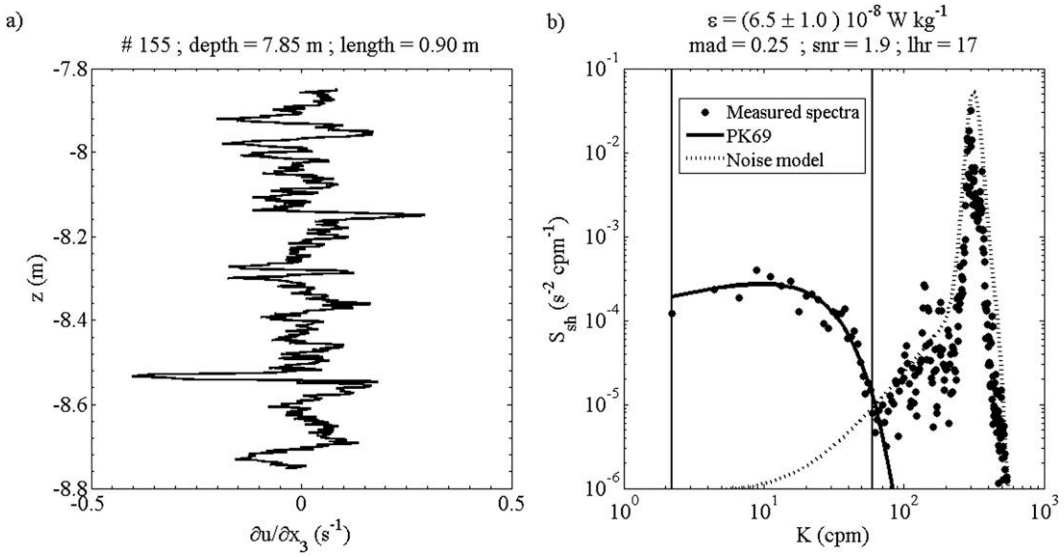

Fig. A.2 (a) Measured shear profile and (b) the corresponding shear spectrum, plotted as a function of wave number *k* (cpm). The best fit of the spectrum to the PK69 model is marked as a solid line and the noise model as a dotted line. Vertical lines indicate the range of the wave numbers at which the fit is performed (Sanchez et al., 2011).

An example of a measured microstructure shear signal, $\partial u/\partial x_3$ for an accepted segment and its corresponding shear spectrum $E_{sh}(k)$ is shown in Fig. A.2. Data were obtained from a microstructure profiler during a field campaign carried out in Lake Banyoles, Catalonia (Spain); as described in detail in Chapter 3, subsection 3.1. The estimated value of ε and its associated error are shown at the top of Fig. A.2b, along with the parameters of the test.

If velocity measurements are available, it is also possible to obtain the dissipation based on the Kolmogorov's 'five-thirds law', which predicts that the one-dimensional velocity spectrum follows the expression

$$E(\tilde{k}) = C_K \, \tilde{\varepsilon}^{\frac{2}{3}} \, \tilde{k}^{-\frac{5}{3}} \tag{A.10}$$

where $C_K = 18/55 \, C_\varepsilon$ is for longitudinal velocity component and $C_K = 24/55 \, C_\varepsilon$ for the transversal one, $C_\varepsilon = 1.6$ is the Kolmogorov constant (Sreenivasan, 1995) and $\tilde{k}$ the wave number (in rad·m^{-1}). Expressed in oceanographic units, this equation can be rewritten as

$$E(k) = 2\pi C_K \, \tilde{\varepsilon}^{\frac{2}{3}} \, k^{-\frac{5}{3}} \tag{A.11}$$

The slope of the logarithmic plot of $E(k)$ as a function of k allows the value of $\tilde{\varepsilon}$ to be estimated. However, it is usual to plot the compensated spectrum which is calculated multiplying the measured spectrum $E(k)$ by $k^{-5/3}$. If $E(k)$ obeys the scaling range shown by (A.11), the plot of the compensated spectrum $E(k) \cdot k^{5/3}$ is independent of the wave number k. Thus, it exhibits a flat behavior over scales in the inertial subrange and from (A.11)

$$E(k) \, k^{\frac{5}{3}} = 2\pi \, C_K \, \tilde{\varepsilon}^{\frac{2}{3}} \tag{A.12}$$

If *A* is the constant value of the compensated spectrum $E(k) \, k^{5/3}$ estimated from the plot, it is possible to estimate the value of the mean dissipation rate $\tilde{\varepsilon}$ through (A.12)

$$\tilde{\varepsilon} = \left(\frac{A}{2\pi C_K} \right)^{\frac{3}{2}} \tag{A.13}$$

The same procedure can be also done with the wave numbers $\tilde{k}$ and $E(\tilde{k})$.

A.3. The vertical diffusivity K_ρ

Another important parameter used to analyze turbulence in a water body is the vertical eddy diffusivity K_ρ. It characterizes the vertical transport of mass into the water column. It can be related to the vertical density flux $\overline{\rho' w}$ using the expression

$$\overline{\rho' w} = -K_\rho \frac{\partial \rho}{\partial z} = -K_\rho N^2 \tag{A.14}$$

where N is the buoyancy frequency. The vertical eddy diffusivity indicates how efficient the turbulent mixing is in the region of study.

Also, the vertical diffusivities can be derived from the *TKE* budget, see equation (A.3). If the term of transport is neglected and stationarity is assumed, the expression for the vertical component w can be rewritten as

$$\langle uw \rangle \frac{dU}{dz} + \tilde{\varepsilon} + \frac{g\langle \rho' w \rangle}{\rho_0} = 0 \tag{A.15}$$

Defining the flux Richardson number R_f as the ratio of energy suppressed by buoyancy forces to the *TKE* production by shear, then

$$R_f = -\frac{g\langle \rho' w \rangle}{\rho_0} \Big/ \langle uw \rangle \frac{dU}{dz} \tag{A.16}$$

and the vertical eddy diffusivity K_ρ can be expressed as

$$K_\rho = \frac{R_f}{1 - R_f} \cdot \frac{\tilde{\varepsilon}}{N^2} \tag{A.17}$$

The first term is known as the mixing efficiency γ

$$\gamma = \frac{R_f}{1 - R_f} \tag{A.18}$$

Although for fully-developed turbulence $\gamma \sim 0.2$, several authors suggest that this parameter is not constant and depends on the state of turbulence (Ivey and Imberger, 1991; Smyth et al., 2001; Brucker and Sharkar, 2007).

B. The log-normal distribution

Let X be a random variable defined in a domain D and its moment-generating function $M_x(t) = \langle e^{t\,X} \rangle$, where $t \in D$. The statistical moments of X, $\langle X^n \rangle$, can be calculated as

$$\langle X^n \rangle = \left. \frac{d^n M_x(t)}{d t^n} \right|_{t=0} \tag{B.1}$$

Let Y be a random variable log-normally distributed. Then, the variable $X = log(Y)$, defined by the natural logarithm of Y, is a Gaussian distribution. The moment-generating function of Y, $M_Y(t)$ is

$$M_Y(t) = \langle e^{t \cdot Y} \rangle = \langle e^{t \cdot e^X} \rangle \tag{B.2}$$

Using (B.2), the statistical moments of the variable Y, $\langle Y^p \rangle$, are calculated as

$$\langle Y^p \rangle = \left. \frac{d^p M_Y(t)}{d t^p} \right|_{t=0} = \langle e^{t \cdot e^X} e^{pX} \rangle \Big|_{t=0} = \langle e^{pX} \rangle = M_X(p) \tag{B.3}$$

This indicates that the statistical moments of Y can be calculated from the moment-generating function of the random variable X, which corresponds to the normal distribution. The expression for $M_x(t)$ is calculated next.

Suppose that X is a normal distribution $X \sim N(\bar{x}, \sigma_x^2)$. To begin, we first consider $\bar{x} = 0$ and $\sigma_x^2 = 1$; this will then be generalized for the other cases. Consequently, $M_x(t)$ can be easily derived using the Gaussian probability distribution expression

$$M_x(t) = \langle e^{t\,X} \rangle = \int_{-\infty}^{+\infty} e^{t\,z} \frac{1}{\sqrt{2\pi}} e^{-\frac{z^2}{2}} dz = e^{\frac{1}{2}t^2} \int_{-\infty}^{+\infty} \frac{1}{\sqrt{2\pi}} e^{-\frac{(z-t)^2}{2}} dz = e^{\frac{1}{2}t^2} \tag{B.4}$$

where the final result comes from the fact that the expression under the integral is the normal distribution $N(\bar{x} = t, \sigma_x^2 = 1)$, which integrates to unity.

For a more general case $X \sim N(\bar{x}, \sigma_x^2)$, the $M_x(t)$ is given by

$$M_x(t) = \left\langle e^{tX} \right\rangle = \int_{-\infty}^{+\infty} e^{tx} \frac{1}{\sigma_x \sqrt{2\pi}} e^{-\frac{(x-\bar{x})^2}{2\sigma_x^2}} dx = e^{\frac{1}{2}\sigma_x^2 t^2 + \bar{x}t} \int_{-\infty}^{+\infty} \frac{1}{\sqrt{2\pi}} e^{-\frac{z^2}{2}} dz = e^{\frac{1}{2}\sigma_x^2 t^2 + \bar{x}t} \tag{B.5}$$

using the standardization process $z = \dfrac{x - \bar{x}}{\sigma_x}$.

Substituting $M_x(t)$ in the (B.3), the statistical moments of the log-normal distribution Y, $\left\langle Y^p \right\rangle$, are expressed as

$$\left\langle Y^p \right\rangle = M_X(p) = e^{\frac{1}{2}\sigma_x^2 p^2 + \bar{x}p} \tag{B.6}$$

Kolmogorov (1962) and Obukhov (1962) postulated in the Refined Similarity Hypothesis (RSH) that the local dissipation rate ε_r averaged over a distance $r << L$ is log-normally distributed. Then, the variable $\phi = log\left(\varepsilon_r^*\right)$, where $\varepsilon_r^* = \varepsilon_r / \tilde{\varepsilon}_r$ and $\tilde{\varepsilon}_r$ is the mean value of ε_r, i.e. $\tilde{\varepsilon}$, is Gaussian with a mean $m = \langle \phi \rangle$ and variance $\sigma^2_{log\,\varepsilon_r^*}$.

Taking the expression (B.6), the statistical moments $\left\langle \varepsilon_r^p \right\rangle$ are

$$\frac{\left\langle \varepsilon_r^p \right\rangle}{\tilde{\varepsilon}^p} = exp\left(\frac{1}{2}\sigma^2_{log\,\varepsilon_r^*} p^2 + m\,p \right) \tag{B.7}$$

For a log-normal distribution $\varepsilon_r^* \sim \Lambda\left(m, s^2\right)$ the mean value is

$$\left\langle \frac{\varepsilon_r}{\tilde{\varepsilon}} \right\rangle = e^{m + \frac{1}{2}s^2} \Rightarrow m = -\frac{1}{2}s^2 \tag{B.8}$$

where m and s^2 are the mean and the variance of $log\left(\varepsilon_r^*\right)$. Then, replacing m in the expression (B.7) and using (B.8) we obtain

$$\frac{\left\langle \varepsilon_r^p \right\rangle}{\tilde{\varepsilon}^p} = exp\left(\frac{1}{2}\sigma^2_{log\,\varepsilon_r^*} \left(p^2 - p\right) \right) \tag{B.9}$$

Kolmogorov (1962) hypothesized mean-square fluctuations of the dissipation scale as

$$\frac{\left\langle \varepsilon_r^2 \right\rangle}{\tilde{\varepsilon}^2} = C_2 \cdot \left(\frac{L}{r} \right)^{\mu}, \text{ for } \eta_K < r << L \tag{B.10}$$

where C_2 and μ are positive constants.

Then, taking the expression of $\varepsilon_r^* = \varepsilon_r / \widetilde{\varepsilon}_r$ the variance is expressed as

$$\sigma^2_{\log \varepsilon_r} = A_\varepsilon + \mu \log\left(\frac{L}{r}\right) \tag{B.11}$$

Substituting (B.11) in equation (B.9) we obtain

$$\frac{\left\langle \varepsilon_r^p \right\rangle}{\widetilde{\varepsilon}^{\,p}} = C_p \left(\frac{L}{r}\right)^{\mu p(p-1)/2} \tag{B.12}$$

C. Another multiplicative cascade models

C.1. Beyond the log-normal model : The B-model

The B-model (Yamazaki, 1990) was introduced as an improved version of the log-normal model. Considering that the smallest eddies are dissipated by viscosity, the probability distribution of the breakage coefficient W, that it is the ratio between the size of 'mother' and 'daughter' eddies, is defined in a finite domain. Thus, the possible values of w satisfy the condition $0 < w < w_{max}$. The maximum value of the random variable w corresponds to case that all the energy was dissipated in one single cell (of volume V) among all the available cells (total volume V_{eddies}). If the scale ratio between two successive breakages is λ_b, then $w_{\max}$ is equivalent to λ_b^d and shown as follows,

$$\Pr(W = w_{\max}) = \frac{V_{active}}{V_{eddies}} = \frac{1 \cdot \cancel{V}}{(r_i / r_{i+1})^d \cdot \cancel{V}} = \left(\frac{r_{i+1}}{r_i}\right)^d = \lambda_b^{-d}, \tag{C.1}$$

and then,

$$w_{max} = \frac{1}{\lambda_b^{-d}} = \lambda_b^d \tag{C.2}$$

Yamazaki (1990) proposed the *beta distribution* as a suitable probability function because it has a finite domain (Evans et al., 2000). This distribution is parameterized in terms of three parameters, a, b, and w_{max} in the following way:

$$f(w; a, b, w_{\max}) = \frac{w^{a-1} \cdot (w_{\max} - w)^{b-1}}{B(a,b) \cdot w_{\max}^{a+b-1}} \qquad \text{for } (0, w_{max}) \tag{C.3}$$

with a, b being positive parameters, and $B(a,b) = \int_0^1 t^{a-1} \cdot (1-t)^{b-1} dt$ (Mood et al., 1974).

A conservative process satisfies $\langle W \rangle = 1$. Then, taking the mean for the beta model distribution, it is possible to relate the parameter b to a and w_{max}

$$\langle W \rangle = 1 = \frac{a}{a+b} \cdot w_{max} \Rightarrow b = a \cdot (1 - w_{max}) \tag{C.4}$$

Taking the universal constants for this distribution as the mean and the variance of the natural logarithm of W, i.e. $\xi = \overline{log(W)}$ and $\theta = \overline{(log(W) - \xi)^2}$, the $K(p)$ of the moments of order p of the energy dissipation rate $\langle \varepsilon_\lambda^p \rangle$ can be expressed as

$$K(p) = p \cdot \xi + p^2 \cdot \frac{\theta}{2} \tag{C.5}$$

and the scaling exponent $S_p(r)$

$$\zeta(p) = \frac{p}{3} - \frac{p}{3}\xi - \frac{p^2}{18}\theta \tag{C.6}$$

Considering the intermittency parameter $\mu = K(2)$, (C.5) leads to

$$\mu = 2\xi + 2\theta \tag{C.7}$$

The power-spectrum of the velocity fluctuations can be written as

$$E_v(k) \approx k^{-\frac{5}{3}+\frac{2}{3}\xi+\frac{2}{9}\theta} \tag{C.8}$$

For the B-model, the power-spectrum exponent is flatter than the 'five-thirds law' predicted in the Kolmogorov theory of 1941.

The model requires some parameters, which are then introduced into the model in order to calculate the other ones. Knowing that μ is in a range between 0.2 and 0.5, Yamazaki (1990) took $\lambda_b = 5$, which was the lowest prime number giving a value of μ as less than 0.2.

The B-model has several limitations in its application because it violates the condition $\zeta(3) = 1$, one of a few exact results obtained from the Navier-Stokes equation, and does not fit well to experimental results for low and high orders moments, eventually becoming negative in this latter case. This is also observed for the log-normal distribution and has no physical sense.

C.2. Corrections to the β-model

C.2.1. The random β-model

The random β-model (Benzi et al., 1984) considers that the value of the factor β in the β-model, which represents the fraction of the space filled by

active eddies at any stage of the cascade, is not constant. Then, it can be selected in a random and independent way. Benzi et al. (1984) proposed a restricted choice with a single free parameter x, $x \in [0,1]$ with β being a random variable characterized by the following probability distribution function

$$\beta(x)\begin{cases}\frac{1}{2} & \text{with probability} \quad x \\ 1 & \text{with probability} \quad 1-x\end{cases} \tag{C.9}$$

The mean value of β is

$$\overline{\beta} = \sum_{i=1}^{2} x_i \cdot p(x_i) = (\frac{1}{2})x + 1 \cdot (1-x) = 1 - \frac{1}{2}x \tag{C.10}$$

Note that if $x = 0$, the mean value $\overline{\beta}$ is 1. Following the definition of β (see above), this means that energy flux is uniformly distributed over the whole fluid and the Kolmogorov prediction is recovered. On the other hand, if $x = 1$, then $\overline{\beta}$ = 0.5. Thus, in the formulation of the random β-model, at least half of the whole volume shows turbulent activity.

Recalling the probability distribution function for the breakage coefficient W defined for the β-model is

$$\begin{cases} Pr(W = \frac{1}{\beta}) = \beta & \text{'alive' sub-eddy} \\ Pr(W = 0) = 1 - \beta & \text{'dead' sub-eddy} \end{cases} \tag{C.11}$$

The expression for the scaling exponent of the moments of $\langle \varepsilon_\lambda^p \rangle$ can be calculated from the probability distribution function of W following (5.17). This yields

$$\langle W^p \rangle = \sum_{i=1}^{2} {w_i}^p \cdot p(w_i) = (\beta)^{-p} \cdot \frac{1}{\beta} = \beta^{-p+1} = x \cdot (2^{p-1} - 1) + 1 \tag{C.12}$$

And the scaling exponents $K(p)$

$$K(p) = log_{\lambda_b} [x \cdot (2^{p-1} - 1) + 1] \tag{C.13}$$

For the exponents of $S_p(r)$ we obtain

$$\zeta(p) = \frac{p}{3} - log_{\lambda_b}\left[x \cdot \left(2^{\frac{p}{3}-1} - 1\right) + 1\right] \tag{C.14}$$

The random β-model fits well to the experimental data and for that reported by Anselmet et al. (1984) a good fit is obtained for $x = 0.125$. However, the application of random β-model is controversial because the value of $\zeta(0) \neq 0$ and this contradicts the mathematical definition of the structure functions.

C.2.2. The bifractal model

A simple correction to the monofractal models (β and random β models) can be made if we imagine the whole space covered by two fractal sets, S_1 and S_2. In this way, bifractality (Frisch, 1995) introduces more elaborate models, which lie between the monofractal and the completely developed multifractal models.

In the bifractal model the results obtained for the β-model are extended to both sets. If the codimensions of each of the sets are c_1 and c_2 respectively, the probability distribution of the normalized dissipation rate $\varepsilon^*_{\lambda,i}$ is defined as

$$\begin{cases} \Pr(\varepsilon^*_{\lambda,i} = \lambda^{c_i}) = \lambda^{-c_i} \\ \Pr(\varepsilon^*_{\lambda,i} = 0) = 1 - \lambda^{-c_i} \end{cases} \tag{C.15}$$

where the upper-index $i = 1,2$ indicates the respective sets which cover the space.

Because of that, the dissipation rate ε_λ is related to the normalized one ε^*_λ by the mean dissipation rate $\tilde{\varepsilon}$, i.e. $\varepsilon_\lambda = \tilde{\varepsilon}\varepsilon^*_\lambda$, and the *p*-order moments of the dissipation rate $\left\langle \varepsilon^p_\lambda \right\rangle$ are

$$\left\langle \varepsilon^p_\lambda \right\rangle = \tilde{\varepsilon}_1 \cdot \lambda^{c_1 p} \lambda^{-c_1} + \tilde{\varepsilon}_2 \cdot \lambda^{c_2 p} \lambda^{-c_2} = \tilde{\varepsilon}_1 \cdot \lambda^{c_1(p-1)} + \tilde{\varepsilon}_2 \cdot \lambda^{c_2(p-1)} \tag{C.16}$$

If $\left\langle \varepsilon^p_\lambda \right\rangle \approx \lambda^{K(p)}$, then

$$K(p) = min\left[c_1(p-1), c_2(p-1)\right] \tag{C.17}$$

Working along similar lines for the *p*-order structure function $S_p(r)$, the scaling exponents can be expressed as

$$\zeta(p) = min\left[\frac{p}{3} + c_1\left(\frac{p}{3}-1\right), \frac{p}{3} + c_2\left(\frac{p}{3}-1\right)\right] \tag{C.18}$$

The expression obtained for exponents of the moments and structure functions can be interpreted as a superposition of two power-laws (Frisch, 1995). In the inertial subrange (i.e. $r << L$), the power-law with the smallest exponent dominates. However, the dominance of the first or second term in $\left\langle \varepsilon_\lambda^p \right\rangle$ or $S_p(r)$ also depends on the value of *p*.

C.2.3. The *p*-model

In the *p*-model (Meneveau and Sreenivasan, 1987), the energy flux at any step of the cascade is binomially distributed in the whole space; instead of being concentrated in a fraction of the volume as it is the case in the monofractal models.

The model starts with an initial eddy size of $r_1 = L$ (i.e. the integral scale of turbulence) with a total energy flux $\tilde{\varepsilon}$. It is broken into λ_b^d eddies of equal size $r_2 = L/\lambda_b$, where d represents the spatial dimension and λ_b the breakage scale ratio. Meneveau and Sreenivasan (1987) choose λ_b = 2 and $d = 1$. The simplest nontrivial choice is that, in the

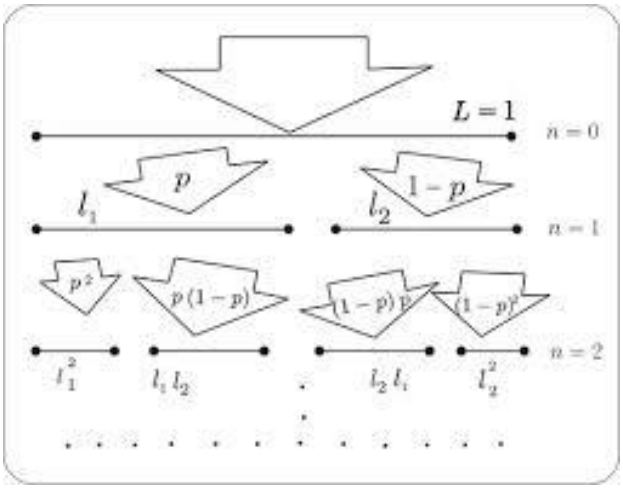

Fig. C.1 Schematic representation of the p-model, (one-dimensional cascade) where each breaking down into two new ones. The energy flux to smaller scales is divided into non-equal fractions *p* and 1-*p* until the Kolmogorov scale is reached.

breakage process, an energy fraction p_1 is distributed equally among one half of the λ_b^d new eddies, and the other, $p_2 = 1 - p_1$, is also distributed similarly among the other half (see Fig. C.1). The process is iterated until one reaches eddies the size of the Kolmogorov scale, η_K.

After *n* iterations we have λ_b^n eddies of equal size $r_{i+1} = L/\lambda_b^n$. In this set of turbulent eddies, there will be $\binom{n}{m}$ eddies with an energy flux density of $p_1^{n-m} \cdot p_2^m \cdot \tilde{\varepsilon}$, with $m = 0,1,....,n$. As a result, the probability distribution of the dissipation rate ε_λ follows a binomial distribution and their statistical moments can be written as

$$\left\langle \varepsilon_\lambda^{\,p} \right\rangle = \sum_{i=0}^{n} \binom{n}{m} p_1^{(n-m)p} \cdot p_2^{mp} \cdot \tilde{\varepsilon}^{\,p} = \tilde{\varepsilon}^{\,p} \cdot \left(p_1^{\,p} + p_2^{\,p} \right)^n \tag{C.19}$$

with scaling exponents

$$K(p) = log_{\lambda_b} \left(p_1^{\,p} + p_2^{\,p} \right) \tag{C.20}$$

Taking in account that $p_2 = 1 - p_1$, the scaling exponent of the *p*-order structure function $S_p(r)$ is

$$\zeta(p) = \frac{p}{3} - log_{\lambda_b} \left[p_1^{\frac{p}{3}} + \left(1 - p_1\right)^{\frac{p}{3}} \right] \tag{C.21}$$

and the power-spectrum exponent δ

$$\delta = 1 + \zeta(2) = \frac{5}{3} - log_{\lambda_b} \left[p_1^{\frac{2}{3}} + \left(1 - p_1\right)^{\frac{2}{3}} \right] \tag{C.22}$$

Experimental data fit remarkably well for values of $p_1 \approx 0.7$. Moreover, in their work Meneveau and Sreenivasan (1987) also included the possibility that eddies could also dissipate an amount of energy directly into the inertial subrange (i.e. $p_1 + p_2 < 1$). This gives a second free parameter p_2. Meneveau and Sreenivasan (1987) obtained a reasonable fit to the curve of $S_p(r)$ for values of $p_1 \approx 0.7$ and $p_2 \approx 0.3$, which provides an illustration of the robustness of the model.

D. Fractal dimension

To properly understand fractional dimensions we start by describing the concept of measuring dimension and using topological dimensions (one, two and three dimensions). A line (dimension $D=1$) of unit length L is cut into a segments. Thus, the scale ratio will be defined as $\lambda' = 1/a$. In Fig. D.1, the number of segments (copies) n per unit length and its line dimension are shown for the case $a=2$ (i.e. half-sized figure).

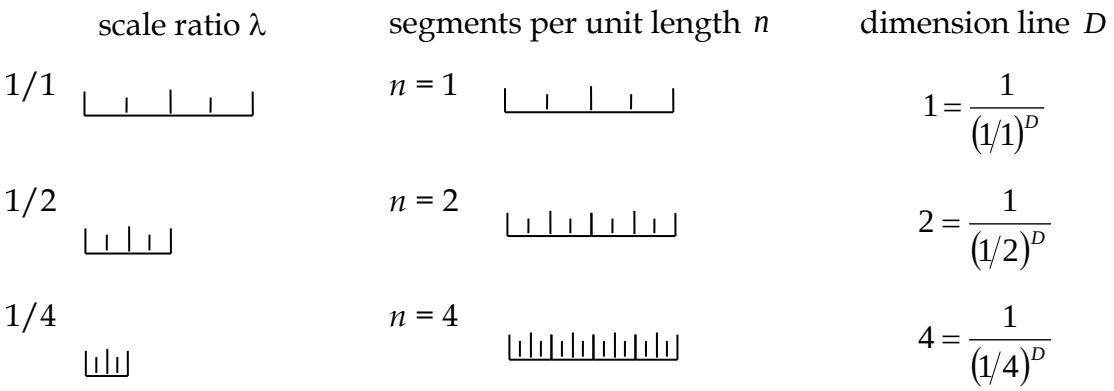

Fig. D.1 Examples of the scale ratio for a line (1D space) and the relation between the number of copies required to obtain the original and its dimension.

The relation between the number of segments *n* and the scale ratio λ' is obtained by raising the inverse of λ' to the appropriate dimension D as

$$n = \left(\frac{1}{\lambda'}\right)^D = (\lambda')^{-D} \tag{D.1}$$

Taking the same process for squares $D=2$, see in Fig. D.2 (this could also be done for cubes, $D=3$).

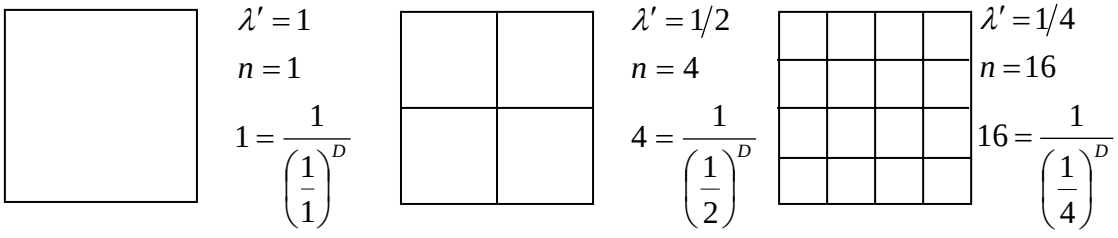

Fig. D.2 . Examples of the scale ratio for a square (2D space) and the relation between the number of copies required to obtain the original and its dimension.

From expression (D.1), fractal dimension D can be calculated as

$$D = \frac{\log(n)}{\log\left(\frac{1}{\lambda'}\right)} \tag{D.2}$$

where n is the number of copies at every iteration and λ' the scale ratio.

With the advent of fractal theory fractional dimensions have been able to be explored. Mandelbrot (1967) began his work on fractals by considering the question of 'How long is the coast of Britain?' As the coast is so irregular, estimations with a ruler depended greatly on the scale of the map used. As scale decreases, more details of the coastline appear and the measured length is longer. Mandelbrot showed that the relation between the scale ratio λ' and the length of the coastline L follows a power law as indicated in (D.1) with a non-integer value for the fractal dimension D.

Examples of fractal geometry are the Koch curve, the Monkey's tree and the Sierpinski triangle, among others (Baird, 2011). Here, we will develop in detail the first one of these, the Koch curve, which is one of the most well-known fractals.

The Koch curve is made from a straight line of length L, (called the initiator) which is then divided into three parts. The middle third is replaced with two lines, each of the same length (i.e. $L/3$) and the other segments remain on each side of the figure. The new object is called the generator, see Fig. D.3. In the following steps, each line is replaced by the generator and each new line has a length of one third ($\lambda' = 1/3$) of the original line. The result

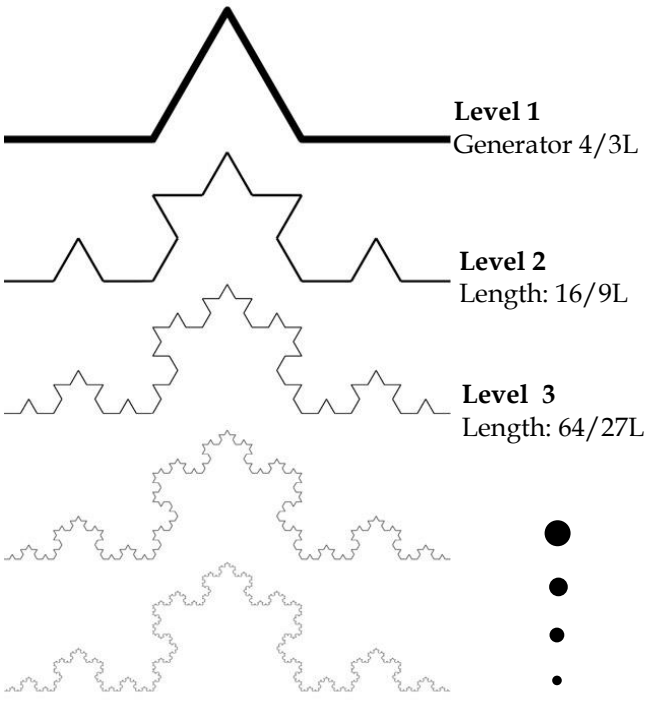

Fig. D.3 The Koch curve. The generator is plotted at the top. Successive steps are plotted in the figure. The length of the curve at each step is shown on the right.

for the first few iterations is shown in Fig. D.3, and then it is clear that the figure is self-similar. Note that the length of the Koch curve increases as the resolution improves: at the *j*th-step of the construction, the unit length is $(1/3)^j L$, but the total length has value of $(4/3)^j L$.

At the first level, the number of segments in the Koch curve is 4 (n = 4) and each line segment has been replaced by the generator scaled by $1/3$. This can also be done with the other levels and using (D.2), the fractal dimension of the Koch curve is

$$D = \frac{\log(4)}{\log(3)} = \frac{\log(16)}{\log(9)} = \ldots = \frac{\log\left(4^N\right)}{\log\left(3^N\right)} = \frac{\log(4)}{\log(3)} \approx 1.26$$

In classical geometry, the length of a curve remains the same independently of the level of resolution. Here, the fractal dimension indicates that the curve has a dimension higher than 1, because it effectively covers an area.

E. Multifractal behavior of the α-model

To describe the multifractal nature of the α-model, different steps of the cascade are shown (Schertzer and Lovejoy, 1983; Tessier et al., 1993). For example, the second step of the cascade generates three possible intensity levels, $\varepsilon_{2,i}^{*}$, (left) with probabilities (right)

$$\varepsilon_2^* \begin{cases} \lambda_b^{2\gamma^+} & \text{with prob.} \quad \lambda_b^{-2c} \ \text{(two boosts)} \\ \lambda_b^{\gamma^+ + \gamma^-} & \text{with prob.} \quad 2\,\lambda_b^{-c}\left(1-\lambda_b^{-c}\right) \ \text{(one boost / one decrease)} \\ \lambda_b^{2\gamma^-} & \text{with prob.} \quad \left(1-\lambda_b^{-c}\right)^2 \ \text{(two decreases)} \end{cases} \tag{E.1}$$

Considering that the scale of resolution is λ_b^2, which is denoted by λ, then the probabilities for the dissipation rate are expressed as

$$\varepsilon_\lambda^* \begin{cases} \lambda^{\gamma^+} & \text{with prob.} \quad \lambda^{-c} \\ \lambda^{\frac{\gamma^+ + \gamma^-}{2}} & \text{with prob.} \quad 2\lambda^{-\frac{c}{2}}\left(1-\lambda^{-\frac{c}{2}}\right) = 2\lambda^{-\frac{c}{2}} - 2\lambda^{-c} \\ \lambda^{\gamma^-} & \text{with prob.} \quad (1-\lambda^{-c}) = 1-2\lambda^{-\frac{c}{2}} + \lambda^{-c} \end{cases} \tag{E.2}$$

Iterating this procedure, after $n = n^+ + n^-$ steps, we find a hierarchy of singularities $\gamma_{n+,n-}$ with $\gamma^- < \gamma_{n+,n-} < \gamma^+$ where

$$\gamma_{n+,n-} = \frac{n^+\gamma^+ + n^-\gamma^-}{n^+ + n^-} \ \text{with } n^+=1,\ldots,n;\ n^- = n - n^+ \tag{E.3}$$

As a binomial process, the probability of the singularities is

$$Pr\left(\varepsilon_n^* = \left(\lambda_b^n\right)^{\gamma_{n+,n-}}\right) = \binom{n}{n^+} \lambda_b^{-cn^+} \cdot \left(1-\lambda_b^{-c}\right)^{n^-} \tag{E.4}$$

An example for two specific singularities γ_1 and γ_2 is shown in Fig. E.1.

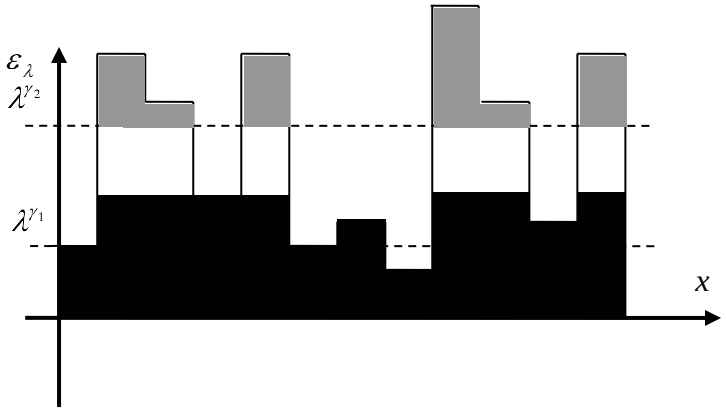

Fig. E.1 A schematic illustration of a multifractal field analyzed over a scale ratio λ, with two scaling thresholds λ^{γ_1} and λ^{γ_2} corresponding to two orders of singularity and with $\gamma_1 < \gamma_2$ (Schertzer and Lovejoy, 1993).

We can replace the cascade of n iterations with scale ratio λ_b at each step for a single step $n+1$ process with a scale ratio λ_b^n where the intensity levels ε_n are associated to a value of singularity γ_i with probability

$$Pr\left(\varepsilon_n^* = \left(\lambda_b^n\right)^{\gamma_i}\right) = \sum_{j=1}^{n} p_{ij} \cdot \left(\lambda_b^n\right)^{-c_{ij}} \qquad \text{(E.5)}$$

Here p_{ij} represents the weights of each fractal set of codimension c_{ij}. A fully-developed cascade is reproduced by analyzing the limit of $n >> 1$, i.e. $\lambda \to \infty$. Several steps are shown in Fig. E.2. Then, the smallest values of c_{ij} dominate in (E.5). Assigning $c_i = min_j\left(c_{ij}\right)$ to every order γ_i (E.5) is rewritten as

$$Pr\left(\varepsilon_n^* = \lambda^{\gamma_i}\right) = \lambda^{-c_i} \qquad \text{(E.6)}$$

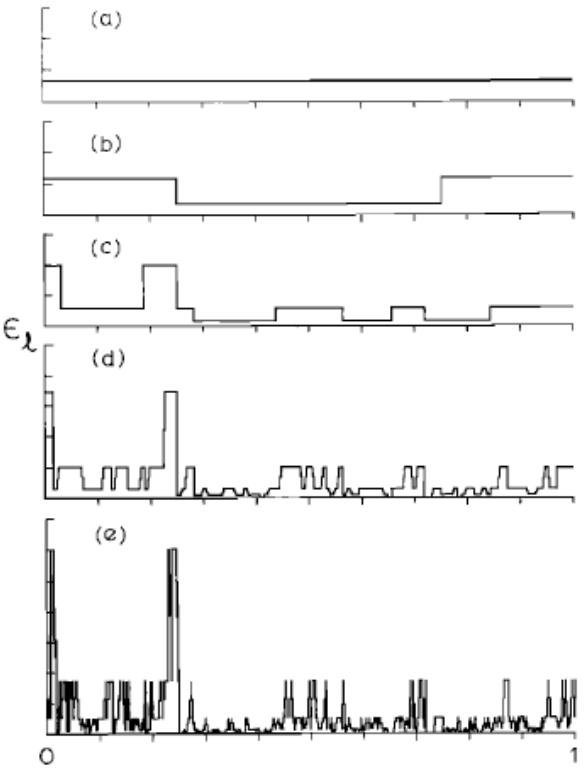

Fig. E.2 Representation of the α - model for five steps, starting with a homogeneous function and being systematically reduced by successive factors of 4. The parameters are chosen in such a way that the area under the curve is maintained at any stage. The model generates peaks that increase at each step (Seuront et al., 1999).

F. Properties of the scaling exponent *K(p)* function

F.1. Dual Legendre transforms

For a fully-developed cascade, it is possible to relate $K(p)$ to the codimension $c(\gamma)$. To deduce this, recall the moments of ε_λ scale as (see Appendix E)

$$\left\langle \varepsilon_n^p \right\rangle \sim \sum_i \lambda^{p\gamma_i} \cdot \lambda^{c_i} \tag{F.1}$$

and for $\lambda \to \infty$

$$\left\langle \varepsilon_\lambda^p \right\rangle \sim \sum_i \lambda^{p\gamma_i} \cdot \lambda^{c_i} \sim \int_0^\infty \lambda^{p\gamma - c} d\gamma \tag{F.2}$$

Approximating the integral using the method of steepest descent (Strikwerda, 2004) it yields

$$\left\langle \varepsilon_\lambda^p \right\rangle \sim \lambda^{max_\gamma (p\gamma - c(\gamma))} \tag{F.3}$$

where

$$K(p) = max_\gamma (p\gamma - c(\gamma)) \tag{F.4}$$

The codimension $c(\gamma)$ function can be obtained from (F.4) using the Mellin transformation $\hat{f}(q)$ which is defined (Flajolet and Sedgewick, 1995) as

$$\left\langle x^{q-1} \right\rangle = \hat{f}(q) = \int_0^\infty x^{q-1} \cdot f(x) \cdot dx \tag{F.5}$$

and also its inverse, $M^{-1}\left(\left\langle x^{q-1} \right\rangle\right)$

$$f(x) = \hat{f}^{-1}\left(\left\langle x^{q-1} \right\rangle\right) = \frac{1}{2\pi i} \int_{c-i\infty}^{c+i\infty} \left\langle x^{q-1} \right\rangle x^{-q} \cdot dq \tag{F.6}$$

If the inverse Mellin transformation is taken, $c(\gamma)$ is expressed as

$$c(\gamma) = \max_p (p\gamma - K(p)) \tag{F.7}$$

These expressions show that $K(p)$ can be obtained from $c(\gamma)$ and vice versa

$$K(p) = max_\gamma (p\gamma - c(\gamma)) \Leftrightarrow c(\gamma) = max_p (p\gamma - K(p)) \tag{F.8}$$

which are known as dual *Legendre transforms*.

From a graphical point of view, the Legendre transformations represent the value of γ (or p) which maximizes the distance between the line $p\gamma$ which crosses at the origin, and the function $c(\gamma)$ (or $K(p)$). Then, $c(\gamma)$ can be interpreted as the envelope of tangencies of $K(p)$ and reciprocally.

F.2. Divergence of the moments and probability distributions

The moments of the dissipation rate $\varepsilon_{\lambda,d}$ for a dressed quantity can be calculated as

$$\left\langle \varepsilon_{\lambda.d}^{p} \right\rangle \sim \int \varepsilon_{\lambda,d}^{p} d\,Pr \tag{F.9}$$

If the moments diverge, it is expected that there is a power-law upper tail in the probability distribution of $\varepsilon_{\lambda,d}$ expressed as

$$Pr\left(\varepsilon_{\lambda,d}^{/} \geq \varepsilon_{\lambda,d}\right) \sim \varepsilon_{\lambda,d}^{-a} \quad \text{with } a = p_D \tag{F.10}$$

Since the extreme events contribute most to the moments, (F.9) can be written as

$$\left\langle \varepsilon_{\lambda.d}^{p} \right\rangle \sim \int \varepsilon_{\lambda,d}^{p} d\,Pr \sim \int \varepsilon_{\lambda,d}^{p} \cdot \varepsilon_{\lambda,d}^{-a-1} d\varepsilon \tag{F.11}$$

From (F.11) it can be seen that there is a critical order p_D ($p_D = a$) at which the moments diverge (Bernardara et al., 2007). Then, for $p \geq p_D$ the moments are affected by the small-scale activity; for $p < p_D$ the small-scale activity remains statistically negligible. Veneziano and Langousis (2010) showed that these upper tails of $\varepsilon_{\lambda,d}$ became more difficult to observe as the scale resolution increases, and are negligible when $\lambda \to \infty$ even when taking large samples.

G. Lévy and log-Lévy probability distributions

G.1. Characteristic function of a random variable

In probability theory, properties of random variables can be analyzed by their characteristic functions, which are also used to proof several probability laws.

Let us consider a random variable X with probability density function $f_X(x)$. The characteristic function of X is the *inverse Fourier transform* of the probability density function $f_X(x)$ defined as

$$\varphi_X(t) = \int_{\Re} e^{itx} f_X(x) dx = \left\langle e^{itX} \right\rangle \tag{G.1}$$

Thus, there is a one-to-one correspondence between $\varphi_X(t)$ and $f_X(x)$.

Considering the moment-generating function of X , $M_X(t)$

$$M_X(t) = \left\langle e^{t \cdot X} \right\rangle \tag{G.2}$$

this can be related to $\varphi_X(t)$ using (G.1) as follows,

$$\varphi_X(t) = M_{iX}(t) = M_X(it) \tag{G.3}$$

Some of relevant properties for the characteristic functions are:

- The characteristic function of the sum of independent random variables corresponds to the product of the characteristic function of each of those variables, i.e.

$$\varphi_{X_1+X_2+\ldots+X_n}(t) = \varphi_{X_1}(t) \cdot \varphi_{X_2}(t) \cdot \ldots \cdot \varphi_{Xn}(t) \tag{G.4}$$

- If $a > 0$ and $b \in \mathbb{R}$, then

$$\varphi_{X+b}(t) = e^{ibt} \varphi_X(t) \tag{G.5}$$

$$\varphi_{aX}(t) = \varphi_X(at) \tag{G.6}$$

All these properties can be trivially deduced from the definition of $\varphi(t)$ (see (G.1)).

G.2. Previous Theorems

Let us consider a set of *n* random variables $\{X_i\}$, $i = 1,2,3,....,n \; \forall n \in \mathbb{N}$ which are identical, independent random variables equally distributed (iid) to a random variable X with probability distribution $F_X(x)$. Then it is verified that

$$\langle X_i \rangle = \langle X \rangle \tag{G.7}$$

$$Var(X_i) = \sigma^2 \tag{G.8}$$

and $$F_{X_i}(x_i) = F_X(x) \tag{G.9}$$

The averaged value $\overline{X}$ of the set is

$$\overline{X} = \frac{X_1 + ... + X_n}{n} = \frac{S_n}{n} \tag{G.10}$$

The mean and the variance of $\overline{X}$ are

$$\langle \overline{X} \rangle = \langle X \rangle \text{ and } Var(\overline{X}) = \frac{\sigma^2}{n} \tag{G.11}$$

and for the sum S_n

$$\langle S_n \rangle = n \langle X \rangle \text{ and } Var(S_n) = n\,\sigma^2 \tag{G.12}$$

If $\langle X \rangle$ is finite, then the *Law of the Large Numbers* (LLN) states that the average of S_n/n converges in probability to $\langle X \rangle$, i.e.

$$\frac{S_n}{n} \xrightarrow{d} \langle X \rangle \quad n \to \infty \tag{G.13}$$

Note that, no assumption for the variance σ^2 is required. Large or infinite variance will make the convergence slower, but the law of large numbers holds anyway.

Suppose now that $\langle X \rangle$ and σ^2 from an arbitrary distribution X are well-defined. Hence, from (G.7) and (G.8), *the Central Limit Theorem* (CLT) states that the mean and the sum of a random sample with sufficiently large size[2] will be normally distributed.

[2] A value of *n* greater than 25 is usually more than enough in practice to provide good approximations using the CLT.

Using (G.11) and (G.12) we obtain

- The **sample mean** $\overline{X} = \frac{1}{n}\sum_{i=1}^{n} X_i$ is normally distributed $\overline{X} \sim N\left(\langle X \rangle, \frac{\sigma^2}{n}\right)$.

  As a standardized random variable, it can be also written as $\overline{\mathrm{Z}} = \frac{\overline{\mathrm{X}} - \langle \mathrm{X} \rangle}{\sigma / \sqrt{\mathrm{n}}}$. Then $\overline{Z} \sim N(0,1)$ as $n \to \infty$.

- The **sample sum** $S_n = \sum_{i=1}^{n} X_i$ is normally distributed $S_n \sim N\left(n\langle X \rangle, n\sigma^2\right)$.

  As a standardized random variable, and it can be also written as $S_n^* = \frac{S_n - n\langle X \rangle}{\sqrt{n}\,\sigma}$ and $S_n^* \sim N(0,1)$ as $n \to \infty$.

As a consequence, for idd random variables, the sample mean and the sample sum belong to the *domain of attraction* of the normal distribution, which is known as an *attractor* distribution.

G.3. Attractor distributions

The form of CLT (as described above) is stated under specific conditions, that is, for finite values of $\langle X \rangle$ and σ^2. However, a more general form of CLT is defined to include other cases such as non-independent summands, non-equally distributed summands or infinite variance. For this latter case, the generalized Central Limit Theorem states that the partial sum S_n of a large number of iid random variables $\{X_i\}$ will approximate to a small set of limiting distributions (*attractor* distributions) and X belongs to a *domain of attraction* if there are two real series, $a_n > 0$ and $b_n \in \mathbb{R}$, such (Laha and Rohatgi, 1979) as

$$\frac{S_n - b_n}{a_n} \xrightarrow{d} F_X(x) \quad \text{as} \quad n \to \infty \tag{G.14}$$

Next, the generalized CLT is proven for two distributions: the Cauchy and the Gaussian distributions.

- Cauchy distribution:

Let us consider a set of *n* iid random variables, each with a standard Cauchy distribution $X \sim C(0,1)$. Then, its density probability distribution is

$$f_X(x) = \frac{1}{\pi(1+x^2)} \tag{G.15}$$

To prove the generalized CLT, the first step is to initially calculate the characteristic function of S_n, which can be obtained from (G.4) as

$$\varphi_{S_n}(t) = (\varphi_X(t))^n \tag{G.16}$$

Thus, it requires the characteristic function $\varphi_X(t)$ for the Cauchy distribution. This can be obtained using (G.1) and the Fourier transform tables (Spiegel, 1982) as

$$\varphi_X(t) = \int_{\Re} e^{itx} \frac{1}{1+x^2} dx = e^{-|t|} \tag{G.17}$$

Then replacing (G.17) in (G.16), it yields

$$\varphi_{S_n}(t) = e^{-n|t|} \tag{G.18}$$

From (G.18) the characteristic function of the sample mean S_n/n is

$$\varphi_{\frac{S_n}{n}}(t) = e^{-|t|} = \varphi_X(t) \tag{G.19}$$

and

$$\lim_{n\to\infty} \frac{S_n}{n} \xrightarrow{d} X \sim C(0,1) \tag{G.20}$$

which is in accordance with the generalized CLT.

- Normal distribution:

Let us consider a set of *n* iid random variables normally distributed $X_i \sim N(0,1)$. Following the same steps described in previous example for the Cauchy distribution, the characteristic function $\varphi_X(t)$ is calculated from (G.3) and (B.4) in Appendix B as

$$\varphi_X(t) = e^{\frac{(it)^2}{2}} = e^{-\frac{t^2}{2}} \tag{G.21}$$

Then, using (G.16), $\varphi_{S_n}(t)$ is

$$\varphi_{S_n}(t) = \left(e^{-\frac{1}{2}t^2} \right)^n = e^{-\frac{nt^2}{2}} \tag{G.22}$$

This equation allows us to determine the characteristic function of $S_n/\sqrt{n}$ as

$$\varphi_{\frac{S_n}{\sqrt{n}}}(t) = e^{-\frac{t^2}{2}} = \varphi_X(t) \tag{G.23}$$

And for large values of *n* we obtain

$$\lim_{n\to\infty} \frac{S_n}{\sqrt{n}} \xrightarrow{d} X \sim N(0,1) \tag{G.24}$$

which is in agreement with the generalized CLT.

G.4. Lévy distributions

G.4.1. Infinitely divisible distributions

A random variable X with a probability distribution F_X and characteristic function φ is *infinitely divisible* (F_X is an *infinitely divisible* law) if $\forall n > 0$ X has the same distribution as the sum of an arbitrary number of *n* iid random variables.

The Cauchy and the normal distributions are infinitely divisible, as shown next.

- <u>For Cauchy distribution:</u>

  By taking (G.18), it is straightforward to derive that $\varphi_{S_n}(t)$ also corresponds to the characteristic function of a Cauchy distribution $C(a,b)$ with $a = 0$ and $b = n$, i.e. $S_n \sim C(0,n)$ if the properties (G.5) and (G.6) are considered.

- For normal distribution:

  By taking (G.22), (G.3) and the expression of $M_x(t)$ for the general case of a variable $X \sim N(\mu,\sigma^2)$ normally distributed (Appendix B), then

  I
  t $M_x(t) = \langle e^{tX} \rangle = e^{\frac{1}{2}\sigma^2 t^2 + \mu t}$, (G.25)

  and it is seen that $\varphi_{S_n}(t)$ is also normally distributed $S_n \sim N(0, \sqrt{n})$.

  If S_n is normalized by a power of *n*, it has the same distribution as X. Consequently, they are infinitely divisible.

G.4.2. Lévy distributions

Let us consider, for example, the standard Cauchy distribution $X \sim C(0,1)$ which is infinitely divisible with $\varphi_{S_n}(t) = e^{-n|t|}$.

The normalized sample sum S_n/n is an invariant under addition and has the same distribution as *X*, i.e.

$$\varphi_{\frac{S_n}{n}}(t) = e^{-|t|} = \varphi_X(t) \quad \text{as} \quad n \to \infty \tag{G.26}$$

Then,

$$\frac{S_n}{n} \overset{d}{=} X \quad \text{for all } n \tag{G.27}$$

A similar conclusion can be obtained if the standard normal distribution $X \sim N(0,1)$ is considered. In this case, the normalized sample sum $S_n/\sqrt{n}$ also shows invariance under addition:

$$\varphi_{\frac{S_n}{\sqrt{n}}}(t) = e^{-\frac{t^2}{2}} = \varphi_X(t) \tag{G.28}$$

that is,

$$\frac{S_n}{\sqrt{n}} \overset{d}{=} X \quad \text{for all } n \tag{G.29}$$

Thus, both distributions have the same probability function F_X.

If other values of the power of *n* exist, (G.20) and (G.24) could be rewritten as

$$\frac{S_n}{n^{\frac{1}{\alpha}}} \xrightarrow{d} X \quad \text{for all } n \tag{G.30}$$

and from (G.26) and (G.28) it appears to be reasonable to attempt a probability distribution whose characteristic function equals

$$\varphi_X(t) = e^{-h|t|^\alpha} \text{ for } \alpha > 0 \text{ and } h > 0 \tag{G.31}$$

which does not represent any characteristic function for any value $\alpha > 2$. These are called *symmetric stable* distributions.

In a more general way, the distribution of *n* iid random variables is *stable* if there is a series $c_n > 0$ and d_n such that S_n verifies that

$$S_n \overset{d}{=} c_n \cdot X + d_n \tag{G.32}$$

It is *strictly stable* if $d_n = 0$, $\forall n \in \mathbb{N}$. The constants $c_n > 0$ are also called *scaling* constants and the constants d_n are known as *location* constants.

Stable distributions are also known as *Lévy distributions*. From (G.32) the variance of S_n for Lévy distributions can be expressed as

$$Var(S_n) = c_n^2 \, Var(X) \tag{G.33}$$

The variance is finite (in the normal distribution case, see (G.29)) for values of c_n equal to

$$c_n = n^{\frac{1}{2}} \tag{G.34}$$

In general,

$$c_n = n^{1/\alpha} \tag{G.35}$$

with infinite variance for $\alpha \neq 2$ and only the case $0 < \alpha \leq 2$ is possible (Feller, 1971). The index α is usually known as the *index of stability* or the *characteristic exponent* of the stable distribution.

Stability ensures that the sum of any number of random variables has, after scaling and translation operations, the same distribution as the individual summands themselves. Then, according to the generalized Central Limit Theorem, Lévy distributions are the only possible limit distributions, i.e. posses a domain of attraction. In line with Feller (1971), the analysis of Lévy

distributions can be considerably simplified because, in practice, the location constants d_n may be disregarded. Thus, a Lévy distribution $F_X(x)$ with an exponent $\alpha \neq 1$ can be centered in arbitrary manner and may be replaced by $F_X(x+d)$, which is strictly stable, being d the centering constant.

G.4.3. Characterization of Lévy distributions

The condition (G.32) does not allow for an analytical parameterization for Lévy distributions to be found exception some special cases (for example, normal and Cauchy distributions). However, there is a concrete way to characterize these distributions based on the general characteristic function $\varphi_X(t)$, described below.

If a random variable X is stable, there is a random variable Z which satisfies

$$X \overset{d}{=} cZ + d \qquad c > 0, \quad d \in \mathbb{R} \tag{G.36}$$

and has a characteristic function $\varphi_Z(t)$ defined by (Uchaikin and Zolotarev, 1999) as

$$\varphi_Z(t) = \left\langle e^{itZ} \right\rangle = \begin{cases} exp\left[-|t|^{\alpha} \cdot \left(1 - i\beta \cdot tan\left(\frac{\pi\alpha}{2} \right) \cdot sgn(t) \right) \right] & \alpha \neq 1 \\ exp\left[-|t| \cdot \left(1 - i\beta \cdot \frac{2}{\pi} \cdot sgn(t) \cdot log(t) \right) \right] & \alpha = 1 \end{cases} \qquad \begin{matrix} 0 < \alpha \leq 2 \\ -1 \leq \beta \leq 1 \end{matrix} \tag{G.37}$$

where $sgn(x)$ is the sign function. Note that $\varphi_Z(t)$ depends on two parameters, that is, α (the index of stability) and β, known as the *skewness parameter*, which takes the asymmetry of the probability distribution into account. Because of the probability distribution, $F_Z(z)$ is uniquely determined by its characteristic function $\varphi_Z(t)$ (see (G.1)), which also depend on two parameters, α and β.

Using (G.36) and (G.37), the probability distribution of X, $F_X(x)$, is obtained. This adds two more parameters, c and d, to completely determine $F_X(x)$, i.e. $F_X(x;\alpha,\beta,c,d)$. These four parameters are detailed next:

a) Location and scaling parameters:

- The *location parameter* $d \in \mathbb{R}$ and this shifts the distribution to the left or to the right.

- The *scaling (dispersion) parameter* $c > 0$ and is a measure of the sparseness of the data. The extreme value $c = 0$ indicates that X is totally concentrated on d, i.e. only a single value exists (degenerate distribution). Note that the normalized variable $Z = (X - d)/c$ will have the same shaped distribution with $d = 0$ and $c = 1$, i.e. $F_z(z;\alpha,\beta,1,0)$.

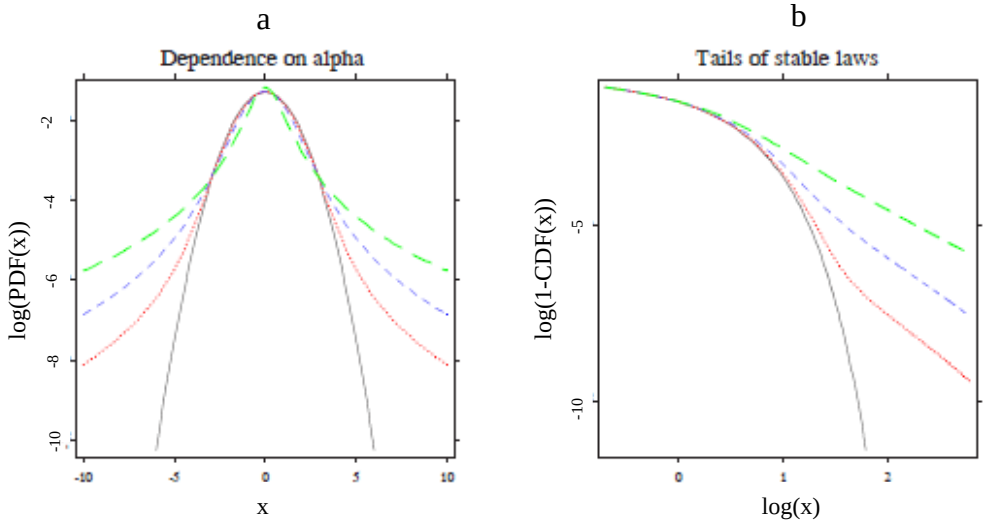

Fig. G.1 (a) Semi-logarithmic plot of symmetric Lévy distributions (β=0) for α = 2 (Gaussian distribution, in black), 1.8 (red), 1.5 (blue) and 1 (green) (b) Cumulative probability distribution plots for α = 2 (Gaussian distribution in black), 1.8 (red), 1.5 (blue) and 1(green). Note that only α = 2 has exponential tails (from Borak et al., 2005).

b) Shape parameters:

- The *index of stability* or *characteristic exponent*: This is directly related to the rate at which the tails of the distribution diminish (details are in the following subsection G.4.4., see also Fig. G.1) and $\alpha \in (0,2]$. To summarize, if $\alpha < 2$ the variance is infinite, whereas if $\alpha > 1$ the mean is finite and equals d (LLN, Section E.2) and if $\alpha \leq 1$ the mean is infinite.

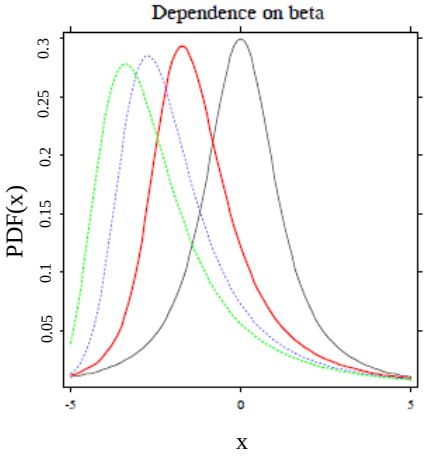

Fig.G.2 Lévy PDFs for $\alpha = 1.2$ and $\beta = 0$ (black), 0.5 (red), 0.8 (blue) and 1(green) (Borak et al., 2005).

- The *skewness parameter*: This parameter is a measure of the asymmetry of the distribution and $\beta \in [-1,1]$. For $\beta = 0$, the distribution is *symmetric* for d (normal and Cauchy distributions for example).

  For $\beta \neq 0$, the distribution is *asymmetric*: when $\beta > 0$ the distribution is skewed to the right; otherwise, it is skewed to the left (see Fig. G.2). For the extreme values $\beta = \pm 1$, Lévy distributions are distributions whose domain is $[d,+\infty)$($\beta = 1$) or (-∞, d] ($\beta = -1$). Otherwise, the domain of the probability distribution is the whole real line.

  As α tends to 2, the effect of β vanishes and the

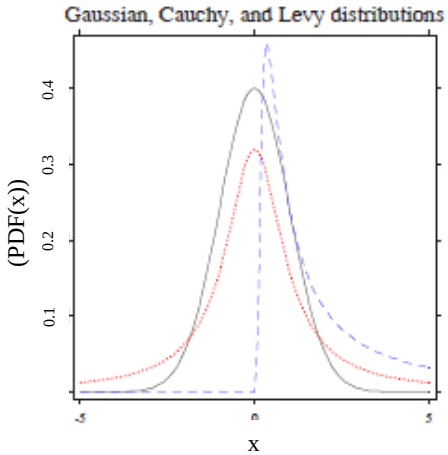

Fig. G.3 Plots of PDFs for α = 2 (Gaussian), α = 1 (Cauchy) and Lévy (α = 0.5, β = 1) for the case of d= 0. The latter is a totally skewed distribution, and its support is (0,+∞). For β = 1 (-1) the function is totally skewed to the right (left) (from Borak et al., 2005)

distribution approaches normal distribution regardless of β, see in Fig. G.3. Note also that from (G.37) they are symmetric if $\beta = 0$ and $d = 0$. Then,

$$\varphi_X(t) = e^{-c^\alpha |t|^\alpha} \tag{G.38}$$

G.4.4. Asymptotic expressions for Lévy distributions

One of the most important characteristics of Lévy distributions is the presence of power-law tails for values of $\alpha < 2$. This property can be derived using the generalized CLT and is detailed next for $\alpha < 1$ following Uchaikin and Zolotarev (1999) and Feller (1971) (the case for $\alpha > 1$ can also be deduced following the same steps as for $\alpha < 1$).

Let us consider a set of *n* iid random variables of a random variable X with strictly stable distribution F_X. Using (G.32) and (G.35), the sample mean S_n/n is equally distributed as $n^{-1+\frac{1}{\alpha}} \cdot X$, i.e.

$$\frac{S_n}{n} \overset{d}{=} n^{-1+\frac{1}{\alpha}} \cdot X \tag{G.39}$$

Note that the left-sided expression tends to ∞ for $n \to \infty$. This indicates that the sample mean S_n/n becomes considerably larger than any of the *n* terms X_i of the mean and this requires the existence of a maximum term M_n

$$M_n = max\{X_1, X_2, ..., X_n\} \tag{G.40}$$

which grows rapidly and dominates S_n.

The probability distribution $F_{M_n}(x) = P(M_n < x)$ implies that $F_{M_n}(x) = P(X_1 < x, X_2 < x, ..., X_n < x)$ and because they are iid random variables, this can be expressed as

$$F_{M_n}(x) = [P(X_i < x)]^n = F_X^n(x) \tag{G.41}$$

If M_n has the major contribution of S_n for $n \to \infty$, then the statistics of S_n are characterized by the probability distribution of M_n. The *survivor*

distribution $R_{S_n}(x)$, with $R_{S_n}(x) = P(S_n > x) = 1 - F_{S_n}(x)$, satisfy the following relation

$$R_{S_n}(x) \sim R_{M_n}(x) \text{ for } x \to \infty \tag{G.42}$$

Since X is a random variable with a stable distribution, then

$$R_{S_n}(x) = P(S_n > x) = P\left(n^{\frac{1}{\alpha}} X > x\right) = P\left(X > n^{-\frac{1}{\alpha}} \cdot x\right) = R_X\left(n^{-\frac{1}{\alpha}} \cdot x\right) \tag{G.43}$$

and from (G.41) and (G.42):

$$R_{S_n}(x) = 1 - F_x^n(x) \text{ can also be obtained} \tag{G.44}$$

Then,

$$R_X\left(n^{-\frac{1}{\alpha}} \cdot x\right) \sim R_X^n(x) \tag{G.45}$$

which can be related to F_X using the variable change $y = n^{-1/\alpha} \cdot x$ as

$$R_X(y) \sim 1 - \left[1 - R_X^n\left(n^{\frac{1}{\alpha}} \cdot y\right)\right] \sim n \cdot R_X\left(n^{\frac{1}{\alpha}} \cdot y\right) \qquad y \to \infty \tag{G.46}$$

The solution for this equation is (with $\beta \neq \pm 1$)

$$R_X(x) \sim A \cdot x^{-\alpha}, \; x \to \infty \tag{G.47}$$

and

$$F_X(-x) \sim B \cdot x^{-\alpha}, \; x \to \infty \tag{G.48}$$

which are known as *hyperbolic tails.*

G.4.5. Statistical moments of Lévy distributions

The existence of hyperbolic tails can cause the divergence of the statistical moments of the random variable X. Concretely, if X has a Lévy distribution with $0 < \alpha < 2$, its moments $M_X(p)$ diverge for $p > \alpha$

$$\left\langle X^p \right\rangle \begin{cases} < \infty & 0 < p \leq \alpha \\ \infty & p > \alpha \end{cases} \tag{G.49}$$

which is trivially deduced from (G.2) and the behavior of F_X for $x \to \infty$ as expressed in (G.47) and (G.48). For the normal distribution, $\alpha = 2$ all the *p*-order moments are well defined.

G.5. Log-Lévy distributions

G.5.1. Statistical moments of log-Lévy distributions

A random variable X has a log-Lévy distribution if the probability distribution of their logarithms, $Y = \log(X)$, follow a Lévy distribution.

The statistical moments of order $\langle Y^p \rangle$ can be expressed in terms of the moment-generating function of X, $M_X(t)$ as (Appendix B, see (B.6))

$$\left\langle Y^p \right\rangle = \left\langle e^{pX} \right\rangle = M_X(p) \tag{G.50}$$

which is the *Laplace transform* of X, $\mathcal{L}_X(p) \equiv \left\langle e^{pX} \right\rangle$. In turn, this is related to the characteristic function of X, $\varphi_X(t)$, see (G.3), as

$$\mathcal{L}_X(p) \equiv \left\langle e^{pX} \right\rangle = \varphi_X(it) \tag{G.51}$$

Recalling (G.5) and (G.6), $\varphi_X(t)$ can be expressed as (see (G.37))

$$\varphi_X(t) = e^{idt}\varphi(cZ) = \begin{cases} exp\left[idt - c^\alpha |t|^\alpha \cdot \left(1 - i\beta \cdot tan\left(\frac{\pi\alpha}{2} \right) \cdot sgn(t) \right) \right] & \alpha \neq 1 \\ exp\left[idt - c|t| \cdot \left(1 + i\beta \cdot \frac{2}{\pi} \cdot sgn(t) \cdot log(t) \right) \right] & \alpha = 1 \end{cases} \tag{G.52}$$

The corresponding Laplace transform can be obtained by replacing $t = p/i = -ip$. Note that the Laplace transform of X is not finite unless β takes the extreme value $\beta = -1$.

$$\mathcal{L}_X(p) \equiv \left\langle e^{pX} \right\rangle = \int_{-\infty}^{+\infty} e^{px} f_X(x;\alpha,\beta,c,d)dx \text{ with } f_X = \frac{dF_X}{dx} \sim x^{-(\alpha+1)} \tag{G.53}$$

For $\forall\beta \in (-1,1]$, the integral diverges because the Lévy distributions are two-sided heavy tailed (see subsection G.4.4) and, thus, $\lim_{x\to\infty} e^{px} f_X(x;\alpha,\beta,c,d) \to \infty$ (Note that $\lim_{x\to-\infty} e^{px} f_X(x;\alpha,\beta,c,d) \to 0$). On the other hand, if $\beta = -1$, Lévy distributions have only one hyperbolic tail, the left one, and the other decays exponentially. Then, $\lim_{x\to\pm\infty} e^{px} f_X(x;\alpha,\beta,c,d) \to 0$, and the Laplace transform $\mathcal{L}_X(p)$ is finite and statistical moments exist.

By replacing $t = p/i = -ip$ and $\beta = -1$ in (G.52), it is possible to obtain the expression for $M_X(p)$ ($\alpha \neq 1$) as

$$\begin{aligned} M_X(p) &= exp\left[d\,p - c^\alpha (-ip)^\alpha \left(1 + i \cdot tan\left(\frac{\pi\alpha}{2}\right)\right)\right] = \\ &= exp\left[dp - c^\alpha p^\alpha \left(1_{-\frac{\pi\alpha}{2}}\right) \cdot sec\left(\frac{\pi\alpha}{2}\right)_{\frac{\pi\alpha}{2}}\right] = \\ &= exp\left[d \cdot p - c^\alpha p^\alpha \; sec\left(\frac{\pi\alpha}{2}\right)\right] \end{aligned} \tag{G.54}$$

And for $= 1$, it is then

$$\begin{aligned} M_X(p) &= exp\left[d\,p - c(-ip)\left(1 - i \cdot \frac{2}{\pi} log(-ip)\right)\right] = \\ &= exp\left[dp + ic\,p \cdot \left(1 - \frac{2}{\pi} i \cdot log\left(pe^{-\frac{\pi}{2}i}\right)\right)\right] = \\ &= exp\left[dp + ic\,p \cdot \left(-\frac{2}{\pi} i \cdot log(p)\right)\right] = \\ &= exp\left[dp + \frac{2}{\pi} c\,p \cdot log(p)\right] = \end{aligned} \tag{G.55}$$

And finally,

$$M_X(p) = \begin{cases} exp\left[d \cdot p - c^\alpha p^\alpha \; sec\left(\frac{\pi\alpha}{2}\right)\right] & p > 0 \qquad \alpha \neq 1 \\ exp\left[d \cdot p + \frac{2c}{\pi} p\, log(p)\right] & p > 0 \qquad \alpha = 1 \end{cases} \tag{G.56}$$

G.5.2. Application of universality to scaling exponents $K(p)$

Let us consider the multiplicative cascade model for a conservative field ε. For the case $\alpha \neq 1$, at scale λ, the moments of the variable ε_λ can be expressed as

$$\left\langle \varepsilon_\lambda^p \right\rangle = \tilde{\varepsilon} \cdot exp\left[d \cdot p - c^\alpha p^\alpha \; sec\left(\frac{\pi\alpha}{2}\right)\right] \qquad p > 0 \tag{G.57}$$

which, in the multiplicative cascade framework, can also written as

$$\left\langle \varepsilon_\lambda^p \right\rangle = \left\langle e^{p\log(\varepsilon_\lambda)} \right\rangle \sim e^{K(q)\log(\lambda)} \tag{G.58}$$

where $\Gamma_\lambda = log(\varepsilon_\lambda)$ is usually known as the *generator* of ε_λ (Schertzer and Lovejoy, 1993). When comparing (G.58) to (G.57), the scaling exponents $K(p)$ of *p*-order moments are

$$K(p) = \frac{d \cdot p - c^\alpha p^\alpha \, sec\left(\frac{\pi\alpha}{2}\right)}{log(\lambda)} \tag{G.59}$$

Recalling that $K(0) = K(1) = 0$ (conservative and space-filling field) and $C_1 = K'(1)$, then

$$K(1) = 0 \Rightarrow d - c^\alpha \sec\left(\frac{\pi\alpha}{2}\right) = 0 \Rightarrow d = c^\alpha \sec\left(\frac{\pi\alpha}{2}\right) \tag{G.60}$$

$$K'(1) = C_1 \Rightarrow d - \alpha c^\alpha \sec\left(\frac{\pi\alpha}{2}\right) = C_1 \cdot \log(\lambda) \tag{G.61}$$

By taking the value of d and replacing this in the last equation we obtain a expression for the term $c^\alpha \, sec\left(\frac{\pi\alpha}{2}\right)$, that is

$$c^\alpha \, sec\left(\frac{\pi\alpha}{2}\right) = -\frac{C_1 \, log(\lambda)}{\alpha - 1} \tag{G.62}$$

Thus, $K(p)$ is

$$K(p) = \frac{c^\alpha \sec\left(\frac{\pi\alpha}{2}\right)}{\log(\lambda)}\left[p - p^\alpha\right] \tag{G.63}$$

$$K(p) = \frac{C_1}{\alpha - 1}\left(p^\alpha - p\right) \text{ for } \alpha \neq 1 \tag{G.64}$$